

**Physicochemical Characterisation of Zinc Oxide  
Nanoparticles for Use in Toxicity Studies**

**Rachel Wallace**

Submitted in accordance with the requirements for the degree of  
Doctor of Philosophy

The University of Leeds  
Institute for Materials Research  
School of Process Environmental and Materials Engineering  
Leeds, LS2 9JT  
United Kingdom

September 2013

The candidate confirms that the work submitted is her own, except where work which has formed part of jointly authored publications has been included. The contribution of the candidate and the other authors to this work has been explicitly indicated below. The candidate confirms that appropriate credit has been given within the thesis where reference has been made to the work of others.

### **List of Publications**

- 1) **Wallace, R.**, Brown, A. P., Brydson, R., Milne, S. J., Hondow, N., & Wang, P. (2012). Characterisation of ZnO nanoparticle suspensions for toxicological applications. *Journal of Physics: Conference Series*, 371, 012080. doi:10.1088/1742-6596/371/1/012080
- 2) **Wallace, R.**, Brown, a. P., Brydson, R., Wegner, K., & Milne, S. J. (2013). Synthesis of ZnO nanoparticles by flame spray pyrolysis and characterisation protocol. *Journal of Materials Science*, 48(18), 6393–6403. doi:10.1007/s10853-013-7439-x
- 3) Mu, Q., David, C. A., Galceran, J., Rey-Castro, C., Krzemiński, Ł., **Wallace, R.**, Bamiduro, F., Milne, S. J., Hondow, N. S., Brydson, R., Vizcay-Barrena, G., Routledge, M. N., Jeuken, L. J. C., and Brown, A. P. A systematic investigation of the physico-chemical factors that contribute to the toxicity of ZnO nanoparticles. Submitted to *Particle and Fibre Toxicology*, July 2013.
- 4) David, C. A., Galceran, J., Rey-Castro, C., Puy, J., Companys, E., Salvador, J., **Wallace, R.**, Vakourov, A. (2012). Dissolution Kinetics and Solubility of ZnO Nanoparticles Followed by AGNES. *The Journal of Physical Chemistry C*, 116(21), 11758–11767. doi:10.1021/jp301671b
- 5) Churchman, A. H., **Wallace, R.**, Milne, S. J., Brown, A. P., Brydson, R., & Beales, P. A. (2013). Serum albumin enhances the membrane activity of ZnO nanoparticles. *Chemical communications (Cambridge, England)*, 49(39), 4172–4. doi:10.1039/c3cc37871c
- 6) Vakourov, A., Lopez, G. M., Drummond-Brydson, **Wallace, R.**, Svendsen, C., & Nelson, A. (2013). ZnO nanoparticle interactions with phospholipid monolayers. *Journal of Colloid and Interface Science*, 404, 161–168. doi:10.1016/j.jcis.2013.05.010
- 7) Adam, N., Schmitt, C., Galceran, J., Companys, E., Vakourov, A., **Wallace, R.**, Knapen, D., Blust, R. (2013). The chronic toxicity of ZnO nanoparticles and ZnCl<sub>2</sub> to *Daphnia magna* and the use of different methods to assess nanoparticle aggregation and dissolution. *Nanotoxicology*. doi:10.3109/17435390.2013.822594

All of the work contained within publication 1) is directly attributable to R. Wallace under the guidance of academic supervisors R. Brydson, S.J. Milne and A.P. Brown, and is discussed in Chapters 3 and 6. The majority of the work in publication 2) was undertaken by R. Wallace with the exception of the synthesis of the ZnO NPs and all data is discussed in Chapters 3 and 5. For publications 3, 4, 5, 6 and 7, R. Wallace provided the physicochemical characterisation data presented in the paper for the ZnO NPs used in the investigation. Results of publication 3 are discussed and presented in Chapters 6 and 7. Results of publication 4 are discussed in Chapters 2 and 6; results of publication 5 are discussed in Chapter 6; and results of publication 6 are discussed in Chapter 1.

This copy has been supplied on the understanding that it is copyright material and that no quotation from the thesis may be published without proper acknowledgement.

© 2012 The University of Leeds and Rachel Wallace.

## Acknowledgements

Firstly, I would like to extend my gratitude to my supervisors, Prof. Rik Brydson Dr Andrew Brown and Dr Steve Milne; without their continuous support and guidance, this project would not have been possible and I would most certainly have thrown in the towel before now!

I would also like to give thanks to Nicole Hondow who helped me to make sense of numerous scientific conundrums I encountered during my PhD. I must also offer my sincere gratitude to all those who have provided me with experimental training and assistance throughout the course of this study, especially Dr Mike Ward who trained me on the TEM, and John Harrington who trained me on the SEM (both Leeds Electron Microscopy and Spectroscopy Centre, LEMAS). I would also like to thank Dr Tim Comyn for his support with XRD, and also Dr Adrian Cunliffe, Miss Sara Dona (Energy Research Institute) and Mr Stuart Micklethwaite (now of LEMAS) for their assistance with ICP-MS, TGA and FTIR spectroscopy. For data collection by XPS, I would like to thank Ben Johnson.

Further thanks must be expressed to Prof Alice Warley and Dr Gema Vizcay-Barrena of the Centre for Ultrastructural Imaging, King's College London for the preparation of the TEM thin sections. I would like to express my gratitude to Kay White and Rachel Mu for the work involving toxicity assays. I would like to extend thanks and to everyone involved on the ENNSATOX project for numerous scientific discussions. The work leading to these results has received funding from the European Union Seventh Framework Programme (FP7-NMP-2008-1.3-2) under grant agreement n° 229244. Finally, I would like to gratefully acknowledge the EPSRC for their sponsorship of this project.

To Peter Newman, I would like to say a big thank you for all of the support I was given throughout the process; and last, but by no means least, I would like to give special thanks to my parents Alan and Rosemary Wallace; I would not be where I am today if it wasn't for you both.



## Abstract

This thesis is focused on the detailed physicochemical characterisation of zinc oxide (ZnO) nanoparticles (NPs) intended for use in toxicological investigations. A characterisation protocol has been developed in order to determine detailed physicochemical characteristics of 5 ZnO NP samples, selected to investigate in *in vitro* toxicity assays. The characterisation protocol aims to establish the samples' distribution of particle sizes, morphology, crystallinity, phase content, purity, surface composition, dispersion and solubility and as such includes the following techniques: inductively coupled plasma mass spectrometry (ICP-MS), X-ray diffraction (XRD), BET gas adsorption, thermogravimetric analysis with evolved gas analysis by Fourier transform infra-red spectroscopy (TGA-EGA with FTIR), FTIR, X-ray photoelectron spectroscopy (XPS), nuclear magnetic resonance spectroscopy (NMR), scanning electron microscopy (SEM), transmission electron microscopy (TEM), dynamic light scattering (DLS), plunge freezing transmission electron microscopy (PF-TEM) and Zeta potential measurement. Initially 12 commercial samples were sourced and screened using TEM to obtain information on the average particle size. 3 of the commercial samples were then selected to carry forward to toxicity studies: EN-Z-1, EN-Z-2 and EN-Z-3. Synthesis of ZnO NPs was investigated in house by a flame spray pyrolysis and a polyol route; 2 synthesized samples were carried forward to the toxicity studies: EN-Z-4 and EN-Z-6. A coating was detected on the surface of EN-Z-1 (a colloidal suspension in water), identified as an aliphatic polyether (TGA-EGA, FTIR, XPS and NMR). Physically and chemically adsorbed H<sub>2</sub>O and CO<sub>2</sub> was detected at the surface of the other 4 samples, which were all dry powders. A small amount hydrozincite was present in EN-Z-2 and EN-Z-3, identified by XRD, TGA-EGA, FTIR, XPS and NMR. Additionally, a small amount of diethylene glycol was identified on the surface of EN-Z-6, left over from synthesis.

The dispersion and solubility of the samples in water, Dulbecco's modified Eagle Medium (DMEM) and bovine serum albumin (BSA) was investigated by DLS, PF-TEM and ICP-MS the results of which are presented in Chapter 6. Most samples showed similar dissolution kinetics and equilibrium solubility with the exception of EN-Z-1 which showed slower dissolution, presumably due to the coating present on

the NPs. Due to the equilibrium solubility of ZnO in DMEM, for concentrations of ZnO below 10  $\mu\text{g/ml}$ , a significant amount is dissolved or re-precipitated as zinc carbonate. The agglomeration and solubility of ZnO NPs was found to increase when suspended in DMEM as compared to in water. The solubility of ZnO was found to increase with decreasing solution temperature (37 and 25  $^{\circ}\text{C}$ ). The addition of BSA was found to have a dispersing effect on ZnO NP suspensions. PF-TEM was investigated as an alternative technique to DLS for measuring size distributions of ZnO NPs in suspensions. It was determined that PF-TEM measurements give an accurate representation of the range of agglomerates in the suspension, however the sampling size is very low and data processing is time consuming and therefore the technique should be used as a complementary technique to DLS.

The cytotoxicity and genotoxicity of ZnO NPs was assessed using the MTT (thiazolyl blue tetrazolium bromide) and comet assay respectively. A lower toxicity was measured for ZnO NP powder samples as compared to the coated colloidal dispersion. The polymer coating enhances NP interaction with lipid membranes which may increase toxicity through increased cellular uptake followed by intracellular dissolution. Coated and uncoated ZnO NPs are taken up by A549 cells and were located in both the cytoplasm and the nucleus. In cells exposed to 100  $\mu\text{g/ml}$  EN-Z-4 and EN-Z-6, smaller than primary particle size NPs were located in the cells, suspected to be zinc carbonate particles formed from dissolved zinc precipitating from solution in the extracellular or intracellular environment.

# Table of Contents

<b>Acknowledgements</b> .....	<b>IV</b>
<b>Abstract</b> .....	<b>V</b>
<b>Table of Contents</b> .....	<b>VII</b>
<b>List of Figures</b> .....	<b>XII</b>
<b>List of Tables</b> .....	<b>XXIII</b>
<b>List of symbols and abbreviations</b> .....	<b>XXV</b>
<b>1 Introduction</b> .....	<b>1</b>
1.1.1 Thesis Overview.....	2
1.2 Nanoparticles – Properties and Applications .....	3
1.2.1 What are Nanoparticles? .....	3
1.2.2 Applications of Nanoparticles.....	3
1.3 Nanotoxicity .....	5
1.3.1 Toxicity of Nanoparticles to Mammals .....	5
1.3.2 Toxicity of Nanoparticles to the Environment.....	6
1.3.3 Characteristics Affecting Toxicity .....	7
1.3.3.1 Size.....	7
1.3.3.2 Agglomeration of Nanoparticles.....	8
1.3.3.3 Morphology .....	8
1.3.3.4 Surface Composition.....	9
1.3.3.5 Solubility of Nanoparticles .....	9
1.3.4 Nanotoxicity Assessment.....	10
<b>2 Zinc Oxide</b> .....	<b>12</b>
2.1 Structure, Properties and Applications.....	12
2.2 Synthesis of ZnO Nanoparticles .....	13
2.2.1 Precipitation of Nanoparticles from Solution .....	15
2.2.2 Polyol Mediated Synthesis.....	16
2.2.3 Flame Spray Pyrolysis .....	20
2.3 Zinc Oxide Nanoparticle Toxicology.....	21
2.3.1 Mammalian Toxicity.....	21

2.3.2	Environmental Toxicity .....	23
2.3.3	Factors Effecting ZnO Nanoparticle Characteristics in Solution.....	24
2.3.3.1	Solubility.....	24
2.3.3.2	Agglomeration State .....	26
<b>3</b>	<b>Experimental Methods .....</b>	<b>29</b>
3.1	Synthesis of ZnO Nanoparticles .....	29
3.1.1	Polyol Synthesis of ZnO Nanoparticles .....	29
3.1.2	Flame Spray Pyrolysis Synthesis of ZnO Nanoparticles .....	30
3.2	Characterisation of ZnO Nanoparticles.....	32
3.2.1	Bulk Sample Characteristics .....	32
3.2.1.1	Inductively Coupled Plasma Mass Spectrometry .....	32
3.2.1.2	X-ray Diffraction .....	33
3.2.1.3	Gas Adsorption (BET).....	34
3.2.1.4	Thermogravimetric Analysis and Evolved Gas Analysis by Fourier transform infrared spectroscopy.....	35
3.2.2	Surface Characterisation .....	35
3.2.2.1	Fourier Transform Infrared Spectroscopy .....	35
3.2.2.2	X-ray Photoelectron Spectroscopy .....	36
3.2.2.3	Carbon 13 Nuclear Magnetic Resonance Spectroscopy .....	37
3.2.3	Nanoparticle Characterisation.....	39
3.2.3.1	Scanning Electron Microscopy.....	39
3.2.3.2	Transmission Electron Microscopy .....	39
3.2.4	Solution Characteristics .....	41
3.2.4.1	Inductively Coupled Plasma Mass Spectrometry .....	41
3.2.4.2	Zeta Potential .....	42
3.2.4.3	Dynamic Light Scattering.....	43
3.2.4.4	Plunge Freezing - Transmission Electron Microscopy.....	44
3.3	Alternative Techniques for Characterizing Nanoparticles in Solutions.....	49

3.3.1.1	Atmospheric Scanning Electron Microscope .....	49
3.3.1.2	Liquid Cell Transmission Electron Microscope .....	50
3.4	Toxicological Assays .....	51
3.4.1	MTT Assay .....	51
3.4.2	Comet Assay .....	52
3.4.3	Statistical Analysis of Toxicity Data .....	54
3.4.4	Uptake Studies .....	55
<b>4</b>	<b>Characterisation of Commercially Sourced ZnO Nanoparticle samples....</b>	<b>56</b>
4.1	Review of Commercial ZnO Nanoparticle samples.....	56
4.2	Characterisation Protocol .....	62
4.2.1	Bulk Sample Characterisation.....	62
4.2.1.1	Inductively Coupled Plasma-Mass Spectrometry.....	62
4.2.1.2	X-ray Diffraction .....	63
4.2.1.3	Gas Adsorption (BET).....	65
4.2.1.4	Thermogravimetric Analysis with Evolved Gas Analysis by Fourier Transform Infrared Spectroscopy.....	70
4.2.2	Surface Characterisation .....	75
4.2.2.1	Fourier Transform Infrared Spectroscopy .....	75
4.2.2.2	X-ray Photoelectron Spectroscopy .....	77
4.2.2.3	Nuclear Magnetic Resonance Spectroscopy.....	83
4.2.3	Nanoparticle Characterisation.....	84
4.2.3.1	Scanning Electron Microscopy.....	84
4.2.3.2	Transmission Electron Microscopy .....	85
4.2.3.3	Dynamic Light scattering.....	90
4.3	Summary .....	94
<b>5</b>	<b>Synthesis and Characterisation of ZnO Nanoparticles .....</b>	<b>95</b>
5.1	ZnO Nanoparticles prepared by the Polyol Route .....	95
5.2	ZnO Nanoparticles Prepared by Flame Spray Pyrolysis Technique .....	110
5.3	Characterisation Protocol .....	116

5.3.1	Bulk Sample Characteristics .....	116
5.3.1.1	Inductively coupled plasma-mass spectroscopy.....	116
5.3.1.2	X-ray Diffraction .....	118
5.3.1.3	Gas Adsorption (BET).....	118
5.3.1.4	Thermogravimetric Analysis with Evolved Gas Analysis by Fourier Transform Infrared Spectroscopy.....	120
5.3.2	Surface Characterisation .....	124
5.3.2.1	Fourier Transform infrared Spectroscopy.....	124
5.3.2.2	X-ray Photoelectron Spectroscopy .....	130
5.3.2.3	Nuclear Magnetic Resonance Spectroscopy.....	136
5.3.3	Nanoparticle Characterisation.....	137
5.3.3.1	Scanning Electron Microscopy.....	137
5.3.3.2	Transmission Electron Microscopy .....	138
5.3.3.3	Dynamic Light Scattering.....	142
5.4	Summary .....	145
<b>6</b>	<b>Dispersion and Solubility of Zinc Oxide Nanoparticles in Solution.....</b>	<b>148</b>
6.1	Solubility of ZnO Nanoparticles .....	149
6.1.1	Dissolution of ZnO Nanoparticles in Varying Media.....	150
6.1.2	ZnO Dissolution Kinetics and Equilibrium Solubility.....	152
6.2	Colloidal Stability of ZnO NPs in Suspension.....	163
6.2.1	Zeta Potential .....	163
6.2.2	Dynamic Light Scattering .....	164
6.2.2.1	ZnO Nanoparticle Colloidal Stability Over Time.....	164
6.2.2.2	Dispersion of ZnO Nanoparticles in Water at Varying Concentrations.....	170
6.2.2.3	Dispersion of ZnO Nanoparticles in Cell Culture Media (with and without serum proteins).....	171
6.2.3	Plunge Freezing Transmission Electron Microscopy .....	175

6.2.3.1	Dispersion of ZnO Nanoparticles in Water at Varying Concentrations.....	176
6.2.3.2	Agglomerate Size Distributions by Plunge Freezing Transmission Electron Microscopy .....	182
6.2.3.3	Dispersion of ZnO Nanoparticles in Biological Media .....	184
6.2.3.4	Agglomerate Size Distributions by Plunge Freezing Transmission Electron Microscopy .....	188
6.3	Comparison of Agglomerate Size Distributions Measured by Plunge Freezing Transmission Electron Microscopy and Dynamic Light Scattering Techniques .....	191
6.3.1	Alternative Techniques for Imaging Nanoparticle Dispersions.....	193
6.3.1.1	Atmospheric Scanning Electron Microscope .....	194
6.3.1.2	Liquid Cell Transmission Electron Microscopy.....	196
6.4	In Summary .....	198
<b>7</b>	<b>Toxicity of ZnO Nanoparticles and Discussion .....</b>	<b>202</b>
7.1	Summary of ZnO Nanoparticle Physicochemical Characteristics .....	202
7.2	Toxicity .....	205
7.2.1	Cytotoxicity.....	205
7.2.2	Genotoxicity .....	212
7.2.3	Cellular Uptake .....	215
7.3	In Summary .....	228
<b>8</b>	<b>Summary of Findings and Conclusions .....</b>	<b>231</b>
8.1	Future Work .....	234
	<b>References .....</b>	<b>236</b>

## List of Figures

Figure 2-1 The wurtzite structure of ZnO with the tetrahedral coordination of Zn - O shown with solid line connections (Vaseem et al., 2010).....	13
Figure 2-2 Plot of La Mer model for the generation of atoms, nucleation, and subsequent growth of NPs (Nguyen & Do, 2011, adapted from La Mer and Dinegar, 1950) .....	15
Figure 2-3 Factors effecting the dissolution of nanomaterials (Misra et al. 2012)....	25
Figure 2-4 Representation of DLVO theory showing the change in potential energy with increasing particle separation.....	27
Figure 3-1 Schematic of the FSP process for ZnO NP synthesis (Tani et al., 2002).	31
Figure 3-2 Schematic diagram of the XPS process showing photoionization of an atom by the ejection of a 1s electron (Watts and Wolstenholme, 2003).....	37
Figure 3-3 PF-TEM images of 10nM QTracker 705 CdTe/ZnS quantum dots; (a) sample kept frozen and imaged in a cryo-TEM; (b) TEM image of the same cluster of particles warmed up in the microscope. (Hondow et al., 2012) .....	46
Figure 3-4 ASEM with inverted SEM structure. An optical microscope is arranged above the SEM with the specimen dish in between. The removable dish features a SiN window (Nishiyama et al., 2010).....	49
Figure 3-5 TEM imaging of NPs in a liquid fully enclosed between two electron transparent silicon nitride membranes (adapted from de Jonge & Ross, 2011).....	50
Figure 3-6 Fluorescence microscope images of A549 cells after exposure to 10 µg/ml ZnO; (a) undamaged cell with DNA intact and (b) damaged cell with DNA in the tail.....	52
Figure 4-1 Results of ICP-MS total quant analysis reporting the concentration of each element present in the sample. ....	63
Figure 4-2 XRD pattern for (a) EN-Z-1 (b) EN-Z-2 and (c) EN-Z-3 commercial ZnO NP samples, with the Miller indices for the reflecting plane labelled. Peaks corresponding to a secondary phase, thought to be hydrozincite, are labelled with an asterix .....	64
Figure 4-3 BET adsorption – desorption isotherm for EN-Z-1.....	68
Figure 4-4 BET adsorption – desorption isotherm for EN-Z-2.....	69



Figure 4-5 BET adsorption – desorption isotherm for EN-Z-3.....	69
Figure 4-6 (a) TGA curve for EN-Z-1 showing loss of sample mass with increasing temperature; (b) associated Gram-Schmidt plot showing increase in FTIR absorbance with increasing temperature and (c) Chemigrams showing FTIR absorbance for specified ranges of wavenumber as temperature rises. ....	72
Figure 4-7 (a) TGA curve for EN-Z-2 showing loss of sample mass with increasing temperature; (b) Gram-Schmidt plot showing increase in FTIR absorbance with increasing temperature and (c) Chemigrams showing FTIR absorbance for specified ranges of wavenumber as temperature rises.....	73
Figure 4-8 (a) TGA curve for EN-Z-3 showing loss of sample mass with increasing temperature; (b) Gram-Schmidt plot showing increase in FTIR absorbance with increasing temperature and (c) Chemigrams showing FTIR absorbance for specified ranges of wavenumber as temperature rises.....	74
Figure 4-9 FTIR spectra obtained for (a) EN-Z-1 (b) EN-Z-2 and (c) EN-Z-3.....	77
Figure 4-10 XPS survey scans for (a) EN-Z-1, (b) EN-Z-2 and (c) EN-Z-3 commercial ZnO samples.....	78
Figure 4-11 XPS spectrum of Zn2p for (a) ) EN-Z-1, (b) EN-Z-2 and (c) EN-Z-3 commercial ZnO samples.....	79
Figure 4-12 The O1s XPS spectrum of (a) EN-Z-1, (b) EN-Z-2 and (c) EN-Z-3 commercial ZnO samples, fitted to three kinds of oxygen species.....	81
Figure 4-13 The C1s XPS spectrum of (a) EN-Z-1, (b) EN-Z-2 and (c) EN-Z-3 commercial ZnO samples, fitted to three kinds of carbon species.....	82
Figure 4-14 The <sup>13</sup> C NMR sprectra for (a) EN-Z-1, (b) EN-Z-2 and (c) EN-Z-3 .....	84
Figure 4-15 SEM images of (a) EN-Z-1, (b) EN-Z-2 and (c) EN-Z-3 commercial ZnO samples. ....	85
Figure 4-16 EN-Z-1 (a) TEM image of a typical cluster of NPs (b) histograms to show the variation in particle length, width and Feret ratio. (c) Higher resolution image of a single particle showing crystal planes. (d) SAED pattern and (e) EDX spectrum obtained from the cluster of particles in (a).....	86
Figure 4-17 EN-Z-2 (a) TEM image of a typical cluster of NPs (b) histograms to show the variation in particle length, width and Feret ratio. (c) Higher resolution	

image of a single particle showing crystal planes. (d) SAED pattern and (e) EDX spectrum obtained from the cluster of particles in (a).....	87
Figure 4-18 EN-Z-3 (a) TEM image of a typical cluster of NPs (b) histograms to show the variation in particle length, width and Feret ratio. (c) Higher resolution image of a single particle showing crystal planes. (d) SAED pattern and (e) EDX spectrum obtained from the cluster of particles in (a).....	88
Figure 4-19 Light scattering profile for 1000 µg/ml suspension of (a) EN-Z-1, (b) EN-Z-2 and (c) EN-Z-3 ZnO NPs dispersed in MilliQ water taken after 20 minutes of ultrasonication.....	93
Figure 5-1 XRD patterns for (a) DEGSYN-0.15-100-1, (b) DEGSYN-0.45-100-1 and (c) DEGSYN-0.90-100-1 ZnO samples with the Miller indices for the reflecting planes labeled above each peak.....	96
Figure 5-2 Schematic illustration of the atomic structure of wurtzite ZnO showing the directions of the 0001 (c axis) and 1010 (a axis) atomic planes. ....	97
Figure 5-3 TEM images of ZnO NPs produced by precipitation under reflux conditions using varying concentrations of ZnAc precursor (a) (b) Degsyn-0.15-100-1, (c) (d) Degsyn-0.45-100-1 and (e) (f) Degsyn-0.90-100-1 .....	100
Figure 5-4 Graph showing the effect of precursor (ZnAc) concentration on the average size of the synthesized ZnO NPs. Error bars for TEM data based on standard deviation from 250 NP measurements. ....	101
Figure 5-5 XRD patterns obtained for (a) Degsyn-0.15-250-1, (b) Degsyn-0.15-250-2, (c) Degsyn-0.45-250-1 and (d) Degsyn-0.45-250-2. ....	102
Figure 5-6 TEM images of (a) Degsyn-0.15-250-1 with an average crystallite length of $30 \pm 24$ nm and width of $19 \pm 15$ nm and an average spherical cluster diameter of $670 \pm 340$ nm, (b) Degsyn-0.15-250-2 with an average crystallite length of $35 \pm 23$ nm and width of $23 \pm 14$ nm and an average spherical cluster diameter of $790 \pm 220$ nm, (c) Degsyn-0.45-250-1 with an average crystallite length of $45 \pm 28$ nm and width of $25 \pm 10$ nm and (d) Degsyn-0.45-250-2 with an average crystallite length of $47 \pm 26$ nm and width of $26 \pm 8$ nm.....	103
Figure 5-7 XRD patterns for (a) Degsyn-0.15-100-2, (b) Degsyn-0.15-100-3, (c) Degsyn-0.45-100-2 and (d) Degsyn-0.45-100-3.....	106

Figure 5-8 TEM images of ZnO NPs prepared by polyol route: (a) Degsyn-0.15-100-2 with an average crystallite length of $32 \pm 18$ and width of $20 \pm 8$ nm and an average spherical cluster size of $620 \pm 250$ nm, (b) Degsyn-0.15-100-3 with an average crystallite length of $29 \pm 12$ and width of $21 \pm 9$ nm and an average spherical cluster size of $800 \pm 310$ nm, (c) Degsyn-0.45-100-2 with an average crystallite length of $42 \pm 13$ and width of $22 \pm 7$ nm, (d) Degsyn-0.45-100-3 with an average crystallite length of $37 \pm 11$ and width of $21 \pm 5$ nm.....	108
Figure 5-9 XRD pattern for (a) FSP 11 (b) FSP 14 and (c) FSP 18 synthesized ZnO NP samples with the Miller indices for the reflecting planes .....	112
Figure 5-10 TEM images of (a) FSP 11 (b) FSP 14 and (c) FSP 18. Size distributions determined by measurement of 250 particles are (a) Feret length = $14 \pm 6$ nm, Feret width = $10 \pm 5$ nm, and Feret ratio = $1.4 \pm 0.15$ , (b) Feret length = $18 \pm 12$ nm, Feret width = $12 \pm 5$ nm and Feret ratio = $1.50 \pm 0.3$ and (c) Feret length = $23 \pm 8$ nm, Feret width = $14 \pm 4$ nm and Feret ratio = $1.64 \pm 0.4$ .....	115
Figure 5-11 Results of ICP-MS analysis reporting the concentrations of each element present in EN-Z-4 and EN-Z-6, with elemental concentrations in nitric acid blank subtracted. ....	117
Figure 5-12 BET adsorption – desorption isotherm for EN-Z-4.....	119
Figure 5-13 BET adsorption – desorption isotherm for EN-Z-6.....	120
Figure 5-14(a) TGA curve for EN-Z-4 showing loss of mass of sample with increasing temperature, (b) associated Gram-Schmidt plot showing increase in total FTIR absorbance with increasing temperature and (c) chemigrams showing FTIR absorbance over specified ranges of wavenumber (indicated on the graph) as temperature rises for EN-Z-4. ....	121
Figure 5-15 (a) TGA curve for EN-Z-6 showing loss of mass of sample with increasing temperature, (b) associated Gram-Schmidt plot showing increase in total FTIR absorbance with increasing temperature and (c) chemigrams showing FTIR absorbance over specified ranges of wavenumber (indicated on the graph) as temperature rises for EN-Z-6. ....	122
Figure 5-16 FTIR spectra of EN-Z-4 (a) shortly after synthesis, (b) after washing (c) after ageing and (d) after heated to $900^{\circ}\text{C}$ .....	126

Figure 5-17 (a) TEM image and (b) SAED pattern showing the sintered ZnO NPs after they have been heated to 800°C for TGA.....	127
Figure 5-18 FTIR spectra of (a) synthesized ZnO NPs in DEG, (b) ZnO NPs after being washed with MilliQ water (c) DEG and (d) Zinc Acetate .....	129
Figure 5-19 XPS survey scan for (a) EN-Z-4 and (b) EN-Z-6 synthesized ZnO samples.....	130
Figure 5-20 XPS spectra of Zn2 <i>p</i> edge for (a) EN-Z-4 and (b) EN-Z-6 with binding energies labeled above each peak. ....	131
Figure 5-21 XPS spectra of O1 <i>s</i> edge for (a) EN-Z-4 and (b) EN-Z-6 with binding energies labeled above each peak. ....	132
Figure 5-22 XPS spectra of C1 <i>s</i> edge for (a) EN-Z-4 and (b) EN-Z-6 with binding energies labeled above each peak .....	133
Figure 5-23 XPS spectrum of (a) O1 <i>s</i> and (b) C1 <i>s</i> edges of EN-Z-4 after ageing. .	135
Figure 5-24 The <sup>13</sup> C NMR spectra for (a) EN-Z-4 and (b) EN-Z-6.....	137
Figure 5-25 SEM images of (a) EN-Z-4 and (b) EN-Z-6 synthesized ZnO NP samples.....	138
Figure 5-26 (a) TEM image of a typical cluster of EN-Z-4 NPs (b) histograms to show the variation in particle length, width and Feret ratio. (c) Higher resolution image of a single particle showing crystal planes. (d) SAED pattern and (e) EDX spectrum obtained from the cluster of particles in (a).....	140
Figure 5-27 (a) TEM image of a typical cluster of EN-Z-6 NPs (b) histograms to show the variation in particle length, width and Feret ratio. (c) Higher resolution image of a single particle showing crystal planes. (d) SAED pattern and (e) EDX spectrum obtained from the cluster of particles in (a).....	141
Figure 5-28 DLS profile for (a) EN-Z-4 and (b) EN-Z-6 ZnO suspensions in water at a concentration of 1000 µg/ml taken immediately after ultrasonication for 20 minutes. The intensity profile is shown in red, the profile converted to volume is shown in blue and the number profile is shown in black.....	144
Figure 6-1 Chart illustrating the effect of the type of media and the temperature on the dissolution of ZnO. Samples were suspended in both water and in DMEM at 25°C and at 37°C for 24 hrs. The solubility of ZnO in a solution of DMEM and BSA	

at 25°C is also reported. Concentration of Zn in solution was measured by ICP-MS.  
..... 151

Figure 6-2 Graphs showing the amount of ZnO that has dissolved into solution, expressed as a percentage of and plotted against the actual total concentration of ZnO in the suspension in DMEM at (a) 0.6, (b) 1.6, (c) 4, (d) 10, (e) 24, and (f) 48 hour.  
..... 158

Figure 6-3 Graphs showing the amount of ZnO that has dissolved into solution, expressed as a percentage of the actual ZnO concentration, plotted against time since sample preparation (hours) for solutions with nominal concentration (a) 1, (b) 3, (c) 10, (d) 30 and (e) 100 µg/ml. The absolute level of Zn in solution for the samples typically reaches a maximum of 9 µg ZnO/ml within 0.6 hour, with the exception of EN-Z-1 which reaches this value after 4 hours. .... 159

Figure 6-4 Graphs showing the pH at increasing time points during the experiment (0.6, 1.6, 4, 10, 24 and 48 hour) for varying nominal concentrations of ZnO in DMEM, i.e. (a) 1 µg/ml, (b) 3 µg/ml, (c) 10 µg/ml, (d) 30 µg/ml, (e) 100 µg/ml. (f) Graph showing how the pH varies for blank DMEM samples where, (1) vials were sealed throughout the duration of the experiment (2) Lids were removed in order to measure the pH at each sampling interval and (3) Volume of 2 mls was removed and pH was measured at each of the sampling intervals. Error bars determined by reported accuracy of the pH meter which was ± 0.1 pH units. .... 162

Figure 6-5 Zeta potential measurements for (a) EN-Z-1, (b) EN-Z-2, (c) EN-Z-3, (d) EN-Z-4 and (e) EN-Z-6 ZnO NP suspensions in MilliQ water at a concentration of 1000 µg/ml and pH of 7.4. .... 166

Figure 6-6 Zeta potential measurements obtained at pH 7.4 for (a) EN-Z-1, (b) EN-Z-2, (c) EN-Z-3, (d) EN-Z-4 and (e) EN-Z-6 at a concentration of 100 µg/ml in water with 10 % w/w BSA, indicating the magnitude of the charge on the particle surface.  
..... 167

Figure 6-7 DLS number profiles of (a) EN-Z-1, (b) EN-Z-2, (c) EN-Z-3, (d) EN-Z-4 and (e) EN-Z-6 suspensions in MilliQ water at a concentration of 1000 µg/ml. Measurements were carried out at T = 0, T = 1, T = 4, T = 10, and T = 24 hour; where T = 0 is immediately after the sample is removed from the ultrasonic bath in which it is placed for 30 minutes after initial dispersion. .... 169

Figure 6-8 Particle size number distributions for (a) EN-Z-1, (b) EN-Z-2, (c) EN-Z-3, (d) EN-Z-4 and (e) EN-Z-6 dispersed in water at varying concentrations (1000, 100 and 10 µg/ml) 24 hours after sample preparation, as determined by DLS. ....	172
Figure 6-9 Particle size number distributions for (a) EN-Z-1, (b) EN-Z-2, (c) EN-Z-3, (d) EN-Z-4 and (e) EN-Z-6 dispersed in DMEM and DMEM-BSA as determined by DLS. ....	175
Figure 6-10 Low magnification TEM images of EN-Z-6 at 1000 µg/ml in water, prepared by (a) the drop-casting method and (b) by the plunge-freezing method (Wallace et al., 2012). ....	177
Figure 6-11 TEM analysis of EN-Z-1 dispersed in water at a concentration of 100 µg/ml, prepared by the plunge freezing route. (a) Low magnification TEM image, (b) TEM image at higher magnification and (c) EDX spectrum obtained for the cluster of particles shown in (b), confirming ZnO composition of NPs. ....	179
Figure 6-12 TEM analysis of EN-Z-2 dispersed in water at a concentration of 100 µg/ml, prepared by the plunge freezing route. (a) Low magnification TEM image of the sample. Higher magnification TEM images of (b) an agglomerate of ZnO NPs, (c) an agglomerate of ZnO NPs with salts present. (d) EDX spectrum obtained for the cluster of particles shown in (b) and (e) an EDX spectrum obtained for the area presented in (c). ....	180
Figure 6-13 TEM analysis of EN-Z-3 dispersed in water at a concentration of 100 µg/ml, prepared by the plunge freezing route. (a) Low magnification TEM image, (b) TEM image at higher magnification and (c) EDX spectrum obtained for the cluster of particles shown in (b). ....	180
Figure 6-14 TEM analysis of EN-Z-4 dispersed in water at a concentration of 100 µg/ml, prepared by the plunge freezing route. (a) Low magnification TEM image, (b) TEM image at higher magnification showing NPs affected by dissolution, (c) TEM image showing NP agglomerate apparently unaffected by dissolution. (d) EDX spectrum obtained for the NPs presented in (b) and (e) EDX spectrum obtained for the NPs presented in (c). ....	181
Figure 6-15 TEM analysis of EN-Z-6 dispersed in water at a concentration of 100 µg/ml, prepared by the plunge freezing route. (a) Low magnification TEM image, (b)	

TEM image at higher magnification and (c) EDX spectrum obtained for the cluster of particles shown in (b).....	181
Figure 6-16 Particle size distributions for (a) EN-Z-1, (b) EN-Z-2, (c) EN-Z-3, (d) EN-Z-4 and (e) EN-Z-6 dispersed in water at varying concentrations (1000, 100 and 10 µg/ml) as determined by PF-TEM. ....	183
Figure 6-17 TEM analysis of EN-Z-1 dispersed in DMEM at a concentration of 100 µg/ml, prepared by the plunge freezing route. (a) Low magnification TEM image. (b) TEM images obtained at higher magnification for an agglomerate of particles and (c) a mixture of ZnO and components of DMEM. (d) EDX spectrum obtained for the cluster of particles shown in (b) and (e) EDX spectrum obtained for the particles shown in (c) with clear evidence for the additional presence of salts.....	185
Figure 6-18 TEM analysis of EN-Z-2 dispersed in DMEM at a concentration of 100 µg/ml, prepared by the plunge freezing route. (a) Low magnification TEM image. TEM images obtained at higher magnification (b) showing the edges of the ZnO particles are dissolving and (c) showing an example of an agglomerate where the individual particles are no longer discernible due to dissolution of ZnO. (d) EDX spectrum obtained for the particles shown in (b) and (e) EDX spectrum obtained for the particles shown in (c). ....	186
Figure 6-19 TEM analysis of EN-Z-3 dispersed in DMEM at a concentration of 100 µg/ml, prepared by the plunge freezing route. (a) Low magnification TEM image showing ZnO NPs and salts. (b) TEM image obtained at higher magnification showing an agglomerate of ZnO showing signs of dissolution at the NP surface. (c) EDX spectrum obtained for the particles shown in (b).....	186
Figure 6-20 TEM analysis of EN-Z-4 dispersed in DMEM at a concentration of 100 µg/ml, prepared by the plunge freezing route. (a) Low magnification TEM image showing ZnO NP agglomerates and salts and (b) image of an agglomerate of ZnO at higher magnification showing evidence of dissolution and (c) EDX spectrum obtained for the NPs shown in (b). ....	187
Figure 6-21 TEM analysis of EN-Z-6 dispersed in DMEM at a concentration of 100 µg/ml, prepared by the plunge freezing route. (a) Low magnification TEM image showing ZnO NPs and salts. TEM images obtained at higher magnification showing (b) the ZnO NP presented in (a) and, (b) an agglomerate of ZnO NPs with a salt	

present in the cluster, (d) EDX spectrum obtained for the NP shown in (b) and (e) EDX spectrum obtained for the NP shown in (c). .....	187
Figure 6-22 TEM analysis of ZnO samples dispersed in DMEM and BSA at a concentration of 100 µg/ml, prepared by plunge freezing route; (a)(i) TEM image of EN-Z-1 and (a)(ii) EDX spectrum for the cluster of particles in (a)(i); (b)(i) TEM image of EN-Z-2 and (b)(ii) EDX spectrum for the cluster of particles in (b)(i); (c)(i) TEM image of EN-Z-3 and (c)(ii) EDX spectrum for the cluster of particles in (c)(i). .....	189
Figure 6-23 Particle size distributions for (a) EN-Z-1, (b) EN-Z-2, (c) EN-Z-3, (d) EN-Z-4 and (e) EN-Z-6 dispersed in DMEM and DMEM-BSA, as determined by PF-TEM. ....	190
Figure 6-24 ASEM analysis of a 100 µg/ml suspension of EN-Z-1. (a) Low magnification (10,000x) ASEM image of the dispersion showing both agglomerates and individual NPs; (b) Image at 30, 000 x magnification displaying a particle moving on the membrane as the image is recorded. ....	195
Figure 6-25 Graph comparing the particle size distributions measured for a 100 µg/ml dispersion of EN-Z-1 in MilliQ water, obtained by DLS, PF-TEM and ASEM. ....	195
Figure 6-26 Liquid cell TEM images of a 100 µg/ml suspension of EN-Z-1 (a) at low magnification showing AuNPs (b) showing an AuNP at high magnification, (c) displaying a ZnO NP agglomerate and (d) showing the flocculates of ZnO or zinc salts produced when the electron beam is focused on a region at high magnification for 10 seconds. ....	197
Figure 7-1 Effect of different samples of ZnO NPs on the viability of A549 lung epithelial cells determined by MTT assay. Cells were exposed to varying concentrations of ZnO NP suspensions in DMEM for 24 hours and at 37°C. Cell viability is plotted as a percentage of the control cell viability. Values plotted are the mean of 3 replicate experiments (n = 3); error bars are ± one standard deviation. (^ = p < 0.05, ^^= p < 0.02, ^^>= p < 0.01, *= p < 0.005, **= p < 0.002, ***= p < 0.001) .....	209
Figure 7-2 Effect of commercial samples of ZnO NPs on the DNA of A549 lung epithelial cells determined using the Comet Assay, by measurement of the	



percentage of DNA in the Comet tail. Cells were exposed to varying concentrations of ZnO NP suspensions in DMEM for 24 hours and at 37°C. Values plotted are mean (n = 3); error bars are ± one standard deviation. ( $\wedge = p < 0.05$ ,  $\wedge\wedge = p < 0.02$ )..... 214

Figure 7-3 Effect of synthesized samples of ZnO NPs on the DNA of A549 lung epithelial cells determined using the Comet Assay, by measurement of the percentage of DNA in the Comet tail. Cells were exposed in DMEM for 24 hours and at 37°C to 1 and 10 µg/ml suspensions of ZnO NPs suspensions and additionally to the supernatant of a centrifuged 10 µg/ml suspension of ZnO NPs. Values plotted are mean (n = 3); error bars are ± one standard deviation. .... 215

Figure 7-4 A549 cells exposed to MilliQ water for 24 hours at 37°C. (a) TEM image of whole grid square showing numerous cells; (b) TEM image of a whole cell; (c) EDX spectrum of the area outlined by the box in (b). .... 217

Figure 7-5 A549 cells exposed to 1000 µg/ml EN-Z-1 for 1 hour. (a) Contrast inverted HAADF STEM image of a whole cell; (b) Contrast inverted HAADF STEM image of the area indicated by the boxed region in (a); (c) TEM image of the area indicated by the boxed region in (b); (d) EDX spectrum from the top nanoparticle in (c) (from Mu et al. 2013)..... 218

Figure 7-6 A549 cells exposed to 100 µg/ml EN-Z-6 for 24 hours at 37°C. (a) Low magnification image of grid square showing numerous cells; (b) contrast inverted HAADF STEM image of a whole cell indicated by the boxed region in (a); (c) contrast inverted HAADF STEM image of the area indicated by the boxed region in (b); (c) TEM image of the area indicated by the box with the dotted outline in (c); (e) EDX spectrum from the top NP in (d); (f) TEM image of the area indicated by the box with the dashed outline in (c); (g) EDX spectrum from the cluster of NPs in (f). .... 221

Figure 7-7 A549 cells exposed to the supernatant of a 100 µg/ml, centrifuged suspension of EN-Z-6, for 24 hours at 37°C. (a) Low magnification image of grid square showing numerous cells; (b) TEM image of a whole cell indicated by the boxed region in (a); (c) TEM image of the cell showing area indicated by the box with the dotted outline (b); (d) TEM image of the area indicated by the box with the dashed outline in (b)..... 222

Figure 7-8 A549 cells exposed to 10 µg/ml EN-Z-6 for 24 hours at 37°C. (a) Low magnification image of grid square showing numerous cells; (b) contrast inverted HAADF STEM image of a whole cell; (c) contrast inverted HAADF STEM image of the nucleus of the cell shown in (b); (d) contrast inverted HAADF STEM image of the left hand side of the cell shown in (b); (e) EDX spectrum of the area indicated by the boxed region in (d). ..... 223

Figure 7-9 A549 cells exposed to 100 µg/ml EN-Z-4 for 24 hours at 37°C. (a) Low magnification image of grid square showing numerous cells; (b) TEM image of a whole cell; (c) contrast inverted HAADF STEM image of region indicated by the boxed area in (b); (d) contrast inverted HAADF STEM image of the region indicated by the boxed area shown in (c); (e) EDX spectrum of the bottom cluster of NPs in (d). ..... 225

Figure 7-10 A549 cells exposed to the supernatant of a 100 µg/ml, centrifuged suspension of EN-Z-4, for 24 hours at 37°C. (a) Low magnification image of grid square showing numerous cells; (b) TEM image of cells indicated by the box with dashed outline in (a); (c) TEM image of the cell indicated by the box with the dotted outline in (a); (d) EDX spectrum of the area indicated by the boxed region in (c). 226

Figure 7-11 A549 cells exposed to 10 µg/ml EN-Z-4, for 24 hours at 37°C. (a) Low magnification image of grid square showing numerous cells; (b) contrast inverted HAADF STEM image of the cell indicated by the box in (a); (c) contrast inverted HAADF STEM image of the area indicated by the boxed region in (b); (d) EDX spectrum of the area indicated by the boxed region in (c). ..... 227

## List of Tables

Table 1-1 Examples of NPs currently used in industry and commercial applications.	4
Table 3-1: Summary of the advantages and disadvantages of each of the techniques included in the characterisation protocol. ....	46
Table 4-1 Summary of commercial samples purchased including a TEM image and particle sizes measured from 250 particles. ....	58
Table 4-2 XRD peak positions, corresponding d-spacings, and relative intensities for EN-Z-1, EN-Z-2, and EN-Z-3 samples. Also listed are the referenced values for zincite extracted from the JCPDS file ref: 01-079-0206.....	66
Table 4-3 Peak list extracted from JCPDS reference file for hydrozincite (ref: 00-014-0256). Also listed are the corresponding peaks present in the EN-Z-2 and EN-Z-3 XRD spectra. ....	67
Table 4-4 Specific surface area measurements for commercial ZnO samples determined by gas adsorption technique (BET).....	70
Table 4-5 Table displaying the percentage concentrations of Zn, O and C in XPS spectra of the ZnO commercial samples. ....	83
Table 4-6 Table displaying the ring diameters, and corresponding calculated d-spacings measured from SAED diffraction patterns of EN-Z-1, EN-Z-2 and EN-Z-3. Also displayed are the d-spacings for zincite extracted from the JCPDS reference file: 01-079-0206.....	89
Table 5-1 Table showing the average crystallite sizes obtained from measurement of the FWHM of each peak for Degsyn-0.15-100-1, Degsyn-0.45-100-1 and Degsyn-0.90-100-1. Miller indices for the measured peaks to which the crystallite sizes refer are listed in the left-hand column.....	97
Table 5-2 Summary of average sizes of primary crystallites measured by TEM and XRD for Degsyn-0.15-100-1, Degsyn-0.45-100-1, Degsyn-0.90-100-1, Degsyn-0.15-250-1, Degsyn-0.15-250-2, Degsyn-0.45-250-1 and Degsyn-0.45-250-2. ....	105
Table 5-3 Table summarizing the average sizes of the particles present in the samples synthesized by the polyol route.....	109
Table 5-4 Specific surface area measurements determined by BET gas adsorption and corresponding calculated average particle size ( $d_{\text{BET}}$ ) .....	111

Table 5-5 XRD peak positions, corresponding d-spacings and relative intensities for FSP 11, FSP 14 and FSP 18. Also listed are the referenced values for zincite extracted from the JCPDS file ref: 01-079-0206 .....	113
Table 5-6 Average crystallite sizes measured by XRD corresponding to atomic planes with listed Miller indices for FSP 11, FSP 14 and FSP 18. ....	115
Table 5-7 Average crystallite sizes for FSP 11, FSP 14 and FSP 18 measured from TEM .....	116
Table 5-8 XRD peak positions, corresponding d-spacings and relative intensities for EN-Z-6. Also listed are the referenced values for zincite extracted from the JCPDS file ref: 01-079-0206 .....	118
Table 5-9 Table reporting the relative concentrations of Zn, O and C in the surface of the synthesized samples, obtained from XPS spectra .....	135
Table 5-10 Table reporting the percentage concentrations of carbon and oxygen species present in the as prepared and aged sample of EN-Z-4, determined by XPS .....	136
Table 5-11 Table displaying the ring diameters and corresponding calculated d-spacings measured from SAED diffraction patterns of EN-Z-4 and EN-Z-6. Also displayed are the d-spacings for zincite extracted from the JCPDS reference file: 01-079-0206 .....	142
Table 6-1 Table showing the actual concentration of ZnO suspended in DMEM at a nominal concentration of 1000 µg ZnO/ml. Quantities are determined by measurement of the zinc concentration by ICP-MS. The degree of variation occurring as a result of the inhomogeneity of the suspensions is reported by measuring 3 samples of the same concentration. ....	155
Table 6-2 Table showing the actual concentration of ZnO measured in suspensions of ZnO in DMEM with nominal concentrations of 1, 3, 10, 30 and 100 µg/ml. Quantities were obtained by measurement of the zinc concentration by ICP-MS. .	155
Table 7-1 Summary of the physicochemical properties of ZnO nanoparticles samples selected for toxicological investigations .....	206

## List of symbols and abbreviations

Atmospheric Scanning Electron Microscopy.....	ASEM
Bovine Serum Albumin.....	BSA
Brunauer-Emmett-Teller.....	BET
Deoxyribonucleic Acid.....	DNA
Diethylene glycol.....	DEG
Dynamic Light Scattering.....	DLS
Engineered NP.....	ENP
Flame Spray Pyrolysis.....	FSP
Foetal Calf Serum.....	FCS
Fourier Transform Infra-red Spectroscopy .....	FTIR
Inductively Coupled Plasma Mass Spectrometry.....	ICP-MS
Liquid Cell Transmission Electron Microscopy.....	LC-TEM
Nanoparticle.....	NP
Natural Organic Matter.....	NOM
Nuclear Magnetic Resonance Spectroscopy .....	NMR
Plunge Freezing Transmission Electron Microscopy.....	PF-TEM
Polyethylene Glycol.....	PEG
Reactive Oxygen Species.....	ROS
Scanning Electron Microscopy.....	SEM
Thermogravimetric Analysis with Evolved Gas Analysis.....	TGA-EGA
Titanium Dioxide.....	TiO <sub>2</sub>
Transmission Electron Microscopy.....	TEM
Tri-n-octylphosphine oxide.....	TOPO
X-ray Diffraction.....	XRD
X-ray Photoelectron Spectroscopy.....	XPS
Zinc Acetate.....	ZnAc
Zinc Acrylate.....	ZnAcr
Zinc Naphthenate.....	ZnNap
Zinc oxide.....	ZnO
Revolutions per minute.....	rpm

# 1 Introduction

It is widely recognised that nanoparticles (NPs) exhibit significantly different physicochemical properties to their bulk counterparts. For this reason, the manufacture and implementation of NPs in commercial products and applications has increased significantly in recent years. The majority of interest in NPs has been focused on synthesis and development for commercial applications. However, as a result of the unique behaviour of NPs, there is concern with regard to the potential toxicity they may pose to both human beings and the natural environment. An understanding of the behaviour and fate of NPs in organisms and the environment is still in its infancy, with only approximately 1 % of peer reviewed scientific publications on NPs specifically addressing a determination of their biological impact (Barcelo and Farre, 2012).

Numerous investigations into the toxicity of NPs to mammals (e.g. Yong et al. 2013; Yah et al. 2012; Elsaesser & Howard, 2012) and to the environment (e.g. Kahru & Dubourguier, 2010; Maurer-Jones et al., 2013) have been conducted. However, the response to NPs that have been transported inside organisms and released into the environment, is complex and diverse and depends on a variety of parameters. Currently, there is inadequate understanding in the scientific community with regard to NP toxicity, which is in part due to a lack of detailed physicochemical characterisation of NPs in biologically relevant environments.

The research carried out for this thesis forms part of a much larger project entitled Engineered Nanoparticles Impact on Aquatic Environments: Structure, Activity and Toxicology (ENNSATOX; Grant number: 229224; 01/07/2009 – 30/06/2012; [www.ennsattox.eu](http://www.ennsattox.eu)). ENNSATOX was a European NMP FP7 small collaborative project that aimed to conduct a comprehensive investigation of the relationship between the structure and functionality of well characterized engineered NPs and their biological activity in aquatic systems (the final report for the ENNSATOX project can be found on the website: [www.ennsattox.eu](http://www.ennsattox.eu)). Three types of NP were investigated in ENNSATOX: silica, titanium dioxide (TiO<sub>2</sub>) and zinc oxide (ZnO). The focus of this thesis is ZnO NPs.

ZnO NPs are already used in a range of commercial products including cosmetic preparations (especially sunscreens), coatings and paints, on account of the large UV absorbance and increasing transparency to light with decreasing particle size (Borm et al. 2006a). Analysis of the health risks associated with ZnO NPs is clearly required, as use of

sunscreens and cosmetics containing the material results in direct exposure to human skin. Production of large quantities of ZnO NPs is required for commercial applications and therefore, there is also the potential for human exposure at the manufacturing stage.

Further fears exist regarding the potential environmental toxicity of ZnO NPs. ZnO NPs may be released into the environment by humans directly, by running off the skin into natural waters, or indirectly through waste and sewage water. Therefore toxicity of NPs to the aquatic environment is of great concern and was a particular focus of ENNSATOX.

Despite a wide range of scientific publications on ZnO NP toxicity already available in the literature, the fundamental mechanisms governing an induced toxic response are not yet fully understood. The size, morphology, crystallinity, surface composition, agglomeration state and solubility are all thought to impact on ZnO NP toxicity. However at present, there is inadequate basic physicochemical characterisation of ZnO NPs used in toxicological investigations and it is for this reason that specific knowledge with regard to ZnO NP toxicity is lacking.

### **1.1.1 Thesis Overview**

This thesis aims to address the current deficit in ZnO NP characterisation by the development of a characterisation protocol. ZnO NPs have been sourced commercially and synthesized in house and their physicochemical characteristics thoroughly investigated, in both dry powder form and in cell culture media. *In vitro* cell viability assays were carried out with the acquired sets of ZnO NPs and the results have been interpreted with cross reference to the results of the detailed characterisation performed on the NP samples. The thesis consists of 7 main chapters; an introduction, a specific literature review concerning ZnO and an experimental section are presented in chapters 1, 2 and 3 respectively. The results are divided into four chapters: Chapter 4 describes the specific physiochemical characterisation required for toxicity studies; furthermore, a detailed characterisation of commercially sourced ZnO NPs is also presented. Chapter 5 describes the laboratory synthesis of ZnO NPs and characterisation of these synthesized samples. Chapter 6 provides results of the dispersion and solubility investigations of ZnO NP samples in water and cell culture media used in toxicity assays. Finally, chapter 7 summarises the results of *in vitro* toxicity assays and identifies relationships between toxicity and NP characteristics.

## **1.2 Nanoparticles – Properties and Applications**

This section introduces the concept of a nanoparticle and nanomaterial. As well as this, the unique properties of NPs are discussed; which make them both desirable for commercial applications, but also raise concerns with regard to their potential toxicity.

### **1.2.1 What are Nanoparticles?**

The requirement for nanomaterial regulation has driven the proposal of numerous definitions of the term “nanomaterial”. The ISO TS 27687 definition proposed by the International Organization for Standardization (ISO) defines a nano-object as a material with one, two or three dimensions in the nanoscale, where the nanoscale encompasses the size regime between 1 and 100 nm. Whereas, the American Standards for Testing Materials (ASTM) stipulates that a NP must have two or three dimensions between 1 and 100 nm. However, many people in the scientific community postulate that nanomaterials should not solely be classified by the size range but that the functional properties should also be taken into consideration.

A common definition of engineered NPs which combines both size and property characteristics is as particles with dimensions of between 1 and 100 nm which have been purposefully manufactured to exhibit specific properties (Auffan et al., 2009; Kreyling et al., 2010). Nanoparticles possess properties that are both quantitatively and qualitatively different from their other forms such as larger bulk particles and ionic forms (i.e. in solution). Although the factors driving the changing properties are varied and often complex, the underlying cause is generally related to the rapidly increasing surface area to volume ratio as one descends down through this size range. An increase in the number of surface atoms relative to those in the bulk core, which have comparatively greater binding energy than atoms in the bulk of a material, gives rise to variations in properties exhibited by nanomaterials such as increased chemical reactivity. The unique properties exhibited by nanomaterials is what leads to their exceptional potential commercial value, but is also of major concern when anticipating the threat they may pose to human health and the environment.

### **1.2.2 Applications of Nanoparticles**

NPs are desirable for applications in a wide range of industries including cosmetics and pharmaceuticals, healthcare, electronics and textiles. As of March 2011, NPs were present in 1,397 commercial products and applications (Project on Emerging Technologies,



2011). Some examples of types of NPs and current applications are reported in Table 1-1. The continued manufacture of engineered NPs for implementation into commercial products and applications will inevitably lead to increased exposure to humans and the environment. Although a significant amount of research into NP toxicity is being carried out, at present, the consequences of NP exposure are not fully understood.

**Table 1-1 Examples of NPs currently used in industry and commercial applications**

Nanoparticle	Applications	Property	Publication
Zinc Oxide	Sunscreens and cosmetics	Transparent to visible light, absorb UV	Daughton & Ternes, 1999
	Dye sensitized solar cells	Improved energy conversion efficiency	Zhang et al. 2008
Silver	Wound dressings	Antibacterial properties	Tiwari, 2008
	Odour prevention in textiles	Antimicrobial properties	Benn and Westerhoff, 2008
Titanium Dioxide	Sunscreens and cosmetics	Transparent to visible light, absorb UV	Daughton & Ternes, 1999
	Self cleaning glass	Transparency to visible light, photocatalytic, superhydrophilic	Zhang et al., 2005
	Water decontamination	Photocatalyst, optical and visible light absorption	Chen et al., 2011
Cerium Dioxide	Catalysts in fuel cells	Improves combustion efficiency	Cassee et al. 2011
Quantum Dots	Traceable drug delivery	Elucidate pharmacokinetics and pharmacodynamics	Qi & Gao, 2008
	Medical imaging and diagnostics	Size tuneable light emission, simultaneous excitation of multiple fluorescent colours	Tan & Zhang, 2005
Gold	Biosensors	Interacting particle surface plasmons and aggregate scattering properties	Rosi & Mirkin, 2005
	Drug delivery	Non-toxic, monodisperse nanoparticles are easily produced easily, surface is readily functionalized	Song et al. 2013
Platinum	Catalyst in fuel cells	Improves combustion efficiency	Coutanceau et al, 2012
Carbon nanotubes	Electronics	Low electron scattering	De Volder et al. 2013
	Photovoltaics	Reduced carrier recombination and photo-oxidation	De Volder et al. 2013
	Antifouling paints	Surface is easy to functionalise	De Volder et al. 2013
	Drug delivery	Functionalization of the surface	Pastorin et al., 2006
Iron Oxide	Cancer hyperthermia	Superparamagnetism	Zhao, 2012
Cadmium Selenide	Photovoltaics	Enhanced luminescence quantum efficiency	Mahmoud & El-Mallah, 2009

### 1.3 Nanotoxicity

The term ‘nanotoxicity’ refers to the potential toxic impacts of NPs on biological and ecological systems (Love et al., 2012). Many biological processes take place at the nano-level, hence there is the potential that engineered nanomaterials may interact with biomolecules and interfere with cellular processes that are critical to life (George et al., 2010).

#### 1.3.1 Toxicity of Nanoparticles to Mammals

Humans may be exposed to nanomaterials directly via inhalation, ingestion, injection or transdermal delivery. Exposure to NPs may be deliberate; for example applying ZnO and TiO<sub>2</sub> NPs in personal care products directly to the skin (Daughton & Ternes, 1999) or injection of quantum dots (Tan & Zhang, 2005) and Fe<sub>3</sub>O<sub>4</sub> (Zhao & Wang, 2009) NPs in medical applications. However, exposure may also be accidental, for example through inhalation of NPs released into the air (Nemnar et al. 2002).

Studies carried out on mammals *in vivo*, indicate that NPs can deposit in the respiratory tract after inhalation and for a number of NPs, oxidative stress-related inflammatory reactions have been observed (Borm et al., 2006). Carbon nanotubes can cause significant lung damage to mammals when instilled in intratracheal doses. For example, mice exposed to a dose of 0.5 mg CNT via intratracheal instillation showed 56 % mortality within 7 days of exposure (Lam et al., 2004). Rats instilled intratracheally with cadmium oxide NPs for 6 hours showed increased inflammation in multiple locations of the alveoli (Takenaka et al. 2004). However, the relevance of lung exposure studies involving administration of NPs by installation are questionable due to the potential for mortality occurring as a result of blockage. Pulmonary toxicity studies with carbon black, nickel, as well as titanium dioxide particles in rats have demonstrated enhanced lung inflammatory potency of NPs as compared to bulk particles of similar composition (Ferin et al., 1992; Oberdörster et al., 1994; Li et al., 1996). Some studies indicate uptake of NPs into the brain after inhalation, via the olfactory epithelium (De Jong & Borm, 2008). Nanoparticle translocation into the systemic circulation may occur after inhalation but conflicting evidence is present on the extent of translocation (Borm et al., 2006). There is evidence from skin penetration studies that dermal applications of metal oxide NPs used in sunscreens lead to very little systemic exposure (Gasparro et al., 1998; Nohynek et al., 2007).

### **1.3.2 Toxicity of Nanoparticles to the Environment**

Naturally occurring NPs have existed in the environment for millions of years; some examples include volcanic dusts in the atmosphere, colloids in fresh water and NPs from soil erosion. It could be argued that organisms in the environment have adapted to living with nanomaterials over the years, and therefore the introduction of new engineered nanomaterials should not be an issue. However, it must be taken into consideration that these manufactured nanomaterials have been designed to have specific surface properties and chemistries that are less likely to be found in natural particles and which may result in them behaving differently. They may therefore present enhanced and novel physicochemical and toxicological properties in comparison to natural NPs (Kahru & Dubourguier, 2010).

The mammalian reports discussed above raise a number of concerns from the perspective of ecotoxicology. Primarily, the lung is representative of typical mucous epithelial tissue and it is possible that similar epithelia in aquatic organisms, such as the gills and gut tissue of fish and invertebrates, could show similar toxic effects. Additionally, the inflammation reactions in rat lung following respiratory exposure raise concern about the long term health of organisms even after short exposures to nanomaterials. However, it could be argued that the milligram doses used in rodent studies are not likely to occur in the environment unless there is an accidental spillage of a batch of nanomaterials.

Although the number of commercial products containing nanomaterials is growing and the novel applications of NPs are continually being developed, there are currently only a few materials that are used in a large number of products and are therefore produced in high volume. Therefore, the environmental exposure to nanomaterials in the next few decades is limited to a small subset of materials. Amongst these NP materials are zinc oxide, titanium dioxide, silver, silica and single- and multi-wall carbon nanotubes (Project on Emerging Technologies, 2011), the applications of which have previously been reported (Table 1-1). The literature with regard to ecotoxicity of nanomaterials is therefore focused primarily on this group of materials. There are various entry points for engineered nanomaterials into the environment, including wastewater treatment plant effluent and sludge (Mueller & Nowack, 2008; Gottschalk et al., 2010).

The toxicity posed by these nanomaterials will undoubtedly vary with exposure dose, yet it is difficult to estimate the relevant concentrations of NPs that will be released at any given time. This is due in part to limited information regarding the prevalence of

NPs in commercial products (Batley et al., 2012). Additionally, the behaviour and state of the NPs will alter once released into the environment, as compared to their behaviour in the original applications. The effect of the changing environment on the dissolution, agglomeration, sedimentation and surface moieties of the NPs could in turn, greatly affect the pathway and extent of environmental release and the toxicity of the NPs (Maurer-Jones et al., 2013). Therefore in order to interpret the toxicity of NPs to organisms, the behaviour of the NPs in the biological and ecological environments must be fully understood.

### **1.3.3 Characteristics Affecting Toxicity**

Oberdörster et al. (2005) proposed a list of physicochemical characteristics that might be important to understand the biological activity and toxicity of NPs. Particle size and size distribution, agglomeration state, morphology, crystal structure, chemical composition, surface area, surface chemistry, surface charge and surface porosity were suggested as key characteristics.

Once within the physiological or aquatic environment, NPs can readily transform due to the high chemical reactivity. Effects such as agglomeration, redox reactions, dissolution and changes in surface composition will be experienced by the NPs which will in turn affect the transport, fate and toxicity of the NPs in the environment (Maurer-Jones et al 2013). When NPs are exposed to biological fluid, the proteins within can bind to the surface of the NPs to form a protein corona, which affects how they are dispersed and internalized by cells (Tenzer et al., 2011; Monopoli et al., 2012). Similarly, in the aquatic environment, dissolved natural organic matter (NOM) may adsorb to the surface of the NPs, thus affecting the physicochemical behaviour.

*In vitro* assays commonly employ cell culture media such as Dulbecco's modified eagle medium (DMEM), in which the behaviour of NPs has been shown to differ as compared to the dry form or when suspended in water. This may significantly impact on their potential toxicity. The ways in which the physiochemical characteristics of NPs can affect toxicity are briefly discussed below.

#### *1.3.3.1 Size*

Surface reactivity as a result of an increase in the ratio of surface to bulk atoms in nanomaterials compared to bulk materials is attributed to some variations in induced toxicity. A growing number of studies show that NPs cause more toxicity than larger particles of the same composition (Carlson et al. 2008; Park et al. 2011; Midander et al.,

2009). However, conflicting and inconclusive data are also reported which often remains unexplained (Rabolli et al., 2010; Warheit et al., 2007); in these cases, I postulate that a more detailed physicochemical characterisation of the sets of NPs used in the study are likely to help uncover explanations for the results observed.

#### *1.3.3.2 Agglomeration of Nanoparticles*

In a review article by Luyts et al. (2013), it was reported that for most experimental studies, nanomaterials are present in an agglomerated form. This may have significant effects on the transport and bioavailability of the material. Due to the increased size, agglomerated NPs may sediment quickly and may not be taken up by suspended cells, thus reducing bioavailability for these cell types; however for adherent cell types, sedimentation of NPs may increase uptake and hence bioavailability. Furthermore in some cases, agglomerates of NPs may initiate frustrated phagocytosis by cells that typically scavenge particles (Luyts et al. 2013), leading to the release of toxic reactive oxygen species (ROS) (Brown et al., 2007). Agglomeration is significant when dealing with complex solutions which are invariably used in toxicity assays. Our group showed decreased interaction of agglomerated ZnO NPs as compared to dispersed NPs, with a model cellular membrane (Vakurov et al., 2013). Furthermore, many studies have demonstrated altered stability of NPs when suspended in cell culture media compared to water, which could affect toxicity (Allouni et al., 2009; Ji et al., 2010; Tantra et al., 2010; Li et al., 2011; Bian et al. 2011; Lankoff et al., 2012).

#### *1.3.3.3 Morphology*

As well as particle size, the morphology of the particle has also been reported to affect toxicity. One concern is that needle-like particles may induce direct physical damage to cells and small organisms by piercing cell membranes. Rigid carbon nanotubes are of major concern owing to their morphological resemblance to asbestos fibres (Donaldson et al., 2010); i.e. when a particle is significantly long and stiff and insoluble, clearance cells are unable to dispose of the particle and toxicity can arise as a result of the particles biopersistence. The bio-availability, measured by uptake of NPs into cells has been shown to differ according to aspect ratio. Numerous investigations found uptake to increase when using NPs of exactly the same material and volume but higher aspect ratio (Gratton et al., 2008; Meng et al., 2011). Conversely, other investigations found uptake was reduced for NPs with higher aspect ratio (Hutter et al., 2010; Chithrani et al., 2006; Zhang et al., 2008). Investigations by Yu et al. (2011) and Herd et al. (2011) reported that no clear relationship

was observed between NP aspect ratio and cellular uptake. Inconsistencies in these results may be explained by modifications on the NPs surface or by dispersion and therefore a greater understanding may be gained by more detailed characterisation of the NPs used.

#### 1.3.3.4 Surface Composition

In many NP applications, such as medical or cosmetic, the surface is generally modified with a coating, so that a specific property is demonstrated. The presence of coatings have been known to interfere with the transport, cellular uptake and cytotoxicity of NPs. For example, a number of *in vitro* investigations reported that NPs functionalized with a positively charged coating induce cytotoxicity to a greater extent than their negatively charged counter parts (Liu et al., 2011; El Badawy et al., 2011; Bhattacharjee et al., 2010; Goodman et al., 2004). This is hypothesized to be a result of increased uptake into lysosomes where the environment is acidic activating the oxidase activity of NPs. Furthermore, the formation of a protein corona around NPs in solutions supplemented with for example serum proteins can affect surface composition and stability which in turn may affect the toxicity.

#### 1.3.3.5 Solubility of Nanoparticles

When considering metal-containing NPs, the dissolution of metal ions from the particles' structure needs to be considered as additional toxicity can be caused by the metal ions or due to the dissolution involving redox processes. This is especially significant for NPs compared to the bulk form because the saturation solubility increases with decreasing particle size, according to the Ostwald–Freundlich equation (Equation 1-1).

$$\frac{S}{S_0} = \exp \left[ \frac{2\gamma\bar{V}}{RT r} \right] \quad \text{Equation 1-1}$$

Where  $S$  is the solubility in the NP dispersion,  $S_0$  is the bulk solubility,  $\gamma$  is the surface energy,  $\bar{V}$  is the molar volume,  $R$  is the gas constant,  $T$  is the temperature, and  $r$  is the primary radius of the NP.

A number of NPs have been investigated *in vitro* to determine whether a toxic response is induced specifically by the particle or released ions, however for many NPs, at present the findings are inconclusive (Christensen et al., 2010; Vandebriel & De Jong, 2012). Assessing NP solubility and the relationship with toxicity is complex as the

solubility of NPs will be affected by parameters such as composition, temperature and pH of the suspending media.

The complex properties exhibited by NPs, and the tendency for their characteristics to change with the environment in which they are placed, means that thorough physicochemical characterisation is fundamental to understanding toxicity results. At present, understanding of the relationship between specific NP physicochemical characteristics and NP toxicity is often inconclusive as a result of inadequate NP characterisation. In order to overcome this issue, a characterisation protocol has been developed here which is discussed in detail in Chapter 4. The protocol aims to ascertain information regarding the NP size, morphology, solubility, dispersion, crystallinity, composition, purity and surface characteristics, so that toxicity results can be interpreted from an informed perspective.

#### **1.3.4 Nanotoxicity Assessment**

When investigating the toxicity of NPs, the key elements of NP screening strategies have been outlined by Oberdörster et al. (2005). The ENNSATOX project is concerned with the potential toxicity of nanomaterials to the aquatic environment and as such relevant tests were chosen as part of the research programme. The interaction of NPs with phospholipid model membranes and additionally *in vivo* investigations using a variety of aquatic organisms were conducted. However, this thesis focuses on the *in vitro* toxicity assessment carried out on ZnO NP samples, measuring the cyto- and geno-toxic responses of cells. *In vitro* studies are important for investigating the aquatic toxicity of NPs even if mammalian cells are employed. Such tests allow us to obtain important information, especially in terms of toxicity mechanisms. The toxicity of NPs to cells can be assessed by a number of assays which fall into one of two categories: functional assays monitor the effects of NPs on various cellular processes, whereas viability assays are concerned with whether or not a particular particle induces significant death in a cell system. Functional assays include assessment of DNA damage and monitoring of levels of ROS production. The most common viability assay monitors metabolic activity, namely the MTT assay. Additionally the uptake of NPs into cells can be monitored.

It is clear from the literature that although numerous investigations into NP toxicity have been carried out, there is a distinct lack of characterisation of NP physicochemical

properties, leading to uncertainties with regard to the specific properties associated with toxicity. In this thesis, a characterisation protocol is to be developed that will be used to obtain a detailed overview of the physiochemical characteristics of ZnO NPs used in toxicity studies. The work aims to develop a more informed understanding of the relationship between ZnO NP properties and any toxicity they elicit.



## 2 Zinc Oxide

This chapter discusses the properties of ZnO NPs which make them desirable for a wide range of commercial applications. Additionally, it summarises the existing literature on ZnO NP toxicity.

### 2.1 Structure, Properties and Applications

ZnO is a widely used metal oxide with unique optoelectronic properties. ZnO crystallises into 3 structures: cubic zinc blende, cubic rock salt and hexagonal wurtzite, however at ambient conditions, ZnO exists in its most thermodynamically stable form, the hexagonal close packed structure – wurtzite. Wurtzite ZnO has lattice parameters  $a = 0.3249$  and  $c = 0.5207$  nm and belongs to the space group  $P6_3mc$ . The structure of wurtzite ZnO can be described simply as a number of alternating planes consisting of tetrahedrally bonded  $Zn^{2+}$  and  $O^{2-}$  ions stacked along the  $c$ -axis which can be seen in Figure 2-1. The tetrahedral coordination (of both Zn and O) in wurtzite ZnO results in a lack of a centre of symmetry which, when combined with large electromechanical coupling, gives rise to piezoelectric and pyroelectric properties. As a consequence ZnO is particularly attractive for mechanical actuators and piezoelectric sensors.

ZnO is a semiconductor material with a wide band-gap of 3.37 eV, capable of absorbing ultra violet (UV) light in the UVA ( $\lambda = 315$ -400 nm) and UVB ( $\lambda = 280$ -315 nm) range. As such ZnO is suitable for use as a UV-screening agent in a wide range of applications including personal care products such as sunscreens and cosmetics and additionally as protective coatings for materials such as wood (Dodd et al., 2006). If the ZnO in these agents is in the form of dispersed nano-sized ZnO particles, the intensity of scattered light is reduced without reducing the UV blocking efficiency, and hence transparent films can be achieved if spread thinly. As a result of the increased photocatalytic activity of nano-ZnO as compared to bulk ZnO, ZnO NPs are being increasingly used as photocatalysts to inactivate bacteria and viruses and for the degradation of environmental pollutants such as dyes, pesticides, and volatile organic compounds under appropriate light irradiation (Dodd et al., 2006; Sapkota et al., 2011).

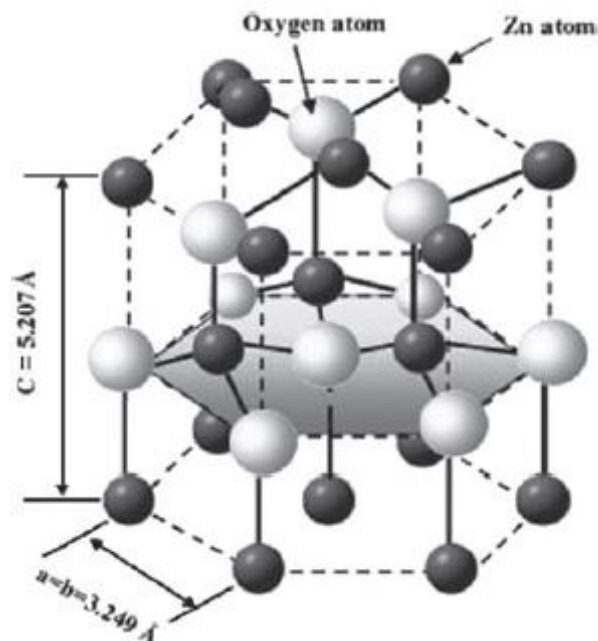


**Figure 2-1** The wurtzite structure of ZnO with the tetrahedral coordination of Zn - O shown with solid line connections (Vaseem et al., 2010)

ZnO NPs are currently used in commercially available products including cosmetic preparations, plastics, ceramics, glass, cement, rubber, lubricants, paints, pigments, foods, batteries and fire retardants. The minimum worldwide tonnage of ZnO NPs produced in 2011 was 33,400 tons. At present, Nanophase and Umicore each produce over 500 tons per year of nanoparticulate ZnO for the cosmetics industry alone (Future Markets Inc., 2012). Such widespread and expanding production and use of ZnO NPs increases the potential for exposure to human beings and release into the environment; therefore it is essential to investigate and understand the toxic potential of ZnO NPs.

## 2.2 Synthesis of ZnO Nanoparticles

In order to assess the toxicity of ZnO NPs, samples containing sets of well-defined NPs are required, so that any toxicity observed can be attributed to specific physicochemical characteristics of the particles. As a result of the polydisperse nature of many commercially available ZnO NP samples, methods of ZnO NP synthesis were also investigated. Desirable characteristics of NP samples for use in products and to assess the effect of size alone in toxicity assays, includes a narrow distribution of size and morphology (samples with standard deviations of  $\leq 5\%$  in diameter are classed as monodispersed; Murray et al., 2000); high purity with the composition of any compounds

present on the surface or doping the NPs known and additionally, a good stability in liquid dispersions.

NPs of ZnO have previously been prepared by physical methods, such as milling and grinding (Shen et al., 2006), by thermal evaporation of ZnO (Wang & Muhammed 1999) or evaporation and oxidation of zinc (Wu et al., 2000). Furthermore, ZnO has also been prepared by chemical solution synthesis routes such as hydrothermal synthesis (Suchanek et al., 2009; Baruah & Dutta, 2009), sol-gel (Meulenkamp et al., 1998; Mondelaers et al., 2002) and precipitation from solution in both aqueous (Hsieh, 2007) and non-aqueous (Jézéquel et al., 1995) mediums. Despite the wide variety of wet chemical methods, the majority of ZnO is produced in industry by gas phase synthesis through oxidation of Zn vapour (Auer et al., 2009). Gas phase synthesis is suitable for preparing ZnO NPs with high crystallinity as the reaction occurs at very high temperatures over a short time span.

Two methods of ZnO NP synthesis are reported in this thesis. The polyol route which involves precipitation of ZnO NPs in a liquid medium; NPs prepared by this technique have previously been reported to produce stable suspensions in liquids and have been used in toxicity assays (Brayner et al., 2006). The ZnO NPs were found to be toxic to bacteria cells (*Escherichia coli* strain MG1655) at concentrations above 140 µg/ml. Nanoparticle internalization within the cells was also reported, however a coating of tri-n-octylphosphine oxide (TOPO) was present on the surface of the NPs in the study, which may affect interaction with the cell membrane and hence affect the uptake.

ZnO NPs have also been synthesized by flame spray pyrolysis (FSP). This method of NP preparation was chosen due to the monodispersed nature of the NPs produced using this technique Tani et al. (2002). Xia et al. (2008) and George et al. (2010) have previously investigated the toxicity of ZnO NPs produced by flame spray pyrolysis. ZnO NPs were found to be toxic to mouse leukaemic monocyte macrophage (RAW 264.7) and human bronchial epithelial (BEAS-2B) cell lines at concentrations as low as 25 µg/ml; the response observed was attributed to the dissolution of ZnO in both the cell culture medium and also within endosomes, leading to the release of toxic Zn<sup>2+</sup>. A review of the literature on both polyol mediated and flame spray pyrolysis methods of ZnO NP synthesis is provided in sections 2.2.2 and 2.2.3 respectively.

### 2.2.1 Precipitation of Nanoparticles from Solution

Chemical synthesis methods offer good control over particle size, morphology and chemical composition. One such technique is the precipitation from solution of insoluble compounds generated by controlled chemical reactions.

The basic model used to describe formation of nanocrystals in a solution was described by La Mer and Dinegar in 1950 (Figure 2-2). The process involves at least two separate stages: nucleation and growth. Initially a new phase must nucleate from a supersaturated solution; nucleation may occur homogeneously within the solution or heterogeneously on a suitable substrate such as inert particulate or surface seeds, reactor walls or impurity particles. Growth of the nuclei will then occur by heterogeneous precipitation of solute molecules on the surface.

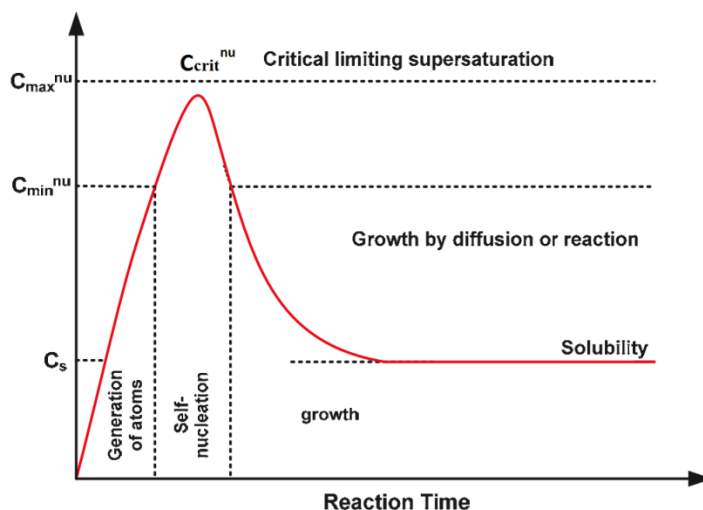


**Figure 2-2 Plot of La Mer model for the generation of atoms, nucleation, and subsequent growth of NPs (Nguyen & Do, 2011, adapted from La Mer and Dinegar, 1950)**

La Mer and Dinegar proposed that in order for a monodispersed system to be produced, homogenous nucleation must be achieved. The synthesis of the colloid should be designed so that the precursor ions are generated at a steady rate, giving a corresponding increase in concentration. In a typical synthesis of inorganic NPs, the precursor compound is decomposed in bulk solution to generate ionic species which then serve as building blocks for nuclei. Increasing the concentration of precursor ions in solution can be achieved by enhancing dissolution of a precursor material by increasing the temperature. The formation of a solid phase in a homogenous liquid environment requires energy and

hence, even at the saturation concentration ( $C_s$ ) nuclei do not yet form. However, once a critical concentration ( $C_{crit}^{nu}$ ) is reached, the supersaturated solution is thermodynamically unstable, which results in the precipitation of a large number of nuclei in a short space of time. Once nucleation occurs, the behaviour is determined by the relative rates of precipitation and generation of the precipitating species. If the precipitation rate (involving both nucleation and growth steps) is much higher than the rate of generation, the concentration will decrease sharply to below  $C_{crit}^{nu}$ , resulting in the termination of nuclei formation. As long as the concentration of ions in solution is in excess of  $C_s$ , growth of the nuclei will proceed to produce NPs, until an equilibrium state is reached between the atoms on the surface of the NPs and the solute ions in solution. In order to produce a monodispersed sample of NPs, homogenous nucleation must occur, i.e. the nuclei must all form at the same time, so that the resultant NPs experience the same period of growth. The size of the particles produced will be determined by the overall quantity of the precipitating species, and by the number of nuclei formed during the nucleation burst (Collins & Taylor, 1992). Due to the high surface energy of NPs, aggregation can often occur during the growth process which leads to polydisperse NPs. This can be prevented by the addition of a surfactant to the solution to coat and stabilize the NPs.

### **2.2.2 Polyol Mediated Synthesis**

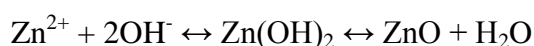
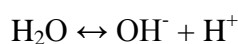
In order to prepare inorganic compounds via precipitation from a liquid phase, solvents such as polyols (alcohols containing multiple hydroxyl groups) offer two interesting properties. Firstly, they act as solvents that can dissolve inorganic compounds as a result of their high dielectric constant. Secondly, owing to their relatively high boiling points they offer a wide operating temperature range for preparing inorganic compounds at low temperature. The general procedure for the polyol mediated synthesis of NPs involves the addition of a precursor salt to a given volume of polyol. The mixture is then heated in order to dissolve the precursor material and once the solution reaches the critical supersaturation concentration, nucleation and growth of NPs proceeds.

The earliest report of ZnO NPs by polyol mediated synthesis was by Collins & Taylor (1992), who also produced zirconia and ceria NPs by this general procedure. In order to produce spherical ZnO NPs with a diameter of 250 nm, a solution of zinc acetate and decanol ( $C_{10}H_{22}O$ ) was heated to reflux. Precipitation of ZnO NPs was observed at 200°C, characterized by the solution transforming into a milky white suspension. ZnO was also formed from refluxed solutions of zinc acetate in ethylene glycol ( $C_2H_6O$ ) and

undecanol (C<sub>11</sub>H<sub>24</sub>O) and additionally, from solutions of zinc nitrate (Zn(NO<sub>3</sub>)<sub>2</sub>) in decanol and ethylene glycol. However, the solid formed in the latter experiments was often brown (rather than white) indicating some degree of nitrogen contamination.

In agreement with the findings of Collins & Taylor, Jézéquel et al. (1995) reported that it is not possible to produce pure ZnO from zinc acetate and ethylene glycol. Alternative polyols were also investigated by Jézéquel et al.; ZnO precipitated when solutions of zinc acetate dihydrate mixed with diethylene glycol (DEG) (C<sub>4</sub>H<sub>10</sub>O<sub>3</sub>), tetraethylene glycol (C<sub>8</sub>H<sub>18</sub>O<sub>5</sub>) and polyethylene glycol (PEG) (C<sub>2</sub>H<sub>4n+2</sub>O<sub>n+1</sub>) were heated, however an unknown phase precipitated when using glycerol (C<sub>3</sub>H<sub>8</sub>O<sub>3</sub>). The authors observed that hydrolysis must play an important role in the formation of ZnO NPs since no oxide can be formed by heating a solution of dehydrated zinc acetate and DEG. Additionally, when using ethylene glycol, the water belonging to the zinc acetate dihydrate is not sufficient to obtain ZnO. Hydrolysis occurs at low temperature however the reaction is accelerated at higher temperatures (near the polyol boiling point). This is termed forced hydrolysis.

The mechanism by which ZnO NPs form in the presence of water is as follows: Zn<sup>2+</sup> ions are obtained by complete dissociation of zinc acetate into Zn<sup>2+</sup> and OAc<sup>-</sup>. The hydroxyl ions for the reaction are obtained from the dissociation of water. Ideally, ZnO NPs are assumed to comprise tetrahedrally coordinated Zn and O atoms and only surface Zn atoms are terminated with an OH<sup>-</sup> ion instead of the oxygen ion. Once ZnO nuclei form, the growth of the clusters occurs by the dehydration of the terminating OH<sup>-</sup> ion using the freely available dissociated OH<sup>-</sup> ion in the solution. The Zn<sup>2+</sup> ions available in the solution brought near the surface of the cluster by the process of diffusion are captured. The growth of the nanocrystal is continued by the Zn<sup>2+</sup> ion capturing the OH<sup>-</sup> ion. The availability of OH<sup>-</sup> ions is dictated by the dissociation of water. When the temperature is increased, the dissociation constant of water increases by a couple of orders of magnitude, providing a larger number of OH<sup>-</sup> ions and thus significantly increasing the rate of the reaction (Viswanatha, 2007). The reaction mechanism for the formation of ZnO can be written as follows:



A number of zinc salts were investigated by Jézéquel et al. (1995). No precipitation of ZnO was observed using zinc sulphate heptahydrate and zinc chloride with added water. Zinc nitrate hexahydrate gave rise to a brown ZnO (consistent with Collins & Taylor) indicating contamination arising from reduction of nitrate anions. The effect of the heating rate on the resultant ZnO NPs was also investigated. Particle size was found to be strongly dependant on this parameter; increasing the rate from 6 to 14 °C min<sup>-1</sup> leads to finer, more monodisperse particles, with average particle sizes measured as 350 ± 30 nm and 200 ± 20 nm respectively. This may be due to the more rapidly increasing concentration of precursor ions in solution leading to a greater number of nuclei forming over a shorter period of nucleation, thus leading to smaller resultant particles. The heating temperature when investigated in the range 100 to 220°C, did not have any significant effect on particle shape and size, however the yield was found to be highest using a temperature of 180°C. TEM analysis of the ZnO NPs revealed that the spherical particles obtained were in fact made up from the agglomeration of much smaller crystallites. XRD revealed the isotropic nature of the single crystal particles whose size was approximately 10 nm. Much larger and more polydisperse spherical particles were observed using tetraethylene glycol with an average size of 1500 nm, compared to DEG where the particles ranged between 200 and 400 nm in diameter. In PEG, the average size of the particles produced was 200 nm, however the shape of the particles was irregular. The concentration of precursor, as predicted by the La Mer model affected the size of the NPs produced. Spherical agglomerates of small crystallites of ZnO were produced when using ZnAc at a concentration below 0.18 mol dm<sup>-3</sup> in DEG. At concentrations between 0.18 and 0.27 mol dm<sup>-3</sup>, the particles formed irregular shapes and agglomerated. Above a ZnAc concentration of 0.27 mol dm<sup>-3</sup> the spherical agglomerates of very small crystallites did not form. Instead, individual crystallites of hexagonal ZnO were observed, with sizes of approximately 60 x 20 nm revealing an increase in the anisotropic nature of the crystallites produced at higher concentration compared to the isotropic nature of the crystallites prepared at low ZnAc concentration.

Using the polyol method, Feldmann & Merikhi (2000) produced a stable suspension of individual crystallites of ZnO with an average size of 80 nm. A solution of ZnAc at a concentration of 0.9 mol dm<sup>-3</sup> in DEG, with 1 ml of H<sub>2</sub>O added was stirred vigorously and heated to 140°C within 30 minutes. The temperature was maintained for 1 hour. The mixture was then heated to 180 °C for 2 hours and then cooled to room temperature.

Brayner et al. (2010) synthesized ZnO NPs using ZnAc, DEG and water at a heating temperature of 180 °C, ageing the reaction for 1 hour. They altered the hydrolysis ratio ( $H = n_{\text{H}_2\text{O}} / n_{\text{Zn}^{2+}}$ ) between 10 and 80 and investigated the effect on the ZnO NPs produced. The authors also investigated the addition of capping agents: tri-n-octylphosphine oxide (TOPO) and polyoxyethylene stearyl ether (Brij-76). For ZnO NPs prepared with a hydrolysis ratio (H), of 2, spherical agglomerates of very small crystallites were produced, similar in size to those produced by Jézéquel et al. (1995) for concentrations of ZnAc lower than  $0.18 \text{ mol dm}^{-3}$ . As the solvent ratio of water to DEG was increased, and hence, H increased, individual crystallites were produced; similar to those particles produced by Jézéquel et al. (1995) at concentrations of ZnAc in excess of  $0.27 \text{ mol dm}^{-3}$ . The length of the elongated crystallites produced was found to increase with increasing H. The addition of capping agents during synthesis significantly affected the size and morphology of the ZnO NPs produced. In the presence of TOPO at H=2, very small NPs of ZnO which were agglomerated and approximately 10 nm in size were produced. When the hydrolysis ratio was increased to 10, a very well dispersed and homogenous sample of spherical ZnO NPs with an average size of 15 nm was produced. Increasing H was found to increase the degree of particle elongation. The particles produced in the presence of TOPO were far more monodispersed than in just water and DEG. When Brij-76 was added during synthesis for H = 2, 30 and 70, spherical particles of ZnO were formed which were heavily agglomerated. However, at H = 10, nanocubes and nanorods forming nanobelts were produced.

Although DEG acts as a chelating agent during this particular type of synthesis and limits the growth of ZnO NPs as well as reducing agglomeration, the study by Brayner et al. (2010) highlights how the additional use of alternative capping agents can affect the size and morphology of the ZnO NPs produced. The superior purity of ZnO NPs produced using ZnAc, as compared to other zinc salts indicates it to be the most suitable zinc precursor for synthesis using this technique. DEG was found to be the most suitable polyol to use. The heating temperature used by most studies was 180 °C as this was the temperature at which the highest yield of ZnO was recorded. The ZnO NP size and morphology can be controlled by altering a few different reaction parameters; e.g. the heating rate, the ZnAc concentration, the hydrolysis ratio and the use of capping agents.



### 2.2.3 Flame Spray Pyrolysis

Flame aerosol synthesis is a promising, scalable gas-phase production method for ZnO NPs. Here, a gaseous (vapour-fed aerosol flame synthesis), liquid (flame-assisted spray pyrolysis and flame spray pyrolysis, FSP) or solid precursor is introduced into a flame and converted to NPs (Teoh et al., 2010). For instance, Jensen et al. (2000) produced ZnO NPs of 25-40 nm in diameter by subliming zinc acetylacetonate into a nitrogen carrier gas and feeding the vapor to a premixed methane-air flame. Matsoukas and Friedlander (1991) introduced an aerosol of solid zinc nitrate particles into a diffusion flame and studied the evolution of the size distribution of the resulting ZnO NPs. However, delivery of a liquid precursor into the flame may be the most effective route, since a broad range of less volatile raw materials is available that can be dissolved in organic solvents or even water, allowing relatively simple liquid precursor handling and dosing. In particular, flame spray pyrolysis (Bouwmeester et al., 2009; Mädler et al., 2002) that benefits from self-sustaining high temperature flames has been shown to be a versatile and scalable method for the production of single- and multi-component oxide and even metal NPs, as is apparent from recent reviews (Teoh et al., 2010; Strobel et al., 2006; Athanassiou et al., 2010).

ZnO NP synthesis with liquid-fed flame reactors has been studied by Marshall et al. (1971), spraying an aqueous solution of zinc acetate into a town gas-air burner. Carroz et al. (1980) produced ZnO NPs of 200 nm diameter by FSP of zinc nitrate solutions in ethanol and methanol. Tani et al. (2002) used FSP to synthesise ZnO NPs employing zinc acrylate as the precursor and methanol as the solvent. Product particle diameters obtained from nitrogen adsorption studies ranged from 10 to 18 nm; size increased as the rate of supply of the precursor solution to the flame increased from 1 ml/min to 4 ml/min. NPs made at higher precursor flow rates were slightly elongated, in agreement with Strobel and Pratsinis (2011) who observed formation of ZnO NPs with  $\approx 1.5$  aspect ratio by FSP employing a zinc-nitrate hexahydrate / ethanol solution. Liewhiran and Phanichphant (2007) reported mainly spheroidal ZnO NPs with occasional hexagonal and rod-like structures in FSP synthesis from zinc-naphthenate/toluene/acetonitrile precursors for application in gas sensors. Height et al. (2006) made pure as well as doped ZnO NPs and rods by FSP conversion of a zinc-naphthenate/toluene precursor solution. The undoped ZnO particles were predominantly spherical with some individual elongated structures.

For FSP, the NP size can be controlled by the feed rate of the precursor solution to the flame. The temperature and height of the flame can also affect the size of the NPs produced and can be controlled by selection of the solvent used.

From a study of the literature, it would appear that two suitable methods for the synthesis of ZnO NPs are polyol mediated synthesis and flame spray pyrolysis. The literature reports that for polyol mediated synthesis, zinc acetate precursor produces monophasic wurtzite ZnO NPs and as such, it will be employed as the zinc precursor here. Diethylene glycol and water will be used as the solvents as previous experiments have reported the synthesis of pure ZnO NPs using this mixture. A temperature of 180 °C was reported to produce the highest yield of ZnO NPs and therefore this temperature will be used for the synthesis experiments. The concentration of ZnAc will be varied in order to investigate the effect on ZnO NP size and morphology. For flame spray pyrolysis, two zinc precursors (zinc acrylate and zinc naphthenate) will be studied in order to investigate the effect on the size of the ZnO NPs produced. The feed rate of the precursor solution to the flame will be varied in order to investigate the effect on the ZnO NPs produced. A detailed overview of the materials and methods employed for the synthesis of ZnO NPs in this investigation is provided in Chapter 3.

## **2.3 Zinc Oxide Nanoparticle Toxicology**

This section reviews the current understanding in the literature with regard to ZnO NP toxicity to humans, other mammals (section 2.3.1) and the environment (section 2.3.2).

### **2.3.1 Mammalian Toxicity**

Analysis of the human health risks associated with ZnO NPs is essential, as use of sunscreens and cosmetics containing ZnO NPs results in direct exposure to human skin. Nonetheless, it is now widely accepted in the scientific community that ZnO NPs do not penetrate through the outermost skin layer – the stratum corneum (Lansdown & Taylor, 1997; Dussert & Gooris, 1997; Gontier et al., 2004; Smijs & Pavel, 2011). Furthermore, ZnO NPs have been present in consumer products for a number of years without any adverse effects being reported thus far. There is agreement amongst scientists, that for ZnO NPs used in sunscreens and cosmetics, the potential risks to human health are outweighed by the benefits provided as a protective barrier from harmful UV radiation (Gasparro et al., 1998; Nohynek et al., 2007).

However, the vast production of ZnO NPs for commercial products, gives rise to the potential for human exposure during manufacturing processes, as well as potential for accumulation in the environment. Therefore probable hazardous routes of exposure are primarily through inhalation and ingestion. The literature involving *in vitro* and *in vivo* studies indicates that acute exposure to ZnO NPs induces a variety of toxic effects. It is difficult to correlate *in vitro* investigations to *in vivo* investigations as *in vitro* studies are more dependent on the type of assay used (Vandebriel & De Jong, 2012).

Cho et al. (2011) reported that the main cause of ZnO NP induced lung injury in rats is a result of rapid pH-dependent dissolution of ZnO NPs inside of phagosomes. The installation of dissolved Zn<sup>2+</sup> into rat lungs showed similar pathologies as were elicited by 10 nm ZnO NPs. Inhalation of 20 nm ZnO NPs (2.5 mg/kg bw) by rats, twice daily for 3 days, resulted in an increased zinc content in the liver after 12 hours and in the kidneys after 36 hours. Histopathological examination showed severe damage to both liver and lung tissues (Wang et al., 2010). Sharma et al. (2012) detected an accumulation of Zn<sup>2+</sup> in the liver of mice fed 300 mg/kg ZnO NPs for 14 consecutive days. This was associated with severe oxidative stress inducing DNA damage. Xia et al. (2011) reported a reduced solubility of 20 nm ZnO NPs when doped with iron (1-10 wt %) and a reduced toxicity was observed in the lungs of mice when exposed to the doped ZnO NPs.

At present, there are contradictory findings reported in the literature for *in vitro* investigations assessing ZnO NP toxicity and the effect of NP size and morphology (Song et al., 2010; Reddy et al., 2007; Pujalté et al., 2011; Bernsten et al., 2010; Deng et al., 2009; Hsiao & Huang, 2011). Clarification of the inconsistencies encountered in these studies may be provided by a more detailed compositional analysis of the NP surface chemistry and agglomeration behaviour. In addition to size and morphology, significant dissolution of ZnO has been reported in a number of *in vitro* investigations, similarly to that reported *in vivo*. Although it is widely considered that dissolved zinc (Zn<sup>2+</sup>) is the mediator of toxic responses to ZnO NPs, there are investigations reporting that direct NP contact with cells is required. It has been suggested that increased levels of Zn<sup>2+</sup> as a result of ZnO NP dissolution gives rise to toxicity via the generation of ROS leading to DNA damage (Song et al., 2010; Xia et al., 2008). Other reports however suggest that toxicity is observed as a result of ROS generation at the NP surface (Lin et al., 2008).

The dissolution of ZnO NPs is most commonly reported as occurring in the extracellular environment (Song et al. (2010)). However studies also report NP dissolution after entering cells, increasing the intracellular Zn<sup>2+</sup> concentration more significantly than

achieved by exposure to similar concentrations of soluble zinc salts (Müller et al., 2010; Gilbert et al., 2012). Moos et al. (2010) reported cytotoxicity in RKO human carcinoma cells to be dependent on ZnO particle contact with the cell and independent of Zn<sup>2+</sup> concentration. A more informed understanding of the dissolution behaviour of ZnO NPs is required and the first step towards this is through detailed characterisation of size, morphology and surface chemistry. For example, the presence of carbonates on the surface of ZnO NPs (Pan et al., 2010) may significantly impact the solubility of the particle and hence affect the degree and/or mechanism of toxicity.

### **2.3.2 Environmental Toxicity**

The potential toxicity of ZnO NPs is not just of concern to humans and mammals, but also the environment. Particularly in the case of sunscreens there is the potential for ZnO NPs to reach the aquatic environment. There is therefore a clear need for investigation into the environmental fate and potential toxicity of ZnO NPs to aquatic biota. In a study by Gottschalk et al. (2009), the predicted environmental concentrations of ZnO NPs were calculated based on probabilistic materials flow analysis from a life cycle perspective of ZnO NP containing products. It was estimated that in Europe in 2008, the concentration in natural surface water was 10 ng/l and treated wastewater was 430 ng/l. Given the widespread application of these ZnO NPs, environmental levels are expected to increase continually (Daughton and Ternes, 1999). However, investigations concerning the ecotoxicological effects of ZnO NPs have been very limited, especially when compared to nanosized TiO<sub>2</sub> - the most extensively studied NPs amongst metal oxides, which are used in many of the same commercial applications as ZnO NPs (Kahru and Dubourguier, 2010).

An article by Ma et al. (2013) reviewing the ecotoxicity of ZnO NPs identified toxic effects of ZnO NPs in both aquatic and terrestrial species, with toxicity measured in some species at 1 µg/ml. The findings demonstrated that if ZnO NPs reach sufficient levels within the natural environment, they could cause significant chronic risk to the environmental biota. However, the review highlighted a lack of characterisation of the ZnO NPs used in the toxicity investigations (Ma et al., 2013; Tables 2, 3 and 4). In the majority of investigations, no TEM or SEM measured particle size was reported, only the manufacturers advertised particle size was given. In many cases, commercially supplied NPs are inhomogenous in size and morphology and the reported size can often be very different from the actual size; evidence for the variability of commercially supplied ZnO NP samples is provided in Chapter 4.

There is one key message that has been consistently repeated throughout my review of the literature: there is a lack of characterisation of ZnO NPs provided in the toxicity investigations to date. The physicochemical characteristics of the ZnO NPs are required prior to testing. However, as ZnO NPs may elicit toxicity by different modes of action which are highly dependent on exposure conditions, a thorough characterisation of the NPs under the relevant exposure conditions is essential for proper interpretation of toxicity data as well as for valid comparison between different studies.

### **2.3.3 Factors Effecting ZnO Nanoparticle Characteristics in Solution**

The dispersion and solubility of ZnO NPs in biologically relevant solutions, such as cell culture media, must be carefully analysed for toxicity assessment.

#### *2.3.3.1 Solubility*

Solubility of NPs is dependent on a variety of conditions, an overview of which are represented schematically in Figure 2-3. For instance, NP size, the adsorption of proteins to the NP surface and the ionic strength and pH of the solution have been shown to influence the dissolution of ZnO to Zn<sup>2+</sup> ions (Bian et al., 2011).

As discussed in the introduction, the radius of curvature of the NPs and hence the size is predicted to effect dissolution. Franklin et al. (2007) measured a stable equilibrium solubility level for bulk ZnO in water at pH 7.6 and 24 °C, equivalent to the complete dissolution of 20 µg/ml ZnO (16 µg/ml Zn). The equilibrium solubility is expected to be higher for smaller particles according to the Ostwald-Freundlich equation (Equation 1-1). This has been confirmed by a number of investigations for very small ZnO NPs. David et al. (2012) found that for NPs with primary particle diameter 20 nm and 70 nm, the solubility was comparable with that of bulk ZnO. However, for NPs with a diameter of 6 nm, the solubility was found to be significantly higher. Furthermore, in an investigation by Bian et al. (2011), size dependent dissolution of ZnO NPs in water was also observed. Equilibrium Zn concentrations of 57, 22 and 10 µg/ml were obtained for NPs with diameters of 4, 15 and 241 nm respectively. Numerous investigations reported that there was no difference between the solubility of nano and bulk ZnO, however in many of these investigations the NPs used had diameters of larger than 20 nm. For example, Mortimer et al. (2010) used NPs with diameters between 50 and 70 nm and found that around 80 % of the mass of ZnO was dissolved for both bulk and nanoparticulate ZnO. Franklin et al.

(2007) reported no difference in dissolution rate and equilibrium concentration for both bulk and nano ZnO (30 nm). Miller et al., (2010) reported dissolution of 70 % of the mass of ZnO for NPs with average diameter of 20-30 nm, for concentrations in the range 0.1 – 1 µg/ml and dissolution of 32 % of the mass of ZnO for an initial ZnO concentration of 10 µg/ml.

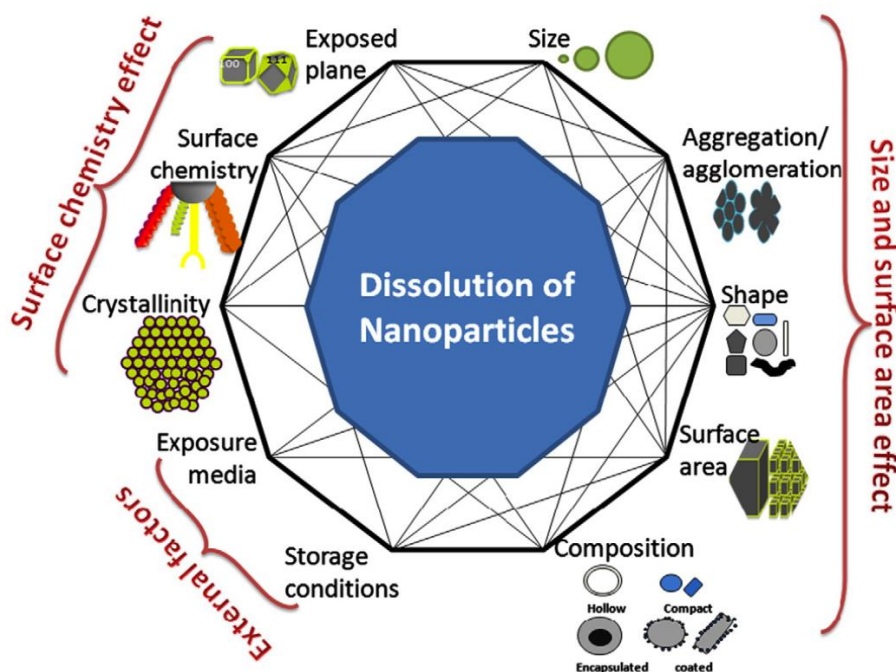


**Figure 2-3 Factors effecting the dissolution of nanomaterials (Misra et al. 2012)**

The morphology of the ZnO NPs can influence the solubility and hence, may affect toxicity. For example, 1D structures, such as nanowires, exhibit very different dissolution behaviour to spherical NPs. ZnO nanowires tend to have a high aspect ratio along their polar (0001) direction. This surface is much more unstable than the other faces of the crystal and as a consequence, the dissolution of ZnO nanowires is extremely anisotropic, with the material dissolving primarily down its polar surface. (Vayssieres et al., 2001; Müller et al., 2010).

The complex biological solutions used in *in vitro* toxicity assays have also been found to affect ZnO NP solution characteristics. The literature reports that both solubility and dispersion alter when dispersed in cell culture media such as Dulbecco’s modified Eagle medium (DMEM) as compared to in water. The dissolution of ZnO has been reported to increase when in DMEM as compared to ultra-pure water (Xia et al, 2008;

Reed et al., 2012). Chemical equilibrium modelling (Visual Minteq) predicts that for ZnO at 100 µg/ml, less-soluble zinc hydrocarbonate (hydrozincite) and zinc phosphate hydrate (hopeite) will re-precipitate in moderately hard water and Roswell Park Memorial Institute (RPMI) cell culture medium respectively. This was verified experimentally by Reed et al. (2012) for solutions of ZnO NPs and by Turney et al. (2012) for soluble zinc salts in RPMI. The age of the sample has also been shown to effect solubility. Reed et al. (2012) investigated the long term dissolution of ZnO NPs in DMEM and found that it increases steadily over time. However, for a 100 µg/ml concentration of ZnO, an instantaneous release of Zn<sup>2+</sup> up to a concentration of approximately 10 µg/ml was observed indicating that lower concentrations of ZnO in DMEM may completely dissolve to Zn<sup>2+</sup>. David et al. (2012) found that there was a non – equilibrium regime in the dissolution process, limited by the kinetics of ZnO dissolution, which was in the order of 1 hour. Hence, freshly prepared ZnO NP suspensions can exhibit a free Zn<sup>2+</sup> concentration far from equilibrium. Perhaps the most critical factor influencing ZnO dissolution is the pH of the solution. The equilibrium solubility of ZnO in water is highly pH dependent and is reported to range from >1000 µg/ml at pH 6 to 1 µg/ml at pH 8 (Stumm & Morgan 1995). For bulk and nanoparticulate ZnO (71, 20 and 6 nm), David et al. (2012) measured a change of 1 order of magnitude in the free zinc concentration, and consequently in the solubility, when the pH was altered by only half a unit between 7.5 and 9. This is significant in the case of toxicity assays which will mostly be carried out around pH 7.4.

The temperature at which cell viability assays are generally conducted is 37°C. This is significant as the solubility of ZnO varies with changing temperature. Reed et al. (2012) reported that the solubility of ZnO was greater at 20°C as compared to 37 °C. This is significant as normally one would expect solubility to increase with increasing temperature as a result of the increase in kinetic energy of both solvent and solute molecules.

#### 2.3.3.2 *Agglomeration State*

The dispersion of ZnO NPs has been shown to vary in biological media compared to in water. For example, the agglomeration of ZnO NPs has been reported to increase when suspended in DMEM as compared to in water (Hsiao & Huang, 2011). This can be explained by Derjaguin, Landau, Verwey and Overbeek (DLVO) theory. The stability of NPs in a suspension, according to DLVO is based on the net balance of two forces: the electrostatic repulsion which prevents agglomeration and a universal attractive Van der Waals force which acts to bind particles together (Derjaguin & Landau, 1993). This theory

assumes the two opposing forces are additive and can be represented in the form of a potential energy diagram (Figure 2-4).

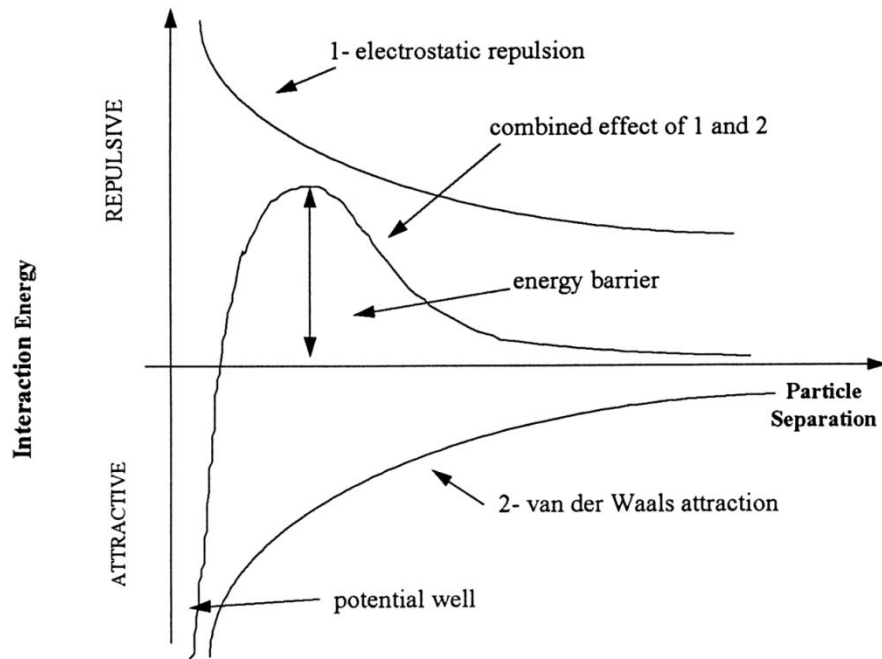


**Figure 2-4 Representation of DLVO theory showing the change in potential energy with increasing particle separation.**

In solutions of low ionic strength, the counter-ion clouds that compensate the charged NP surface extend far from the particle surface, which prevents agglomeration and Van der Waals attractive forces from binding the particles together. When the ionic strength of the solution increases, the charge exhibited by the counter-ions at the surface of the NP is screened by the ions in solution and therefore the repulsive force between NPs diminishes and agglomeration increases. Hence, a reduction in ZnO NP stability is observed in DMEM compared to in water due to the high ionic strength of DMEM. Furthermore, supplementary serum proteins present in DMEM, which are often added to toxicity assays in order to maintain cell viability, have been shown to reduce ZnO NP agglomeration (Bian et al., 2011).

This is due to adsorption of bovine serum albumin (BSA) onto the surface of the NPs enhancing stability by promoting the electrosteric repulsion between particles. Additionally the size and surface charge of the NPs will also affect the stability of NPs in suspension. The pH of the solution will determine the concentration of  $\text{OH}^-$  or  $\text{H}^+$  ions adsorbed to the



NP surface and hence alter the surface charge which will in turn affect the degree of agglomeration.

It is clear from the literature that there is a need for thorough physicochemical characterisation of ZnO NPs in the cell culture media used in toxicological assays. This includes characterisation of the size and size distribution, morphology, surface area, crystallinity, chemical composition, surface composition, solubility and degree of agglomeration. A systematic approach must be adopted when characterizing NPs for toxicological investigations so that results from a variety of studies can be compared. For this reason, a characterisation protocol has been developed which may be applied in future toxicity experiments. The experimental techniques employed in this protocol are described in Chapter 3 with a table (Table 3-1) summarising the advantages and disadvantages associated with each of the characterisation techniques. A more detailed description of the characterisation protocol is provided in Chapter 4.

### 3 Experimental Methods

In order to investigate the potential toxicity of ZnO NPs, it was necessary to source relevant samples from commercial suppliers. Samples were also obtained from the Swiss Federal Institute of Technology (ETH) in Zurich, synthesized by Dr. Karsten Wegner using flame spray pyrolysis. In addition, the synthesis of NPs in house was investigated, with the aim to control particle size and morphology. ZnO NPs produced in-house were synthesized by the polyol route. Section 3.1 describes the materials and methods used in the present work, for the synthesis of ZnO NPs.

At present, there is a lack of detailed characterisation of ZnO NP samples used in toxicity studies. In this study a characterisation protocol has been developed which may be employed to carry out systematic and adequate physicochemical characterisation of NPs used in toxicity assays. Information regarding the size, morphology, composition, phase content, purity, surface chemistry, surface area, solubility and dispersion of the ZnO NP samples is required and as such, a characterisation protocol should include the following techniques: Inductively coupled plasma mass spectrometry (ICP-MS), X-ray diffraction (XRD), BET gas adsorption, thermogravimetric analysis with evolved gas analysis by Fourier transform infra-red spectroscopy (TGA-EGA with FTIR), FTIR, X-ray photoelectron spectroscopy (XPS), nuclear magnetic resonance spectroscopy (NMR), scanning electron microscopy (SEM), transmission electron microscopy (TEM), dynamic light scattering (DLS), plunge freezing transmission electron microscopy (PF-TEM) and Zeta potential measurement. The techniques are described in detail in section 3.2.

In this study, the *in vitro* toxicity of ZnO NPs was investigated using adenocarcinomic human alveolar epithelial (A549) cells. The cytotoxicity and genotoxicity of ZnO NPs was assessed using the thiazolyl blue tetrazolium bromide (MTT) assay and single cell gel electrophoresis (comet assay) respectively which are described in detail in section 3.4.

#### 3.1 Synthesis of ZnO Nanoparticles

The materials and methods employed for the synthesis of ZnO NPs by polyol route and flame spray pyrolysis are outlined in sections 3.1.1 and 3.1.2 respectively.

##### 3.1.1 Polyol Synthesis of ZnO Nanoparticles

Zinc oxide NPs were synthesized by polyol mediated synthesis (Feldmann and Merikhi, 2000). Zinc Acetate dihydrate ( $\text{ZnC}_4\text{H}_{10}\text{O}_6$ : ZnAc: Sigma Aldrich Reagent >

99%) was added to 50 ml of diethylene glycol (DEG) (Sigma Aldrich ACS Reagent 99%) in a 100 ml round bottom flask along with 1 ml of MilliQ water (Wallace et al., 2012). Three different precursor solutions were prepared by adding 1.68, 5.03 and 10.06 g of ZnAc to obtain concentrations of 0.15, 0.45 and 0.9 mol dm<sup>-3</sup> respectively. The solutions were stirred continuously with a stir bar at a speed of 7000 rpm, from the beginning until the end of the reaction. The round bottom flask was lowered into an oil bath ensuring the precursor solution was fully submerged. The solution was heated to 140°C under reflux conditions, using an air condenser, for 1 hour by which time the zinc acetate was completely dissolved and the solution was clear. The temperature of the solution was then increased to 180°C and remained there for a further 2 hours after which a milky white suspension was observed, confirming the presence of precipitated ZnO NPs. The suspensions were then centrifuged at 6000 rpm and the supernatant was removed using a pipette. The NPs in the residue were then re-suspended in MilliQ water by placing in an ultrasonic bath for 15 minutes. The suspension was then centrifuged and the procedure was repeated a further 5 times. The washed suspension was poured into an evaporation dish and then placed into a low temperature oven at 30°C for 72 hours, after which a white residue remained. A pestle and mortar was then used to grind the residue into a fine white powder. Experiments were repeated in order to investigate consistency between samples produced. The nomenclature used for the samples is:

Degsyn-ZnAc Concentration-Round bottom flask volume-Experiment number.

For example, the second batch of ZnO NPs produced using 0.15 mol dm<sup>-3</sup> and a 100 ml round bottom flask will be identified as Degsyn-0.15-100-2.

### **3.1.2 Flame Spray Pyrolysis Synthesis of ZnO Nanoparticles**

Synthesis of ZnO NPs was carried out using a flame spray reactor (Mädler et al., 2002) by Dr. Karsten Wegner at ETH, Zurich. A schematic of the set - up is shown in Figure 3-1 (Tani et al., 2002). Two precursor solutions were investigated: (1) Zinc acrylate (ZnC<sub>6</sub>H<sub>6</sub>O<sub>4</sub>: ZAc: Fluka, 98%) was used as zinc precursor. A mixture of 94 % v/v methanol (J.T. Baker) and 6 % v/v acetic acid (Scharlau, reagent grade) was used as solvent; (2) Zinc naphthenate (ZnC<sub>22</sub>H<sub>14</sub>O<sub>4</sub>: ZnNp: Strem Chemicals, Inc.; 65% in mineral spirits, 10 wt % zinc) was used as the zinc precursor and toluene (Sigma Aldrich) was selected as the solvent (Wallace et al., 2013). Ultrasonication of the precursor mixtures resulted in transparent 0.5 mol/l solutions.

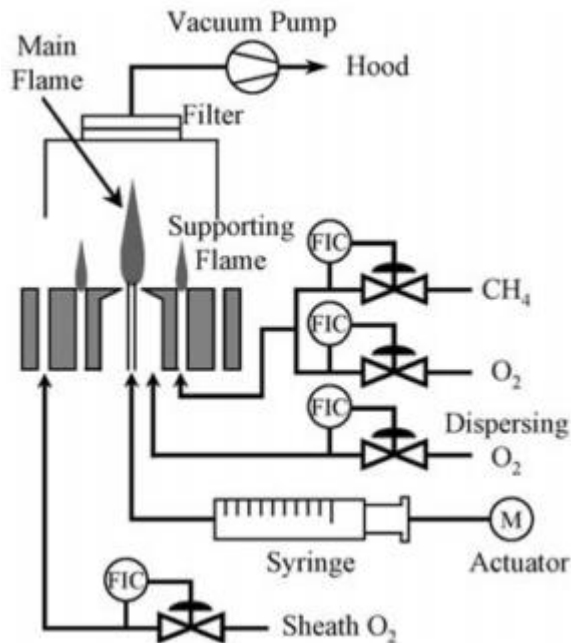


**Figure 3-1 Schematic of the FSP process for ZnO NP synthesis (Tani et al., 2002)**

Two samples of ZnO were synthesized using ZnAcr precursor solution by varying the rate of flow of the precursor solution to the flame. The ZnAcr precursor solution was supplied to the oxygen-assisted atomizer nozzle at 1 and 4 ml/min with the aid of a syringe pump (Lambda, VIT-FIT). The precursor solution was dispersed into droplets by a 3.85 l/min oxygen co-flow. The atomizer was surrounded by a ring of eighteen premixed (methane+oxygen) supporting flames placed at 6-mm radius from the centre of the nozzle. The total flow rates of methane and oxygen were 1.58 and 1.52 l/min, respectively (Tani et al., 2002). The ZnNp precursor solution was delivered to oxygen-assisted atomizer nozzle at a rate of 5 ml/min with the help of a syringe pump and atomized with co-flowing 5 l/min of oxygen dispersion gas at 3 bar pressure drop. The oxygen and methane supporting flame feed rates were 2.5 l/min and 1.25 l/min respectively. The flow rates of all gases (PanGas,  $\geq 99.5\%$ ) were adjusted with calibrated mass flow controllers (Bronkhorst EL-FLOW) and are reported at 25°C and 1 atm. Product NPs were collected on glass-fibre filters (Whatman GF 6, 254 mm diameter) with the help of a vacuum pump (Busch Seco SV1040). Samples were assigned names based on the average particle size of the ZnO NPs produced as determined by BET gas adsorption and assuming spherical non-contacting particles. ZnO NPs synthesized using ZnAcr with precursor flow rates of 1 ml/min and 4 ml/min were named FSP 11 and FSP 14 respectively. The sample prepared using ZnNp was assigned the name FSP 18.

## **3.2 Characterisation of ZnO Nanoparticles**

As has been outlined in Chapter 2, it is crucial that ZnO NP samples are thoroughly characterised. In order to employ a systematic approach to the investigations, a characterisation protocol has been developed. All of the techniques described in Section 3.2 are included in the characterisation protocol, which is discussed in greater detail in Section 4.2. A summary of the advantages and disadvantages associated with each of the characterisation techniques is presented at end of this section in Table 3-1.

### **3.2.1 Bulk Sample Characteristics**

Information regarding the purity, crystallinity and phase content of the ZnO NP samples was acquired by ICP-MS, XRD, BET and TGA-EGA; particle size and morphology can also be inferred from XRD and BET. Descriptions of these techniques are provided in this section (3.2.1).

#### *3.2.1.1 Inductively Coupled Plasma Mass Spectrometry*

Inductively coupled plasma-mass spectrometry (ICP-MS) is a technique employed for the elemental characterisation of a sample. It can simultaneously measure most of the elements in the periodic table, at concentrations as low as parts per trillion (ppt). The sample, usually in the form of a solution, is pumped to a nebulizer where it is converted into a fine aerosol. A high-voltage spark creates a source of electrons which forms a plasma discharge (~10,000 K) which results in the atomization and subsequent ionization of the analyte elements. Ions are separated according to their mass-to-charge ratio by a quadrupole. An ion detector identifies the element by the mass-to-charge ratio of the ions it interacts with and converts the ions into an electrical signal which is then processed and converted into a concentration in ppb (Taylor, 2001).

Quantification of all elements was obtained for the samples in order to determine the concentration of impurities present. Investigations were carried out using a PerkinElmer SCIEX ELAN DRC-e ICP-MS with a PerkinElmer S10 Autosampler. Results for ICP-MS are presented in a bar chart with the relative concentration plotted as a function of the mass to charge ratio, an example of which can be found in Figure 4-1.

### *Sample Preparation*

Suspensions of ZnO NPs were prepared at a concentration of 1000 µg/ml and placed in to an ultrasonic bath for 25 minutes. A 10 µl aliquot of the suspension was taken and acid digested using 6 µl of 70 % nitric acid (HNO<sub>3</sub>) in order to dissolve the ZnO. This was then diluted with 9.984 mls of MilliQ water to obtain a nominal ZnO concentration of 1 µg/ml (1ppm). This was to ensure that the concentration of zinc was within the detection limits of the ICP-MS instrument. The samples were then placed into the autosampler for analysis. The instrument was calibrated using solutions of known zinc concentration ranging from 1 to 1000 ppb.

#### *3.2.1.2 X-ray Diffraction*

X-ray powder diffraction (XRD) is a non-destructive technique that enables the determination of the crystalline phase or phases present in a specimen and estimation of the average crystallite size and strain. An X-ray beam of known wavelength is targeted at a sample through a range of incident angles between the X-ray source and detector. When the incident X-rays of known wavelength,  $\lambda$ , reach the sample, the lattice planes within the crystalline structure of the sample material cause the X-rays to diffract. At specific angles of incidence the distance between a parallel set of atomic planes,  $d$ , will cause the reflected X-rays to interfere constructively. The angle of incidence relative to the normal,  $\theta$ , must satisfy Bragg's Law (Equation 3-1) in order for the reflected X-rays to interfere constructively.

$$n\lambda = 2d\sin\theta \quad \text{Equation 3-1}$$

Where;  $n$  is an integer number (the diffraction order). Peaks occur on an X-ray pattern at  $2\theta$  positions where Bragg's Law is satisfied. The peak positions and relative intensities can be used to determine a material's crystal structure. Identification of phases present in the XRD pattern, is carried out by comparison to known reference patterns using powder diffraction files (PDF), held by the International Centre for Diffraction Data (ICDD), formerly JCPDS (Joint Committee for Powder Diffraction Standards). The  $d$ -spacing's of lattice planes ( $hkl$ ) and unit cell parameters ( $abc$ ) can be obtained and for samples containing sub-micrometer crystalline particles, the mean crystallite size,  $\tau$ , (of a specific crystal plane,  $hkl$ ) can also be determined by measurement of the peak broadening (assuming no strain) and application of the Scherrer equation (Equation 3-2).

$$\tau = k\lambda / \beta\cos\theta \quad \text{Equation 3-2}$$

Where,  $k$  is the shape factor (typically 0.9 for equiaxed crystals),  $\lambda$  is the X-ray wavelength,  $\beta$  is the line broadening at half the maximum intensity (FWHM) in radians, and  $\theta$  is the Bragg angle (Cullity, 2001).

Characterisation by XRD was carried out using a Philips PANalytical X'Pert X-ray diffractometer with a Cu  $K\alpha_1$  X-ray source ( $\lambda = 1.545 \text{ \AA}$ ) scanning over a range of  $5\text{-}80^\circ 2\theta$ . Approximately 0.5 g of the powder was packed into a shallow open sample holder ensuring the surface was flat. Phase identification and crystallographic information were obtained using the PANalytical HighScore software. Examples of XRD patterns for ZnO are presented in Figure 4-2.

### 3.2.1.3 Gas Adsorption (BET)

Brunauer-Emmett-Teller (BET) analysis provides precise specific surface area (SSA) evaluation of materials by nitrogen multilayer adsorption measured as a function of relative pressure using a fully automated analyser. In gas adsorption analysis, the BET adsorption-desorption isotherms of  $N_2$  gas onto the surface of the samples are measured. The surface of the sample is cooled with liquid  $N_2$  in order to increase adsorption to a detectable level. The data collected is displayed in the form of a BET isotherm, which plots the amount of gas adsorbed as a function of the relative pressure (CERAM, 2012) (see Figure 4-3). BET theory provides a mathematical model for the process of gas sorption and is used to determine the SSA ( $m^2/g$ ) of the specimen from the isotherms. From the SSA measurement, the BET-equivalent average diameter of the particles,  $d_{BET}$ , was calculated assuming monodisperse spheres and a zinc oxide density,  $\rho$ , of  $5.606 \text{ g/cm}^3$  using Equation 3-3:

$$d_{BET} = 6000 / (SSA \times \rho) \quad \text{Equation 3-3}$$

### Sample Preparation

Samples were weighed into a specimen tube and the exact mass of the powder added was recorded. To eliminate unwanted vapours and gases adsorbed on the surface of the samples, all were degassed in  $N_2$  for 1 hour at  $250^\circ\text{C}$ , in a Micromeritics Flow Prep 060 Sample Degas System. Nitrogen adsorption-desorption isotherms were measured with a

Micromeritics Tristar 3000 automated gas adsorption analyser at 77 K. The BET method was utilized to calculate the specific surface area of the samples.

#### *3.2.1.4 Thermogravimetric Analysis and Evolved Gas Analysis by Fourier transform infrared spectroscopy*

In order to further investigate the purity and composition of the ZnO samples, thermogravimetric analysis (TGA) was performed with evolved gas analysis (EGA) by Fourier transform infrared spectroscopy. In TGA the change in mass of a sample is monitored with varying temperature. In order to determine the composition of the gas or vapors produced that give rise to the reduction in mass, the evolved gases can be analysed by FTIR. An FTIR spectrum of the evolved gases can be taken at chosen time intervals over the entire range of temperatures.

A Shimadzu TGA 50 thermogravimetric analyser performed TGA and evolved gases were analysed by a Thermo Scientific IS10 FTIR spectrometer with a Thermo Scientific FTIR/TGA interface attached. The sample was heated from 10°C to 800°C, at a rate of 10°C/min in a N<sub>2</sub> environment. An FTIR spectrum was acquired every minute in order to identify the gases evolved.

#### *Sample Preparation*

Approximately 100 mg of ZnO powder was weighed into the sample holder and placed into the TGA instrument where any subsequent mass loss was accurately determined. A Gram-Schmidt chart is obtained showing the total intensity of absorbance over the entire range of wavenumbers and whole range of temperatures (see Figure 4-6 (b)). It is also possible to plot the absorbance intensity for a specific wavenumber range (Figure 4-6 (c)).

### **3.2.2 Surface Characterisation**

Details of the techniques employed to characterize the NP surface, i.e. FTIR, XPS and NMR, are provided in this section.

#### *3.2.2.1 Fourier Transform Infrared Spectroscopy*

Fourier transform infrared spectroscopy (FTIR) enables the identification of chemical groups and compounds through the interaction of infrared energy with a



specimen (Ferraro and Krishnan, 1990). Specific chemical bonds in a sample absorb at characteristic frequencies related to the vibrational energy of the chemical bond, and the remaining infrared signal is transmitted through the sample. For FTIR, the frequency of infra-red radiation,  $\nu$ , is converted to wave number,  $\bar{\nu}$ , through the relation:

$$\nu = c \cdot \bar{\nu} \quad \text{Equation 3-4}$$

Where  $c$  is the speed of light ( $3 \times 10^{10} \text{ cm.s}^{-1}$ ). The signal is then processed and a spectrum is formed displaying the absorbance/transmittance over the range of wavenumbers. Examples of FTIR spectra acquired for samples of ZnO are presented in Figure 4-9. Fourier transform infra-red spectroscopy has been carried out using a Thermo Scientific Nicolet iS10 FTIR spectrometer running OMNIC processing software, fitted with an attenuated total reflection (ATR) accessory. The ATR contains a diamond crystal that internally reflects the IR beam allowing for improved transmission into the sample (0.5-5  $\mu\text{m}$ ).

#### 3.2.2.2 X-ray Photoelectron Spectroscopy

X-ray photo-electron spectroscopy (XPS) is an analytical technique that can identify elements present in the top few nanometres of a sample. It can also provide information regarding the chemical state of the elements detected and the stoichiometry of the elements in the samples. The basic components of an X-ray Photoelectron Spectrometer consist of the sample under investigation, an X-ray source, an electron energy analyser and an electron detector and processing unit, existing entirely under ultra-high vacuum (UHV) conditions. In XPS, the specimen is irradiated with X-ray photons of energy,  $h\nu$ , which are absorbed by atoms in the material leading to photoemission - the ejection of photoelectrons from the inner orbitals. The process of photoemission is shown schematically in Figure 3-2 where an electron from the K shell is ejected from the atom (a 1s photoelectron). The binding energy of the photoelectron can be calculated from the kinetic energy which is measured by the instrument. The binding energy identifies specifically the element and atomic energy level from which the electron has been ejected. The XPS spectrum produced, displays the binding energy (eV) on the x-axis and intensity

(a.u.) on the y-axis. An example of a spectrum acquired for ZnO is presented in Figure 4-10.

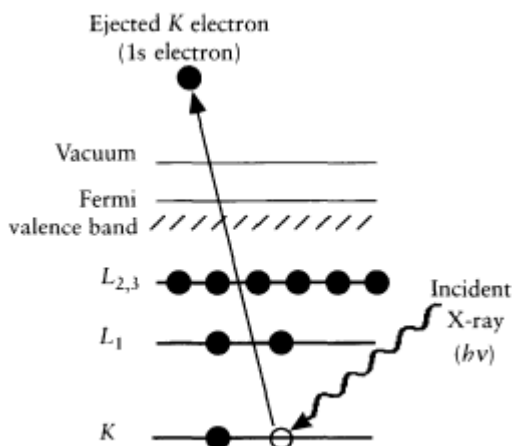


**Figure 3-2 Schematic diagram of the XPS process showing photoionization of an atom by the ejection of a 1s electron (Watts and Wolstenholme, 2003)**

The chemical environment of an element can be determined by measuring the deviation of a peak relative to the known elemental energy. The area under each peak is proportional to the amount of each element present in the analysed volume of the sample surface. (Watts and Wolstenholme, 2003). XPS measurements were performed using a VG Escalab 250 XPS with monochromated aluminium K- $\alpha$  X-ray source (Spot size diameter = 500  $\mu\text{m}$ ; Power = 150 W). The binding energy scale was calibrated by setting the carbon 1s peak to 285 eV. Spectra were analysed using mixed Gaussian-Lorentzian peak fitting within the processing software CasaXPS.

### *Sample Preparation*

Approximately 50mm x 50 mm squares of indium were pressed onto a metal slide. Around 10  $\mu\text{g}$  of each ZnO powder was pressed down into the indium substrate and the excess powder was dusted off. The slide was then placed into the sample chamber.

### *3.2.2.3 Carbon 13 Nuclear Magnetic Resonance Spectroscopy*

Carbon 13 Nuclear Magnetic Resonance spectroscopy ( $^{13}\text{C}$  NMR) relies on the phenomena of nuclear magnetic resonance to determine information about the chemical properties of  $^{13}\text{C}$  atoms in a specimen. Approximately 1.1% of naturally occurring carbon

is  $^{13}\text{C}$ , and compared with the most abundant form of carbon,  $^{12}\text{C}$ , its' nuclei are spin  $\frac{1}{2}$  nuclei. This nuclear spin means that  $^{13}\text{C}$  nuclei act as magnets. When the nuclei are in a magnetic field, they are in one of two states, a relaxed state at a lower energy where the magnetic moment is pointing in the same direction as the field, or an excited state at a higher energy, where the magnetic moment is oriented in the opposite direction to the field. These two states are separated by a difference in energy ( $\Delta E$ ) which depends on the size of the nuclear magnetic moment and the strength of the magnetic field. The difference in energy between the two states can be measured by applying electromagnetic radiation. When the energy supplied equals the difference between the two energy levels, nuclear spin transitions are observed (Hore, 1995). Absorption of the energy by the nuclear spins causes transitions from low to high energies, as well as high to low energies, a phenomenon termed resonance. The energy required to make the transition is usually in the range of energies found in radio waves and is typically applied as a short pulse (microseconds). The energy absorbed by the nuclear spin induces a voltage that can be detected by a coil or wire and amplified. The chemical environment in which carbon is present, alters the energy required for the nuclear spin transition to occur. When surrounded by bonding electrons, the effect of the magnetic field experienced by the  $^{13}\text{C}$  nuclei is not as great, as the electron act as a shield, therefore the magnetic field must be increased in order to induce the transition. The more electronegative the element that the carbon atom is bonded to, the less effective the shielding from the electrons is and therefore the magnetic field would need to be reduced. The spectra produced has the chemical shift ( $\delta$ ) displayed in parts per million (ppm), examples of which are presented in Figure 4-14. The zero point is at the right end of the scale and is where a peak for the  $^{13}\text{C}$  atoms in tetramethylsilane ( $(\text{CH}_3)_4\text{Si}$ ) occur.

Measurements were carried out externally at the EPSRC National Solid-state NMR service at Durham. Solid-state  $^{13}\text{C}$  spectra were recorded at 100.56 MHz using a Varian VNMRS spectrometer and a 4 mm (rotor o.d.) magic-angle spinning probe in order to remove the effect of sample orientation relative to the magnetic field. They were obtained using cross-polarisation with a 2 s recycle delay, 1 ms contact time, at ambient probe temperature ( $\sim 25^\circ\text{C}$ ) and at a sample spin-rate of 6.8 kHz. Dependent on the sample, between 20,000 and 120,000 repetitions were accumulated. Spectral referencing was with respect to an external sample of neat tetramethylsilane,  $\text{Si}(\text{CH}_3)_4$  ( $\delta = 0.000$  ppm).

### **3.2.3 Nanoparticle Characterisation**

In order to investigate the size, size distribution and morphology of the NPs in greater detail, SEM and TEM were employed. TEM also enabled compositional analysis of the samples.

#### *3.2.3.1 Scanning Electron Microscopy*

In SEM, a focused, high energy beam of electrons (typical energy = 3-30kV) rasters over the surface of a specimen and provides morphological and structural information down to a resolution of approximately 10 nm. The electrons interact with the atoms at the surface of the specimen, ionizing them and releasing secondary electrons (SE) from the top few nanometers. These electrons are counted by a detector and an image is formed of the topography of the sample, pixel by pixel.

Secondary electron images were taken using a LEO 1530 Gemini FEG-SEM operated at 3 keV, 3.0 mm working distance and employing an in-lens electron detector. Sample analysis and image acquisition was performed using Zeiss SmartSEM™ software. SEM was performed on the samples in order to obtain information regarding the range of sizes and morphologies of the primary particles present. However, size distributions were not obtained for the samples due to poor image quality, examples of which are provided in Figure 4-15.

#### *Sample Preparation*

A suspension of the powders was prepared in MilliQ water at a concentration of 1000 µg/ml. A few drops of the suspension are cast directly onto an aluminium support stub. The water is evaporated by blowing hot air across the surface of the stub. The sample was then coated using an Agar High Resolution Pt/Pd Sputter Coater (thickness = 5 nm) to provide a conductive surface and to prevent charging.

#### *3.2.3.2 Transmission Electron Microscopy*

Transmission electron microscopy (TEM) allows for comprehensive analysis of an ultrathin sample (ideally < 100 nm thick) at the NP level. Bright field imaging, high resolution imaging, selected area electron diffraction (SAED) and energy dispersive X-ray spectroscopy (EDX), can provide information regarding the particle sizes, size distribution and morphology of the particles present in the sample, as well as revealing information regarding the composition and crystalline phase of the sample. In TEM, a high energy

electron beam is produced using a tungsten filament (electron gun) and accelerated at 50-200kV through a series of electromagnetic lenses. The electron beam is transmitted through the sample and the diffracted beam is magnified to form an image of the specimen on a fluorescent viewing screen (Williams and Carter, 1996; Fultz and Howe, 2002).

Energy dispersive X-ray spectroscopy (EDX) was performed on the sample to obtain compositional information and identify any potential impurities. High energy electrons are focused onto the sample which can knock out electrons from within the inner shells of atoms in the sample. An electron from a higher energy orbital will drop down to fill the electron hole, and the loss of energy is emitted in the form of an X-ray photon, the energy of which is characteristic of the element. The data output is presented in an EDX spectrum of relative X-ray intensity as a function of energy (eV) (Williams and Carter, 1996).

Selected area electron diffraction (SAED) was also performed on the samples in the TEM in order to determine the crystalline phase. In SAED, the electron beam is focused on to the sample through a selective aperture. As the wavelength of the electron beam is the same order of magnitude as the distance between atoms in the sample material, the atoms act as a diffraction grating. In the case of a polycrystalline materials, a series of rings of dots will be observed. The SAED pattern can be used to determine d-spacings of the atomic planes and hence identify the crystalline material.

TEM analysis was performed on a Phillips FEI Tecnai TF20 field emission gun TEM operating at an accelerating voltage of 200 kV, fitted with an Oxford Instruments INCA 350 energy dispersive X-ray (EDX) system/80mm X-Max silicon drift detector (SDD) and Gatan Orius SC600A charge-coupled device (CCD) camera. Examples of TEM images, an EDX spectrum and SAED pattern obtained for ZnO are presented in Figure 4-16.

#### *Sample preparation*

A suspension of ZnO was prepared at a concentration of 1000 µg/ml in MilliQ water. In order to break up agglomerates the sample was placed in an ultrasonic bath for 15 minutes. A few drops of the sample were then drop cast onto a TEM grid (Holey carbon 400 mesh Cu, Agar Scientific Ltd.).

### 3.2.4 Solution Characteristics

As the assays employed to investigate ZnO NP toxicity take place in liquid media i.e. Dulbecco's Modified Eagle Medium (DMEM), information must be obtained regarding the NP behaviour when suspended in suspension. The solubility and stability of the ZnO NPs must be investigated in order to gain a comprehensive understanding of the complex solutions delivered to the cells in the toxicity assays. Investigation of dispersion characteristics was achieved through use of dynamic light scattering (DLS), inductively coupled plasma-mass spectrometry (ICP-MS) and plunge freezing – transmission electron microscopy (PF-TEM) techniques. The conventional drop casting preparation route for TEM grids is not suitable for characterising dispersions as the NPs tend to agglomerate as the sample dries. Liquid cell TEM and an atmospheric SEM (ASEM) were also employed to investigate ZnO NP suspensions. The benefit of these two techniques is that they enable *in situ* observation of NP suspensions. Liquid cell TEM and ASEM are not included in the characterisation protocol.

#### 3.2.4.1 Inductively Coupled Plasma Mass Spectrometry

The analytical technique, inductively coupled plasma-mass spectrometry (ICP-MS) is described in section 3.2.1.1. The concentration of only one element, Zn, is under investigation in this adaptation of the technique. In order to determine the solubility of ZnO NPs when in a liquid medium, dispersions of the NPs are prepared and allowed to age accordingly. The particles are then removed via ultracentrifugation (14,500 rpm) and the supernatant withdrawn and analysed in the ICP-MS instrument. The use of ICP-MS as a technique to determine  $Zn^{2+}$  ion concentration in dispersions of zinc oxide NPs has previously been reported (Xia et al., 2008; George et al., 2010). Limitations to this technique include failure to remove entirely, the solid fraction of NPs, however characterisation of the supernatant using SEM or TEM can confirm whether or not there are NPs still present.

Investigations were carried out using a PerkinElmer SCIEX ELAN DRC-e ICP-MS with a PerkinElmer S10 Autosampler. A VWR Zinc Nitrate (Solspen) standard salt solution over a range of concentrations was used in order to calibrate the ICP-MS instrument. After each sample run, the sample holder was washed with 2 % nitric acid and the tubes were flushed. The ICP-MS instrument has an upper concentration limit of around 1 part per million to which it is capable of detecting an element in the sample. Therefore

samples were diluted appropriately to ensure the concentration of zinc in the sample could be detected by the instrument.

#### *Sample Preparation*

Sample preparation was designed to produce suspensions of ZnO that would mimic the conditions of the toxicity assays. Experiments investigating NP exposure to cells are carried out at 37°C in Dulbecco's Modified Eagle Medium (DMEM). The solubility of the ZnO samples was investigated as a function of ZnO NP concentration, time, temperature and medium composition. The solubility of ZnO NPs in DMEM, DMEM with supplementary BSA and water was investigated. The different temperatures investigated were 25 and 37 °C and the ZnO concentrations studied were 100, 30, 10, 3 and 1 µg/ml. In order to separate the ZnO NPs from the solution, samples were centrifuged at 14,500 rpm for 36 minutes. The supernatant was then withdrawn and analysed by ICP-MS. In order to determine dissolution kinetics for ZnO NPs, solubility was determined over time. As the time for centrifugation is 0.6 hours (36 minutes), the shortest age of a sample was 0.6 hours. Therefore the time intervals investigated were  $t = 0.6, 1.6, 4, 10, 24$  and 48 hours. The solubility data acquired is presented as the amount of dissolved ZnO (as a percentage of the total concentration of ZnO in the suspension) plotted as a function of the variable investigated.

#### *3.2.4.2 Zeta Potential*

Zeta potential is a physical property exhibited by particles in a suspension and is an indication of the stability of a suspension. Most particles dispersed in a system will have a surface charge resulting from either adsorption of charged species or ionisation of surface groups. This charge will change the distribution of the surrounding ions in the solvent, forming an electrical double layer. The liquid layer surrounding the particle exists as two parts; an inner region called the Stern layer, where the ions are tightly adsorbed to the surface of the particles and an outer region called the diffuse layer, where they are less strongly associated (Taroco et al. 2011). Within the diffuse layer there is a boundary called the slipping plane which marks the point where the surrounding ions cease to exist as a stable entity with the particle. The potential at this boundary is the zeta potential. The magnitude of the zeta potential gives an indication of the stability of the suspension as particles with a relatively high zeta potential (+30 or – 30 mV) will tend to repel each other and hence remain in suspension (Malvern Instruments, Zeta Potential).

There are a number of factors that will affect the zeta potential of a sample, such as pH and ionic strength. For example, increasing the pH will make the value of the zeta potential more negative, as the number of OH<sup>-</sup> ions adsorbed to the NP surface will increase. Solutions with high ionic strength reduce NP stability as the charge of the NPs is screened by the ions in solution.

The zeta potential of a suspension of particles can be determined by measuring the electrophoresis of the particles when an electric field is applied across the suspension. Electrophoresis is the movement of a charged particle relative to the liquid in which it is suspended under the influence of an applied electric field. When an electric field is passed across the sample, the charged particles will migrate towards the electrode which is oppositely charged. The velocity at which they move towards the electrode is proportional to the magnitude of the zeta potential. The velocity of the particles is measured by a laser.

Zeta potential measurements were carried out using a Malvern Zetasizer Nano ZS instrument. A chart is produced counts plotted as a function of charge (mV). A chart is produced presenting the counts measured as a function of charge (mV); the zeta potential is determined as the charge with maximum counts. Examples of zeta potential charts are presented in Figure 6-5. Zeta potential sample preparation was synonymous with that of DLS which is described in the following section (see Section 3.2.4.3).

#### 3.2.4.3 *Dynamic Light Scattering*

Dynamic Light Scattering (DLS) is the technique most commonly employed for investigating *in situ* the sizes and size distribution of particles and/or agglomerates in liquids. In DLS, the velocity at which particles are diffusing due to Brownian motion is measured by the scattering of a laser light. The velocity of Brownian motion of a particle is defined by a property known as the translational diffusion coefficient, D. This can be used to derive the hydrodynamic diameter (based on a sphere) by the Stokes-Einstein equation (Equation 3-5):

$$d(H) = kT / 3\pi\eta D \quad \text{Equation 3-5}$$

Where d(H) is the hydrodynamic diameter, D is the translational diffusion coefficient, k is Boltzmann's constant, T is the absolute temperature and  $\eta$  is the viscosity. Although DLS provides rapid measurement of particle size distributions in a suspension, there are intrinsic



limitations associated with the technique. DLS works on the assumption that all of the particles suspended in the liquid are spherical. Additionally, the technique is not capable of distinguishing between particles of different compositions, and relies on knowledge of the refractive index of the suspended particle as well as the viscosity and concentration of the liquid medium (Berne and Pecora, 1990). DLS is more sensitive to the larger size fraction of a polydispersed suspension due to the intensity of scattered light being proportional to  $d^6$  (where  $d$  is the diameter of the scattering particle). There are both upper and lower NP concentrations at which the instrument can accurately measure the particle sizes present. Finally, if the dispersing media contains a solid fraction of un-dissolved macromolecules, there is a chance that the DLS will measure these as suspended particles if they are significantly more concentrated than the particles of interest.

Dynamic light scattering (DLS) measurements were carried out using a Malvern Zetasizer Nano ZS instrument. Data manipulation was performed by the DTS Nano software to determine the particle size distribution. The dispersion of the ZnO NP samples in deionised MilliQ water (with a resistivity of 15 MΩcm), Dulbecco's modified eagle medium (DMEM) and DMEM with 10 % w/w bovine serum albumin (DMEM-BSA) was investigated. All samples were prepared at 3 different concentrations of ZnO, 1000, 100, and 10 µg/ml. The suspensions were ultrasonically agitated for 20 minutes prior to DLS analysis. Examples of hydrodynamic size distributions for ZnO NP suspensions measured by DLS size, plotted as a function of intensity, volume and number are presented in Figure 4-19.

#### *3.2.4.4 Plunge Freezing - Transmission Electron Microscopy*

A technique often employed to complement DLS is TEM. The primary particle size obtained from measurements from TEM images of a sample is often in excellent agreement with DLS measurements in a simple monodispersed system (Zheng et al., 2002). However, quantitative comparison of size distributions of agglomerates obtained by DLS and TEM cannot be performed due to the drop casting sample preparation technique used in TEM. This method involves dropping and drying a solution on a grid. However, the drying effects that occur during this process cause the particles to agglomerate, which means that the agglomerates observed in TEM images are not representative of the state of the particles when in suspension (Dutta et al., 2007). Furthermore as discussed in section 3.2.4.3, there are inherent limitations with DLS.

An alternative method of TEM sample preparation involves plunge freezing (PF) a solution onto a TEM grid at a speed quick enough to vitrify the aqueous phase and ensure that there is no significant movement of suspended material. This can be achieved by placing a small volume of the sample onto a carbon support film which has undergone oxygen plasma treatment in order to increase the hydrophilicity. The support film is then blotted in order to create a thin layer of the dispersion and plunged into liquid ethane which preserves its features and vitrifies the sample (Dobro et al., 2010, White et al., 1998). The vitrified sample can then be analysed in its vitrified state in a cryogenic-TEM (i.e. a TEM with a cooled sample holder and cryoshielding). However, there are limitations associated with cryogenic TEM as the electron beam interacts with the sample and can cause it to melt. Images must be taken at low magnification making features difficult to identify. The layer of vitrified ice can also decrease the resolution of features in the sample. In a study by Hondow et al. (2012), it is reported that if the prepared TEM grid is allowed to warm up to room temperature in a rotary pumped vacuum desiccator, the position of the particles do not move. The sample can then be imaged in a conventional TEM and the size of the agglomerates measured will be representative of the dispersion and can therefore be compared with DLS.

#### *Sample Preparation*

In order to prepare plunge frozen TEM specimens, TEM grids purchased from Agar Scientific (Carbon film on copper mesh) were glow discharge treated using a Cressington 208C Carbon Coater at 5kV for 30 seconds. The vitrification instrument used was an FEI Vitrobot Mark IV. Temperature was maintained at 20 C and humidity at 100 %. A 30 second delay was implemented prior to blotting, followed by a 3.5 s blotting time and a blot force of 6. After the specimen was plunged into liquid ethane, it was immediately transferred to a liquid nitrogen cooled container which was then immersed in liquid nitrogen. The grid was then warmed to room temperature in a rotary pumped vacuum desiccator. The examples of TEM images of CdTe/ZnS quantum dots prepared by PF technique, presented in Figure 3-3, show that the particles do not significantly move around on the carbon support film when warmed up under vacuum conditions.

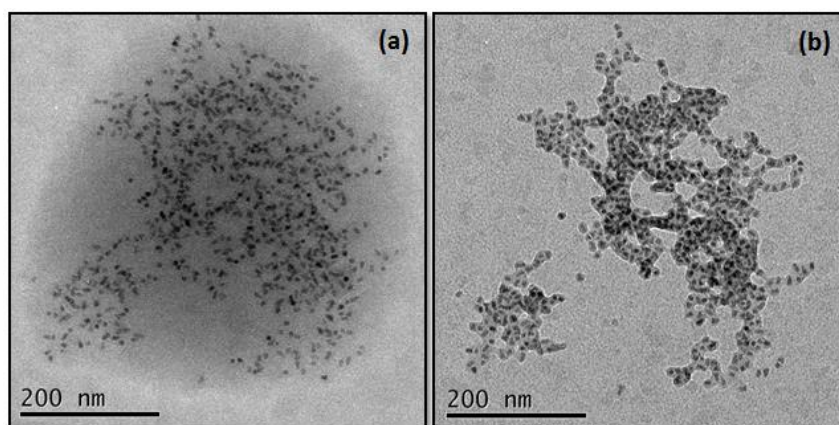


**Figure 3-3** PF-TEM images of 10nM QTracker 705 CdTe/ZnS quantum dots; (a) sample kept frozen and imaged in a cryo-TEM; (b) TEM image of the same cluster of particles warmed up in the microscope. (Hondow et al., 2012)

**Table 3-1: Summary of the advantages and disadvantages of each of the techniques included in the characterisation protocol.**

Technique	Advantages	Disadvantages
<b>X-ray Diffraction (XRD)</b>	Bulk analysis of sample. Sample can be used again after analysis.	Lengthy analysis required for low sample masses.
<b>Gas adsorption (BET)</b>	Bulk analysis of sample. Sample can be used again after analysis if stable up to 250°C.	Relatively large amount of powder required. Agglomerated particles and coatings on particles may confound results.
<b>Thermogravimetric Analysis (TGA) with Evolved Gas Analysis (EGA) by Fourier Transform Infra-red Spectroscopy (FTIR)</b>	The temperature at which a species is evolved is known. This information can help to identify the compound from which it came.	Destructive technique – sintering of the ZnO NPs is observed during the heat treatment (below 900°C).
<b>Fourier Transform Infra-red Spectroscopy (FTIR)</b>	Very small amount of sample required.	Difficult to identify exact composition of unknown materials. Ambiguity arises through overlap of bands for different functional groups.

Technique	Advantages	Disadvantages
<p align="center"><b>X-ray Photoelectron Spectroscopy (XPS)</b></p>	<p>Very small amount of sample required.</p>	<p>Only probes the surface few nanometres of the sample. Not a stand alone technique for identification of chemical bonds.</p>
<p align="center"><b>Carbon 13 Nuclear Magnetic Resonance Spectroscopy (NMR)</b></p>	<p>Non-destructive technique.</p>	<p>Information is obtained only about bonds containing carbon.</p>
<p align="center"><b>Transmission Electron Microscopy (TEM) Imaging, Energy Dispersive X-ray Spectroscopy, Electron Energy Loss Spectroscopy, Selected Area Electron Diffraction</b></p>	<p>Images of primary particle size. Can be done on a single particle or group of particles.</p>	<p>Potentially too small a specimen size to be representative of the sample. Drying can change dispersion state. Time consuming.</p>
<p align="center"><b>Scanning Electron Microscopy (SEM) Imaging and Energy Dispersive X-ray Spectroscopy (EDX)</b></p>	<p>Larger selection of sample can be investigated than in TEM.</p>	<p>Limited magnification resulting in poorer resolution of nano sized particles than TEM. Drying can change dispersion state.</p>
<p align="center"><b>Dynamic Light Scattering (DLS)</b></p>	<p>Fast measurement. Works very well for monodisperse, stable NP suspensions.</p>	<p>Technique struggles with too low/high concentration of NPs, complex dispersing media, polydisperse, unstable samples.</p>
<p align="center"><b>Zeta Potential (ZP)</b></p>	<p>Fast measurement.</p>	<p>Technique struggles if suspension is unstable. Complex suspending media can interfere with zeta potential measurements.</p>

Technique	Advantages	Disadvantages
<p><b>Inductively coupled plasma - mass spectrometry (ICP-MS)</b></p>	<p>Many samples (100s) can be carried out at once as technique is automated.</p>	<p>Possibility that NPs remain in the supernatant, therefore additional analysis must be carried out in order to confirm this is not the case.</p>
<p><b>Plunge freezing-Transmission Electron Microscopy (PF-TEM)</b></p>	<p>Direct measurement of agglomerates is achieved unlike DLS which relies on mathematical approximations to obtain size distributions.</p>	<p>A minimum of 250 agglomerates are measured so the process is time consuming. Very small sample size therefore could be argued that it is not representative.</p>

### 3.3 Alternative Techniques for Characterizing Nanoparticles in Solutions

The techniques detailed in this section enable direct imaging of NPs in solutions in the SEM and TEM. Liquid cell transmission electron microscopy (LC-TEM) and atmospheric scanning electron microscopy (ASEM) were carried out at the University of York.

#### 3.3.1.1 Atmospheric Scanning Electron Microscope

An atmospheric scanning electron microscope (ASEM) (JEOL ClairScope JASM-6200) (Nishiyama et al., 2010) is capable of observe dynamic phenomena in liquid or gas under atmospheric pressure in real time (Nishiyama et al., 2010; Suga et al., 2011). In this instrument, the SEM has an inverted structure, with the electron gun at the bottom as can be seen in Figure 3-4.

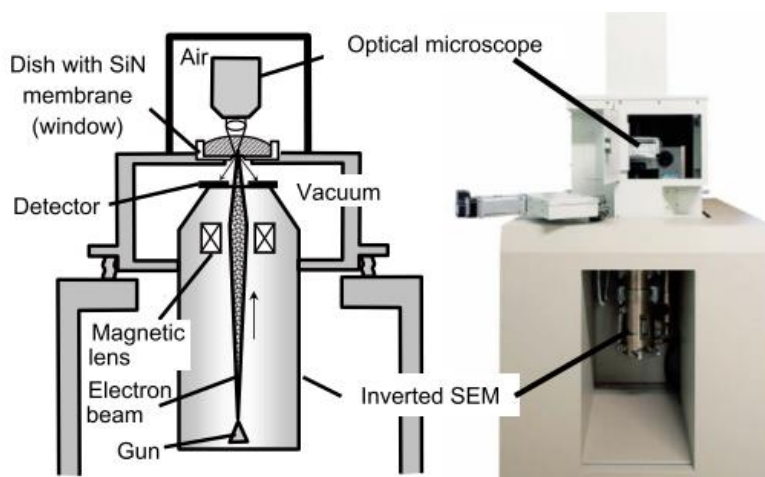


**Figure 3-4 ASEM with inverted SEM structure. An optical microscope is arranged above the SEM with the specimen dish in between. The removable dish features a SiN window (Nishiyama et al., 2010)**

An optical microscope is situated above the SEM with the specimen dish in between. An electron-permeable window made of atmospheric pressure-resistant 100 nm-thick silicon nitride (SiN) film, set into the bottom of the open ASEM sample dish, allows an electron beam to be projected from underneath the sample. A detector positioned below captures backscattered electrons.

### 3.3.1.2 Liquid Cell Transmission Electron Microscope

Liquid cell transmission electron microscope (TEM) enables the imaging of materials in liquids, directly in a TEM. In order to achieve this, a thin yet stable layer of liquid must be formed. This is achieved by means of a hermetically sealed enclosure, or 'liquid cell', that constrains the liquid into a layer less than a few micrometres thick (De Jonge & Ross, 2011) as is presented schematically in Figure 3-5.

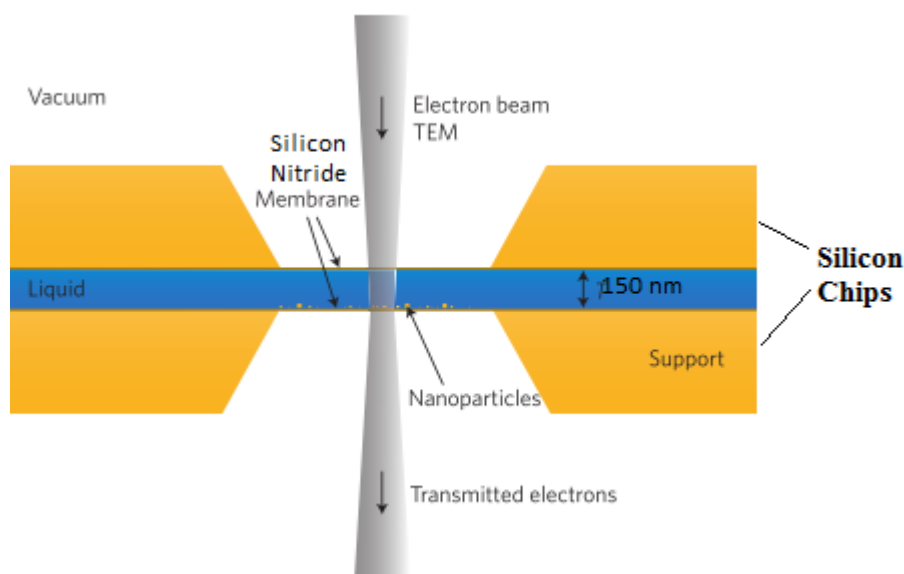


**Figure 3-5 TEM imaging of NPs in a liquid fully enclosed between two electron transparent silicon nitride membranes (adapted from de Jonge & Ross, 2011).**

In order to carry out imaging of the sample, a double aberration corrected JEOL 2200 FS TEM operating at 200 keV in STEM mode was employed. A Protochips Poseiden Liquid Flow TEM holder was used, and the liquid cell was formed by two Poseiden silicon E-chips placed on top of one another with an electron transparent viewing pane in the centre of the chips made from silicon nitride. The viewing window is 50 x 400  $\mu\text{m}$  and the space between the silicon chips is 150 nm. The 10  $\mu\text{g}/\text{ml}$  ZnO NP suspension flow into the chamber was maintained at 150  $\mu\text{l}/\text{hour}$  using a Harvard Apparatus Syringe Pump.

### **3.4 Toxicological Assays**

The cytotoxicity and genotoxicity of the ZnO NPs was investigated using the MTT and Comet assay respectively. For both the MTT and comet assay, the toxicity of ZnO NPs samples to A549 lung epithelial cells was investigated for an exposure time of 24 hours. A549 lung epithelial cells were cultured in DMEM with 10% foetal calf serum (DMEM-FCS).

#### **3.4.1 MTT Assay**

Cytotoxicity was measured by determining cell viability using the MTT (3-(4,5-Dimethylthiazol-2-yl)-2,5-diphenyl tetrazolium bromide) colorimetric assay. The MTT solution reduces from a yellow tetrazole to purple formazan in the mitochondria of living cells (where reductase enzymes are active). Cell viability is measured by the percentage of light absorbance at a certain wavelength (typically between 500 and 600 nm) using a spectrometer.

Cells were seeded at a density of 20,000 cells/well. The DMEM-FCS was removed using a Vacuboy suction device and the cells were then washed with Dulbecco's phosphate buffer solution (DPBS).

100  $\mu$ l of varying concentrations of ZnO suspensions in MilliQ water was added to each well and diluted with 900  $\mu$ l of DMEM (no FCS). The resultant concentrations of ZnO in DMEM were 1000, 100, 10, 1 and 0.1  $\mu$ g/ml. The wells were then placed in the incubator (37°C / 10% CO<sub>2</sub>) for 24 hours after which time, 10  $\mu$ l MTT1 dye was added to each well and then replaced in the incubator for 4 hrs. 100  $\mu$ l MTT2 was added and the wells were placed back in to the incubator overnight. Optical absorbance was then measured using a reference wavelength of 540 nm. The results, expressed as percentage viability are calibrated against untreated control wells (without ZnO particles), thus determining the effectiveness of the particles in causing cell death. The charts produced show the percentage cell viability plotted as a function of ZnO NP concentration, examples of which are presented in Figure 7-1. For each concentration of ZnO, the experiment was repeated 3 times. The cell viability was taken as an average of the 3 measurements and the standard deviation was calculated.



### 3.4.2 Comet Assay

Single-cell gel electrophoresis (comet assay) is a technique for measuring the damage induced to the deoxyribonucleic acid (DNA) in cells (genotoxicity). After cells have been exposed to a material of which the genotoxicity is to be determined, they are embedded in agarose on a microscope slides and lysed with detergent and high salt to form nucleoids containing supercoiled loops of DNA linked to the nuclear matrix. When a current is passed across them in an electrophoresis tank, loops containing breaks will uncoil and due to the negative charge of DNA, will migrate towards the anode resulting in structures resembling comets. The treated nucleoids are then stained and can be observed by fluorescence microscopy, examples of which are presented in Figure 3-6 showing (a) an undamaged cell and (b) a damaged cell. The intensity of the comet tail relative to the head reflects the number of DNA breaks. The average percentage of DNA in the comet tail is expressed as a measure of the genotoxicity.

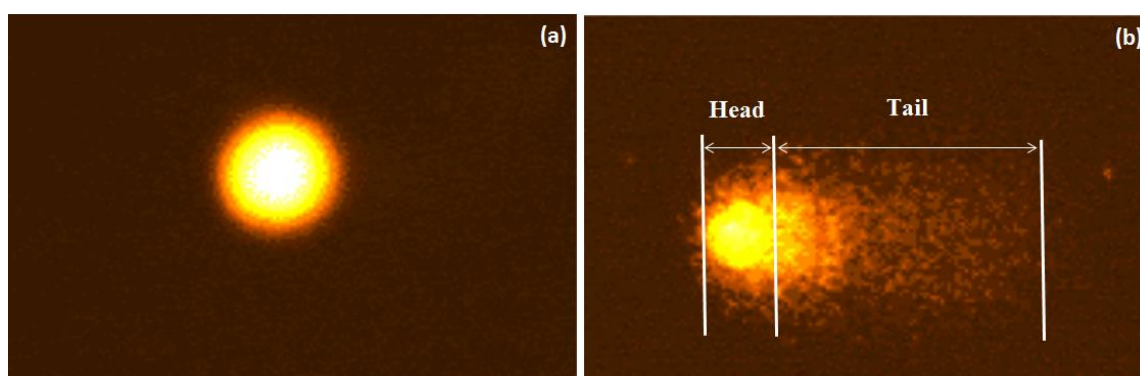


**Figure 3-6 Fluorescence microscope images of A549 cells after exposure to 10 µg/ml ZnO; (a) undamaged cell with DNA intact and (b) damaged cell with DNA in the tail.**

#### *Sample Preparation*

Description of solutions used in the comet assay:

**Lysis buffer:** 2.5M NaCl – 146.1g/L, 100mM Na<sub>2</sub>EDTA – 37.2g/L, 1% N-lauroyl sarcosine – 10g/L, 10mM TRIS [pH 10] – 1.2g/L, 1% Triton (added immediately before lysis), 10% DMSO (added immediately before lysis).

**Running buffer:** 2ml/L of 1mM EDTA -18.6g/100ml (add NaOH to dissolve then bring to pH 8 with HCl), 1.5L of 300mM NaOH – 12g/L

**Neutralising buffer:** 400mM TRIS pH 7.5 – 48.6g/L (pH to 7.5 with HCl)

**Ethidium bromide:** 500µg/ml stock soln - 20µl/ml

All solutions made in de-ionized water.

A work station (hood with extraction) was sterilized using ethanol and Virkon and prior to any containers entering the sterile atmosphere, they too were cleaned using the same solutions. The cells were divided equally into 6 well plates where they attached to the floor of the well. The DMEM-FCS was removed using a Vacuboy suction system, being careful not to damage the cells in the process. 2mls of DPBS was added to each well in order to wash the cells and subsequently removed. 1.8 mls of DMEM (no FCS) was then added to each well, followed by 200 µl of ZnO suspensions of varying concentrations. Cell suspensions are then stored in a cell culture incubator (37°C / 10% CO<sub>2</sub>) for 24 hours. Microscope slides used as a substrate for the cells during electrophoresis, were coated in 1% normal agarose in DPBS solution at 37°C. 100µl agarose is spread evenly onto warm slides using a clean slide. These were left to dry completely and stored for up to 1 week at room temperature in an air tight box.

After exposure, 60µl of the cell suspension was added to 200µl of 1% low melting point agarose in PBS (kept at 37°C). Duplicates of 100µl cells suspended in agarose were placed onto one prepared slide side by side then covered with coverslips in order to spread the agarose evenly. The prepared slide was immediately placed on an ice block for a maximum of 30 seconds to set the agarose but avoid disruption of the cells. The coverslips were removed and placed in a black box and immersed in lysis buffer at 4 °C for a minimum of 1 hour. In a dark room, the slides were then immersed in freshly prepared cold running buffer in the electrophoresis tank. The nucleoids were then left to unwind for 40 minutes.

A voltage of 23 V was then applied for 20 minutes – again this was carried out in a dark room. After electrophoresis, the slides were carefully removed from the tank and covered with cold neutralising buffer for 5 minutes. They were then stained with

25µl ethidium bromide solution and a coverslip added. The slides were then stored in an airtight box at 4°C for a maximum of 2 days.

The slides were then scored using a fluorescence microscope. The percentage head and tail DNA of 125 cells per treatment were analysed, using the Komet 5.5 software. Control cells were treated with 1.8 ml DMEM and 200 µl MilliQ water. Experiments were carried out in triplicate. The average percentage of DNA damage and standard deviation was calculated and the results are plotted as bar charts with percentage DNA damage plotted as a function of ZnO NP concentration, examples of which are shown in Figure 7-2.

### 3.4.3 Statistical Analysis of Toxicity Data

The statistical difference between control and treated cells was statistically analysed by paired Student's *t*-test. The difference between two sample means measured in terms of the standard error of those means (*t*) was calculated using the following equation:

$$t = (\bar{X}_1 - \bar{X}_2) / (s_1^2/n_1 + s_2^2/n_2)^{1/2} \quad \text{Equation 3-6}$$

Where  $\bar{X}_1$  is the mean of sample 1,  $\bar{X}_2$  is the mean of sample 2,  $n_1$  is the number of samples from which the average was obtained for sample 1,  $n_2$  is the number of samples from which the average was obtained for sample 2,  $s_1$  is the standard deviation of sample 1 and  $s_2$  is the standard deviation of sample 2. The outcome of the *t*-test is called the *t*-value. The *t*-value was then converted into a *p*-value using a *t*-table (T Distribution Critical Value Table, 2013). The *p*-value is always between 0 and 1 and gives the probability of the difference in the data being due to sampling error or chance. Any measurement with  $p < 0.05$  is taken to be statistically, significantly different to the control experiment.

#### **3.4.4 Uptake Studies**

The toxicological effect of ZnO NPs to cells was also investigated by monitoring NP uptake *in vitro*. After incubation with ZnO NPs at 37°C and 10 % CO<sub>2</sub> in DMEM, cells were prepared for TEM analysis. This was achieved by harvesting the cells and then placing in fixative (2% glutaraldehyde and 2% formaldehyde in 100 mM PIPES buffer). The cells were then washed in a buffer, then spun into pellets and fixed in 2% osmium tetroxide. Following dehydration by a series of ascending strength alcohols and washing with dry acetone, the specimens were infiltrated with Spurr's resin which was polymerised at 60 °C for 24 h. From the polymerised block, sections were cut with a nominal thickness of 100 nm using an ultra-microtome (Leica Ultra-cut E) and placed on a copper grid (Agar Scientific). Sections were stained with uranyl acetate and then analysed using TEM and STEM.

## **4 Characterisation of Commercially Sourced ZnO Nanoparticle samples**

In order to obtain a set of ZnO NPs suitable for use in toxicity assays, a variety of samples were sourced from commercial suppliers. In total, 12 samples were sourced comprising 3 colloidal dispersions of ZnO NPs in water (some with coatings added to the particles to aid in the dispersion) and 9 dry powder samples. In order to correlate toxicity assay results to a specific well defined set of NP characteristics, it is essential to thoroughly characterise each ZnO sample. Required characteristics of the NPs are the size, morphology, composition, purity, phase content, agglomeration and dissolution at appropriate solution concentrations. This chapter screens all 12 samples (section 4.1) and then concentrates on more detailed characterisation of just three commercial samples (section 4.2) selected to go forward for dispersion and solubility characterisation (Chapter 6) and toxicity studies (Chapter 7), on the basis of their differing physicochemical characteristics. The characterisation techniques discussed in chapter 3 are employed in order to acquire all of the desired physicochemical characteristics of the ZnO NP samples.

### **4.1 Review of Commercial ZnO Nanoparticle samples**

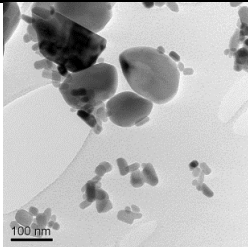
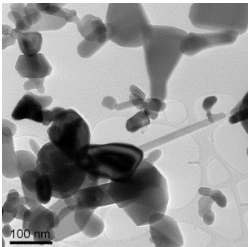
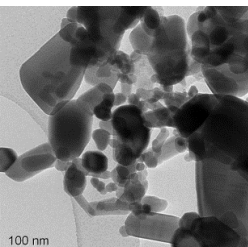
Initially all 12 samples were screened by TEM in order to determine the NP size distribution and morphology. The results of these investigations are presented in Table 4-1 where a great deal of variation between samples is evident. The Feret lengths (the greatest distance between two parallel lines that just do not intersect in an image of the particle) and Feret widths (the smallest distance between two parallel lines that just do not intersect in an image of the particle) (Xu and Di Guida, 2003) of 250 particles from each sample were measured from TEM images. For each particle measured, the Feret ratio (Feret ratio = Feret Length /Feret Width) was obtained. The average particle Feret length, Feret width and Feret ratio for each sample was calculated from the 250 particle measurements and are reported along with the standard deviation in Table 4-1. Results indicate that the majority of samples have large size distributions and contain particles of varying morphology. This indicates that in order to obtain samples with narrow size distributions, either a method of

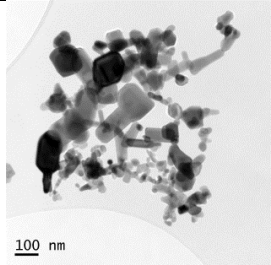
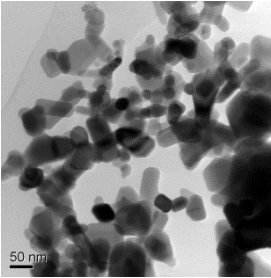
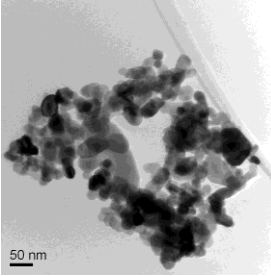
particle separation by size must be developed, or more controlled methods of synthesis need to be developed. The synthesis of ZnO NPs by a number of techniques is discussed in Chapter 5 however, it was thought to be important to continue investigations with commercial samples, as these particles are a more accurate representation of the particles being used in commercial applications such as sunscreens and cosmetics. Hence, the need to determine their toxicity is of direct environmental relevance.

Three commercial ZnO NPs were chosen to investigate in the toxicity studies and assigned sample codes: Alfa Aesar Nanotek 40 % wt colloidal dispersion in water (EN-Z-1), Alfa Aesar Metals Basis dry powder (EN-Z-2) and Micronisers Pty Limited Nanosun dry powder (EN-Z-3) (Table 4-1 Summary of commercial samples purchased including a TEM image and particle sizes measured from 250 particles. Table 4-1). EN-Z-1 was selected in order to investigate a sample received as a colloidal dispersion in water, which may most closely mimic the state in which the NPs will be delivered to the environment if in the form of a suncream or cosmetic etc. Of the commercial colloidal dispersions available, EN-Z-1 has the narrowest size distribution (Length:  $30 \pm 20$  nm; Width:  $16 \pm 10$  nm; Feret Ratio:  $1.9 \pm 0.8$ ). Information obtained from the vendor revealed that these particles are made by Physical Vapor Synthesis; a solid metal is fed into an electric arc to generate a high temperature vapor, a reactant gas is added to the vapor, and the result is then cooled and condensed to form NPs (TechServices, 2012). EN-Z-2 ZnO nanopowder was selected for its relatively narrow size distribution (Length:  $40 \pm 20$  nm; Width:  $30 \pm 12$  nm; Feret Ratio:  $1.45 \pm 0.3$ ). The vendor would not disclose any information regarding the synthesis procedure for these NPs. EN-Z-3 was chosen because it is used in a commercially available sunscreen and has a relatively narrow size distribution (Length:  $38 \pm 10$  nm; Width:  $30 \pm 7$  nm; Feret Ratio:  $1.34 \pm 0.25$ ). EN-Z-3 is produced by mechanical milling of bulk ZnO ([www.micronisers.com](http://www.micronisers.com)).

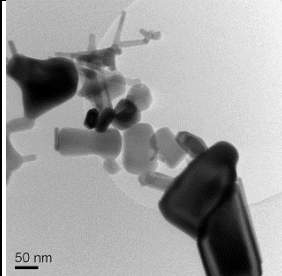
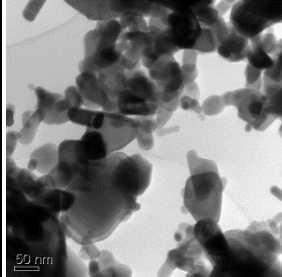
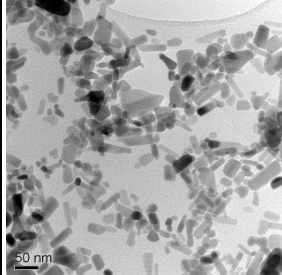
As the ENNSATOX project was going to be investigating a number of different ZnO NP samples as well as other NP materials, it became clear that the development and implementation of a characterisation protocol was necessary to ensure a systematic approach was adopted.

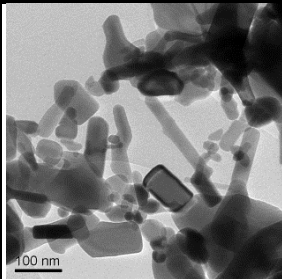
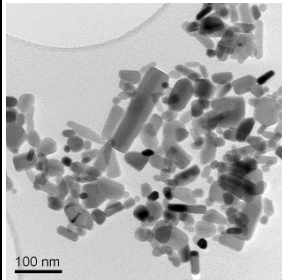
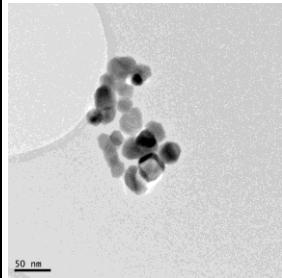
**Table 4-1 Summary of commercial samples purchased including a TEM image and particle sizes measured from 250 particles.**

Sample Name	Supplier	Nominal Size Quoted by Supplier (nm)	Supplier Purity (%)	Form	Average Particle Size (nm) L = Feret Length; W = Width; FR = Feret Ratio	Morphology	TEM image
ZnO	Io-Li-Tec	10-200	99.9	Dry powder	$L = 105 \pm 67$ ; $W = 45 \pm 28$ ; $FR = 2.9 \pm 2.2$	Ranging from spherical to elongated, faceted and equiaxial	
ZnO < 50 nm	Sigma Aldrich	10-100	96.1	Dry powder	$L = 113 \pm 51$ ; $W = 26 \pm 38$ ; $FR = 3.61 \pm 2.26$	Ranging from spherical to elongated, faceted and equiaxial	
ZnO < 100 nm	Sigma Aldrich	10-200	99.5	Dry powder	$L = 80 \pm 30$ ; $W = 37 \pm 26$ ; $FR = 2.74 \pm 1.15$	Ranging from spherical to elongated, faceted and equiaxial.	

Sample Name	Supplier	Nominal Size Quoted by Supplier (nm)	Supplier Purity (%)	Form	Average Particle Size (nm) L = Feret Length; W = Width; FR = Feret Ratio	Morphology	TEM image
NanoGard	Alfa Aesar	10-200	99	Dry powder	$L = 140 \pm 50$ ; $W = 67 \pm 30$ ; $FR = 2.45 \pm 1.23$	Ranging from spherical to elongated, faceted and equiaxial	
NanoGard Low Lead	Alfa Aesar	10-200	99	Dry powder	$L = 150 \pm 130$ ; $W = 44 \pm 35$ ; $FR = 4.4 \pm 4.9$	Ranging from spherical to elongated, faceted and equiaxial.	
Metals Basis ZnO EN-Z-2	Alfa Aesar	20-30	99	Dry powder	$L = 40 \pm 20$ ; $W = 30 \pm 12$ ; $FR = 1.45 \pm 0.3$	Mostly spherical, faceted, equiaxial.	



Sample Name	Supplier	Nominal Size Quoted by Supplier (nm)	Supplier Purity (%)	Form	Average Particle Size (nm) L = Feret Length; W = Width; FR = Feret Ratio	Morphology	TEM image
ZnO Nanotek® Organosilane Coated	Alfa Aesar	40-100	99%	Dry; organosilane coated, hydrophobic, polar.	$L = 100 \pm 35$ ; $W = 40 \pm 35$ ; $FR = 3.56 \pm 2.1$	Ranging from spherical to elongated, faceted and equiaxial.	
ZnO, Nanotek®	Alfa Aesar	40-100	99	Dry powder	$L = 102 \pm 52$ ; $W = 48 \pm 37$ ; $FR = 3.35 \pm 3.20$	Ranging from spherical to elongated, faceted and equiaxial	
ZnO, Nanotek®, 40% in H2O EN-Z-1	Alfa Aesar	40	40 % concentration	40% colloidal dispersion in H <sub>2</sub> O	$L = 30 \pm 20$ ; $W = 16 \pm 10$ ; $FR = 1.9 \pm 0.8$	Mostly elongated and faceted.	

Sample Name	Supplier	Nominal Size Quoted by Supplier (nm)	Supplier Purity (%)	Form	Average Particle Size (nm) L = Feret Length; W = Width; FR = Feret Ratio	Morphology	TEM image
ZnO NanoShield®, 50% IN H2O	Alfa Aesar	70	50 % concentration	50% colloidal dispersion in H <sub>2</sub> O with cationic surfactant (unknown)	L = 114 ± 47; W = 30 ± 15 ; FR = 4.5 ± 2.5	Spherical, elongated, faceted, equiaxial.	
ZnO, NanoArc®, 40% in H2O	Alfa Aesar	30	40 % concentration	40% colloidal dispersion in H <sub>2</sub> O with non-ionic surfactant (unknown)	L = 90 ± 78; W = 30 ± 22 ; FR = 3.7 ± 2.7	Spherical, elongated, faceted, equiaxial.	
Nanosun EN-Z-3	Micronisers Pty Limited	n/a	n/a	Dry powder	L = 38 ± 10; W = 30 ± 7 ; FR = 1.34 ± 0.25	Spherical, faceted, equiaxial.	

## 4.2 Characterisation Protocol

In order to obtain information regarding a NP sample's distribution of particle sizes and morphologies, crystallinity, composition and purity, agglomeration behaviour and solubility, a variety of techniques were required (Chapter 3). The characterisation techniques were divided into four categories: bulk powder characterisation (ICP-MS, TGA-EGA, XRD, BET and Helium pycnometry), surface or surfactant characterisation (FTIR, XPS and NMR), NP characterisation (SEM, TEM, and DLS) and NP solution characterisation (DLS, Zeta potential, ICP-MS, PF-TEM) The characterisation protocol (Wallace et al., 2013) was applied to each of the samples chosen to be investigated in the ENNSATOX project.

Results for bulk sample characterisation, surface characterisation and particle characterisation techniques for in house synthesized samples of ZnO are reported in Chapter 5. Characterisation of NP solutions revealing information regarding solubility and dispersion is reported in Chapter 6. Results for bulk sample characterisation, surface characterisation and particle characterisation techniques for commercial samples of ZnO are reported in this chapter (Chapter 4).

N.B. For the techniques requiring dry powder samples, EN-Z-1 was dried in an oven for 72 hours at 30°C in order to remove the water content of the sample.

### 4.2.1 Bulk Sample Characterisation

ICP-MS, XRD, BET, Helium pycnometry and TGA-EGA using FTIR were employed in order to determine information regarding the composition, phase, purity and particle size of the bulk powder.

#### 4.2.1.1 Inductively Coupled Plasma-Mass Spectrometry

Aqueous suspensions of each of the samples of ZnO were prepared as described in section 3.2.1.1 and were then analysed using ICP-MS in order to obtain an overview of the concentrations of any impurities present in the samples. The MilliQ water used was also analysed as well as a blank of water with HNO<sub>3</sub>. The detected concentration of each element in EN-Z-1, EN-Z-2 and EN-Z-3 is presented in Figure 4-1. The data presented has the concentrations of each element measured for the HNO<sub>3</sub> blank subtracted. The main peak is that of zinc which is expected,

although the actual concentration measured for each sample varies considerably from the nominal concentration expected, especially in the case of EN-Z-1. ICP-MS does not detect gases and therefore there is no peak for oxygen. Small amounts of sodium, silicon and calcium are detected can be seen to derive from the water. Although triple distilled MilliQ water was used, the amount of impurities present in the water would depend on the age/use of the filter in the system.

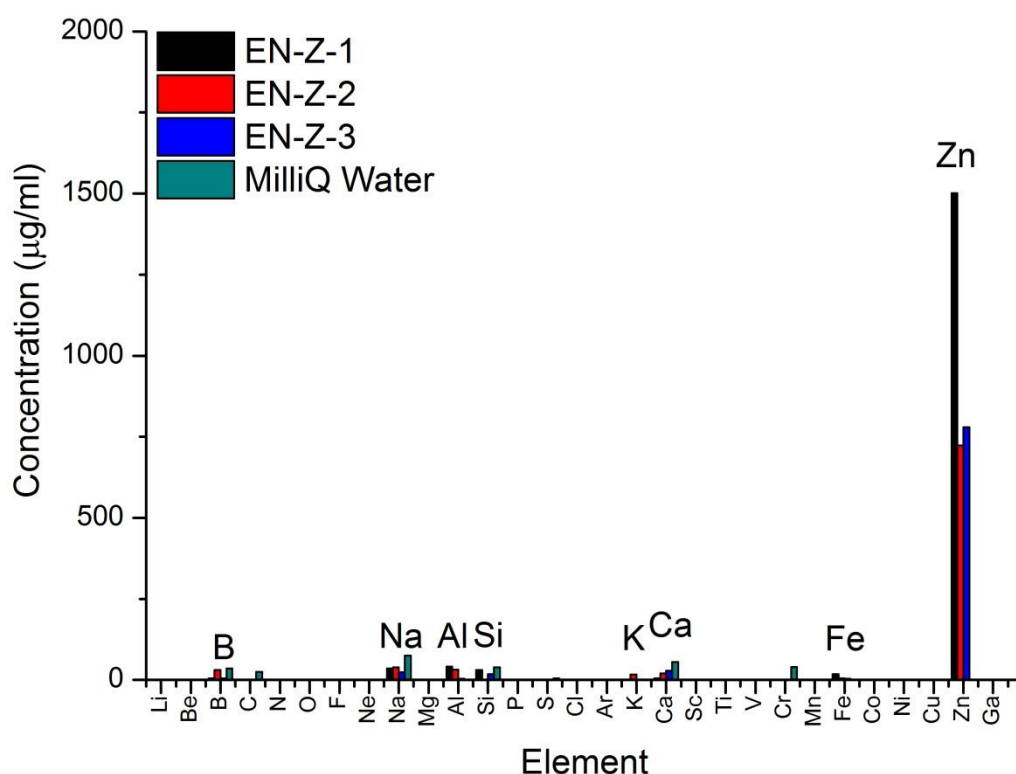


**Figure 4-1 Results of ICP-MS total quant analysis reporting the concentration of each element present in the sample.**

#### 4.2.1.2 X-ray Diffraction

The XRD patterns collected from the commercial powders are shown in Figure 4-2 with the Miller indices of the diffracting planes indicated above each peak in Figure 4-2 (a).

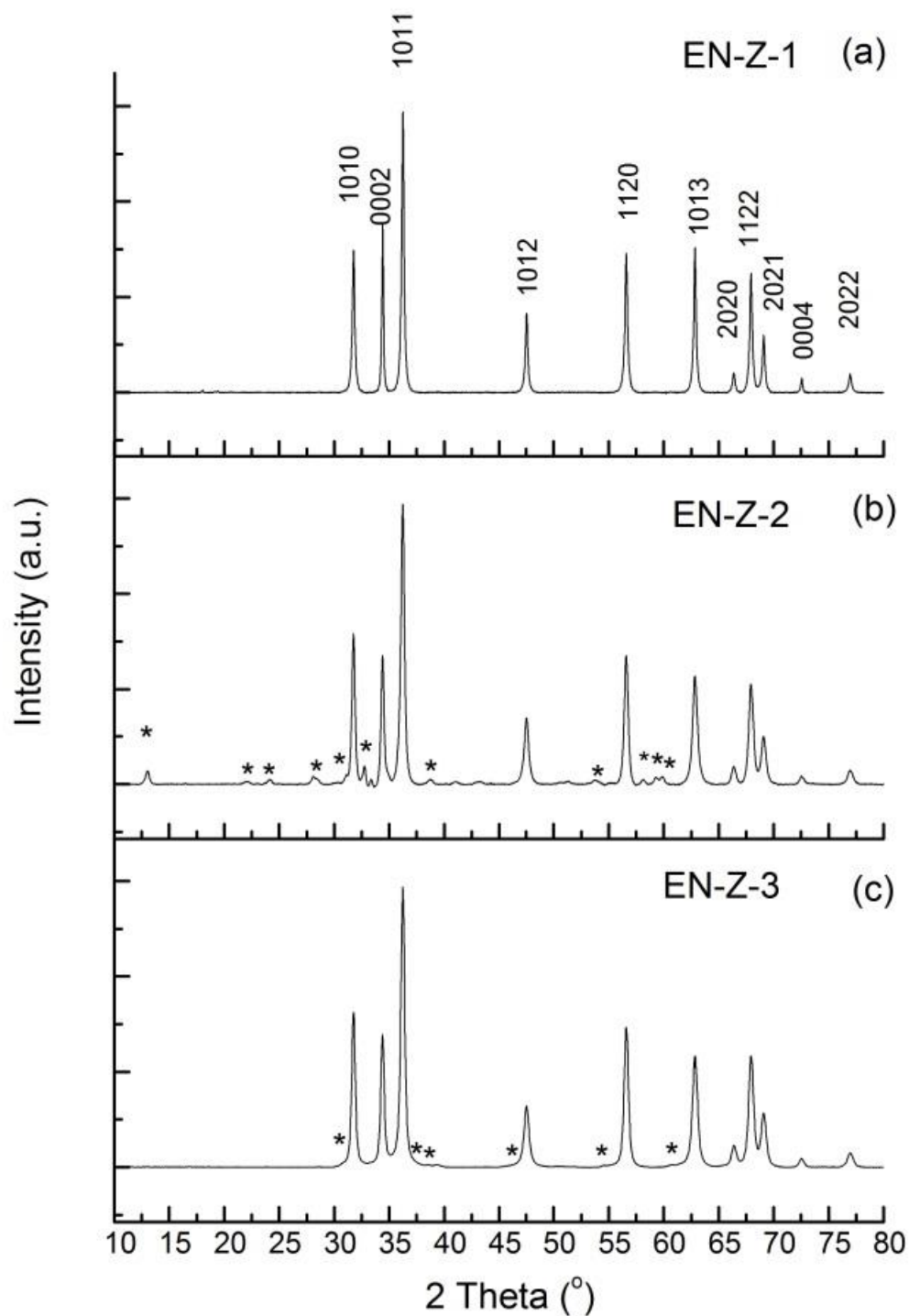


**Figure 4-2 XRD pattern for (a) EN-Z-1 (b) EN-Z-2 and (c) EN-Z-3 commercial ZnO NP samples, with the Miller indices for the reflecting plane labelled. Peaks corresponding to a secondary phase, thought to be hydrozincite, are labelled with an asterix**

The peaks in the patterns for EN-Z-1 in Figure 4-2 (a) are consistent with that of the JCPDS reference file for the hexagonal-close-packed Wurtzite structure of zincite (ref: 01-079-0206); Reference pattern and ZnO samples peak positions, with relative intensities and corresponding d-spacings are presented in Table 4-2.

The EN-Z-2 powder pattern in Figure 4-2 (b) and the EN-Z-3 powder pattern in Figure 4-2 (c) also contain all of the peaks consistent with the zincite reference pattern. However, additional peaks are also observed, that have been labelled with an asterisk, which indicate there is a secondary phase in the sample. The peaks are relatively clear in the EN-Z-2 sample, however for the EN-Z-3 sample, the pattern must be closely inspected to identify them, indicating that the impurity is not as prevalent in EN-Z-3. The peak positions observed are consistent with the most intense peaks of the JCPDS reference file for hydrozincite ( $Zn_5.(CO_3)_2.OH_6$ ) (ref: 00-014-0256); See Table 4-3. The largest intensity peak in the reference pattern for the 311 plane of hydrozincite, which occurs at  $30.591^\circ 2\theta$  is present in both the EN-Z-2 and EN-Z-3 samples. The synthesis of Wurtzite zinc oxide containing varying amounts of hydrozincite phase has previously been reported (Music et al. 2002; Bitenc et al., 2012). The average crystallite size was estimated from each of the peaks, using the Scherrer equation and assuming no contribution to the broadening from residual strain (Cullity, 2001). Using all of the values obtained, an average crystallite size was calculated for each sample; EN-Z-1 =  $52 \pm 15$  nm; EN-Z-2 =  $29 \pm 5$  nm EN-Z-3 =  $33 \pm 8$  nm.

#### 4.2.1.3 Gas Adsorption (BET)

The specific surface area (SSA) of each sample was determined by gas adsorption technique (BET). Adsorption-desorption isotherms for EN-Z-1, EN-Z-2 and EN-Z-3 are presented in Figure 4-3, Figure 4-4 and Figure 4-5 respectively. It is clear that the adsorption-desorption isotherm for EN-Z-1 is considerably different to the isotherms for EN-Z-2 and EN-Z-3, indicating there may be significant differences between the samples in relation to particle morphology or porosity. The SSA values measured are reported in Table 4-4 along with the corresponding calculated average particle sizes.

**Table 4-2 XRD peak positions, corresponding d-spacings, and relative intensities for EN-Z-1, EN-Z-2, and EN-Z-3 samples. Also listed are the referenced values for zincite extracted from the JCPDS file ref: 01-079-0206**

Number	ZnO <i>hkl</i>	2 $\theta$ ( $^{\circ}$ )				d-spacing ( $\text{\AA}$ )				Relative Intensity (%)			
		JCPDS Ref:	Experimental XRD Pattern			JCPDS Ref:	Experimental XRD Pattern			JCPDS Ref:	Experimental XRD Pattern		
			EN-Z-1	EN-Z-2	EN-Z-3		EN-Z-1	EN-Z-2	EN-Z-3		EN-Z-1	EN-Z-2	EN-Z-3
1	10 $\bar{1}$ 0	31.77	31.77	31.75	31.75	2.815	2.815	2.816	2.816	57.6	50.7	53.8	55.2
2	0002	34.42	34.42	34.40	34.39	2.603	2.604	2.605	2.606	41.4	59.6	46.0	46.0
3	10 $\bar{1}$ 1	36.25	36.26	36.24	36.23	2.476	2.476	2.477	2.477	100	100.0	100.0	100.0
4	10 $\bar{1}$ 2	47.54	47.54	47.54	47.52	1.911	1.911	1.911	1.912	21.4	28.2	23.6	21.3
5	11 $\bar{2}$ 0	56.6	56.61	56.59	56.60	1.625	1.625	1.625	1.625	30.7	49.6	46.1	50.1
6	10 $\bar{1}$ 3	62.86	62.86	62.84	62.83	1.477	1.477	1.478	1.478	26.4	51.6	38.6	39.3
7	20 $\bar{2}$ 0	66.37	66.36	66.40	66.40	1.407	1.408	1.407	1.407	4	7.0	6.4	6.4
8	11 $\bar{2}$ 2	67.95	67.96	67.93	67.95	1.378	1.378	1.379	1.379	21.7	42.4	35.8	38.6
9	20 $\bar{2}$ 1	69.09	69.08	69.10	69.07	1.359	1.359	1.358	1.359	10.5	20.4	17.1	18.2
10	0004	72.57	72.57	72.92	72.53	1.302	1.302	1.296	1.302	1.6	5.2	3.0	3.0
11	20 $\bar{2}$ 2	76.96	76.95	76.85	76.99	1.238	1.238	1.239	1.238	3.3	6.6	4.6	4.8

**Table 4-3 Peak list extracted from JCPDS reference file for hydrozincite (ref: 00-014-0256). Also listed are the corresponding peaks present in the EN-Z-2 and EN-Z-3 XRD spectra.**

No.	Zn <sub>5</sub> (CO <sub>3</sub> ) <sub>2</sub> (OH) <sub>6</sub> hkl	2θ(°)			d-spacing (Å)			Relative Intensity (%)		
		JCPDS Reference	Experimental XRD		JCPDS Reference	Experimental XRD		JCPDS Reference	Experimental XRD	
			EN-Z-2	EN-Z-3		EN-Z-2	EN-Z-3		EN-Z-2	EN-Z-3
1	200	13.283	13.251	-	6.66	6.68	-	32.0	4.7	-
2	001	16.494	-	-	5.37	-	-	6.0	-	-
3	201	19.936	-	-	4.45	-	-	6.0	-	-
4	201	22.206	22.301	-	4	3.98	-	13.0	1.6	-
5	111	23.267	-	-	3.82	-	-	3.0	-	-
6	310	24.367	24.335	-	3.65	3.65	-	13.0	1.3	-
7	311	28.401	28.368	-	3.14	3.14	-	16.0	2.1	-
8	401	29.858	-	-	2.99	-	-	3.0	-	-
9	311	30.591	30.601	30.596	2.92	2.92	2.92	100.0	2	2.7
10	021	32.902	32.854	-	2.72	2.72	-	23.0	3.4	-
11	510	36.343	-	-	2.47	-	-	13.0	-	-
12	511	38.61	38.602	38.511	2.33	2.33	2.34	6.0	1.5	2.7
13	420	39.312	-	39.320	2.29	-	2.29	6.0	-	2
14	312	40.041	-	-	2.25	-	-	3.0	-	-
15	402	40.798	-	-	2.21	-	-	6.0	-	-
16	511	41.584	-	-	2.17	-	-	3.0	-	-
17	022	44.6	-	-	2.03	-	-	6.0	-	-
18	330	47.569	-	47.499	1.91	-	1.91	6.0	-	1.1
19	710	49.29	-	-	1.847	-	-	3.0	-	-
20	331	50.315	-	-	1.812	-	-	6.0	-	-
21	331	51.533	-	-	1.772	-	-	6.0	-	-
22	621	54.337	54.204	54.309	1.687	1.69	1.69	16.0	1.1	1.9
23	132	55.55	-	-	1.653	-	-	3.0	-	-
24	712	58.519	58.552	-	1.576	1.58	-	13.0	1.7	-
25	023	59.43	59.495	-	1.554	1.55	-	10.0	1.9	-
26	332	60.722	60.622	60.712	1.524	1.53	1.52	6.0	2.2	0.9
27	223	62.028	-	-	1.495	-	-	3.0	-	-
28	603	63.445	-	-	1.465	-	-	16.0	-	-
29	910	64.179	-	-	1.45	-	-	3.0	-	-
30	821	66.71	-	-	1.401	-	-	3.0	-	-
31	911	68.482	-	-	1.369	-	-	10.0	-	-
32	242	1.346	-	-	13	-	-	13.0	-	-
33	640	72.935	-	-	1.296	-	-	3.0	-	-
34	442	73.997	-	-	1.28	-	-	3.0	-	-
35	150	75.586	-	-	1.257	-	-	2.0	-	-
36	024	77.4	-	-	1.232	-	-	13.0	-	-
37	604	80.191	-	-	1.196	-	-	6.0	-	-
38	243	83.928	-	-	1.152	-	-	6.0	-	-



The average particle size approximated from BET for EN-Z-2 and EN-Z-3 are 37 and 25 nm respectively. These values are in relatively good agreement with XRD crystallite size determinations of  $29 \pm 5$  nm for EN-Z-2 and  $33 \pm 8$  nm for EN-Z-3; falling within the standard deviation, indicating that the particles are predominantly single crystals. However, the average particle size obtained by BET for EN-Z-1, 387 nm, is significantly larger than the value determined by XRD,  $52 \pm 15$  nm. The discrepancy between measurements may indicate that the particles are polycrystalline, or heavily agglomerated. During the de-gassing process prior to BET measurements, the samples are heated to 250°C. If a coating is present on the surface of the particles, (EN-Z-1 is received as a colloidal dispersion therefore this may be a possibility), the thermal treatment may cause the structure of the coating to alter or be partially decomposed. It is possible that a decomposed layer of the coating may encapsulate or aggregate a group of particles, which would result in a reduction in the effective surface area. Additional analysis of the samples by DLS and PF-TEM is required in order to clarify the results.

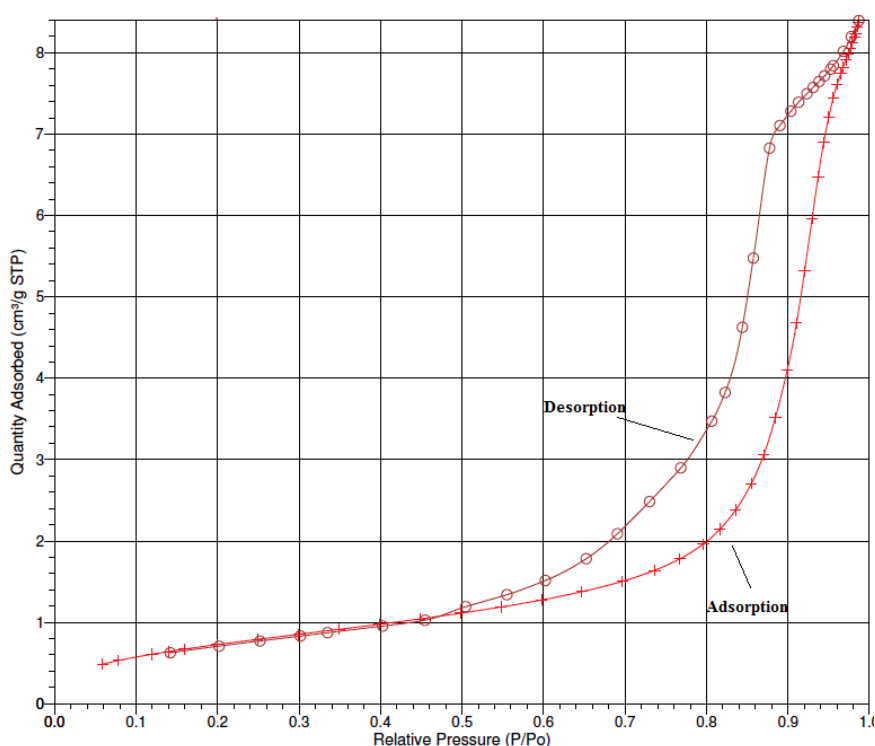


**Figure 4-3 BET adsorption – desorption isotherm for EN-Z-1**

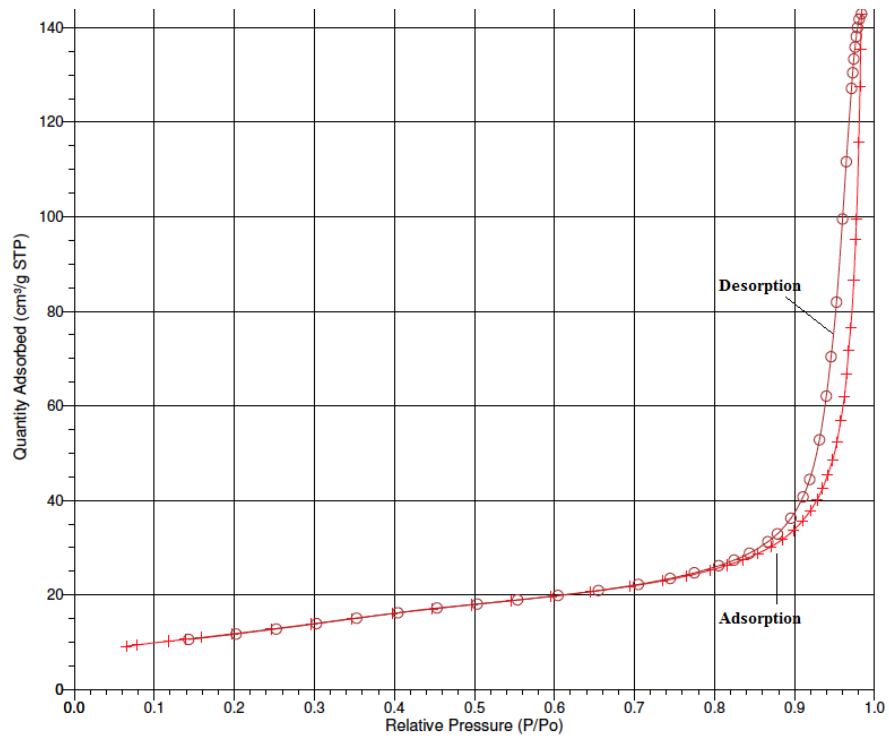


**Figure 4-4 BET adsorption – desorption isotherm for EN-Z-2**

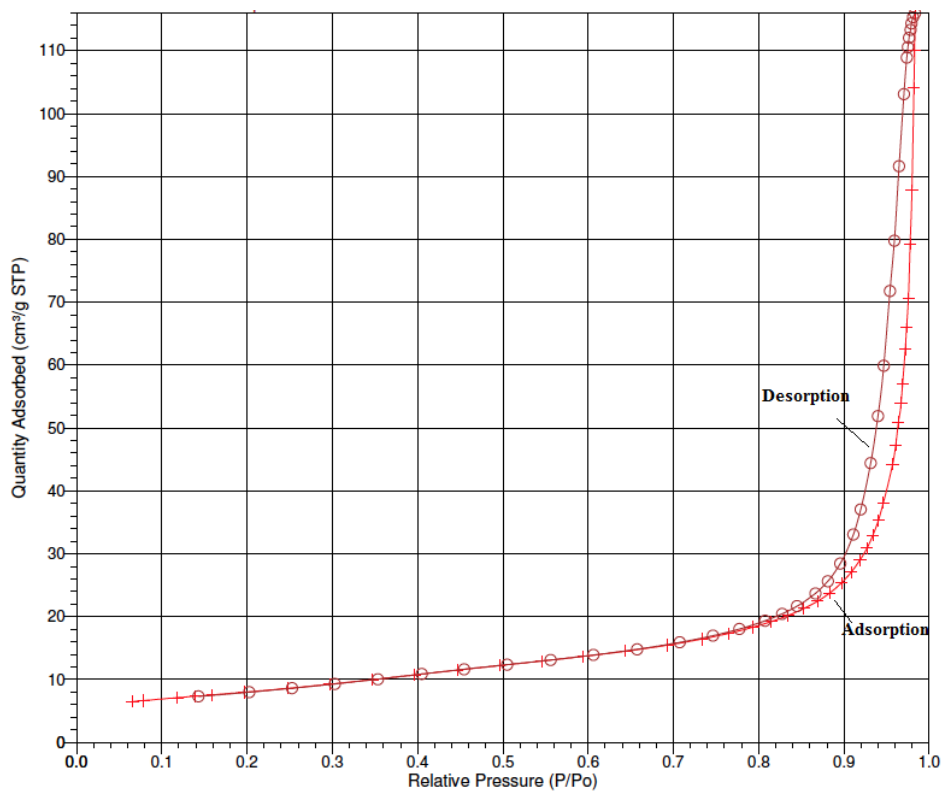


**Figure 4-5 BET adsorption – desorption isotherm for EN-Z-3**

**Table 4-4 Specific surface area measurements for commercial ZnO samples determined by gas adsorption technique (BET)**

<b>Sample Name</b>	<b>Specific Surface Area (m<sup>2</sup>/g)</b>	<b>Standard Deviation (m<sup>2</sup>/g)</b>	<b>Particle Size (nm)</b>
<b>EN-Z-1</b>	2.77	0.013	386.60
<b>EN-Z-2</b>	43.61	0.317	24.52
<b>EN-Z-3</b>	28.77	0.060	37.18

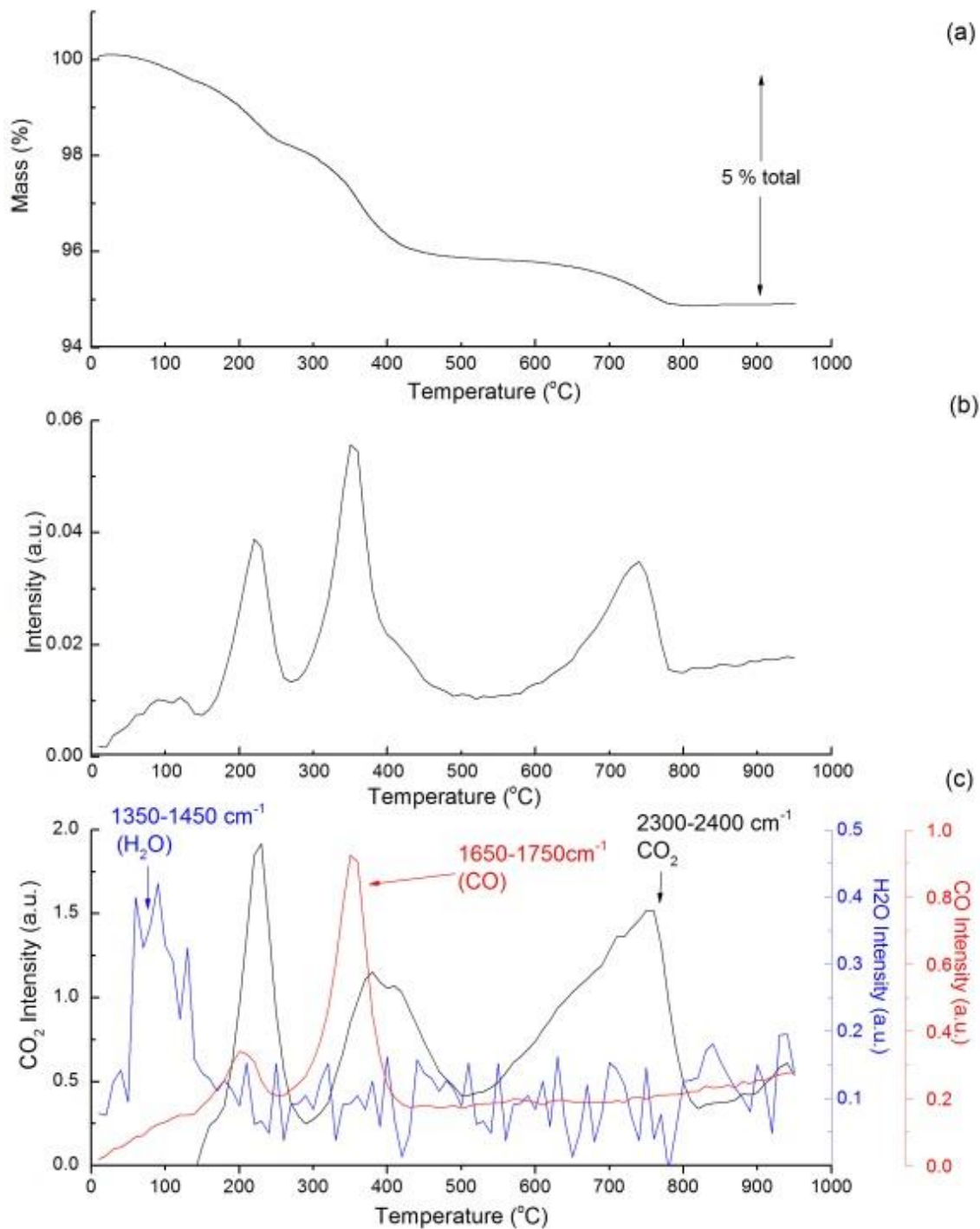
*4.2.1.4 Thermogravimetric Analysis with Evolved Gas Analysis by Fourier Transform Infrared Spectroscopy*

Figure 4-6, Figure 4-7 and Figure 4-8 (a) present the results of TGA experiments heating to 950 °C, performed on the samples with the mass loss expressed as a percentage of the total initial starting mass. Evolved gas analysis was performed on the sample in order to confirm the composition of the gases emanating from the sample during TGA. The reduction in mass observed in Figure 4-6, Figure 4-7 and Figure 4-8 (a) can be explained by the increase in overall absorbance observed in the Gram-Schmidt plots presented in Figure 4-6, Figure 4-7 and Figure 4-8 (b). Figure 4-6, Figure 4-7 and Figure 4-8 (c) show how the absorbance intensity changes for specific wavenumber ranges as the temperature rises, with the wavenumber range labelled on the graph.

The TGA curve for EN-Z-1 displays a very small mass drop between 50°C and 150°C in which the sample loses approximately 0.5% of the total mass. This can be explained by evaporation of water weakly adsorbed to the NP surface (Li et al., 2010). Evidence for this is observed in Figure 4-6 (c) which shows the absorbance detected in the range 1350-1450 cm<sup>-1</sup>, indicative of O-H bending, increasing in intensity over the same temperature range, 50°C to 150°C. There is then a steeper reduction in weight between 150 and 250°C where the sample loses around 1.5% of its total mass. Figure 4-6 (c) shows two peaks of absorbance in the range 2250-2400 cm<sup>-1</sup>, indicative of carbon dioxide evolving between 150 and 250°C. Two more

stages of CO<sub>2</sub> evolution are observed between 300 and 500°C and then again between 500 and 800°C. The evolution of CO<sub>2</sub> between 30 and 500 °C is consistent with the thermal decomposition of ZnCO<sub>3</sub> (Dollimore et al. 1979) which may indicate that after drying the EN-Z-1 colloidal dispersion to obtain a powder, atmospheric CO<sub>2</sub> has adsorbed to the surface to form ZnCO<sub>3</sub>. However, the other two phases of CO<sub>2</sub> evolution are at temperatures that are not consistent with ZnCO<sub>3</sub> thermal decomposition. Therefore it is postulated that additional impurities are present in the sample. It is possible that these evolutions may be attributed to a coating, the unconfirmed presence of which has previously been discussed in light of the unusual BET results. The sample loses more than 2% of its mass between 300 and 400°C. Although this is partially accounted for by CO<sub>2</sub> gas evolution, there is also carbon monoxide gas being evolved. Evidence for this is observed in Figure 4-6 which shows a peak of absorbance in the range 1650-1700 cm<sup>-1</sup>, indicative of CO evolving from the sample. Again, this may be a result of decomposition of the compound which may be present on the surface of the NPs. If the evolution of CO and CO<sub>2</sub> gas has been correctly assigned to the coating, it would suggest that it is an organic compound. Above 800°C the mass of the sample stabilises.

The TGA for the EN-Z-2 sample in Figure 4-7 shows a small loss of mass between 50 and 150 °C. This is due to water evaporation, evidence for which is observed in Figure 4-7 (c) which shows a peak of absorbance in the range 1350-1450 cm<sup>-1</sup> over the same temperature range. There is a steep drop in the curve between 220 and 260 °C which reflects a 3% loss of mass of the sample. This may be attributed to the evolution of CO<sub>2</sub> evident in Figure 4-7 by the increase in absorption over the range 2300-2400 cm<sup>-1</sup>. There is also an increase in absorption over the range 1350-1450 cm<sup>-1</sup> which indicates evaporation of water from the sample. The loss in mass between 220 and 260 °C may be attributed to the thermal decomposition of hydrozincite to form H<sub>2</sub>O and CO<sub>2</sub> gas which is reported to occur around 220 °C and is in very good agreement with the results presented in this study (Ray et al., 2008; Li et al., 2005). The EN-Z-3 sample follows the same trend as the EN-Z-2 sample, however the mass losses and intensities of the absorption for CO<sub>2</sub> and H<sub>2</sub>O are not as high. This may suggest that there is a smaller amount of hydrozincite present in this sample which is in agreement with the qualitative results reported by XRD.



**Figure 4-6 (a) TGA curve for EN-Z-1 showing loss of sample mass with increasing temperature; (b) associated Gram-Schmidt plot showing increase in FTIR absorbance with increasing temperature and (c) Chemigrams showing FTIR absorbance for specified ranges of wavenumber as temperature rises.**

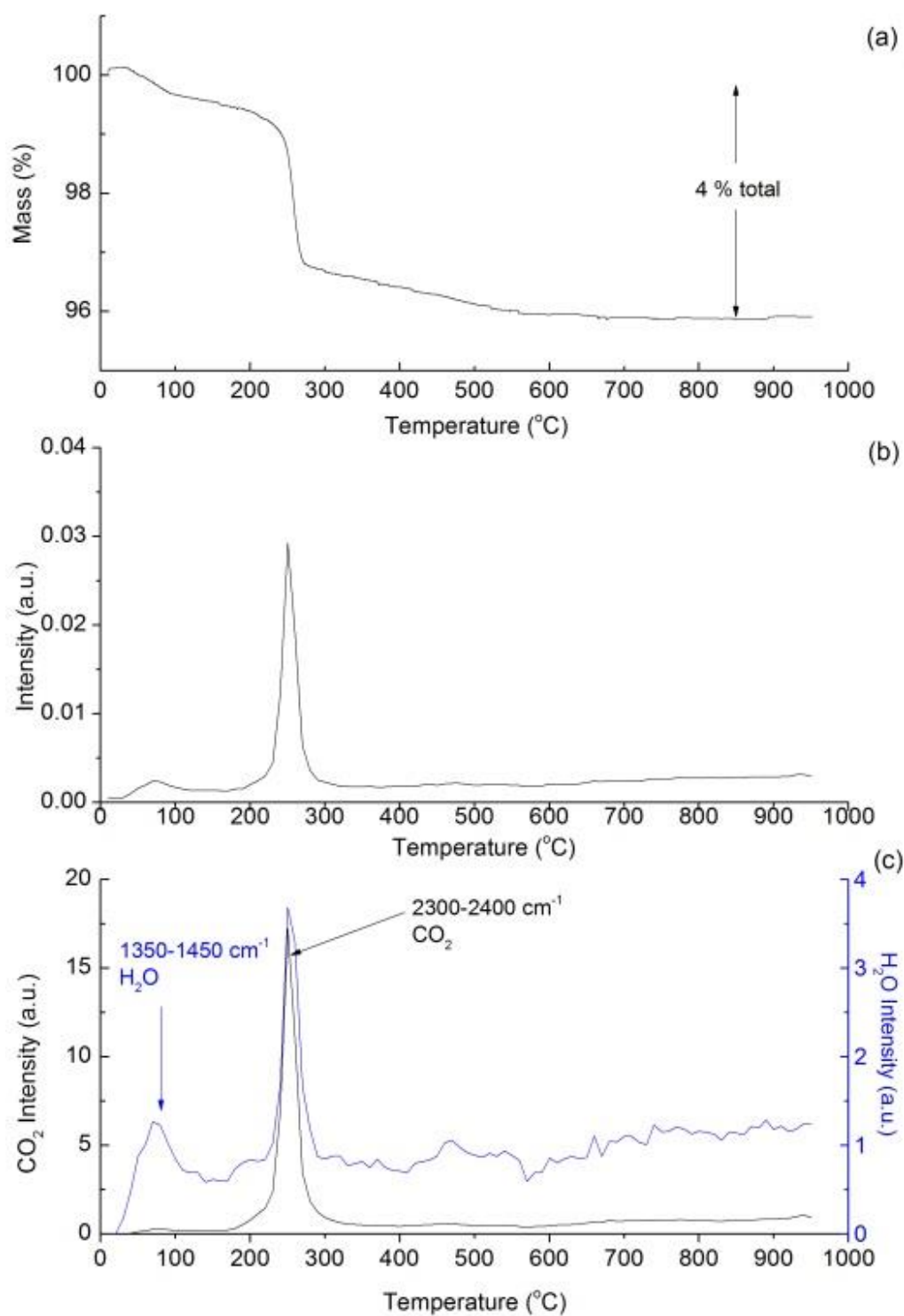


**Figure 4-7 (a) TGA curve for EN-Z-2 showing loss of sample mass with increasing temperature; (b) Gram-Schmidt plot showing increase in FTIR absorbance with increasing temperature and (c) Chemigrams showing FTIR absorbance for specified ranges of wavenumber as temperature rises.**

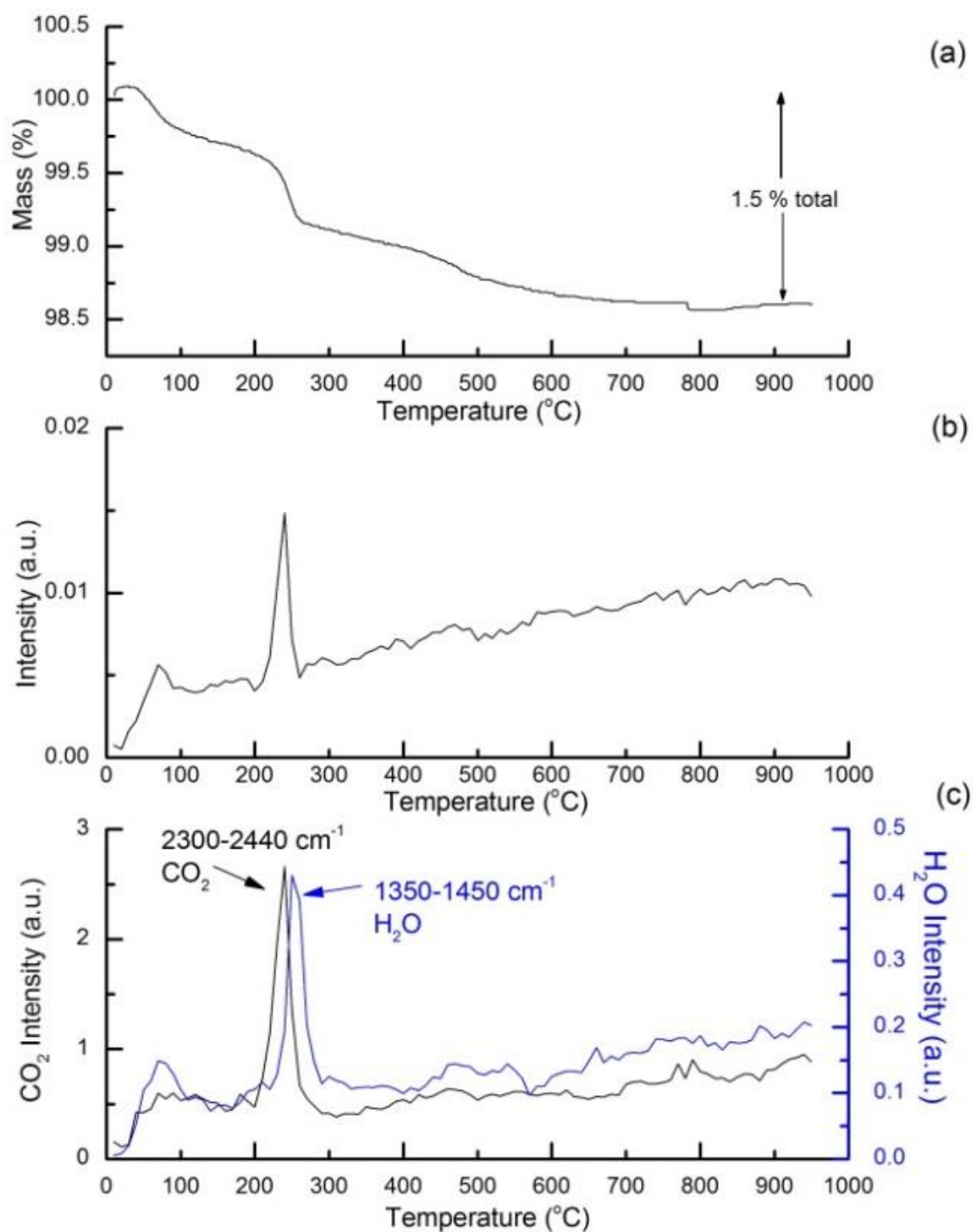


**Figure 4-8 (a) TGA curve for EN-Z-3 showing loss of sample mass with increasing temperature; (b) Gram-Schmidt plot showing increase in FTIR absorbance with increasing temperature and (c) Chemigrams showing FTIR absorbance for specified ranges of wavenumber as temperature rises.**

#### 4.2.2 Surface Characterisation

Fourier transform infrared spectroscopy (FTIR), X-ray photoelectron spectroscopy (XPS) and solid state carbon 13 nuclear magnetic resonance spectroscopy ( $^{13}\text{C}$  NMR) techniques were employed to investigate the surface composition of the samples.

##### 4.2.2.1 Fourier Transform Infrared Spectroscopy

The FTIR spectra for the commercial ZnO NP samples are presented in Figure 4-9.

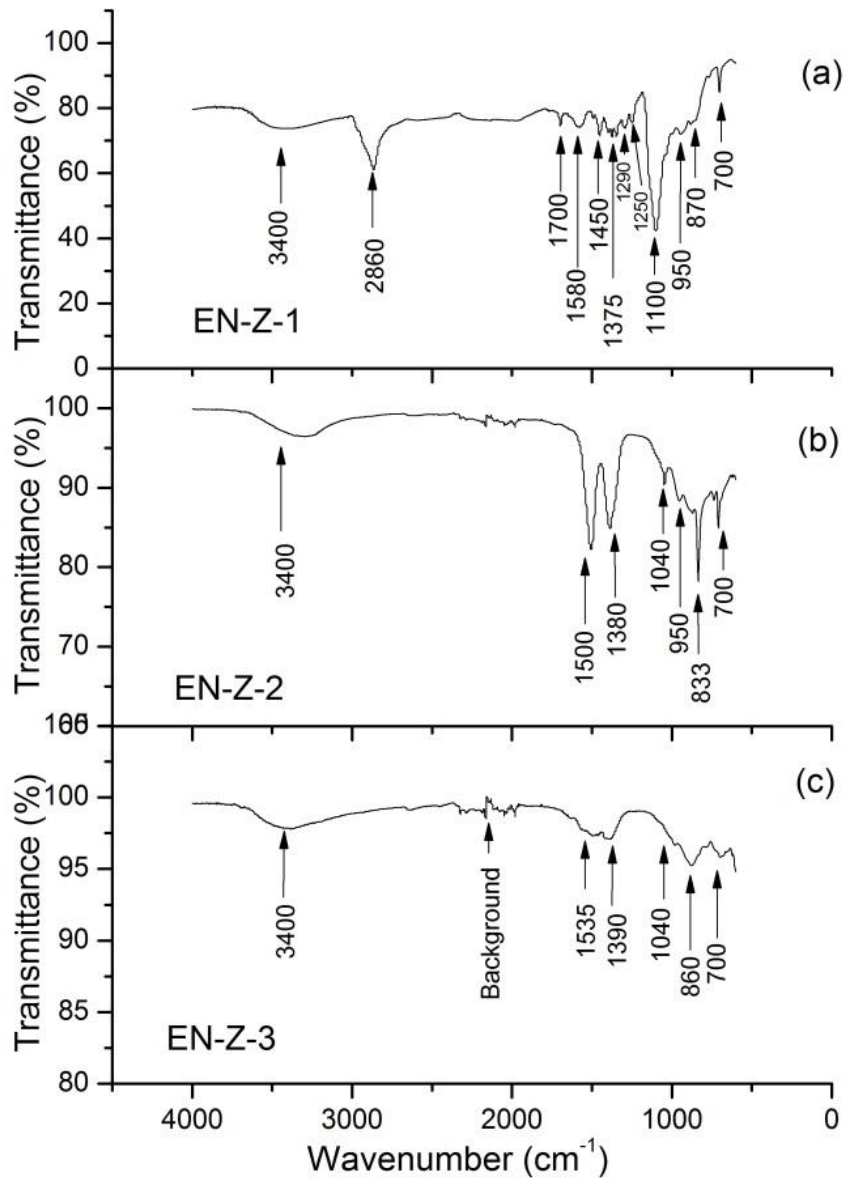
The EN-Z-1 FTIR spectrum presented in Figure 4-9 (a) suggests the presence of an organic compound (in agreement with the TGA-EGA results), identified by the strong band at  $2860\text{ cm}^{-1}$  which is characteristic of the C-H  $\text{sp}^3$  stretch of alkanes. The weaker bands at  $1450$  and  $1375\text{ cm}^{-1}$  are characteristic of C-H bending of methyl groups. The weak band at  $1700\text{ cm}^{-1}$  may be explained by the C-O stretch of a carbonyl group (Socrates, 2001). The broad band at  $3400\text{ cm}^{-1}$  is characteristic of the O-H stretch which may be due to the presence of alcohol or carboxylic acid groups present in the organic compound, and/or may be attributed to the presence of water molecules (Socrates, 2001). This may be a result of incomplete evaporation of the water from the sample during the drying procedure or may be due to adsorbed moisture from the atmosphere. The strongest band in the spectrum, present at  $1100\text{ cm}^{-1}$  is difficult to assign to a particular functional group. The C-O stretch present in both alcohols and ethers absorbs over this range. The compound detected here is likely to be acting as a dispersing agent to aid the stability of the ZnO NP suspension. For this reason, it is likely that the strong band at  $1100\text{ cm}^{-1}$  may be attributed to the C-O-C bend of a compound similar to polyethylene glycol (PEG), as this type of compound is commonly employed to disperse NPs in suspensions (Manson et al., 2011). Furthermore, all other band assignments are consistent with those for the FTIR spectrum for PEG with the exception of the carbonyl group. Therefore, the coating composition may be an aliphatic polyether with a carbonyl group.

Figure 4-9 (b) shows the FTIR spectrum for EN-Z-2. The bands present in the spectrum indicate that there are carbonates present in the sample. The free ion,  $(\text{CO}_3)_2$  exhibits four normal vibration modes: the symmetric C-O stretching mode



(v1); the out-of-plane CO<sub>3</sub> deformation mode (v2); a doubly degenerate asymmetric C-O stretching mode (v3) and a doubly degenerate in plane OCO bending mode (v4). (Andersen, 1991; Nakamoto, 1997). The broad band from 1570-1280 cm<sup>-1</sup> can be assigned to the C-O stretch v3, which has split into two components with band maxima at 1500 and 1380 cm<sup>-1</sup>. The splitting of the band indicates that the carbonate being detected is coordinated to zinc ions, as this reduces the symmetry of the carbonate molecule causing degenerate vibrations to split (Nakamoto, 1997). The bands at 1040, 833 and 700 cm<sup>-1</sup> occur as a result of the symmetric C-O stretching mode (v1), the out-of-plane CO<sub>3</sub> deformation mode (v2) and the OCO bending mode (v4) respectively. The broad band between 3600 and 3000 cm<sup>-1</sup> with a maximum at 3300 cm<sup>-1</sup> is likely to be due to O-H stretch of the hydroxyl vibration as a result of the sample absorbing moisture from the surroundings (Xiong et al., 2007). As well as the carbonate bands, bands at around 3300 cm<sup>-1</sup> corresponding to structural O-H groups, would also be expected for hydrozincite, the compound detected by XRD (Figure 4-2) (Music et al., 2002). However it cannot be determined whether or not these sharp bands are present due to the broad band observed for the vibration of non structural H<sub>2</sub>O molecules.

The EN-Z-3 FTIR spectrum is shown in Figure 4-9 (c) and also contains evidence of carbonate molecules. The split band between 1680 - 1300 cm<sup>-1</sup> with component band maxima at 1535 and 1390 cm<sup>-1</sup> can be assigned to the split v3 stretching mode. The bands at 1040, 860 and 700 cm<sup>-1</sup> can be assigned to the v1, v2 and v3 vibrations respectively and the broad band between 3700 and 3000 cm<sup>-1</sup> with a band maximum of 3300 cm<sup>-1</sup> is most likely a result of O-H stretching of the hydroxyl vibration from absorbed moisture. The intensity of the bands is much less than in the EN-Z-2 sample indicating that it is not as carbonated or hydrated. The FTIR spectra obtained for the ZnO samples indicate that zinc carbonate [Zn(CO)<sub>3</sub>] is present in all of the samples. There is also evidence for the hydrozincite compound detected in EN-Z-2 and EN-Z-3 samples by XRD (Figure 4-2).



**Figure 4-9** FTIR spectra obtained for (a) EN-Z-1 (b) EN-Z-2 and (c) EN-Z-3

#### 4.2.2.2 X-ray Photoelectron Spectroscopy

In order to further investigate the surface composition of the ZnO NP samples, XPS was performed. The survey scans for EN-Z-1, EN-Z-2 and EN-Z-3 are presented in Figure 4-10 (a), (b) and (c) respectively. Higher magnification spectra for the  $Zn2p_{3/2}$ ,  $O1s$  and  $C1s$  edges are presented in Figure 4-11, Figure 4-12, and Figure 4-13 respectively. The percentage concentrations of each element were determined by photoelectron peak area integration, and are reported in Table 4-5.

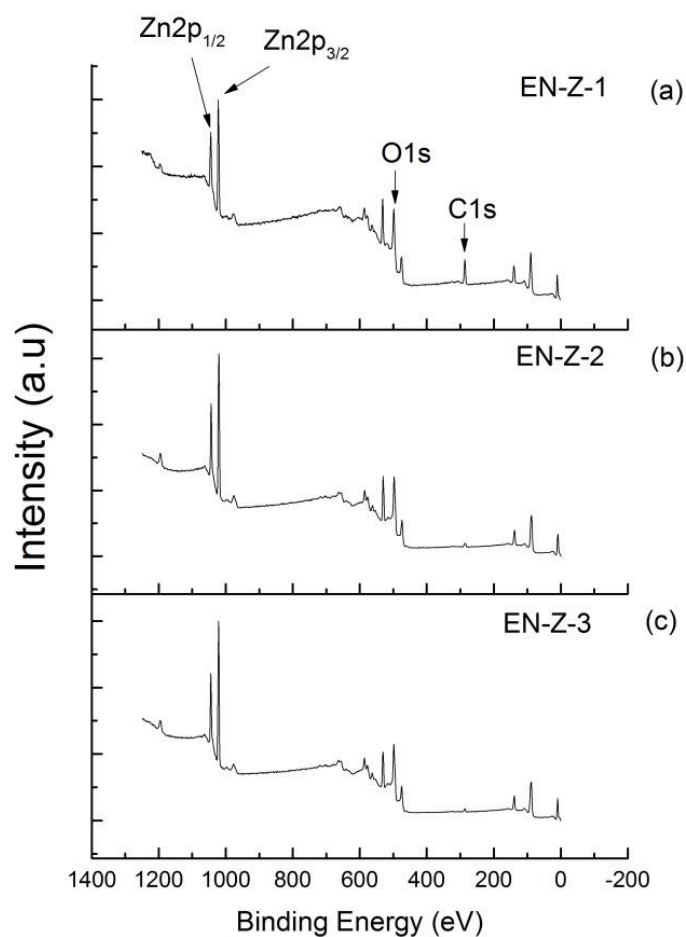


**Figure 4-10 XPS survey scans for (a) EN-Z-1, (b) EN-Z-2 and (c) EN-Z-3 commercial ZnO samples.**

The Zn2p<sub>3/2</sub> binding energies for EN-Z-1, EN-Z-2 and EN-Z-3 samples were found at 1021.5, 1020.8 and 1021.3 eV respectively. The Zn2p<sub>1/2</sub> binding energy for EN-Z-1, EN-Z-2 and EN-Z-3 samples were found at 1044.6, 1043.9 and 1044.4 eV respectively. The binding energies are in good agreement with those reported in the literature indicating that the species of zinc detected is that belonging to ZnO (Mar et al., 1993; Chen et al., 2011).

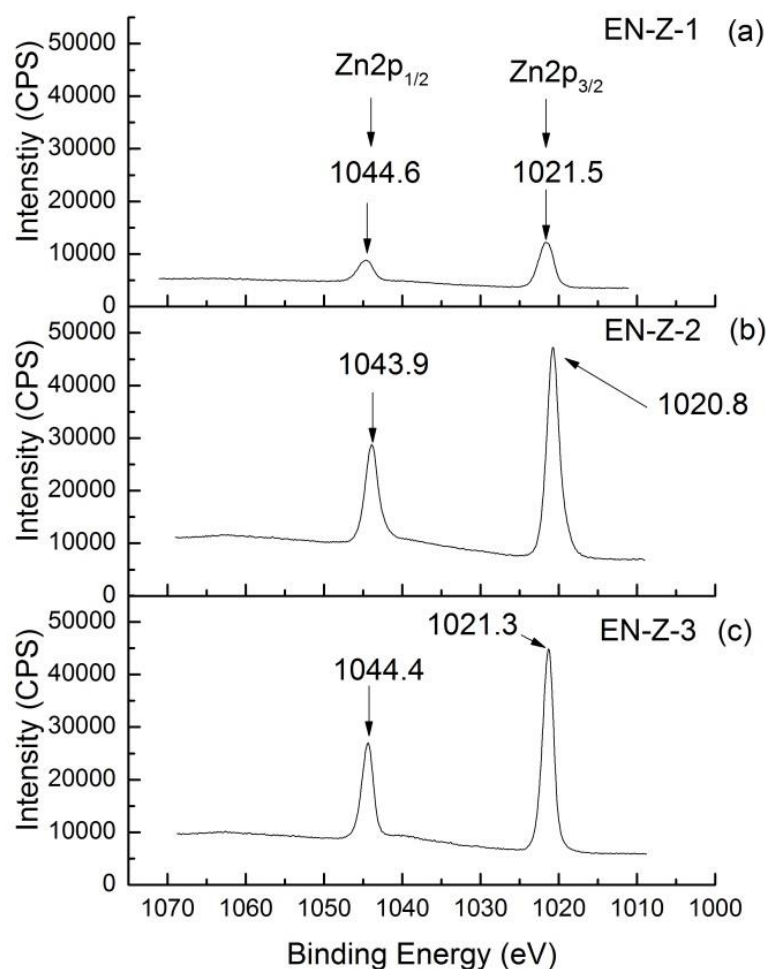


**Figure 4-11 XPS spectrum of Zn2p for (a) ) EN-Z-1, (b) EN-Z-2 and (c) EN-Z-3 commercial ZnO samples.**

Three mixed Gaussian-Lorentzian peaks were fitted to the O1s spectra revealing three types of oxygen species to be present in the three samples. The largest oxygen peak for each sample at 530.1 eV in EN-Z-1, 529.7 eV in EN-Z-2 and 530.0 eV in EN-Z-3 correspond to the oxygen in the crystal lattice of ZnO, in good agreement with values reported in the literature (Mar et al., 1993; Zhang et al. 2005; Chen et al., 2011). The middle peak of the O1s spectra at 531.7, 531.3 and 531.4 eV for EN-Z-1, EN-Z-2 and EN-Z-3 respectively is due to hydrated oxide species (Zhang et al., 2005) and/or O=C oxygen species (Liquiang et al., 2004). Hydrated oxide species may occur as a result of H<sub>2</sub>O that has chemically adsorbed at the surface of the NPs. This species was previously identified by FTIR (Figure 4-6). This

peak is larger for the EN-Z-2 sample, which may be explained by the presence of hydrozincite, as identified by XRD (Figure 4-2). The O=C oxygen species may be present as a result of zinc carbonate. In the case of the EN-Z-1 sample, there may be carbonyl group present in the organic coating that has previously been detected by FTIR (Figure 4-6). The highest binding energy oxygen species is at 532.9, 532.5 and 532.4 eV for EN-Z-1, EN-Z-2 and EN-Z-3 respectively and may be attributed to loosely bound oxygen on the surface of the ZnO NPs belonging to a specific species such as physically adsorbed H<sub>2</sub>O or CO<sub>2</sub> (Mar et al, 1993; Islam et al., 1996; Au et al., 1988; Zhang et al. 2005). The slightly higher binding energy in the EN-Z-1 sample at 532.9 eV may be attributed to alcohol or ether oxygen that may be present in the organic coating (Lopez et al., 1991). The C1s edges of the XPS spectra for the ZnO samples are presented in Figure 4-13 and identify three different carbon species. The peak at 285 eV in the EN-Z-1 spectrum in Figure 4-13 (a) corresponds to aliphatic carbon. This may be due to carbonaceous surface contamination however this peak is relatively large which suggests a contribution from the aliphatic carbon present in the organic compound identified by FTIR (Figure 4-6). The peak at 286.5 eV may be attributable to C-O carbon present in carbonate species (Stoch et al., 1991), however it is more likely due to carbon in a carbonyl group (Sharma et., 2004), present in the organic compound previously detected by FTIR (Figure 4-6). The peak at 288.9 eV may be attributed to the carbon species present in physically adsorbed carbon dioxide molecules, however it is at a slightly higher binding energy than the corresponding peaks for the EN-Z-2 and EN-Z-3 and therefore could be indicative of a species of carbon in a carboxylate group (O-C=O) (Jiang et al., 2013). This is likely to be part of the organic compound coating EN-Z-1.

The EN-Z-2 and EN-Z-3 C1s peaks at 284.6 and 284.9 eV respectively correspond to C-H carbon that is present as a result of hydrocarbon contamination from the atmosphere at the extreme surface of the sample (Światowska-Mrowiecka et al, 2008). The peaks at 286.3 eV for EN-Z-2 and 286.5 eV for EN-Z-3 are characteristic of C-O oxygen species and therefore correspond to the chemically adsorbed carbonate molecules detected previously by FTIR (Figure 4-9) and also by the O1s spectra (Figure 4-12) (Stoch et al., 1991). The peaks at binding energies of

288.9 and 289.1 eV can be attributed to the carbon species present in physically adsorbed CO<sub>2</sub> molecules (Au et al., 1988).

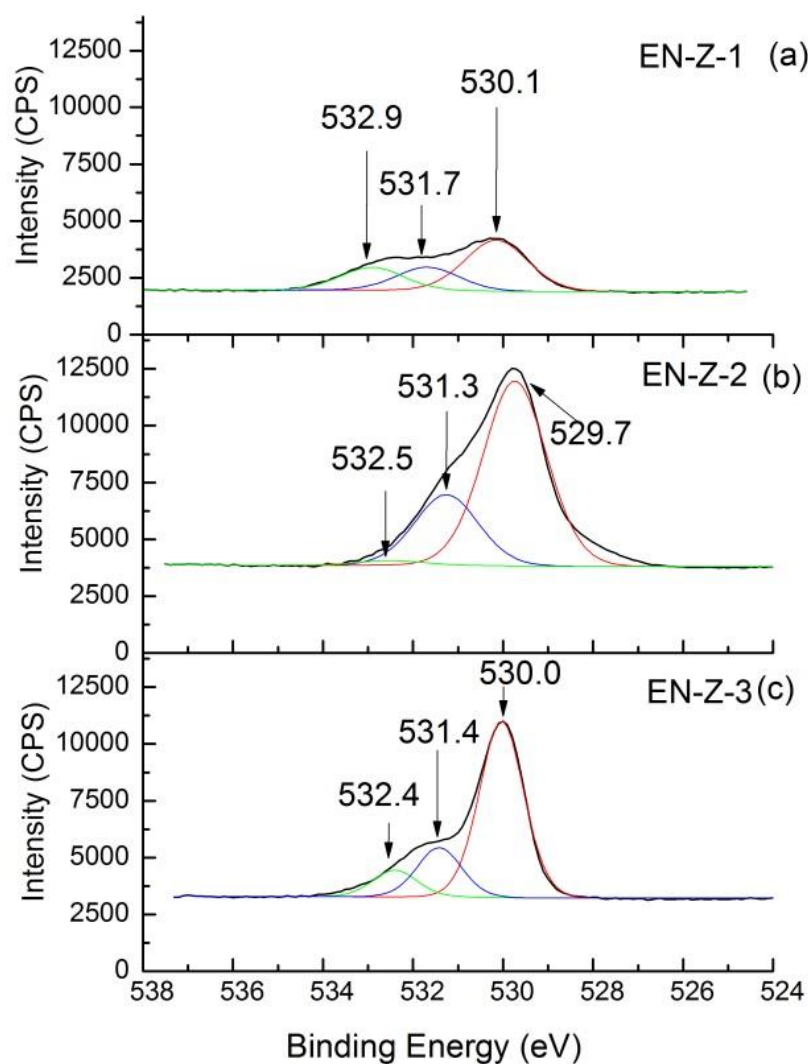


**Figure 4-12** The O1s XPS spectrum of (a) EN-Z-1, (b) EN-Z-2 and (c) EN-Z-3 commercial ZnO samples, fitted to three kinds of oxygen species

Table 4-5 reports the percentage concentrations of zinc, oxygen and carbon at the surface of the sample. Theoretically, the ratio of Zn:O should be 1:1 however this is not the case in any of the samples with measured ratios of 1:3 for EN-Z-1, 1:2.1 for EN-Z-2 and 1:1.67 for EN-Z-3. The excess oxygen is a result of the physically and chemically adsorbed CO<sub>2</sub> and H<sub>2</sub>O and for the EN-Z-1 sample there is also

oxygen present in the coating. The concentration of carbon in the EN-Z-1 samples is more than triple the value for the other samples. This is as a result of the organic coating compound that has been detected by both TGA-EGA (Figure 4-6) and FTIR (Figure 4-9), and as XPS only measures the top few nanometres of the sample, this supports the theory that the compound is at the surface of the NPs. The excess carbon in EN-Z-2 and EN-Z-3 is most likely due to the detected carbonate species, as well as physically adsorbed CO<sub>2</sub> and carbonaceous contamination.

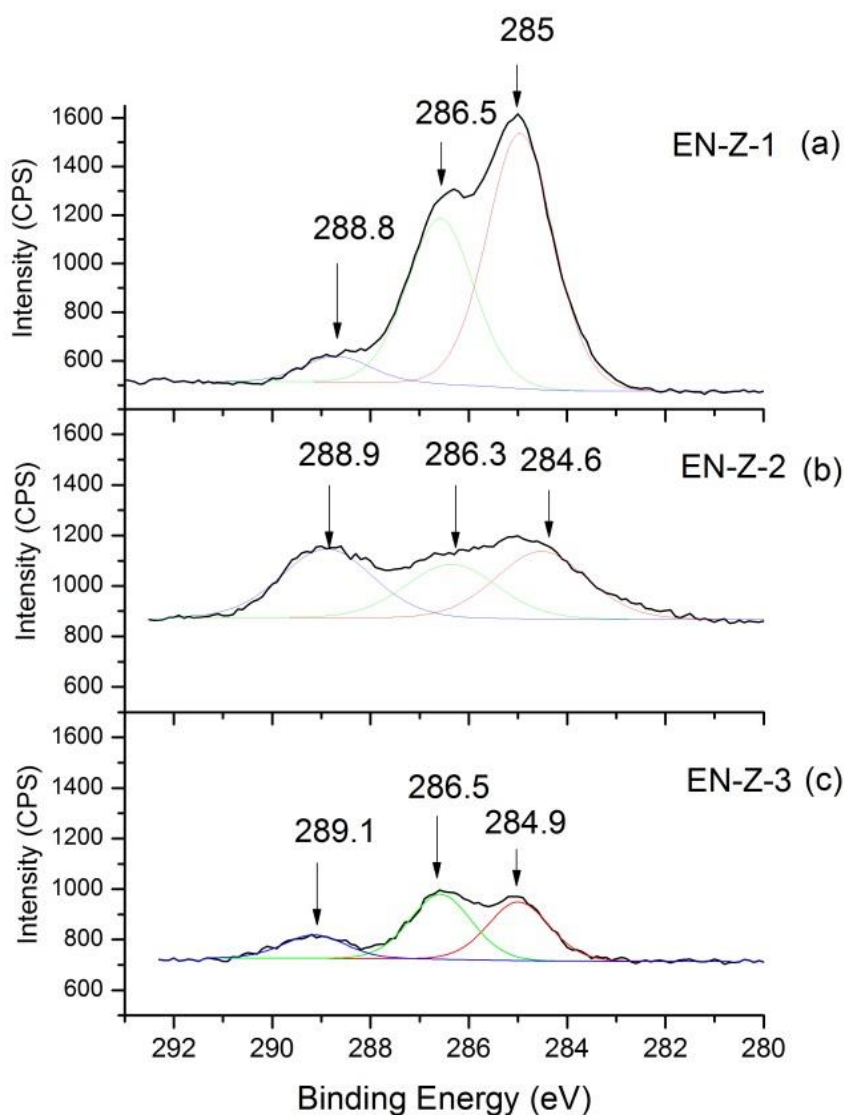


**Figure 4-13** The C1s XPS spectrum of (a) EN-Z-1, (b) EN-Z-2 and (c) EN-Z-3 commercial ZnO samples, fitted to three kinds of carbon species.

**Table 4-5 Table displaying the percentage concentrations of Zn, O and C in XPS spectra of the ZnO commercial samples.**

Sample	Concentration (%)		
	Zn2p	O1s	C1s
EN-Z-1	12	37	51
EN-Z-2	27	57	16
EN-Z-3	33	55	12

#### 4.2.2.3 Nuclear Magnetic Resonance Spectroscopy

The samples were analysed by solid state  $^{13}\text{C}$  NMR and the spectra obtained are displayed in Figure 4-14. The EN-Z-1 spectrum in Figure 4-14 (a) indicates that the sample contains a considerable variety of carbon species. There are a number of broad lines (40.9, 128, 142, 171 and 181 ppm) from a disordered, but relatively rigid component. The line at 171 ppm is characteristic of a C=O group that has shifted to a lower ppm as a result of electron acceptance from Zn atoms due to interaction with a ZnO surface (Tang et al. 2006). The group of narrower lines at 17.6, 20.1 and 23.8 ppm are characteristic of methyl groups. The group of lines between 61.8 and 75.5 ppm may be due to alcohol or ether (consistent with FTIR (Figure 4-9) and XPS (Figure 4-13)).

The NMR spectrum for EN-Z-2 is presented in Figure 4-14 (b). The lines at 164 and 168 ppm are indicative of the presence of carbonate in more than one type of environment. This is in agreement with the XRD (Figure 4-2), FTIR (Figure 4-9) and XPS (Figure 4-13) results previously reported in which more than one type of carbonate have been identified; i.e.  $\text{ZnCO}_3$  and  $\text{Zn}_5(\text{CO}_3)_2\text{OH}_6$ . The signal around 30 ppm is most probably due to experimental background, caused by contaminants such as grease on the rotor (Solid State NMR Service, 2012).

The EN-Z-3 spectrum presented in Figure 4-14 (c) had very weak signal and is the result of overnight accumulation. There is a baseline/background roll which in particular accounts for the bump around 130 ppm. There is a small signal at 166 ppm



which is characteristic of carbonate that has a source of hydrogen, i.e. hydrozincite. Again, there is some signal at around 30 ppm.

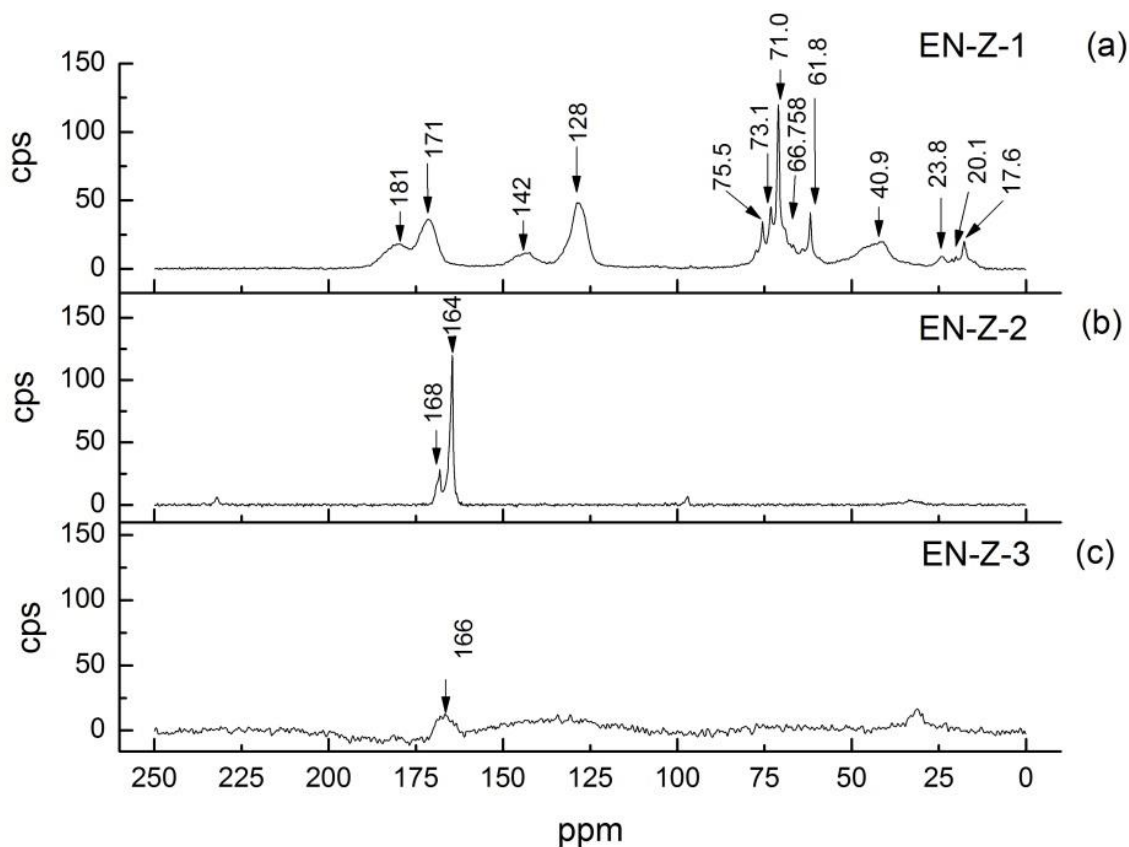


**Figure 4-14** The  $^{13}\text{C}$  NMR spectra for (a) EN-Z-1, (b) EN-Z-2 and (c) EN-Z-3

### 4.2.3 Nanoparticle Characterisation

Scanning electron microscopy (SEM), transmission electron microscopy (TEM) and dynamic light scattering (DLS) were employed to investigate the samples at the individual particle level.

#### 4.2.3.1 Scanning Electron Microscopy

Scanning electron microscope (SEM) images of EN-Z-1, EN-Z-2 and EN-Z-3 are presented in Figure 4-15 (a), (b) and (c) respectively. The primary particles are visible in all of the images however the samples appear to be heavily agglomerated to sizes in the region of a few hundred nanometres, and it is difficult to obtain an

accurate distribution of primary particle sizes. It was therefore necessary to investigate the samples under the TEM.

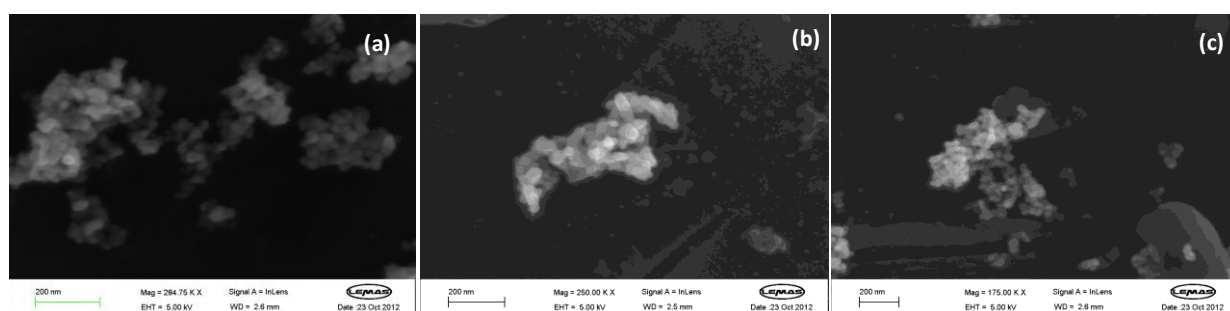


**Figure 4-15 SEM images of (a) EN-Z-1, (b) EN-Z-2 and (c) EN-Z-3 commercial ZnO samples.**

#### 4.2.3.2 Transmission Electron Microscopy

Transmission electron microscope (TEM) images of clusters of particles in EN-Z-1, EN-Z-2 and EN-Z-3 ZnO samples are presented in Figure 4-16, Figure 4-17, and Figure 4-18 (a) respectively. The widths and lengths of 250 particles from each sample were measured and the Feret ratio for each particle calculated. The data are presented in histograms in Figure 4-16, Figure 4-17, and Figure 4-18 (b) for EN-Z-1, EN-Z-2 and EN-Z-3 respectively. EN-Z-1 has an average particle length of  $30 \pm 20$  nm; width of  $16 \pm 10$  nm; and aspect ratio of  $1.9 \pm 0.8$  indicating that the particles are predominately elongated and have a relatively wide size distribution. EN-Z-2 has an average particle length of  $40 \pm 20$  nm; width of  $30 \pm 12$  nm; and aspect ratio of  $1.45 \pm 0.3$  indicating that the particles are predominately elongated but not as much as in the case of the EN-Z-1 sample. Additionally, the size distribution is narrower than EN-Z-1. EN-Z-3 has an average particle length of  $38 \pm 10$  nm; width of  $30 \pm 7$  nm; and aspect ratio of  $1.34 \pm 0.25$ . EN-Z-3 has the narrowest particle size distribution and the most homogenous distribution of particles with regard to morphology. High resolution images of a single particle of EN-Z-1, EN-Z-2 and EN-Z-3 samples are presented in Figure 4-16, Figure 4-17, and Figure 4-18 (c) where the atomic lattice planes are clearly discernible and are indexed to a single crystal of hexagonal ZnO. The particles imaged are marked in Figure 4-16, Figure 4-17, and

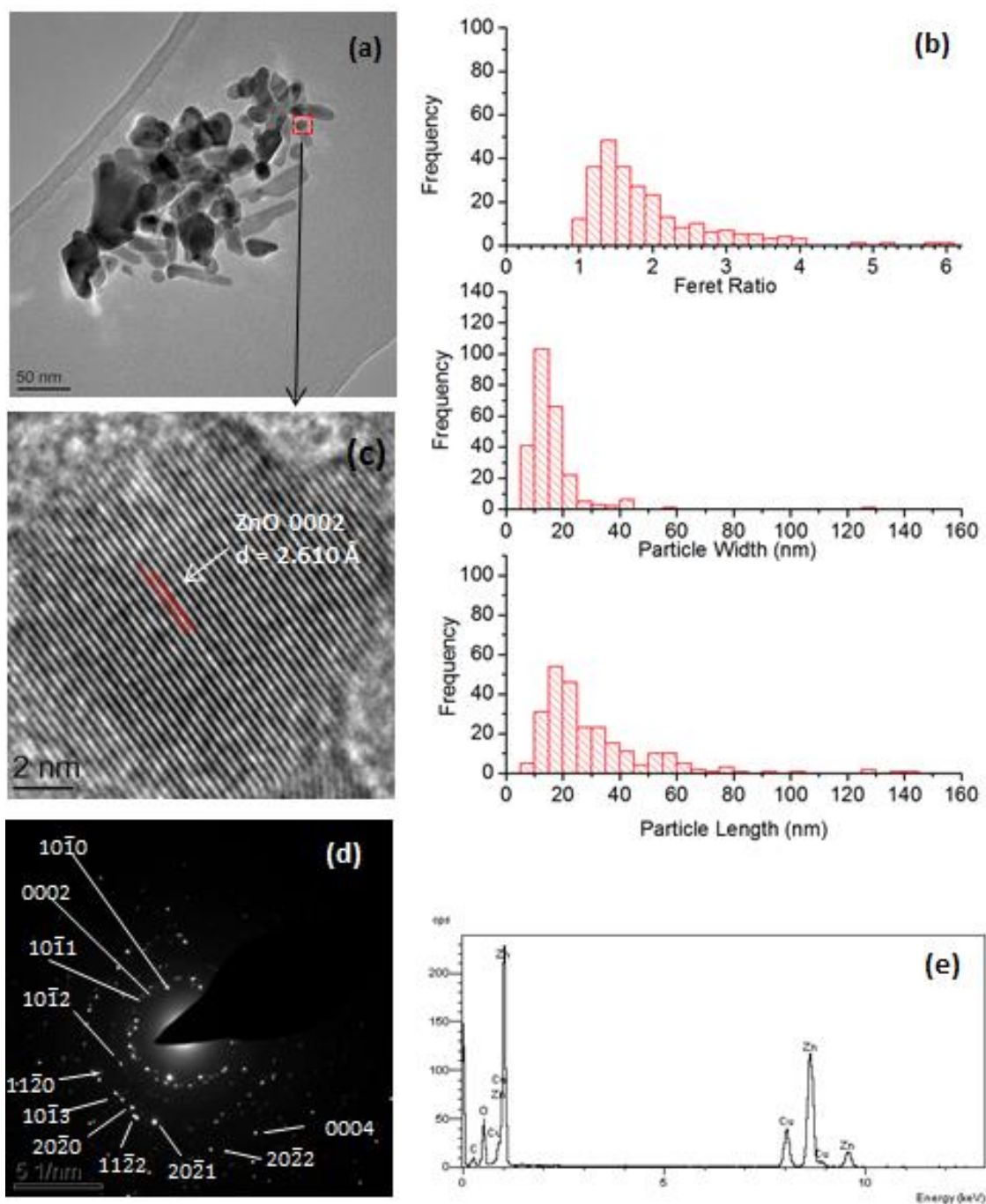


**Figure 4-16 EN-Z-1 (a) TEM image of a typical cluster of NPs (b) histograms to show the variation in particle length, width and Feret ratio. (c) Higher resolution image of a single particle showing crystal planes. (d) SAED pattern and (e) EDX spectrum obtained from the cluster of particles in (a).**

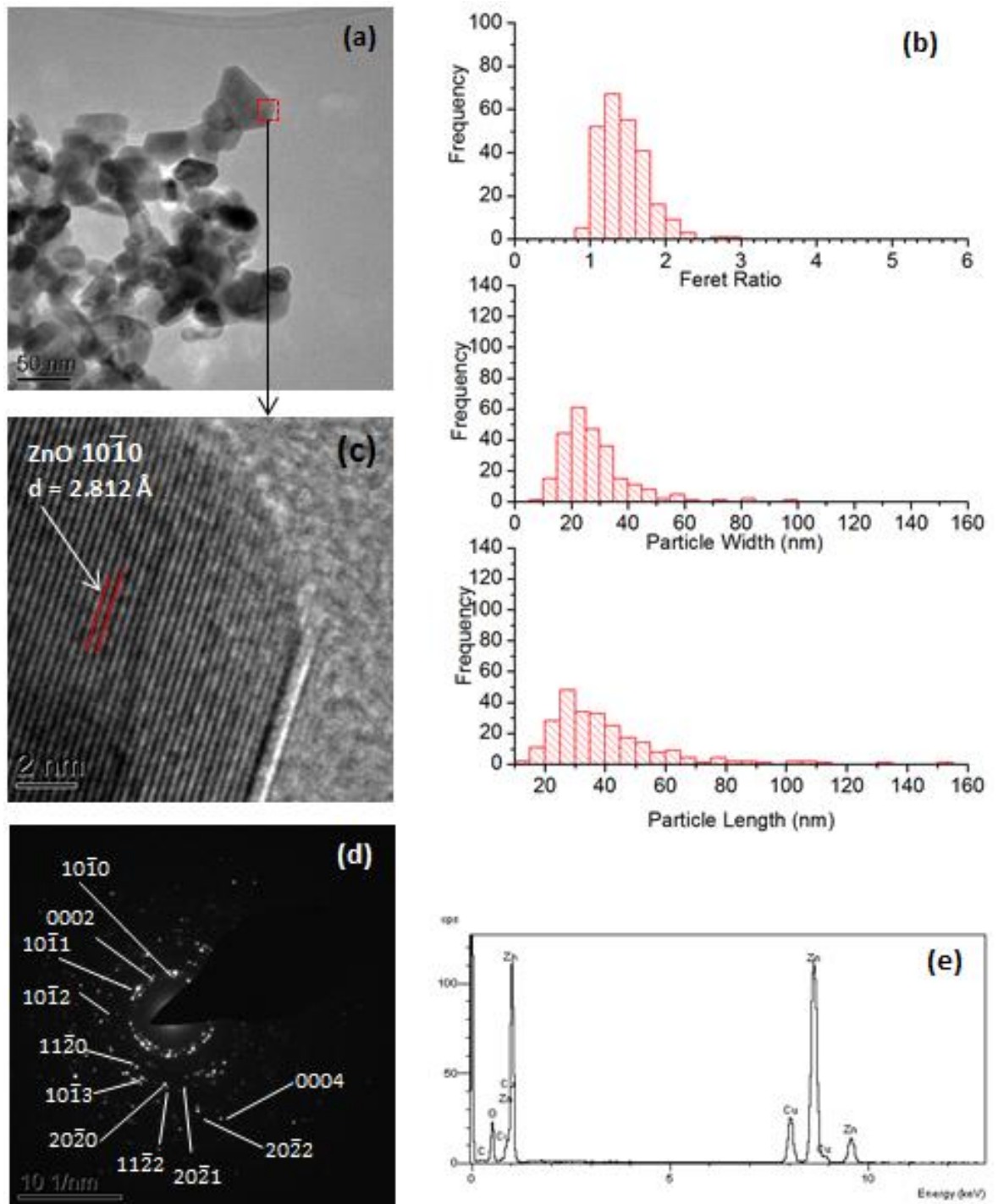


**Figure 4-17 EN-Z-2** (a) TEM image of a typical cluster of NPs (b) histograms to show the variation in particle length, width and Feret ratio. (c) Higher resolution image of a single particle showing crystal planes. (d) SAED pattern and (e) EDX spectrum obtained from the cluster of particles in (a).

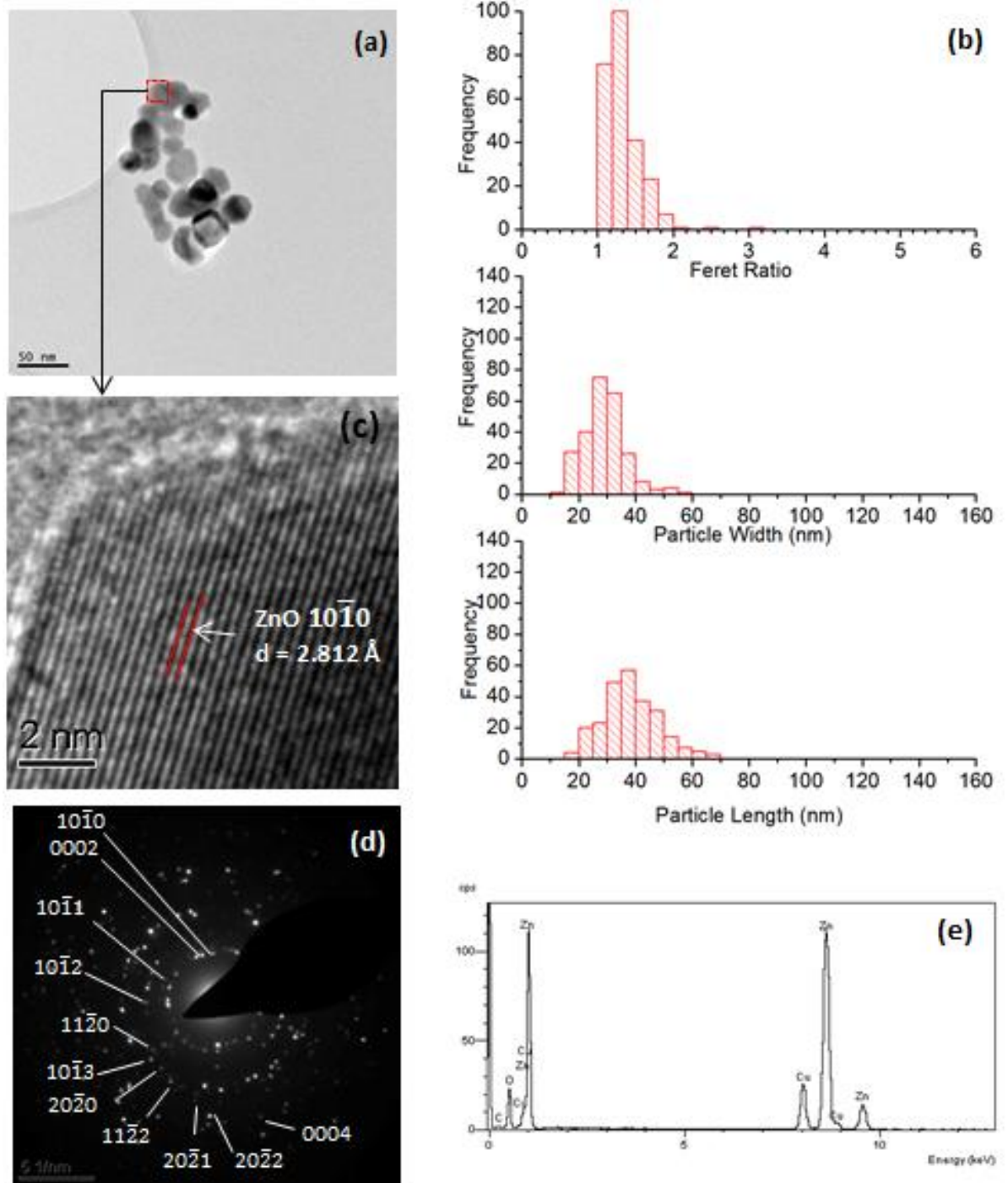


**Figure 4-18 EN-Z-3 (a) TEM image of a typical cluster of NPs (b) histograms to show the variation in particle length, width and Feret ratio. (c) Higher resolution image of a single particle showing crystal planes. (d) SAED pattern and (e) EDX spectrum obtained from the cluster of particles in (a).**

**Table 4-6 Table displaying the ring diameters, and corresponding calculated d-spacings measured from SAED diffraction patterns of EN-Z-1, EN-Z-2 and EN-Z-3. Also displayed are the d-spacings for zincite extracted from the JCPDS reference file: 01-079-0206**

ZnO <i>hkil</i>	JCPDS Ref: 01-079-0206	EN-Z-1		EN-Z-2		EN-Z-3	
	d-spacing (Å)	Ring Diameter (1/nm)	d-spacing (Å)	Ring Diameter (1/nm)	d-spacing (Å)	Ring Diameter (1/nm)	d-spacing (Å)
10 $\bar{1}$ 0	2.82	7.12	2.81	7.10	2.82	7.07	2.83
0002	2.60	7.69	2.60	7.66	2.61	7.66	2.61
10 $\bar{1}$ 1	2.48	8.18	2.45	8.16	2.45	8.16	2.48
10 $\bar{1}$ 2	1.91	10.64	1.88	10.71	1.87	10.71	1.93
11 $\bar{2}$ 0	1.63	12.27	1.63	12.26	1.63	12.26	1.62
10 $\bar{1}$ 3	1.48	13.52	1.48	13.41	1.49	13.41	1.46
20 $\bar{2}$ 0	1.41	14.32	1.40	14.34	1.40	14.34	1.41
11 $\bar{2}$ 2	1.38	14.60	1.37	14.51	1.38	14.51	1.39
20 $\bar{2}$ 1	1.36	14.63	1.36	14.69	1.36	14.69	1.37
0004	1.30	15.39	1.30	15.59	1.28	15.59	1.30
20 $\bar{2}$ 2	1.24	16.39	1.22	16.20	1.23	16.21	1.23

Figure 4-18 (a) with a box drawn around them. The images confirm that the primary particles are predominantly single crystals in nature. The measured d-spacing in Figure 4-16 (c) for EN-Z-1, is 2.61 Å which corresponds to the 0002 plane of Zincite, thus confirming the presence of ZnO. In Figure 4-18 and Figure 4-19 (c) displaying EN-Z-2 and EN-Z-3 particles, the measured d-spacings are 2.82 Å and



2.819 Å respectively which correspond to the d-spacing of the  $10\bar{1}0$  plane of zincite. This confirms the presence of Wurtzite ZnO in all three samples.

Taking into account the average particle lengths and widths, the size values are in good agreement with both XRD (Figure 4-2) and BET (Table 4-4) crystallite size determinations for EN-Z-2 and EN-Z-3. Although the TEM (Figure 4-16) and XRD (Figure 4-2) particle size estimates for EN-Z-1 are in good agreement, the BET (Table 4-4) result is not. The SAED patterns for EN-Z-1, EN-Z-2 and EN-Z-3 are presented in Figure 4-16, Figure 4-17, and Figure 4-18 (d) respectively. The d-spacings corresponding to the ring diameters in the patterns are reported in Table 4-6 and are in good agreement with the d-spacings reported for the JCPDS Zincite reference XRD pattern (ref: 01-079-0206). The EDX spectra obtained from the EN-Z-1, EN-Z-2 and EN-Z-3 respectively are presented in Figure 4-16, Figure 4-17, and Figure 4-18 (e) and confirm the presence of only zinc and oxygen in the samples. The copper peaks present in all 3 samples' EDX spectra are from the copper grid bars on the TEM grid and also possibly from the sample holder. The carbon peak is primarily from the carbon support film on the TEM grid.

#### 4.2.3.3 *Dynamic Light scattering*

Particle size distribution data obtained by DLS for NP samples suspended in MilliQ deionised water at a final solution pH of 7.4, are shown in Figure 4-19. The ZnO NP concentration is 1000 µg/ml and the samples were placed into an ultra sonic bath for 30 minutes prior to the measurement being carried out. DLS was carried out to investigate the particle size distribution and dispersion behaviour of the sample when in a liquid medium. This will improve our understanding of what is actually being presented to cells in a toxicity assay that is carried out in biological media, be it primary particles or agglomerates of NPs. By simply looking at the three suspensions of ZnO NPs, it was apparent that the stability varied from sample to sample; EN-Z-1 is stable, EN-Z-2 sediments rapidly within minutes, and EN-Z-3 sediments after a few hours.

The light scattering profile of the suspensions is converted into plots of intensity, volume and number using the instrumental software. The Rayleigh approximation states that the intensity of light scattered by a particle is proportional to the diameter of the particle ( $I \propto d^6$ ). The intensity profile for EN-Z-1 in Figure 4-19 (a) displays a peak at 142 nm. The intensity plot shows the relative intensity of light scattered by each of the size groups. The volume plot has a peak at 106 nm. The volume plot is formed by conversion of the intensity profile using Mie theory which takes into account the greater relative scattering of the larger particles compared to the small (Malvern, 2000). This explains why the peak is at a smaller diameter. The number profile for EN-Z-1 is derived from the volume plot and displays the relative percentage of particles in each size class. The number plot displays the narrowest particle size distribution at the smallest particle diameter, however as it is derived using a mathematical approximation, it is not necessarily the most accurate. However, the number plot is perhaps the best profile to take into consideration when trying to determine the distribution of particle sizes in the sample when in suspension. The decrease in particle size moving from intensity to volume to number is an indication that the sample is polydisperse and that the particles are agglomerated. This is confirmed by comparison with size distributions obtained from TEM particle size measurements where the average primary particle length is  $30 \pm 20$  nm (Figure 4-16). The number plot ranges from 30 – 250 nm and therefore indicates that there are primary particles present. DLS assumes spherical particles and does therefore not account for the elongated particles that are present in the sample. These factors will reduce the accuracy with which DLS measures the distribution of particle sizes in the sample.

The average particle length determined by TEM for EN-Z-2 is  $40 \pm 20$  nm (Figure 4-17), however the intensity profile presented in Figure 4-19 (b) indicates that the sample has a bimodal size distribution with a primary peak at 531 nm and a secondary peak at 164 nm. When converted to the volume profile, the primary peak shifts to 142 nm and the secondary peak is around 459 nm. When the plot is converted to number, there is a primary peak between 70 and 300 nm with a maximum at 122 nm. The secondary peak at 459 nm has a much lower intensity than in the volume and intensity profile as the greater scattering intensity of the larger



agglomerates has been accounted for. The results indicate that the sample is agglomerated into clusters of particles over a wide range of distributions in sizes, and that there are no, or very few isolated primary particles in the dispersion. However, the intensity of the signal from the large agglomerates may actually be swamping much of the signal from the smaller fraction of the sample and so it is not a certainty that there are no isolated primary particles present.

The light scattering profiles for EN-Z-3 are presented in Figure 4-19 (c). The intensity profile has a peak maximum at 164 nm which reduces to 142 nm in the volume profile. The number profile indicates that the diameters of the particles in the sample range between 50 and 200 nm in diameter with the majority of the particles around 106 nm in diameter. Comparing this to the average particle size obtained by TEM measurements of  $38 \pm 10$  nm (Figure 4-18), it can be concluded that all of the particles are agglomerated into small clusters of particles. These results prove crucial to the investigations as they reveal that the behaviour of the NPs in a liquid medium, indicating as to how they will behave in the toxicity assays and therefore giving a more accurate representation of what the cells are actually exposed to.

It must be noted that the DLS measurements of the samples are taken immediately after 30 minutes agitation in the ultrasonic bath. Acute exposure experiments can last up to 48 hours and therefore it is essential to investigate the dispersion properties of the NPs over this full time period. Toxicity assays are invariably conducted in biological media such as Dulbecco's modified eagle medium (DMEM) and Roswell Park Memorial Institute (RPMI) medium so it is important to investigate the dispersion characteristics in the appropriate biological media. As well as the particle and agglomerate size distribution, other dispersion characteristics such as the solubility of the sample need to be investigated. The dispersion and stability characteristics of ZnO NP samples are reported in detail in Chapter 6.

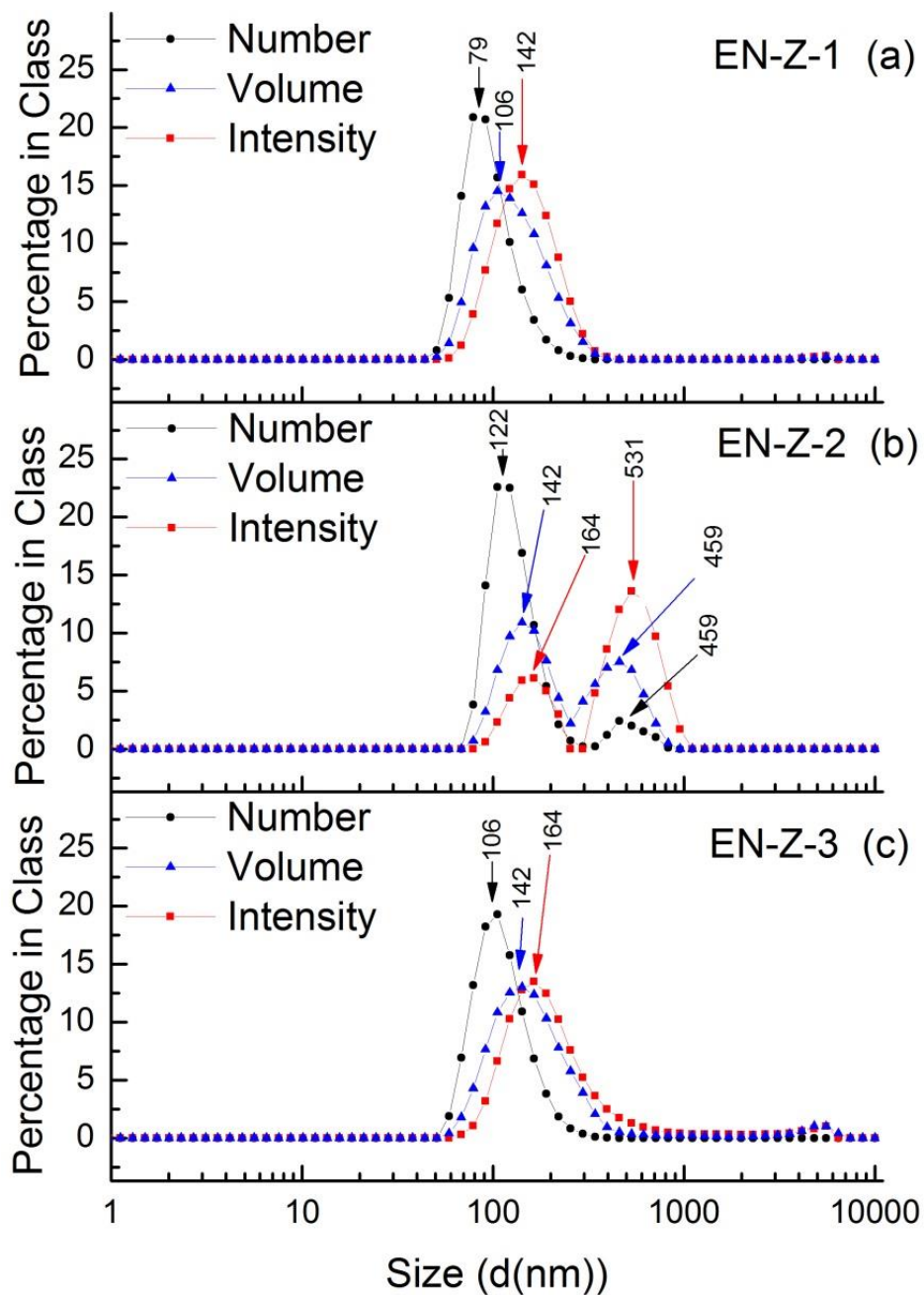


**Figure 4-19** Light scattering profile for 1000  $\mu\text{g/ml}$  suspension of (a) EN-Z-1, (b) EN-Z-2 and (c) EN-Z-3 ZnO NPs dispersed in MilliQ water taken after 20 minutes of ultrasonication.

### 4.3 Summary

The ZnO NP samples that have been investigated in this chapter reveal that commercial ZnO samples are relatively variable in size, size distribution, surface composition and purity. The EN-Z-1 sample has a wide distribution of sizes and morphologies, but due to the presence of a coating, the particles have excellent stability in aqueous dispersion remaining in suspension for weeks after preparation. Although it is known that the coating is organic and contains C-O and C=O groups, it cannot be specifically identified. The lack of knowledge with regard to the exact chemical composition of the organic coating will make it difficult to determine whether any toxicity to cells observed from exposure to the EN-Z-1 sample is a result of the particles, the coating present on the surface or a combination of the two.

The EN-Z-2 sample has a narrower size distribution however there is an additional phase of  $\text{Zn}_5(\text{CO}_3)_2(\text{H}_2\text{O})_6$  present in the sample. The powder does not disperse into primary particles when suspended in water, and even immediately after sonication relatively large agglomerates still exist.

The EN-Z-3 sample has a relatively narrow size distribution and only a few varieties of particle morphology. Results from XRD and TGA indicate there is a very low concentration of a secondary phase present, possibly hydrozincite. The particles disperse well in water initially however the primary particle size is not achieved and sedimentation of the particles occurs within hours of preparing the dispersion.

The impurities detected in the samples, i.e. the carbonate/hydroxide layer, the hydrozincite phase and the organic coating, could contribute to a significant effect on the particle toxicity. The presence of the impurities will alter the weight of the samples thus samples made up for toxicity assays will contain an underestimated dose of ZnO. The impurities detected at the surface of the particles could significantly affect their chemical and physical properties such as their solubility which has been shown to effect ZnO toxicity (Reed et al., 2012; Xia et al., 2008). ZnO solubility is also investigated in this project and the detailed results are presented in Chapter 6.

Due to the variable nature of the commercial ZnO samples, presence of impurities and poor dispersion characteristics, more homogenous samples of ZnO were synthesized in house and these results are reported in Chapter 5.

## 5 Synthesis and Characterisation of ZnO Nanoparticles

The commercially sourced samples of nanoparticulate ZnO characterised in Chapter 4, presented a wide variety of particle sizes and morphologies. Without the aid of an organic coating to promote the stabilisation of the particles, the dispersion of the commercial ZnO NP samples was found to be poor, with sedimentation occurring within hours of a suspension being prepared.

In order to obtain samples with a narrow size distribution, high purity and good dispersion characteristics, the synthesis of samples of ZnO NPs was investigated. Particles produced by a flame spray pyrolysis (FSP) technique as outlined in Chapter 3, were prepared at ETH Zürich, Switzerland (Swiss Federal Institute of Technology, Zurich) by Dr. Karsten Wegner. The in-house synthesis of ZnO NPs was also investigated using the polyol route discussed in Chapter 3.

In order to determine particle size, morphology and phase content, characterisation of synthesized samples were screened using X-ray diffraction (XRD) and transmission electron microscopy (TEM). Two samples were selected for toxicological investigations, on the basis of their physicochemical characteristics (EN-Z-4 and EN-Z-6). The full characterisation protocol, described in Section 4.2 was employed to obtain a detailed overview of the physicochemical characteristics of the two samples selected for the toxicity assays.

### 5.1 ZnO Nanoparticles prepared by the Polyol Route

For all ZnO NP samples synthesized by the polyol route in this investigation, the primary crystallite sizes were measured by XRD and TEM and are reported in Table 5-3. The average crystallite size and standard deviation for a sample was determined from TEM by measurement of the Feret lengths and Feret widths of 250 NPs in TEM images. The average crystallite sizes determined by XRD are in good agreement with the average crystallite sizes measured by TEM for all samples prepared by this technique.

The XRD patterns for Degsyn-0.15-100-1, Degsyn-0.45-100-1 and Degsyn-0.90-100-1 are presented in Figure 5-1 (a), (b) and (c) respectively with the Miller indices of the reflecting planes labeled above the peaks in (a). The peaks in the

patterns are consistent with that of the JCPDS reference file for the hexagonal wurtzite structure of zincite (ref: 01-079-0206). The average crystallite size was determined by measurement of the full width at half the maximum intensity (FWHM) and using the Scherrer equation (Cullity, 2001) (Equation 3.2). The average crystallite sizes obtained by measurement of the FWHM were consistent for all peaks in a given spectrum with the exception of the 0002 peak (see Table 5-1).

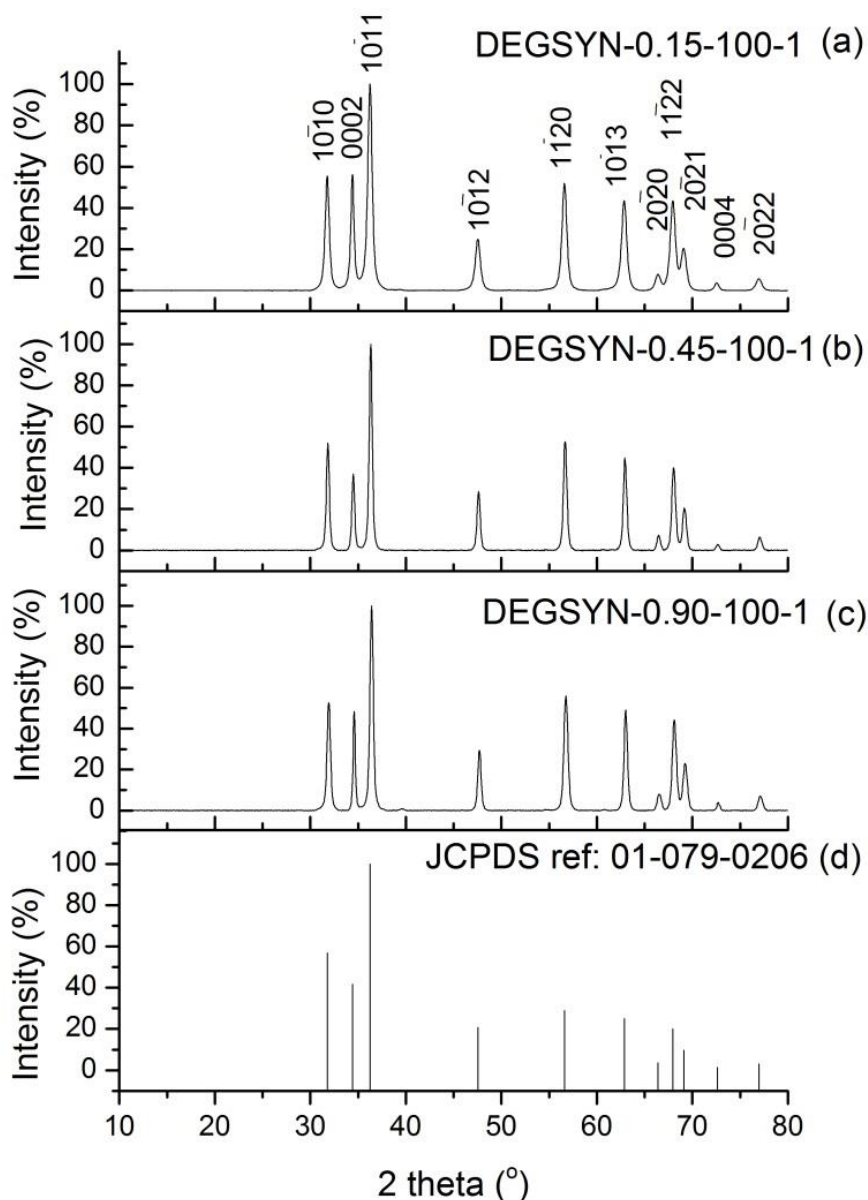


**Figure 5-1 XRD patterns for (a) DEGSYN-0.15-100-1, (b) DEGSYN-0.45-100-1 and (c) DEGSYN-0.90-100-1 ZnO samples with the Miller indices for the reflecting planes labeled above each peak**

**Table 5-1** Table showing the average crystallite sizes obtained from measurement of the FWHM of each peak for Degsyn-0.15-100-1, Degsyn-0.45-100-1 and Degsyn-0.90-100-1. Miller indices for the measured peaks to which the crystallite sizes refer are listed in the left-hand column.

<b>ZnO <math>hkl</math></b>	<b>Average Particle Size from XRD (nm)</b>		
	<b>Degsyn-0.15-100-</b>	<b>Degsyn-0.45-100-</b>	<b>Degsyn-0.90-100-</b>
<b>10<math>\bar{1}</math>0</b>	15	25	22
<b>0002</b>	16	27	45
<b>10<math>\bar{1}</math>1</b>	15	25	23
<b>10<math>\bar{1}</math>2</b>	14	25	24
<b>11<math>\bar{2}</math>0</b>	15	24	20
<b>10<math>\bar{1}</math>3</b>	14	24	24

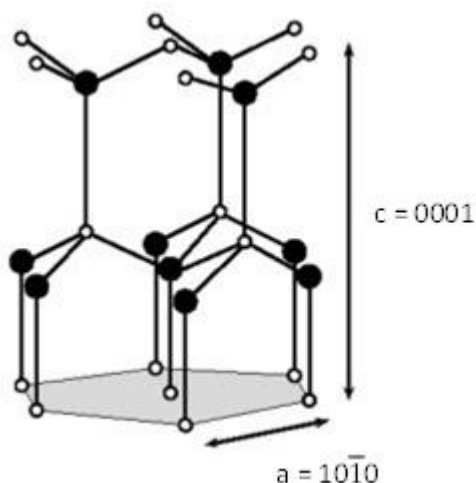


**Figure 5-2** Schematic illustration of the atomic structure of wurtzite ZnO showing the directions of the 0001 (c axis) and 1010 (a axis) atomic planes.

The average crystallite sizes determined from measurement of the FWHM of the 0002 peak for Degsyn-0.15-100-1, Degsyn-0.45-100-1 and Degsyn-0.90-100-1 are 16, 27 and 48 nm respectively. The average crystallite sizes determined from measurement of the FWHM of the 10 $\bar{1}$ 0 peak (the planes perpendicular to the 0002 as can be seen in Figure 5-2) give average crystallite sizes of 15, 25 and 22 nm for

Degsyn-0.15-100-1, Degsyn-0.45-100-1 and Degsyn-0.90-100-1 respectively. XRD results indicate that with increasing ZnAc concentration, an increase in ZnO crystallite size is observed. The growth of the ZnO crystallites is preferential along the c-axis, demonstrated by the increase in the average crystallite size obtained from the 0002 peak of the XRD spectra. The average crystallite size in the  $10\bar{1}0$  direction (along the a-axis) increases when the concentration of ZnAc is increased from 0.15 to  $0.45 \text{ mol dm}^{-3}$ , however when the concentration is increased to  $0.90 \text{ mol dm}^{-3}$ , no further increase is observed (Table 5-1). In order to obtain more detailed information with regard to the size distribution and morphology of the NPs produced, TEM was also employed to characterize the samples.

Images obtained from TEM analysis of Degsyn-0.15-100-1, Degsyn-0.45-100-1 and Degsyn-0.90-100-1 are presented in Figure 5-3. Images of Degsyn-0.15-100-1 reveal that the sample consists of spherical clusters with an average size of  $380 \pm 150 \text{ nm}$  (Figure 5-3 (a)). Upon inspection of the spherical clusters, it is observed that they are formed from aggregated crystallites with an average length of  $14 \pm 5 \text{ nm}$  and an average width of  $11 \pm 3 \text{ nm}$  (Figure 5-3 (b)). The spherical clusters observed are consistent with those prepared by Jézéquel et al. (1995), following a similar synthesis procedure. In the study by Jezequel et al. (1995), the temperature was raised to  $180^\circ\text{C}$  and aged for 15 minutes. In the present study, the temperature is maintained at  $140^\circ\text{C}$  for 1 hour, and then raised to  $180^\circ\text{C}$  for a further 2 hours. The heating method in the present study was followed from the synthesis procedure outlined by Feldmann and Merikhi, (2000), where ZnO NPs were synthesized in DEG using a ZnAc concentration of  $0.90 \text{ mol dm}^{-3}$ .

TEM images of Degsyn-0.45-100-1 are presented in Figure 5-3 (c) and (d). In contrast to Degsyn-0.15-100-1, there are no spherical clusters observed in this sample, only individual primary crystallites with an average length of  $27 \pm 5 \text{ nm}$  and an average width of  $23 \pm 6 \text{ nm}$ . The particle size distribution for this sample, indicated by the standard deviations of the average lengths and widths, is very narrow and the majority of particles are equi-axial. The disappearance of the spherical clusters of crystallites on increasing the ZnAc concentration has previously been reported (Jézéquel et al. 1995), however the primary crystallites observed by

Jézéquel et al. (1995) appear elongated and polydisperse, unlike the ZnO NPs produced here.

TEM images of Degsyn-0.90-100-1, presented in Figure 5-3 (e) and (f) reveal that the sample consists of crystallites with an average length of  $50 \pm 25$  nm and an average width of  $24 \pm 8$  nm. Although the standard deviation for the particle widths is small, the standard deviation for the particle lengths is relatively large, indicating a wide distribution of elongated particles with relatively similar widths.

The TEM results indicate an increase in the average size of the ZnO crystallites with increasing ZnAc concentration, which is in agreement with findings by XRD. The increase in crystallite size occurs because the growth of NPs will proceed until the concentration of growth species has decreased to equilibrium solubility concentration (Cao, 2004). This will be reached more rapidly in the sample using a ZnAc concentration of  $0.15 \text{ mol dm}^{-3}$  than in the sample using a concentration of  $0.90 \text{ mol dm}^{-3}$  as the concentration is lower to begin with and therefore closer to the equilibrium concentration. The final size of the NPs is also dependant on the number of nuclei formed in the nucleation step of the growth process, which is also a function of the precursor concentration. Growth of the rod-like particles is preferential along the c-axis (see Figure 5-4).

It is proposed that the crystallites cease to aggregate into spherical clusters when the concentration of ZnAc is increased, due to the increase in the sizes of primary crystallites. When the initial crystallites are very small, around 14 nm in Degsyn-0.15-100-1, they have a high surface energy and it is energetically favourable for them to aggregate into spheres. As the size of the crystallites increases in Degsyn-0.45-100-1 and Degsyn-0.90-100-1, and the surface free energy reduces, the driving force for aggregation decreases.

Due to the near-monodisperse nature of the ZnO NPs produced in Degsyn-0.45-100-1, it was decided to use this sample for the toxicity studies. In addition Degsyn-0.15-100-1 was also selected. This would provide a direct comparison between two sets of NPs with the only variable being the size of the NPs or aggregates of NPs in the case of Degsyn-0.15-100-1. However, the mass of ZnO produced in the synthesis procedures was insufficient to provide all members of the ENNSATOX consortium with an appropriate quantity. The particles sent out to the



various recipients were required to be produced in the same synthesis batch; therefore it was necessary to scale the reaction up. To achieve this, the volumes of the precursors were doubled i.e. to obtain concentrations of 0.15 and 0.45 mol dm<sup>-3</sup>, 3.34 g and 10.05 g of ZnAc was added to 100 ml of DEG and 2 ml of H<sub>2</sub>O. A 250 ml round bottom flask was used as the reaction vessel as opposed to the 100 ml round bottom flask used for the aforementioned samples.

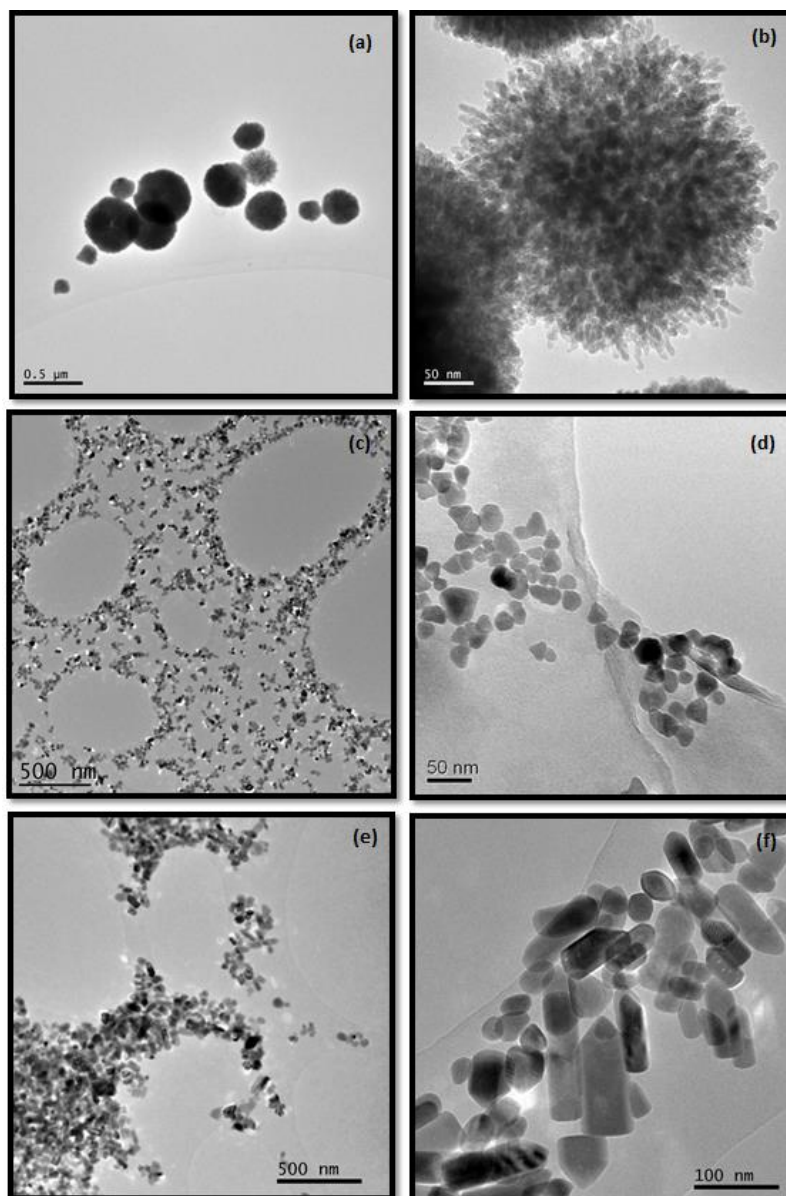


**Figure 5-3 TEM images of ZnO NPs produced by precipitation under reflux conditions using varying concentrations of ZnAc precursor (a) (b) Degsyn-0.15-100-1, (c) (d) Degsyn-0.45-100-1 and (e) (f) Degsyn-0.90-100-1**

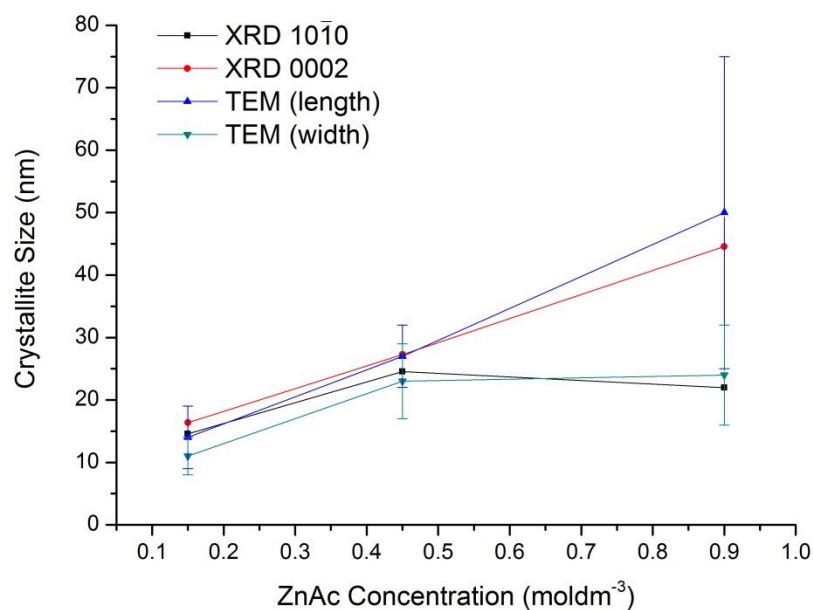


**Figure 5-4** Graph showing the effect of precursor (ZnAc) concentration on the average size of the synthesized ZnO NPs. Error bars for TEM data based on standard deviation from 250 NP measurements.

In order to investigate the reproducibility of the synthesized ZnO NPs, experiments using the same precursor concentration were carried out in duplicate. The synthesized samples, Degsyn-0.15-250-1, Degsyn-0.15-250-2, Degsyn-0.45-250-1 and Degsyn-0.45-250-2 were characterized by XRD and the resulting patterns are presented in Figure 5-5 (a), (b), (c) and (d) respectively. The peaks present in the XRD patterns for all samples are consistent with that of the JCPDS reference file for zincite (ref: 01-079-0206) indicating that the composition of the samples is wurtzite ZnO. Furthermore, TEM images of Degsyn-0.15-250-1, Degsyn-0.15-250-2, Degsyn-0.45-250-1 and Degsyn-0.45-250-2 are presented in Figure 5-6 (a), (b), (c) and (d) respectively. The crystallite sizes determined by XRD and TEM for the four samples synthesized using a 250 ml round bottom flask are presented in Table 5-2.

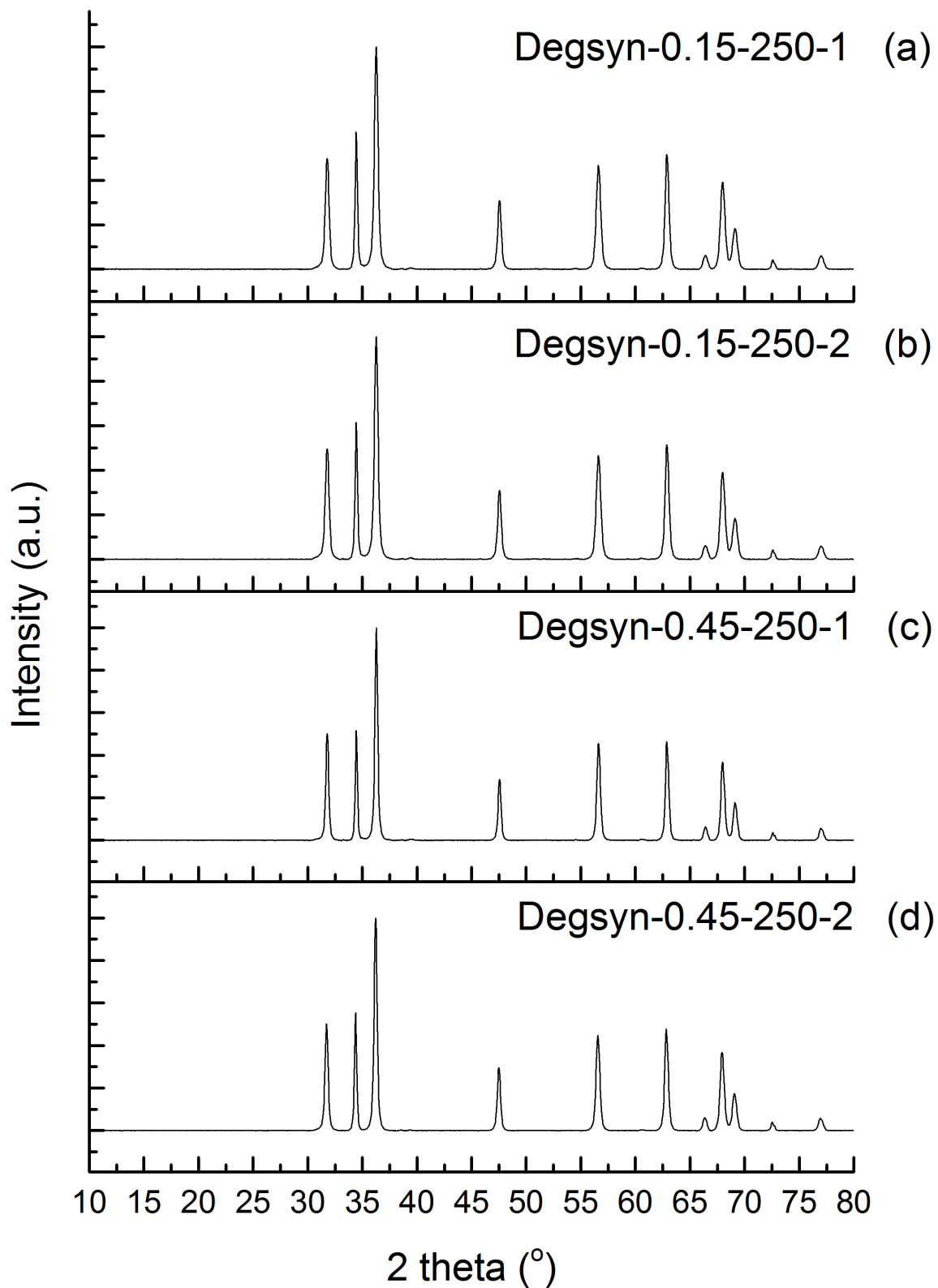


**Figure 5-5 XRD patterns obtained for (a) Degsyn-0.15-250-1, (b) Degsyn-0.15-250-2, (c) Degsyn-0.45-250-1 and (d) Degsyn-0.45-250-2.**

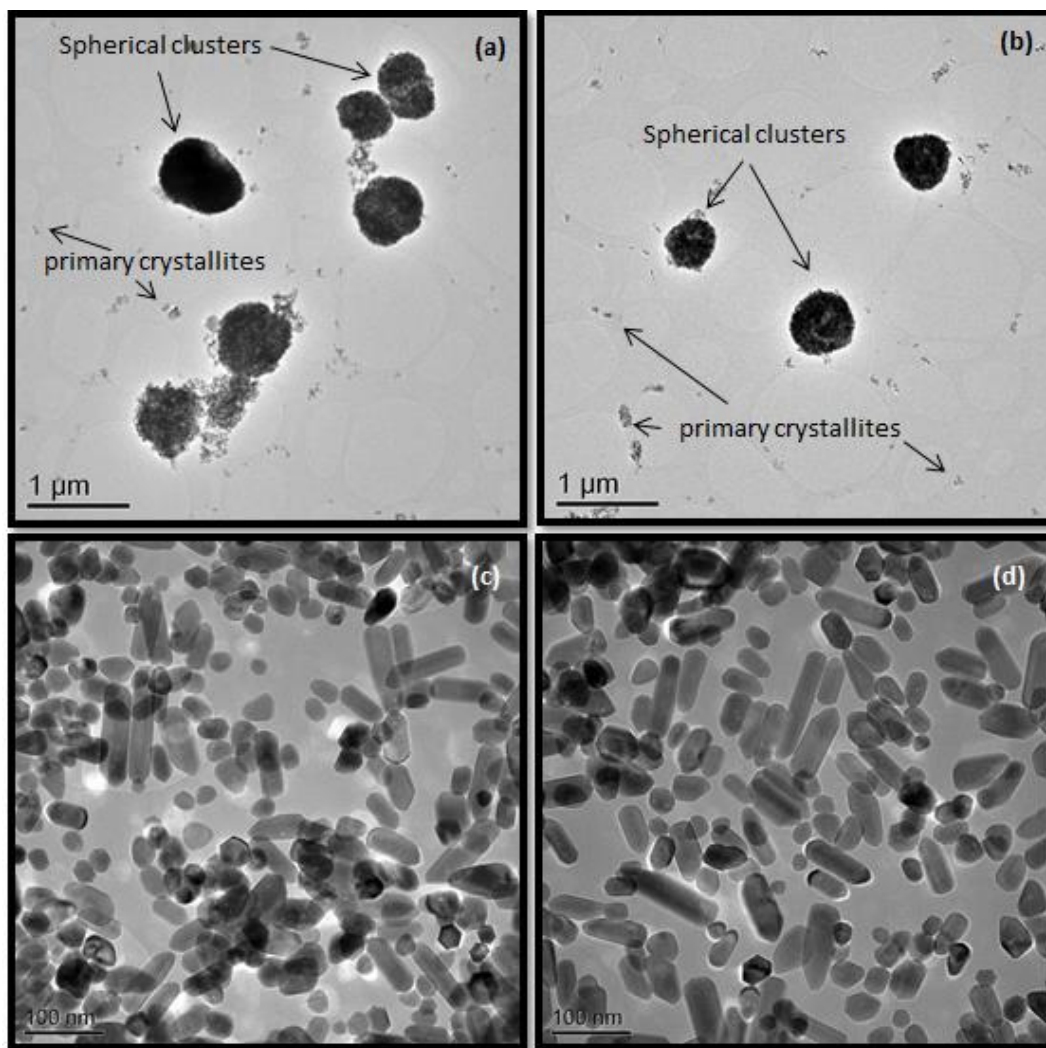


**Figure 5-6 TEM images of (a) Degryst-0.15-250-1 with an average crystallite length of  $30 \pm 24$  nm and width of  $19 \pm 15$  nm and an average spherical cluster diameter of  $670 \pm 340$  nm, (b) Degryst-0.15-250-2 with an average crystallite length of  $35 \pm 23$  nm and width of  $23 \pm 14$  nm and an average spherical cluster diameter of  $790 \pm 220$  nm, (c) Degryst-0.45-250-1 with an average crystallite length of  $45 \pm 28$  nm and width of  $25 \pm 10$  nm and (d) Degryst-0.45-250-2 with an average crystallite length of  $47 \pm 26$  nm and width of  $26 \pm 8$  nm.**

Comparing the sizes of the crystallites in samples prepared using a 250 ml round bottom flask with those prepared using a 100 ml round bottom flask, it is apparent that the width of the primary crystallites measured by TEM and XRD is approximately constant for all of the samples. However, the lengths of the primary

crystallites produced for the samples using a 250 ml round bottom flask are significantly larger and the distribution of lengths is wider than in the previously synthesized samples at corresponding concentration, using a 100 ml round bottom flask (Table 5-2).

In contrast to Degsyn-0.15-100-1, the crystallites in Degsyn-0.15-250-1 and Degsyn-0.15-250-2 are both isolated and aggregated into spherical clusters, as can be seen in Figure 5-6 (a) and (b) respectively. This may be a result of the increase in the crystallite size observed (Table 5-2), which would reduce the tendency of the NPs to aggregate. There is a small increase in the average sizes of the spherical clusters observed in Degsyn-0.15-250-1 and Degsyn-0.15-250-2 as compared to Degsyn-0.15-100-1 (Table 5-2).

The standard deviations measured for the average spherical cluster sizes indicate that the distribution of sizes is wider for the 250 ml round bottom flask samples. Moreover the morphology of the clusters observed do not appear as spherical for the 250 ml round bottom flask samples, as for the 100 ml round bottom flask samples.

There are a number of factors that may cause the crystallite sizes and distribution of sizes to increase as a result of the scaling up of the process. The speed and size of the magnetic stirrer was not increased for the scaled up process, which may have resulted in inhomogenous mixing of the precursor solution (Chen et al. 2000). A non-uniform distribution of precursor concentration will lead to a prolonged nucleation phase, leading to varying growth times for the crystallites produced and hence a distribution of sizes (La Mer & Dinegar, 1950).

The water used for both the 100 ml RBF synthesis experiments and the 250 ml RBF synthesis experiments was MilliQ triple distilled water. However, there was a significant amount of time (approximately 2 months) between the two sets of experiments and therefore the quality of the water may have been compromised if the filter had not been changed. Evidence for impurities detected by ICP-MS in the MilliQ water used is presented in Figure 5-11. Impurities in the water can result in the inhomogenous nucleation of ZnO nuclei and hence inhomogenous growth of crystallites.

**Table 5-2 Summary of average sizes of primary crystallites measured by TEM and XRD for Degsyn-0.15-100-1, Degsyn-0.45-100-1, Degsyn-0.90-100-1, Degsyn-0.15-250-1, Degsyn-0.15-250-2, Degsyn-0.45-250-1 and Degsyn-0.45-250-2.**

Sample	ZnAc Concentration (mol/dm <sup>3</sup> )	RBF Volume (ml)	Spherical Cluster Size (nm)	Crystallite size (nm)			
				TEM (length)	TEM (width)	XRD (0002)	XRD (1010)
Degsyn-0.15-100-1	0.15	100	380 ± 150	14 ± 5	11 ± 3	16	14
Degsyn-0.45-100-1	0.45	100	-	27 ± 5	23 ± 6	27	24
Degsyn-0.90-100-1	0.90	100	-	50 ± 25	24 ± 8	48	22
Degsyn-0.15-250-1	0.15	250	670 ± 340	30 ± 24	19 ± 15	33	20
Degsyn-0.15-250-2	0.15	250	790 ± 220	35 ± 23	23 ± 14	34	21
Degsyn-0.45-250-1	0.45	250	-	45 ± 28	25 ± 10	47	26
Degsyn-0.45-250-2	0.45	250	-	47 ± 26	26 ± 8	45	25

A new hotplate with temperature regulator was purchased between the two sets of experiments. The thermistor was programmed to maintain the temperature at 140°C for 1 hour and then 180°C for a further 2 hours. However, the new system was often observed to fluctuate in temperature significantly. Additionally, the temperature throughout the reaction vessel may have varied significantly for the larger volume due to heat transfer problems.

In order to determine whether the scaling up of the process was responsible for the increase in ZnO NP size, experiments were repeated in duplicate using a 100 ml RBF and ZnAc concentrations of 0.15 and 0.45 mol dm<sup>-3</sup>. Samples produced were named accordingly as Degsyn-0.15-100-2, Degsyn-0.15-100-3, Degsyn-0.45-100-2 and Degsyn-0.45-100-3. The XRD spectra for Degsyn-0.15-100-2, Degsyn-0.15-

100-3, Degsyn-0.45-100-2 and Degsyn-0.45-100-3, presented in Figure 5-7 (a), (b), (c) and (d) respectively indicate that all four samples are monophasic wurtzite ZnO.

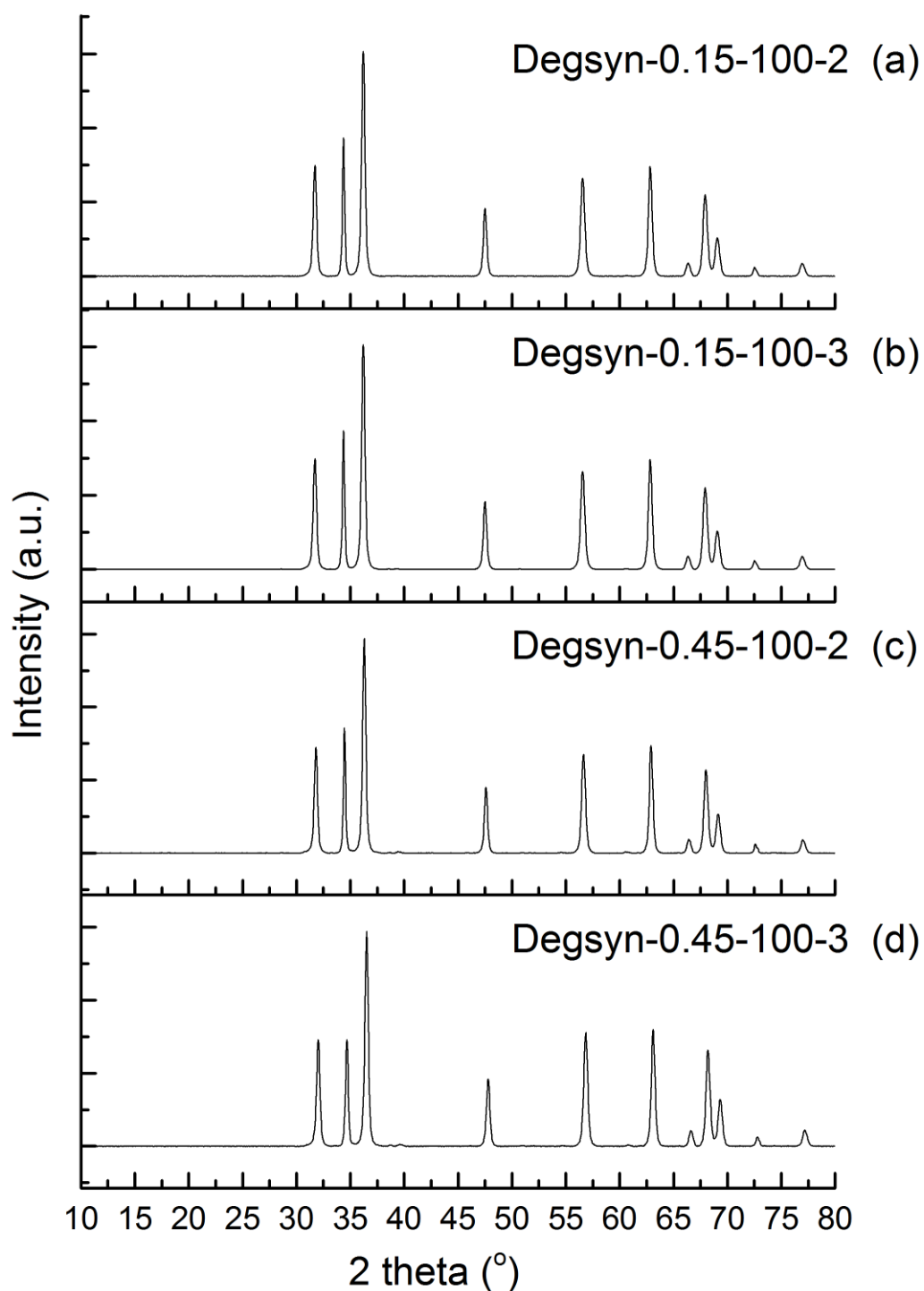


**Figure 5-7 XRD patterns for (a) Degsyn-0.15-100-2, (b) Degsyn-0.15-100-3, (c) Degsyn-0.45-100-2 and (d) Degsyn-0.45-100-3**

TEM images of Degsyn-0.15-100-2 and Degsyn-0.15-100-3 are presented in Figure 5-8 (a) and (b) respectively and reveal that the samples consist of a bimodal size distribution, similar to that observed in Degsyn-0.15-250-1 and Degsyn-0.15-250-2 (Figure 5-6 (a) and (b)). This is in contrast to Degsyn-0.15-100-1 (Figure 5-3 (a) and (b)) where all primary crystallites are observed in spherical clusters. The average crystallite sizes and spherical cluster sizes measured by XRD and TEM are reported in Table 5-3. The average crystallite sizes measured for the three samples prepared using a ZnAc concentration of  $0.15 \text{ mol dm}^{-3}$  and a round bottom flask volume of 100 ml were compared; the average length of the crystallites produced in Degsyn-0.15-100-2 and Degsyn-0.15-100-3 (Table 5-3) is approximately double compared to the previously synthesized sample under the same experimental conditions – Degsyn-0.15-100-1 (Table 5-3). Additionally the average width of the crystallites is significantly greater than that obtained for Degsyn-0.15-100-1. The increase in the average crystallite sizes measured for Degsyn 0.15-100-2 and Degsyn 0.15-100-3 as compared to Degsyn 0.15-100-1 explains why a bimodal distribution is observed for the samples. The decrease in the surface free energy as a result of increasing crystallite size, reduces the driving force for agglomeration.

A summary of the crystallite and particle sizes measured by XRD and TEM for all samples synthesized by the polyol route, is presented in Table 5-3. Comparing the average crystallite sizes for samples prepared using a ZnAc concentration of  $0.45 \text{ mol dm}^{-3}$  and a round bottom flask volume of 100 ml indicates that there is a lack of consistency between the previously prepared samples and the newly prepared samples. The average crystallite widths measured for Degsyn-0.45-100-2 and Degsyn-0.45-100-3 are reasonably similar to those measured for Degsyn-0.45-100-1 (Table 5-3). However, the average crystallite lengths measured for the newly synthesized samples are significantly larger than the value measured for Degsyn-0.45-100-1 (Table 5-3). An observation that is consistent between the samples prepared with a concentration of  $0.15 \text{ mol dm}^{-3}$  and  $0.45 \text{ mol dm}^{-3}$  ZnAc, is that there is an increase in the average length of the crystallites obtained, between the first time the experiment was carried out compared to the second and third repeats. Additionally, for samples prepared using a concentration of  $0.15 \text{ mol dm}^{-3}$  ZnAc, the width of the crystallites Degsyn-0.15-100-1 is much smaller than for any of the other



samples. This indicates that the scaling up of the synthesis procedure was not the cause for the observed increase in particle sizes for the ZnO NPs samples, and that it is due to inconsistencies in the experimental parameters. The most likely explanation for the batch to batch variation is due to the newly purchased heating apparatus used for the second and third synthesis experiments.

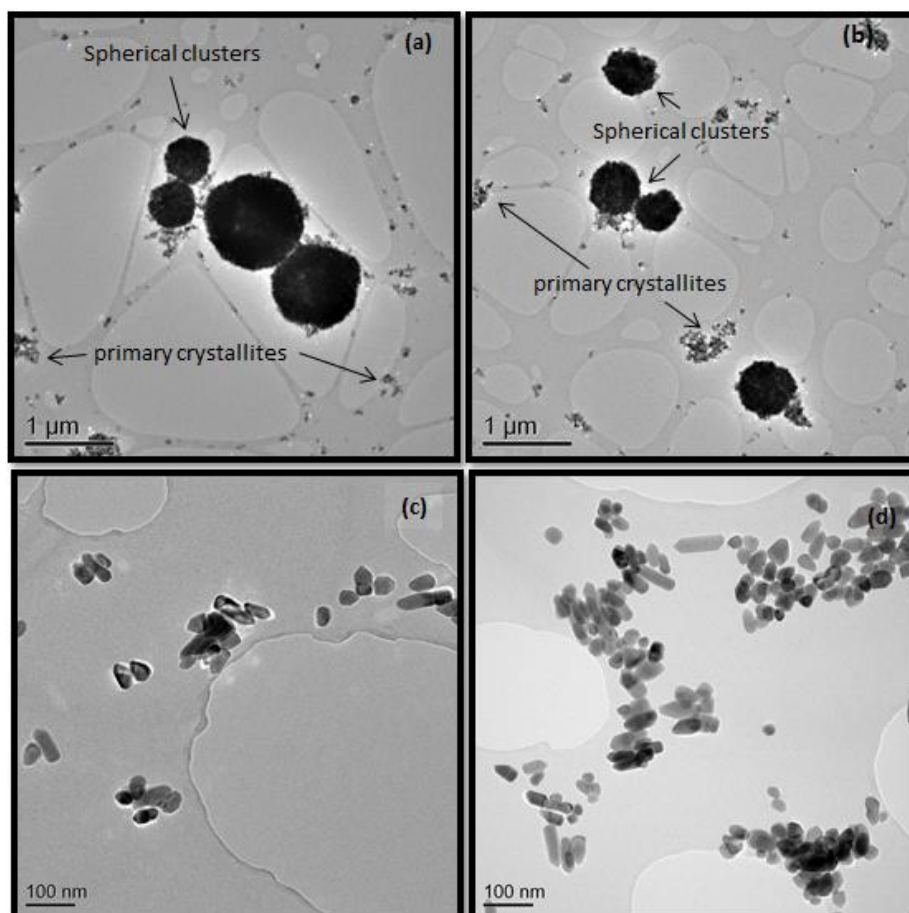


**Figure 5-8 TEM images of ZnO NPs prepared by polyol route: (a) Degsyn-0.15-100-2 with an average crystallite length of  $32 \pm 18$  and width of  $20 \pm 8$  nm and an average spherical cluster size of  $620 \pm 250$  nm, (b) Degsyn-0.15-100-3 with an average crystallite length of  $29 \pm 12$  and width of  $21 \pm 9$  nm and an average spherical cluster size of  $800 \pm 310$  nm, (c) Degsyn-0.45-100-2 with an average crystallite length of  $42 \pm 13$  and width of  $22 \pm 7$  nm, (d) Degsyn-0.45-100-3 with an average crystallite length of  $37 \pm 11$  and width of  $21 \pm 5$  nm**

**Table 5-3 Table summarizing the average sizes of the particles present in the samples synthesized by the polyol route.**

Sample	ZnAc Concentration (mol/dm <sup>3</sup> )	RBF Volume (ml)	Spherical Agglomerate Size (nm)	Crystallite size (nm)			
				TEM (length)	TEM (width)	XRD (0002)	XRD (1010)
Degsyn-0.15-100-1	0.15	100	380 ± 150	14 ± 5	11 ± 3	16	14
Degsyn-0.15-100-2	0.15	100	620 ± 250	32 ± 18	20 ± 8	31	22
Degsyn-0.15-100-3	0.15	100	800 ± 310	29 ± 12	21 ± 9	30	20
Degsyn-0.15-250-1	0.15	250	670 ± 340	30 ± 24	19 ± 15	33	20
Degsyn-0.15-250-2	0.15	250	790 ± 220	35 ± 23	23 ± 14	34	21
Degsyn-0.45-100-1	0.45	100	-	27 ± 5	23 ± 6	27	24
Degsyn-0.45-100-2	0.45	100	-	42 ± 13	22 ± 7	42	23
Degsyn-0.45-100-3	0.45	100	-	37 ± 11	21 ± 5	39	23
Degsyn-0.45-250-1	0.45	250	-	45 ± 28	25 ± 10	47	26
Degsyn-0.45-250-2	0.45	250	-	47 ± 26	26 ± 8	45	25
Degsyn-0.90-100-1	0.90	100	-	50 ± 25	24 ± 8	48	22

As was mentioned previously, it was extremely difficult to maintain a fixed temperature with the new apparatus, resulting in inhomogeneous heating of the sample, which would in turn lead to a prolonged nucleation step and hence a wider distribution of ZnO NP sizes.

In our future work, we hope to be able to confirm that the change in the hot plate used, is the cause for the decrease in ZnO NP homogeneity. This will be achieved by monitoring the temperature of the precursor solution throughout the synthesis experiment over 5 minute intervals.

Although the particles produced in Degsyn-0.45-100-1 had a narrower size distribution, it was required that the particles sent out for toxicity testing were produced in the same batch. Therefore, Degsyn-0.45-250-2 where a larger sample volume was produced, was selected to be sent out to the ENNSATOX consortium members. The characterisation protocol results for this sample are presented in section 5.3. Due to the bimodal distribution of the samples prepared using a ZnAc concentration of  $0.15 \text{ mol dm}^{-3}$  and a RBF volume of 250 ml, it was decided not to carry any of these samples forward to the toxicity testing stage.

Diethylene glycol (DEG) is a known toxin (Winek et al., 1978), making it necessary to separate the ZnO NPs from the prepared suspensions, prior to toxicological investigation being carried out. In order to achieve this, the suspension was centrifuged for 15 minutes at 6000 rpm and the DEG supernatant was removed. The sedimented particles were then re-dispersed in MilliQ water by placing in an ultrasonic bath for a further 15 minutes. The centrifugation and re-dispersion in MilliQ water procedure was repeated 6 times. Subsequently, the sample was dried overnight in an oven at  $60^\circ\text{C}$  to evaporate off the water and a dry white powder was obtained. The effect of the washing process on the surface composition of the NPs was investigated by FTIR and was found to drastically reduce the amount of DEG on the NP surface. The results are presented in section 5.3.2.1 (Figure 5-18), where they are discussed in greater detail.

## **5.2 ZnO Nanoparticles Prepared by Flame Spray Pyrolysis Technique**

Two samples of ZnO were prepared by Dr. Karsten Wegner at ETH Zurich, using zinc acrylate (ZnAc) and methanol as precursor materials. The precursor

solution feed rate was increased from 1 ml/min to 3 ml/min to investigate the effect on the resultant NPs. Additionally a sample was prepared using zinc naphthenate (ZnNap) and toluene as precursor materials and a solution feed rate of 5 ml/min was employed.

The surface area of the synthesized powders were analyzed by the BET gas adsorption technique, the results of which are reported in Table 5-4 along with the corresponding average particle size, deduced from BET. The average particle size for the samples prepared using a precursor solution feed rate of 1, 3 and 5 ml/min was 11.4, 14.6 and 18.1 nm respectively. Powders were named according to the average particle size obtained from BET measurements.

**Table 5-4 Specific surface area measurements determined by BET gas adsorption and corresponding calculated average particle size ( $d_{\text{BET}}$ )**

<b>Sample Name</b>	<b>Specific Surface Area (<math>\text{m}^2/\text{g}</math>)</b>	<b>Particle Size (<math>d_{\text{BET}}</math>) (nm)</b>
FSP 11	93.88	11.4
FSP 14	73.31	14.6
FSP 18	59.46	18.1

In order to investigate the phase and composition of the powders produced, XRD analysis was performed, the results of which are displayed in Figure 5-9. The XRD patterns obtained are consistent with that from the JCPDS reference file for the hexagonal wurtzite structure of zincite (ref: 01-079-0206), see Table 5-5, that has also been observed in other flame-synthesized ZnO powders (Tani et al., 2002; Liewhiran & Phanichphant, 2007). The average crystallite sizes were estimated from 6 peaks for each sample and the results are presented in Table 5-6. For all of the samples, the 0002 peak was slightly narrower than the other peaks indicating a slightly larger crystallite size along these planes, as was the case for the ZnO NPs prepared by the polyol route. This is confirmed by TEM (Figure 5-10) where a number of elongated particles are observed. The other XRD peaks all gave values to within approximately 1 nm of each other. The crystallite sizes, and increase in

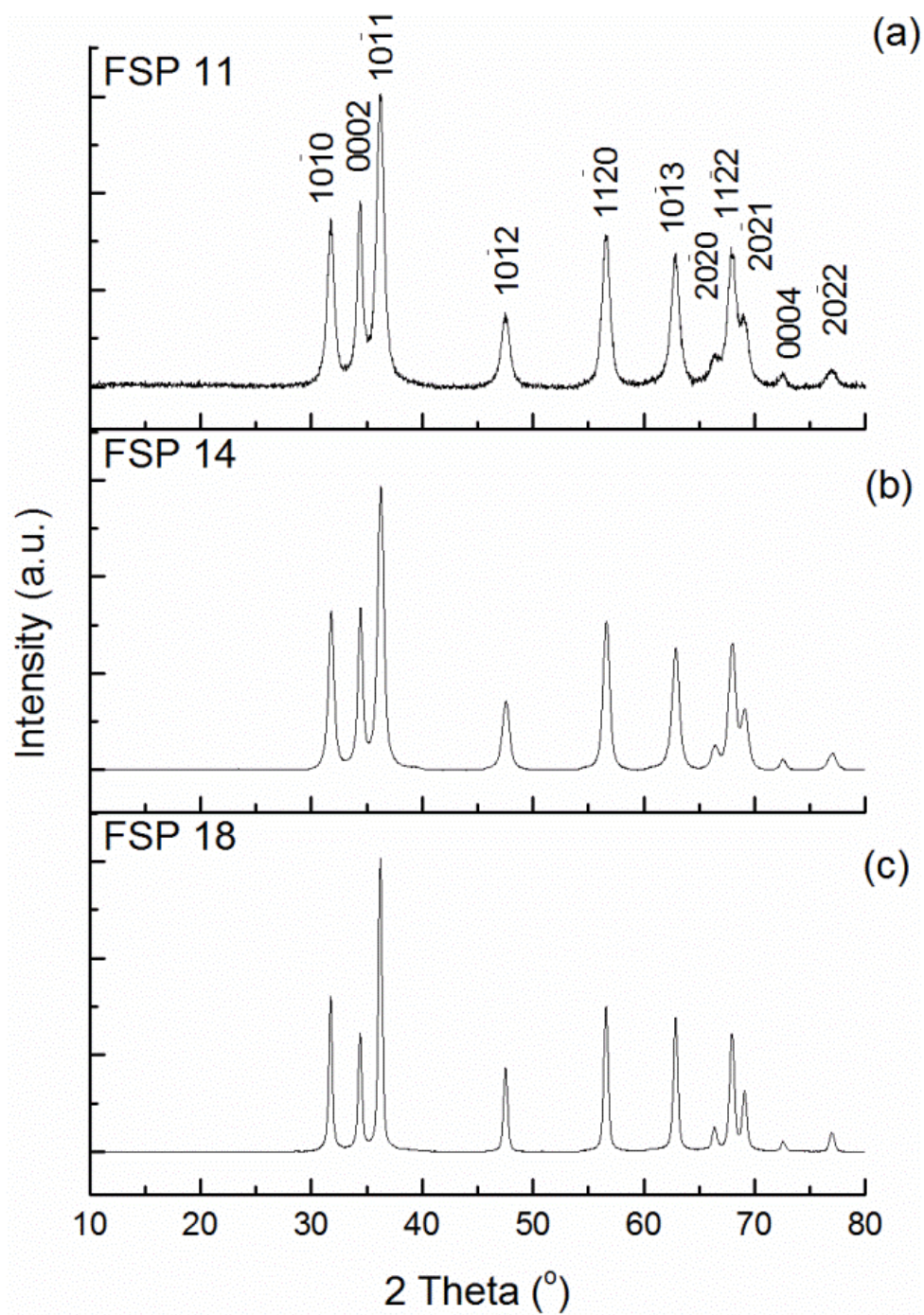


**Figure 5-9 XRD pattern for (a) FSP 11 (b) FSP 14 and (c) FSP 18 synthesized ZnO NP samples with the Miller indices for the reflecting planes**

**Table 5-5 XRD peak positions, corresponding d-spacings and relative intensities for FSP 11, FSP 14 and FSP 18. Also listed are the referenced values for zincite extracted from the JCPDS file ref: 01-079-0206**

Number	ZnO <i>hkil</i>	2 $\theta$ (°)				d-spacing (Å)				Relative Intensity (%)			
		JCPDS Ref:	Experimental XRD Pattern			JCPDS Ref:	Experimental XRD Pattern			JCPDS Ref:	Experimental XRD Pattern		
			FSP 11	FSP 14	FSP 18		FSP 11	FSP 14	FSP 18		FSP 11	FSP 14	FSP 18
1	10 $\bar{1}$ 0	31.77	31.77	31.83	31.72	2.815	2.815	2.809	2.819	58	57	52	53
2	0002	34.42	34.44	34.40	34.42	2.603	2.602	2.605	2.604	41	63	58	40
3	10 $\bar{1}$ 1	36.25	36.25	36.24	36.23	2.476	2.476	2.477	2.477	100	100	100	100
4	10 $\bar{1}$ 2	47.54	47.53	47.59	47.53	1.911	1.911	1.909	1.911	21	24	25	29
5	11 $\bar{1}$ 0	56.6	56.59	56.66	56.59	1.625	1.625	1.623	1.625	31	50	54	50
6	10 $\bar{1}$ 3	62.86	62.86	62.93	62.82	1.477	1.477	1.476	1.478	26	43	42	46
7	20 $\bar{1}$ 0	66.37	66.63	66.48	66.36	1.407	1.403	1.405	1.407	4	10	8	9
8	11 $\bar{1}$ 2	67.95	67.92	67.97	67.95	1.378	1.379	1.378	1.378	22	46	43	40
9	20 $\bar{1}$ 1	69.09	68.98	69.13	69.06	1.359	1.360	1.358	1.359	11	24	20	21
10	0004	72.57	72.41	72.57	72.56	1.302	24.799	1.302	1.302	2	4	3	4
11	20 $\bar{1}$ 2	76.96	77.16	77.08	76.95	1.238	1.235	1.236	1.238	3	4	5	7



crystallite size with increasing solution feed rate, for FSP 11 and FSP 14 are consistent with Tani et al. (2002) using the same precursor solution and feed rates, indicating that higher precursor concentration and temperature resulted in larger particles. The crystallite sizes for FSP 18 are consistent with Height et al. (2006) using the same precursor solution and reactant flow rates but an additional 5 l/min of oxygen sheath gas. For undoped ZnO nanopowder they obtained a specific surface area of 53 m<sup>2</sup>/g, while the average crystallite sizes determined from the (0002) and (10 $\bar{1}$ 0) peaks were 27 and 18 nm, respectively. The additional oxygen sheath gas in the experiments of Height et al. (2006) might have resulted in a hotter flame and slightly larger particles by increased particle residence times in the flame.

Liewhiran and Phanichphant (2007) obtained somewhat smaller average crystallite sizes of  $d_{\text{BET}}$ , 16.8 nm and  $d_{\text{XRD}}$ , 18 nm, but used a toluene /acetonitrile ( $\Delta H_{\text{C}}=-1256$  kJ/mol) solvent mixture with lower enthalpy of combustion compared to pure toluene ( $\Delta H_{\text{C}}=-3910$  kJ/mol) and otherwise similar synthesis conditions. Thus, smaller particles are expected when grown in shorter and colder flames.

Interestingly, Tani et al. (2002) produced similar-sized particles with  $d_{\text{BET}}$  18.4 nm, from a methanol-based solution fed at 4 ml/min and dispersed with 3.85 l/min oxygen (pilot flame: 1.58 l/min CH<sub>4</sub> and 1.52 l/min O<sub>2</sub>). Given the low combustion enthalpy of methanol ( $\Delta H_{\text{C}}= -726.1$  kJ/mol) and shorter high temperature residence times, smaller product primary particles than from the toluene-based flame here would have been expected.

TEM images of the ZnO samples showing the interparticle variation in sizes and morphologies to have only a small distribution are presented in Figure 5-10. The average particle lengths, widths and Feret ratios measured for the samples from TEM images are presented in Table 5-7. Results indicate an increase in particle size and Feret ratio with increasing precursor feed rate. Taking into account the average particle lengths and widths, the size values are in reasonably good agreement with both BET (Table 5-4) and XRD (Table 5-6) crystallite size determinations. The particle morphologies present in FSP 11 and FSP 14 are qualitatively consistent with those produced by Tani et al. (2002) at precursor feed rates of 1 and 3 ml/min, although no quantitative analysis of TEM images is reported in the study. The ZnO

NPs obtained by Tani et al. (2002) at their highest precursor feed rate of 4 ml/min are also elongated, but no Feret ratio was reported. Due to only small differences in size distribution between the three samples prepared by flame spray pyrolysis, only one sample, FSP 18, was chosen to move forward to toxicity screening experiments.

**Table 5-6 Average crystallite sizes measured by XRD corresponding to atomic planes with listed Miller indices for FSP 11, FSP 14 and FSP 18.**

<b>ZnO <i>hkil</i></b>	<b>Average crystallite size (nm)</b>		
	<b>FSP 11</b>	<b>FSP 14</b>	<b>FSP 18</b>
10 $\bar{1}$ 0	10.8	13.8	18.1
0002	14.6	16.7	23.3
10 $\bar{1}$ 1	10.3	14.6	19.8
10 $\bar{1}$ 2	10.1	13.4	22.3
11 $\bar{1}$ 0	10.5	13.3	21.4
10 $\bar{1}$ 3	10.3	13.8	20.5

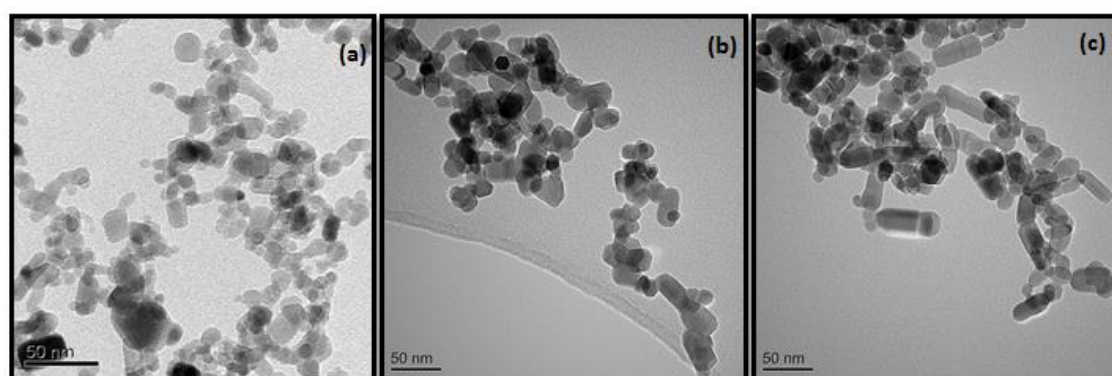


**Figure 5-10 TEM images of (a) FSP 11 (b) FSP 14 and (c) FSP 18. Size distributions determined by measurement of 250 particles are (a) Feret length =  $14 \pm 6$  nm, Feret width =  $10 \pm 5$  nm, and Feret ratio =  $1.4 \pm 0.15$ , (b) Feret length =  $18 \pm 12$  nm, Feret width =  $12 \pm 5$  nm and Feret ratio =  $1.50 \pm 0.3$  and (c) Feret length =  $23 \pm 8$  nm, Feret width =  $14 \pm 4$  nm and Feret ratio =  $1.64 \pm 0.4$ .**



**Table 5-7 Average crystallite sizes for FSP 11, FSP 14 and FSP 18 measured from TEM**

Sample	Average Particle Size (nm)		
	Length	Width	Feret Ratio
FSP 11	14 ± 6	10 ± 5	1.4 ± 0.15
FSP 14	18 ± 12	12 ± 5	1.5 ± 0.3
FSP 18	23 ± 8	14 ± 4	1.64 ± 0.4

### **5.3 Characterisation Protocol**

Once samples had been selected for toxicological investigations, the characterisation protocol discussed previously in section 4-2 was employed in order to obtain a more detailed analysis of the synthesized samples' physiochemical properties. Like all ZnO NP samples tested in the ENNSATOX project, the two synthesized samples were assigned identification codes. For the remainder of the thesis, the samples will be referred to with the associated ENNSATOX code: i.e. FSP 18 as EN-Z-4 and Degsyn-0.45-250-2 as EN-Z-6. Characterisation of the bulk powder, the sample surface and NP characterisation results are reported in this section. Much of the characterisation data acquired for EN-Z-4 is presented in the investigation by Wallace et al. (2013).

#### **5.3.1 Bulk Sample Characteristics**

##### *5.3.1.1 Inductively coupled plasma-mass spectroscopy*

Digested ZnO suspensions, prepared by the method outlined in section 3.2.1.1 were analyzed by ICP-MS in order to obtain an overview of the total concentrations of all of the elements present in the samples, thus highlighting any potential impurities. A blank sample of 6 µl HNO<sub>3</sub> and 9.994 ml MilliQ water was also analyzed. The concentrations obtained for the HNO<sub>3</sub> and water blank were

subtracted from the measurements obtained for ZnO NP suspensions and the resultant concentrations are presented in Figure 5-11 (the concentrations have been multiplied by 1000 in order to account for the dilution). A sample of MilliQ water was also analyzed by ICP-MS in order to investigate the purity. The calcium and sodium impurities present in the ZnO NP suspensions can be seen to occur as a result of the water used. The main peak for the EN-Z-4 and EN-Z-6 samples was that of zinc which is expected however the concentration is slightly lower than the nominal concentration of zinc in the prepared suspensions. This may be attributed to errors arising during sample preparation, i.e. inaccurate weighing of the powders or inhomogenous sampling in the dilution stages. The NPs in the suspensions are agglomerated and polydisperse (Figure 5-28), which means that when a volume is removed, the amount of solid in the aliquot will vary each time. There is no oxygen peak as the instrument does not detect gases.

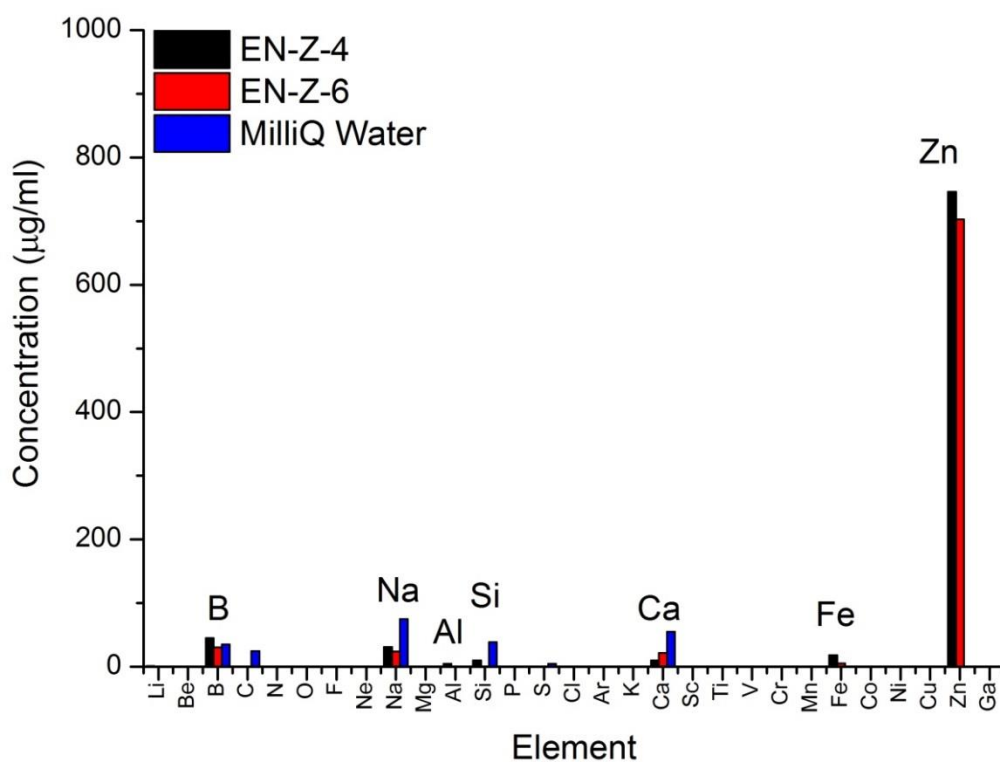


**Figure 5-11 Results of ICP-MS analysis reporting the concentrations of each element present in EN-Z-4 and EN-Z-6, with elemental concentrations in nitric acid blank subtracted.**

### 5.3.1.2 X-ray Diffraction

X-ray diffraction patterns were presented earlier in Figure 5-5 (d) and Figure 5-9 (c) for EN-Z-6 and EN-Z-4 respectively. A list of the peak positions and relative intensities from the XRD patterns for EN-Z-6 is presented in Table 5-8. The peak positions and relative intensities are in excellent agreement with the JCPDS file for zincite (ref: 01-079-0206), indicating the sample is wurtzite ZnO. A list of the peak positions and relative intensities for EN-Z-4 has already been reported in Table 5-5.

**Table 5-8 XRD peak positions, corresponding d-spacings and relative intensities for EN-Z-6. Also listed are the referenced values for zincite extracted from the JCPDS file ref: 01-079-0206**

Number	ZnO <i>hkl</i>	2 $\theta$ ( $^{\circ}$ )		d-spacing ( $\text{\AA}$ )		Relative Intensity (%)	
		JCPDS Ref:	EN-Z-6	JCPDS Ref:	EN-Z-6	JCPDS Ref:	EN-Z-6
1	10 $\bar{1}$ 0	31.77	31.78	2.815	2.814	57.6	50.4
2	0002	34.42	34.45	2.603	2.601	41.4	51.8
3	10 $\bar{1}$ 1	36.25	36.27	2.476	2.475	100	100.1
4	10 $\bar{1}$ 2	47.54	47.55	1.911	1.910	21.4	28.9
5	11 $\bar{1}$ 0	56.61	56.63	1.625	1.624	30.7	45.7
6	10 $\bar{1}$ 3	62.86	62.87	1.477	1.476	26.4	46.5
7	20 $\bar{1}$ 0	66.37	66.40	1.407	1.399	4	6.5
8	11 $\bar{1}$ 2	67.95	67.98	1.378	1.376	21.7	36.8
9	20 $\bar{1}$ 1	69.09	69.10	1.359	1.359	10.5	17.9
10	0004	72.57	72.57	1.302	1.302	1.6	3.9
11	20 $\bar{1}$ 2	76.96	76.99	1.238	1.236	3.3	5.8

### 5.3.1.3 Gas Adsorption (BET)

The BET adsorption-desorption isotherms for EN-Z-4 and EN-Z-6 are presented in Figure 5-12 and Figure 5-13 respectively and are consistent with those obtained for EN-Z-2 and EN-Z-3. The specific surface area (SSA) determined by gas

adsorption technique for EN-Z-4 is  $59.5 \text{ m}^2/\text{g}$ , corresponding to an average particle size of 18 nm (Table 5-4). which is in good agreement with crystallite size estimations from both XRD (Figure 5-9) where the average particle length and width were measured as 23 and 18 nm respectively; and TEM (Figure 5-10), where the average particle length and width were measured as  $23 \pm 8$  and  $14 \pm 4$  nm respectively.

The SSA measured for EN-Z-6 is  $25.3 \text{ m}^2/\text{g}$  which corresponds to an average particle diameter of 42 nm. This is in reasonable agreement with the crystallite size estimations from both XRD (Figure 5-5), where the average particle length and width were measured as 45 and 25 nm respectively; and TEM (Figure 5-6), where the average particle length and width were measured as  $47 \pm 26$  and  $26 \pm 8$  nm respectively. The average particle diameter for BET is calculated from the specific surface area assuming a monodisperse sample consisting of spherical particles, which may account for the minor discrepancy between the average particle size estimated from BET and those estimated from XRD and TEM. EN-Z-6 consists of mostly rod-like particles. A rod with a length of 45 nm has a significantly different surface area to a sphere with 45 nm diameter and therefore this creates a discrepancy when converting from SSA to average particle size.

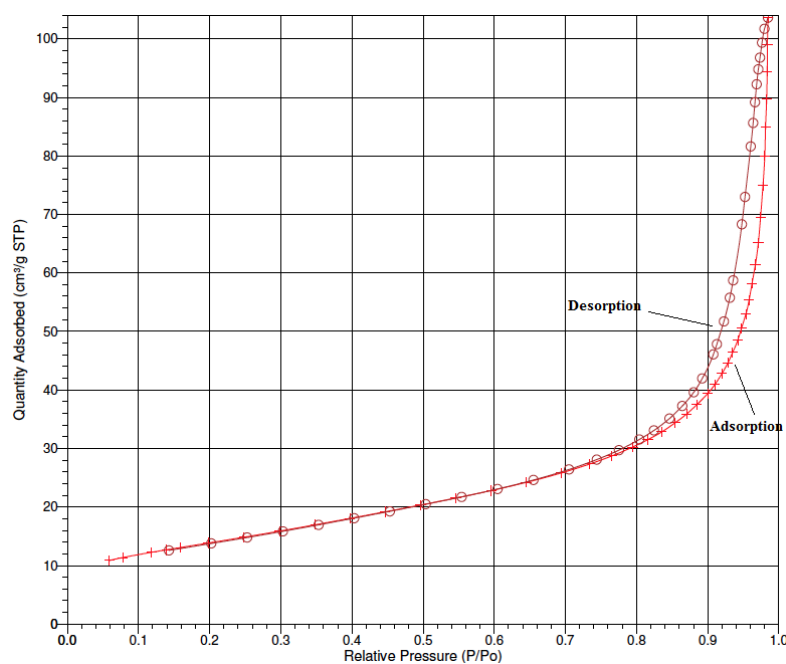


**Figure 5-12 BET adsorption – desorption isotherm for EN-Z-4**

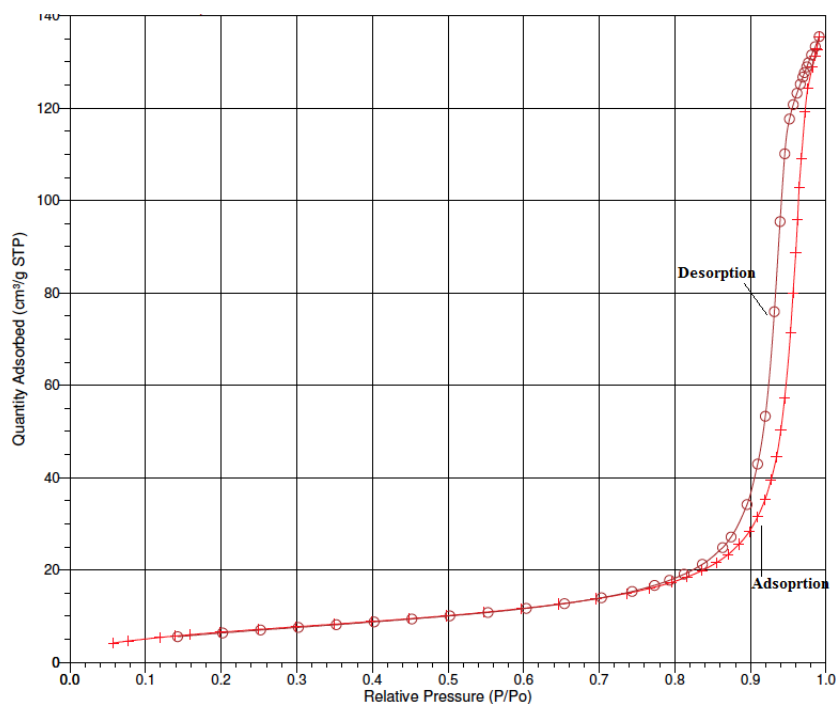


**Figure 5-13 BET adsorption – desorption isotherm for EN-Z-6**

#### 5.3.1.4 Thermogravimetric Analysis with Evolved Gas Analysis by Fourier Transform Infrared Spectroscopy

Figure 5-14(a) and Figure 5-15 (a) display the results of TGA experiments performed on the samples by heating to 950°C, with the mass loss expressed as a percentage of the total initial starting mass. Evolved gas analysis was performed in order to confirm the composition of the gases evaporating from the sample during TGA. The reduction in mass observed in Figure 5-14(a) and Figure 5-15 (a) can be explained by the increase in the overall absorbance observed in the Gram-Schmidt plots presented in Figure 5-14 (b) and Figure 5-15 (b). The change in the intensity of absorbance over specific ranges of wavenumber (labeled on the graph), as the temperature rises, are presented in Figure 5-14 (c) and Figure 5-15 (c).

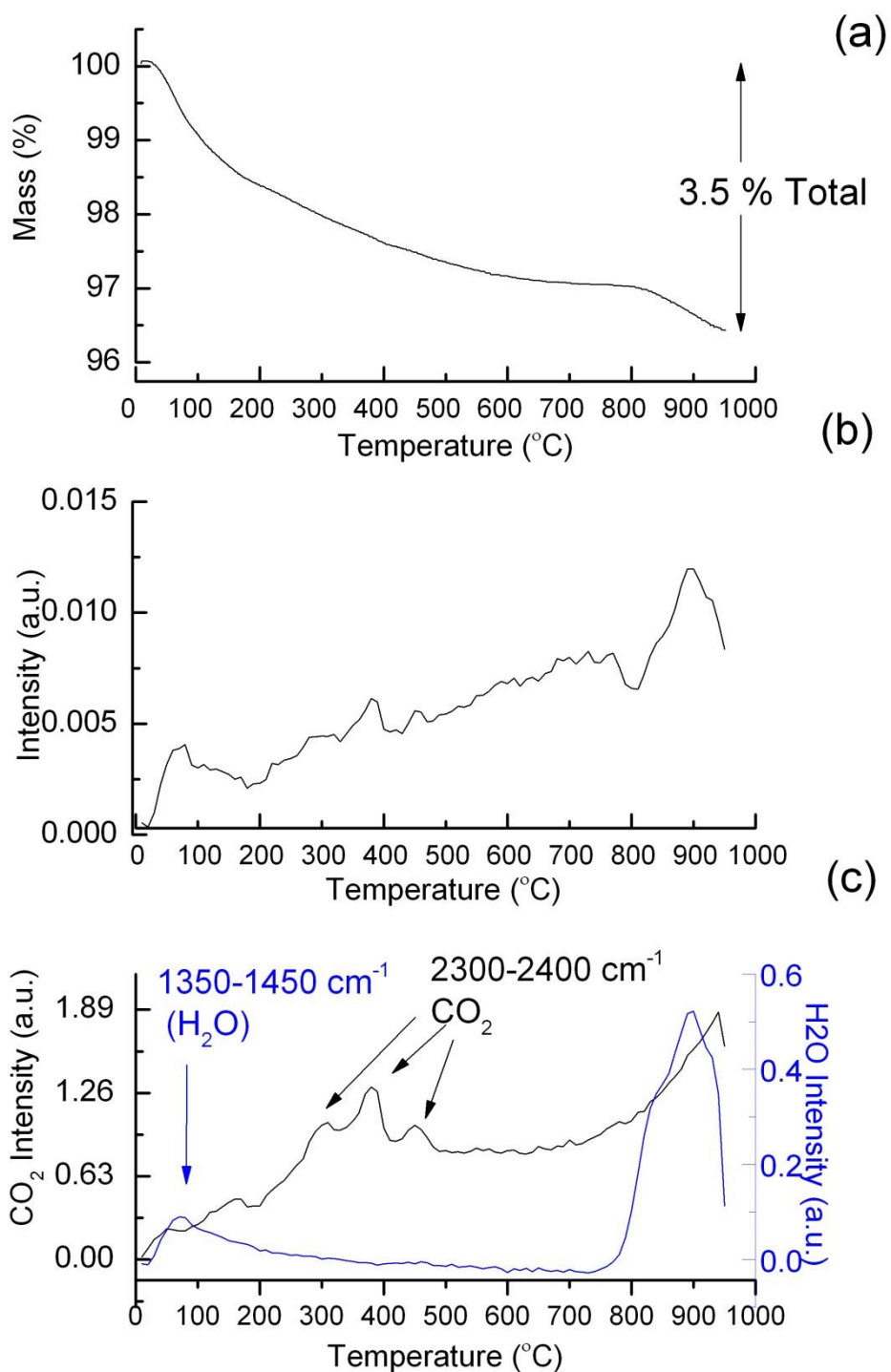


**Figure 5-14(a) TGA curve for EN-Z-4 showing loss of mass of sample with increasing temperature, (b) associated Gram-Schmidt plot showing increase in total FTIR absorbance with increasing temperature and (c) chemigrams showing FTIR absorbance over specified ranges of wavenumber (indicated on the graph) as temperature rises for EN-Z-4.**

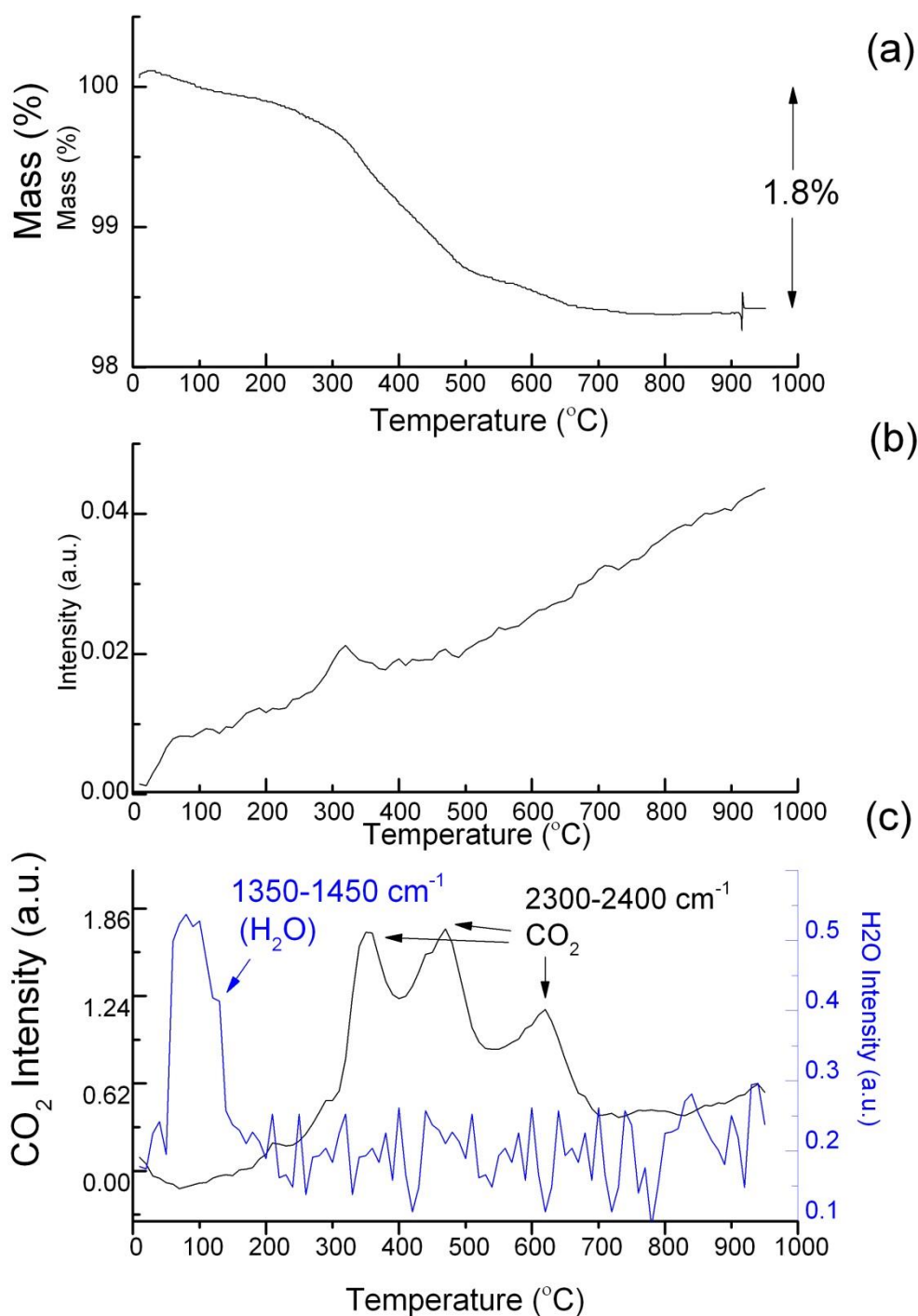


**Figure 5-15 (a) TGA curve for EN-Z-6 showing loss of mass of sample with increasing temperature, (b) associated Gram-Schmidt plot showing increase in total FTIR absorbance with increasing temperature and (c) chemigrams showing FTIR absorbance over specified ranges of wavenumber (indicated on the graph) as temperature rises for EN-Z-6.**

The steep drop observed in the TGA for EN-Z-4 (Figure 5-14 (a)) between 50°C and 150°C in which the sample loses around 1.5% of its total mass may be explained by adsorbed water vapour evaporating from the sample. Evidence for this is observed in Figure 5-14 (c) which shows the absorbance detected in the range 1350-1450 cm<sup>-1</sup>, indicative of O-H bending, increasing in intensity over the same temperature range, 50°C to 150°C. There is then a more gradual reduction in weight between 150 and 650°C where the sample loses around 1.5 % of its total mass. This is associated with a number of peaks with absorbance in the range 2300 to 2400 cm<sup>-1</sup> which is typical of CO<sub>2</sub> evolution. This may be attributed to the decomposition of zinc carbonate present at the surface of the NPs decomposing to form carbon dioxide (see Figure 5-16). Evidence for this is observed in Figure 5-14 (c) which shows an increase in absorbance in the range 2250-2400 cm<sup>-1</sup>, indicative of carbon dioxide evolving between 200 and 500°C with a maximum peak at 370°C. Dollimore et al. (1979) investigating the thermal decomposition of zinc carbonate, reported a continuous weight loss between 370 and 560°C with a maximum rate of weight loss at 450°C. The rate of heating was consistent with our studies however the experiment by Dollimore et al. (1979) was carried out in air, as opposed to in nitrogen which may account for the discrepancy of around 80 °C. However, there is a possibility that CO<sub>2</sub> may also be formed by decomposition of residual organic precursors present on the surface of the particles rather than by decomposition of inorganic carbonates. During synthesis, the maximum flame temperature is around 2200 - 2700°C (Mädler et al, 2002; Gröhn et al., 2012) yet our investigations infer that some of the precursor derivatives do not fully decompose. This may be because the particles experience the flame temperature for a fraction of a second, whereas in TGA analysis, despite the lower temperatures, the dwell times are much longer, (heating rate 10°C/s) enabling decomposition reactions to proceed to completion. Moreover, Gröhn et al. (2012) also observed individual precursor droplets escaping the spray that might contaminate the product ZnO NPs on the collection filter.

Following the gradual loss of mass between 200 and 700°C, the sample stabilizes until the temperature reaches 800°C (Figure 5-14). Approximately 0.5 % of the total mass of the sample is lost between 800 and 950 °C which is accompanied by an increase in absorbance in the range 1350-1450cm<sup>-1</sup>. Initially this was thought to



be an experimental error however repetitions of the TGA experiment produced consistent results. A loss in mass is not observed between 800 and 950 °C with other samples of ZnO analysed in the same way (Figure 4-3, Figure 4-4, Figure 4-5 and Figure 5-12) and therefore it appears to be unique to the sample. At present the composition of the gas evolving from the sample is unknown and requires further investigation in order explain this phenomena.

The TGA result for EN-Z-6 is presented in Figure 5-15 (a) and reveals a loss of mass between 50 and 150°C corresponding to the evaporation of water from the sample evident by the increase in absorption in the range 1350-1450  $\text{cm}^{-1}$  observed over the same temperature range in Figure 5-15 (c). There is a gradual loss of mass between 200 and 500 °C consistent with that observed for EN-Z-4, which may be attributed to evolution of  $\text{CO}_2$  by decomposition of zinc carbonate on the surface of the NPs, evident by the peaks in absorption in the range 2300-2400  $\text{cm}^{-1}$  between 200 and 500 °C in Figure 5-15 (c). There is another peak in  $\text{CO}_2$  evolution occurring around 600°C. This may be due to DEG that has not been removed fully during the washing procedure.

### 5.3.2 Surface Characterisation

Fourier transform infrared spectroscopy (FTIR), X-ray photoelectron spectroscopy (XPS) and solid state carbon 13 nuclear magnetic resonance spectroscopy ( $^{13}\text{C}$ -NMR) techniques were employed to investigate the surface composition of the samples. EN-Z-4 was investigated by XPS and FTIR over time in order to determine the effect of ageing on the composition of the sample surface.

#### 5.3.2.1 Fourier Transform infrared Spectroscopy

Figure 5-16 (a) shows the FTIR spectrum obtained for the as-prepared sample of EN-Z-4. The strong band  $\leq 550 \text{ cm}^{-1}$  is characteristic of the broad band of absorption that indicates ZnO lattice bonding (Wahab et al., 2009; Umar et al., 2009; Li et al., 2010). The band at 1680  $\text{cm}^{-1}$  is characteristic of C=O stretching of an organic carbonyl group. It may be due to aldehyde, ketone or carboxylic acid compounds that have formed due to partial decomposition of the precursor compound zinc naphthenate in the toluene-fuelled flame during the synthesis

process, previously detected by TGA with EGA (Figure 5-14). The band at  $3400\text{ cm}^{-1}$  relates to the O-H stretch of the hydroxyl vibration and hence indicates hydration of the sample. Literature reports that the characteristic band here for O-H occurs between  $3200\text{-}3600\text{ cm}^{-1}$  (Socrates, 2001), however the band present in the current sample spectrum continues down to  $2800\text{ cm}^{-1}$ . It is possible that the O-H band is masking another absorption band that can most probably be attributed to the asymmetrical stretch of a C-H bond present in the carbonyl containing compound mentioned above. In addition to the potentially organic impurity, the spectrum also indicates the presence of carbonate groups, which are likely to occur as a result of  $\text{CO}_2$  adsorption on storage. The broad band from  $1500\text{-}1250\text{ cm}^{-1}$  can be attributed to the C-O stretch of a carbonate group, ( $\nu_3$ ), which has split into two components with band maxima at  $1400$  and  $1345\text{ cm}^{-1}$ . The splitting of the band indicates that the carbonate being detected is coordinated to zinc ions, as this reduces the symmetry of the carbonate molecule causing vibrations to split (Nakamoto, 1997). The bands at  $1065$ ,  $878$  and  $696\text{ cm}^{-1}$  occur as a result of the symmetric C-O stretching mode ( $\nu_1$ ), the out-of-plane  $\text{CO}_3$  deformation mode ( $\nu_2$ ) and the OCO bending mode ( $\nu_4$ ) respectively (Nakamoto, 1997).

The FTIR spectrum in Figure 5-16 (b) is of an aged sample of EN-Z-4 and, as expected, the bands occurring as a result of sample hydration and carbonation increase in strength. Formation of surface carbonates and hydroxides is typically observed with zinc oxide exposed to ambient air since  $\text{ZnCO}_3$  is a stable phase if  $\text{CO}_2$  is present and  $\text{Zn(OH)}_2$  is close to stability in humid air (Klimm et al, 2011). Thus it must be taken into account that ZnO surfaces exposed to air may easily form layers of carbonate and/or hydroxide not only by adsorption but also by chemical reaction (Pan et al., 2010; Klimm et al., 2011). The FTIR spectrum in Figure 5-16 (c) shows the spectra taken after washing the sample through a series of steps whereby the ZnO NPs were suspended in MilliQ water, sonicated and then centrifuged. The precipitated particles were then re-suspended in MilliQ water and the process was repeated 6 times, after which the sample was dried in an oven at  $60^\circ\text{C}$ . This process appears to have no effect on the resultant FTIR spectra.

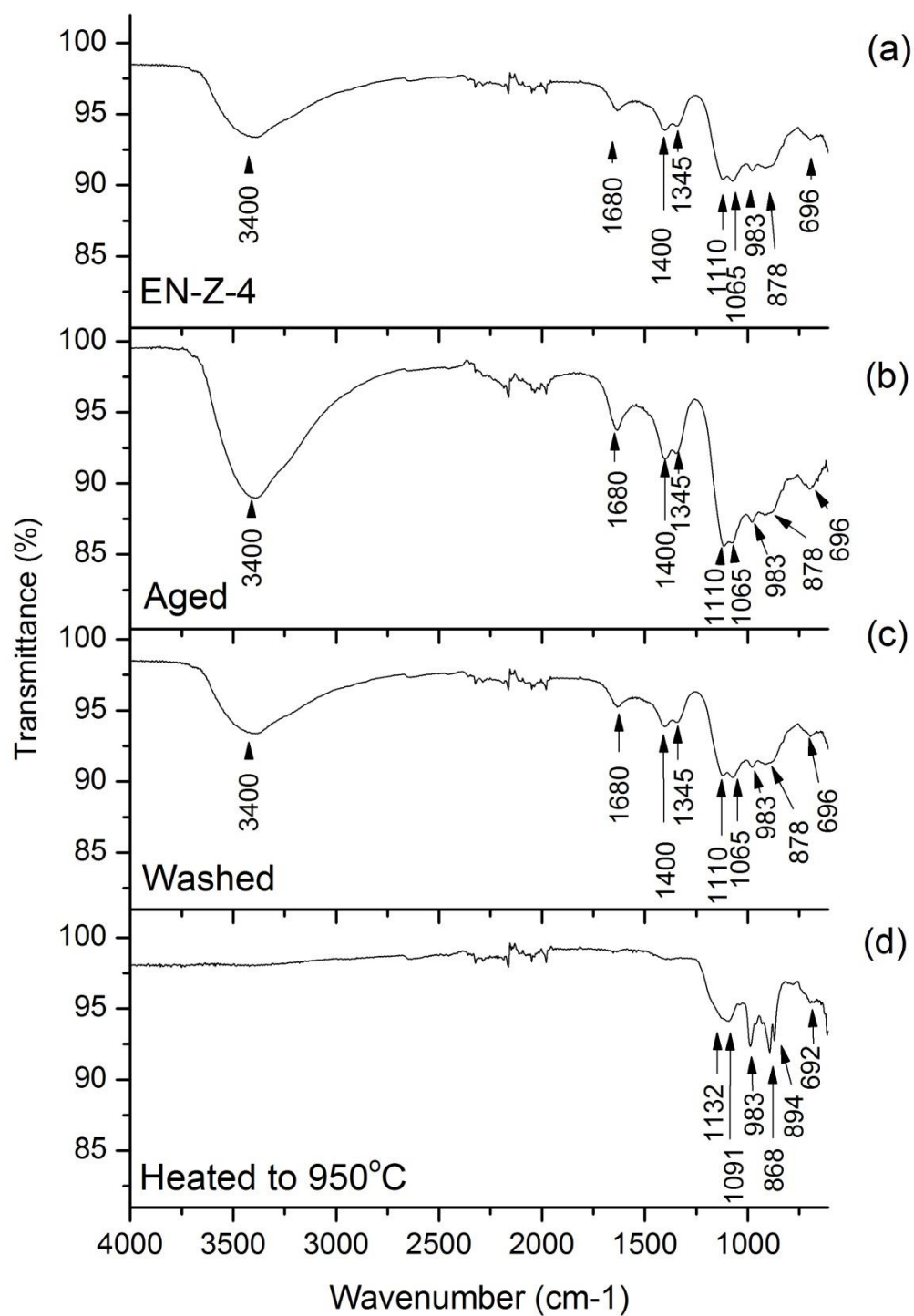


**Figure 5-16** FTIR spectra of EN-Z-4 (a) shortly after synthesis, (b) after washing (c) after ageing and (d) after heated to 900°C

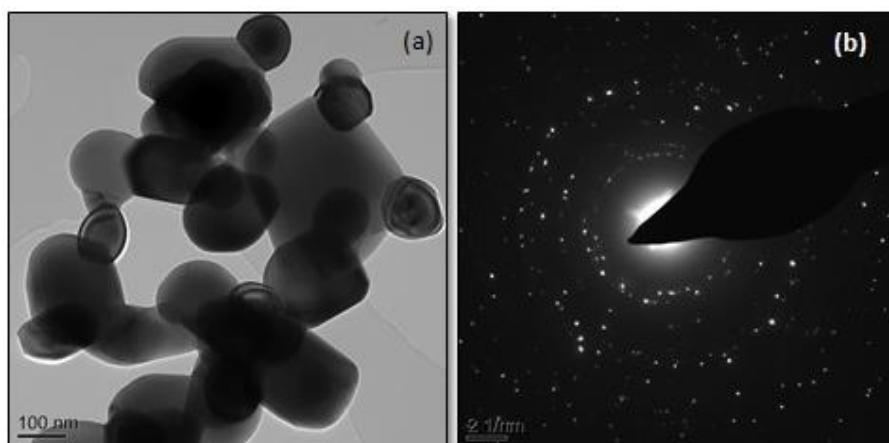


**Figure 5-17 (a) TEM image and (b) SAED pattern showing the sintered ZnO NPs after they have been heated to 800°C for TGA.**

The FTIR spectrum in Figure 5-16 (d) was obtained immediately after the sample had been heated to 950°C during the TGA experiment, in order to investigate whether the presence of carbonate, hydroxyl and potential organic contaminants on the surface were diminished. The O-H, C=O and C-H bands were no longer detectable, suggesting that all of the moisture, as well as the organic substances responsible for the suspected C=O and C-H bands, were removed during high temperature heat treatment. Although after heating to this temperature, the composition of the powder remains consistent with wurtzite zincite, as confirmed by SAED ((Figure 5-17(b)), the high temperature causes the NPs to sinter into larger particles (Figure 5-17), therefore this is not a suitable method for purifying the particles. A sharpening and decrease in intensity of absorbance due to inorganic carbonate bands is observed after heating to 950 °C, indicating a reduction, but not removal of the surface carbonate phase. It may be that the entire surface-carbonate was removed during heat treatment but transferal from the furnace to the FTIR instrument resulted in a limited degree of re-carbonation even in the short time the surface was exposed to air.

An FTIR spectrum of the colloidal suspension of EN-Z-6 ZnO NPs in DEG obtained immediately after synthesis is presented in Figure 5-18 (a). Comparing the spectrum for colloidal EN-Z-6 in DEG with the FTIR spectrum obtained for pure

DEG presented in Figure 5-18 (c), it can be seen that the majority of the peaks observed in Figure 5-18 (a) are a result of DEG. There is an additional band present in the colloidal EN-Z-6 in DEG FTIR spectrum (Figure 5-18 (a)) compared with the DEG FTIR spectrum (Figure 5-18 (c)), located at  $1730\text{ cm}^{-1}$ . This band is likely to be due to the C=O stretching of a carbonyl group (Socrates, 2001), the presence of which may be explained by a variety of reasons. Firstly, the entirety of the zinc acetate precursor may not have reacted, giving rise to residue remaining in the sample. The FTIR of ZnAc, presented in Figure 5-18 (d), has a band at  $1730\text{ cm}^{-1}$  attributable to the C=O stretch. However ZnAc also has a strong band at  $1575\text{ cm}^{-1}$  which does not appear in the FTIR spectrum for colloidal EN-Z-6 in DEG, indicating that there is likely to be alternative explanation for the band at  $1730\text{ cm}^{-1}$ . Although the degradation products of DEG are not reported in the literature, it is well documented that when heated, ethylene glycol, propylene glycol and polyethylene glycol all form carboxylic acids such as glycolic, glyoxylic, formic, carbonic and oxalic as degradation products (Rossiter et al., 1983; Rossiter et al., 1985; Clifton et al., 1985), all of which have bands at  $1730\text{ cm}^{-1}$  corresponding to the stretch of C=O bonds present in the carboxylic acid functional group (COOH). Bands associated with the O-H bond present in the functional group would occur between  $2800\text{-}3300\text{ cm}^{-1}$  however due to the O-H bands present in the DEG spectrum at similar frequencies it is not possible to confirm their presence. Therefore the band at  $1730\text{ cm}^{-1}$  may be present as a result of products formed from the degradation of DEG upon heating. After washing with distilled water, the band at  $1730\text{ cm}^{-1}$  disappears (Figure 5-16 (b)).

The FTIR for the washed EN-Z-6 sample is presented in Figure 5-18 (b) and indicates that the majority of the bands associated with DEG and the band at  $1730\text{ cm}^{-1}$  associated with a carbonyl group are removed. There are however very weak bands remaining at  $2920$  and  $2850\text{ cm}^{-1}$  associated with asymmetric and symmetric  $\text{CH}_2$  stretching indicating that the DEG has not been fully removed. This is consistent with the impurities detected by TGA with EGA (Figure 5-15). The broad band at  $3400\text{ cm}^{-1}$  may be due to the O-H stretch of residual DEG or carboxylic acids formed from its degradation. However, as the  $\text{CH}_2$  have been reduced to a significantly greater degree, it is probable that the band is also due the O-H stretching

of water molecules present as a result of incomplete evaporation during the drying process. Alternatively, water molecules from the atmosphere may have adsorbed on to the surface of the particles after drying.

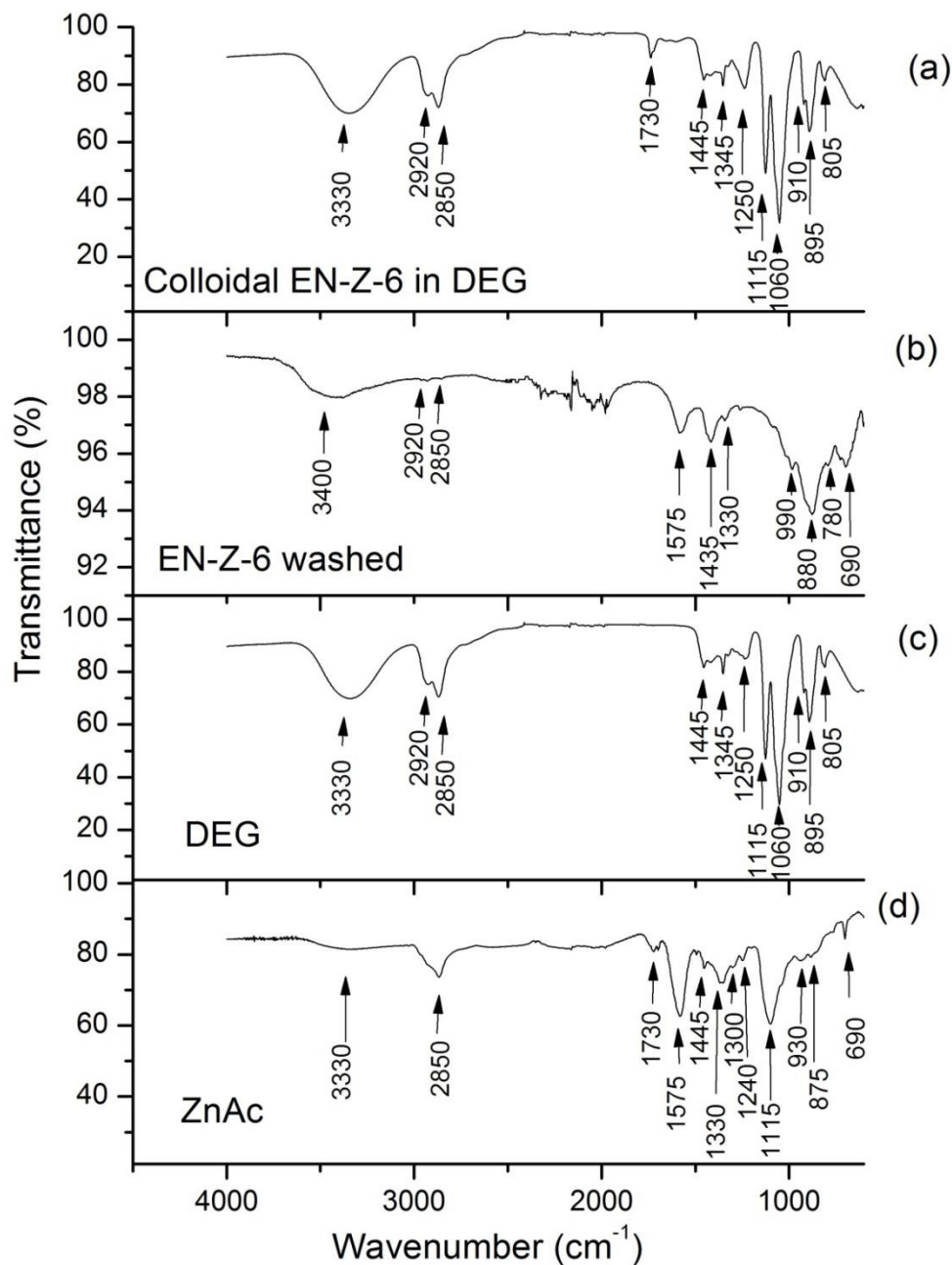


**Figure 5-18** FTIR spectra of (a) synthesized ZnO NPs in DEG, (b) ZnO NPs after being washed with MilliQ water (c) DEG and (d) Zinc Acetate

### 5.3.2.2 X-ray Photoelectron Spectroscopy

The survey scans for EN-Z-4 and EN-Z-6 are presented in Figure 5-19 (a) and (b) respectively. Higher magnification spectra for the Zn2p<sub>3/2</sub>, O1s and C1s edges are presented in Figure 5-20, Figure 5-21 and Figure 5-22 respectively. For EN-Z-4, XPS was performed close to the time of synthesis of the sample (T=1 month), and then again 8 months later (T=9 months) in order to investigate the extent to which the sample was adsorbing atmospheric CO<sub>2</sub> and the spectra obtained for the O1s and C1s edges are presented in Figure 5-23 (a) and (b) respectively. The percentage concentrations of each element were determined by photoelectron peak area integration and are reported in Table 5-9.

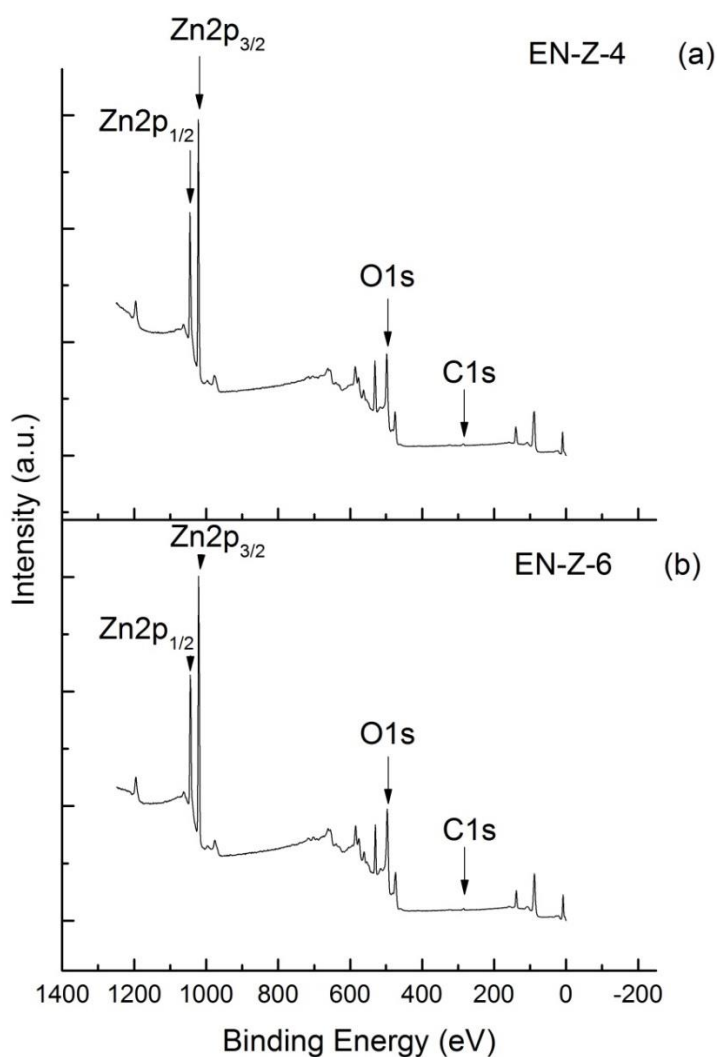


**Figure 5-19** XPS survey scan for (a) EN-Z-4 and (b) EN-Z-6 synthesized ZnO samples.

The  $Zn2p_{3/2}$  binding energies for EN-Z-4 and EN-Z-6 were found at 1021.8 and 1021.1 eV respectively. The  $Zn2p_{1/2}$  binding energies for EN-Z-4 and EN-Z-6 were found at 1044.9 and 1044.2 eV respectively (Figure 5-20). Values obtained are in good agreement with those reported in the literature indicating that the species of zinc detected is that belonging to ZnO (Mar et al., 1993; Chen et al., 2011).

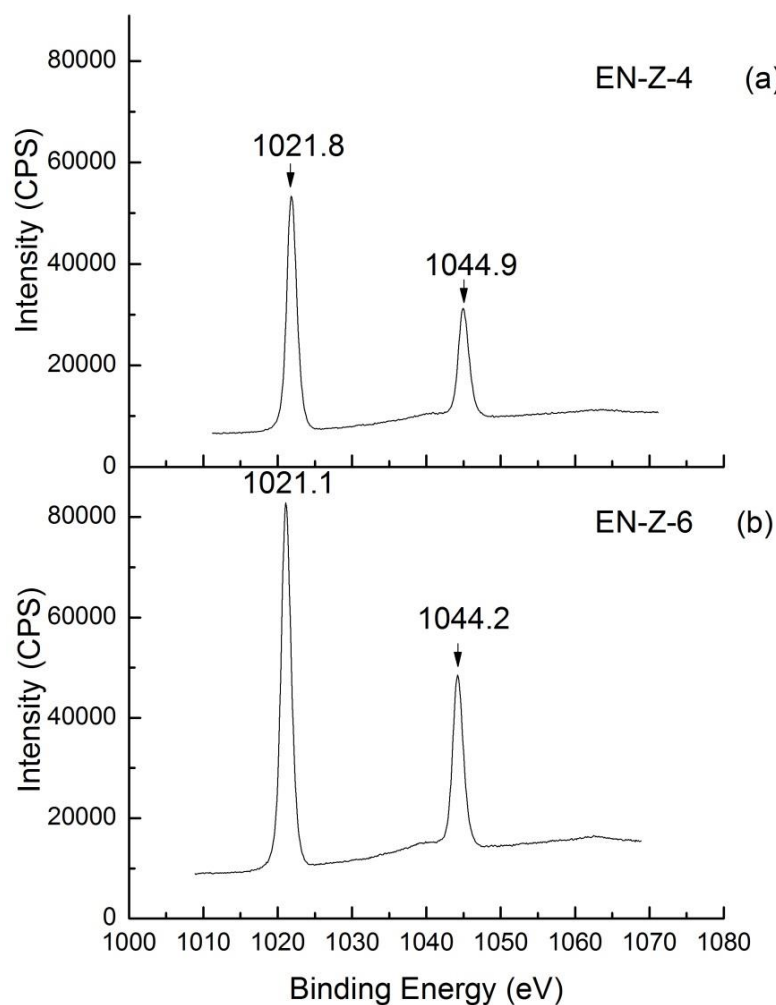


**Figure 5-20 XPS spectra of  $Zn2p$  edge for (a) EN-Z-4 and (b) EN-Z-6 with binding energies labeled above each peak.**

Three mixed Gaussian-Lorentzian peaks were fitted to the  $O1s$  edge of the spectra revealing three types of oxygen species to be present in both of the synthesized ZnO samples (Figure 5-21). The largest peak for EN-Z-4 (Figure 5-21 (a)) and EN-Z-6 (Figure 5-21 (b)), at 530.4 and 530.1 eV respectively, may be



attributed to the oxygen in the crystal lattice of ZnO, in good agreement with the literature values reported (Mar et al., 1993; Zhang et al., 2005; Chen et al., 2011).

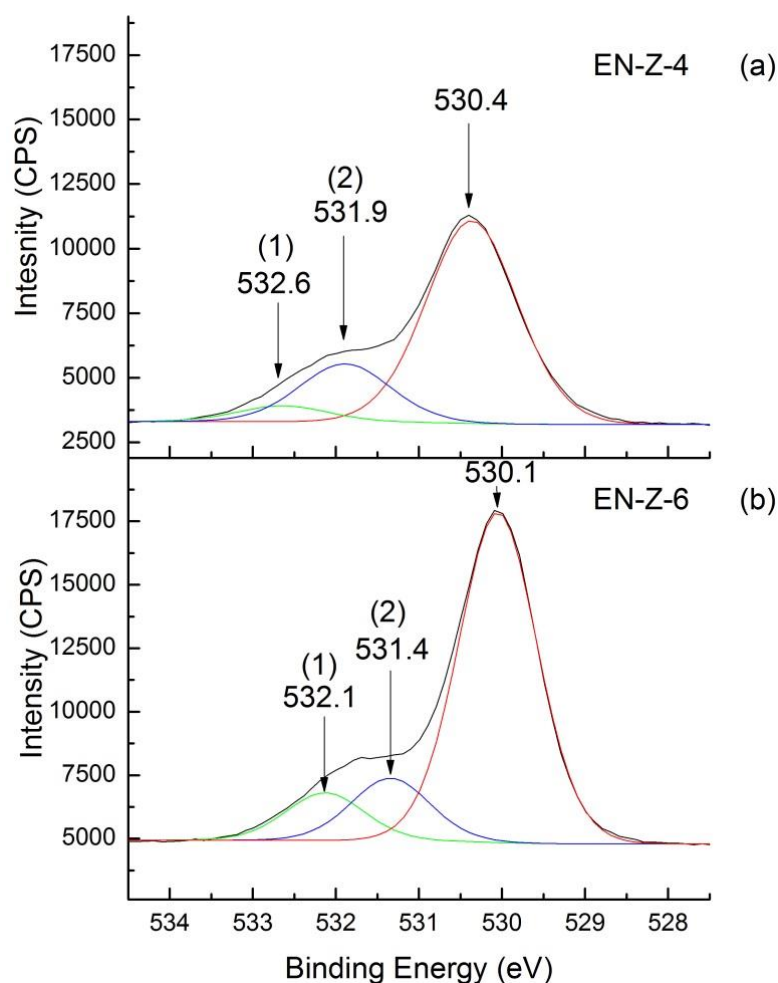


**Figure 5-21 XPS spectra of O1s edge for (a) EN-Z-4 and (b) EN-Z-6 with binding energies labeled above each peak.**

The central peaks at 531.9 and 521.4 eV for EN-Z-4 and EN-Z-6 respectively correspond to hydrated oxide species (Zhang et al, 2005) and/or O=C oxygen species (Liquiang et al., 2004). The hydrated oxide species corresponds to chemically adsorbed water molecules, previously detected in both samples by TGA with EGA (Figure 5-14 and Figure 5-15) and FTIR (Figure 5-16 and Figure 5-18). The highest binding energy peak for the oxygen species present in the samples is at 532.6 and 532.1 eV for EN-Z-4 and EN-Z-6 respectively. This may be attributed to loosely bound oxygen on the surface of the ZnO NPs belonging to physically adsorbed CO<sub>2</sub>

or H<sub>2</sub>O (Mar. et al, 1993; Islam et al., 1996; Au et al., 1988; Zhang et al. 2005), previously detected for both EN-Z-4 and EN-Z-6 by TGA with EGA (Figure 5-14 and Figure 5-15) and FTIR (Figure 5-16 and Figure 5-18).

The C1s edges of the XPS spectra for EN-Z-4 and EN-Z-6 are shown in Figure 5-22 (a) and Figure 5-22 (b) respectively and indicate that there are three types of carbon species present in both of the synthesized samples.

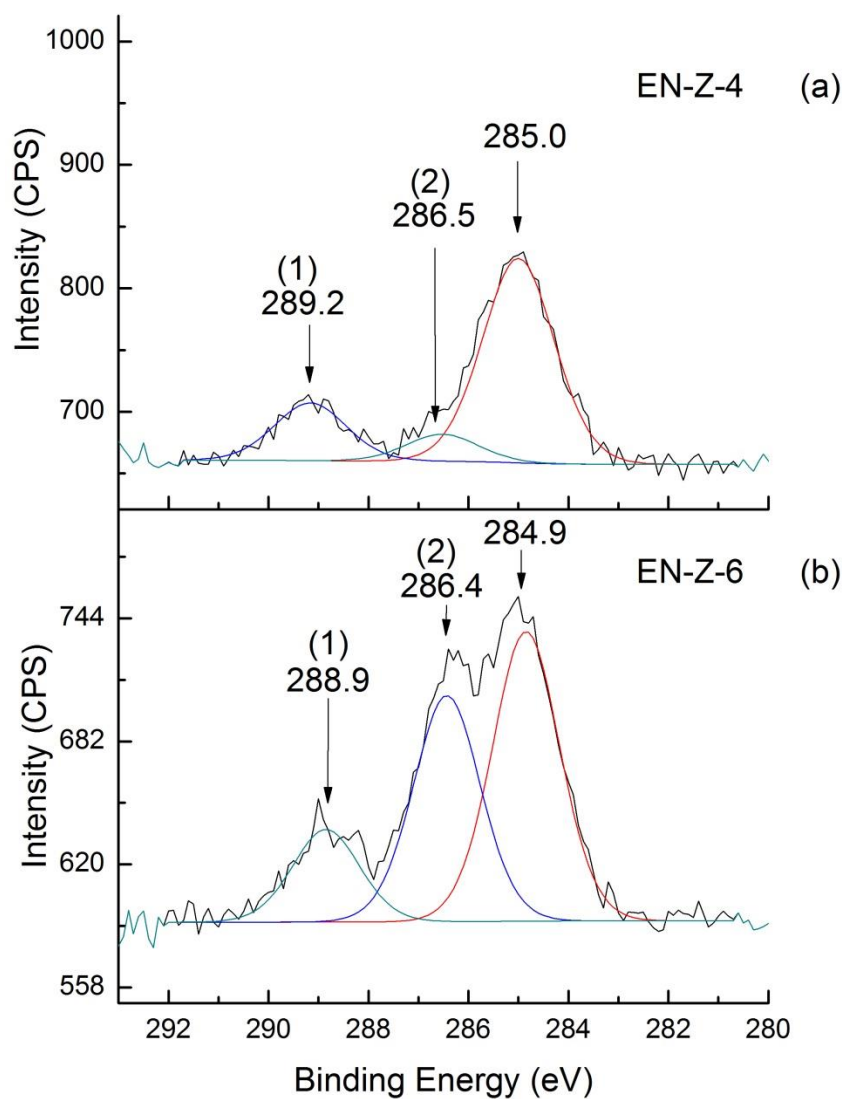


**Figure 5-22 XPS spectra of C1s edge for (a) EN-Z-4 and (b) EN-Z-6 with binding energies labeled above each peak**

The peaks at 285.0 eV and 284.9 eV in the EN-Z-4 and EN-Z-6 spectra respectively, correspond to adventitious carbon (Światowska-Mrowiecka et al, 2008). These peaks may also be a result of the aliphatic carbon present in the contaminants detected in the samples by TGA with EGA (Figure 5-14 and Figure 5-15) and FTIR (Figure 5-16 and Figure 5-18). The peaks at 286.5 and 286.4 eV in the EN-Z-4 and EN-Z-6 spectra respectively are most likely to be due to carbonate species formed by chemical adsorption of CO<sub>2</sub> (Stoch et al., 1991). The peaks at 289.2 and 288.9 eV in the spectra for EN-Z-4 and EN-Z-6 respectively may be attributed to the carbon species present in physically adsorbed carbon dioxide molecules (Hirsch and Hirshwald, 1988). These peaks may also be indicative of the species of carbon in a carboxylate group (O-C=O), which is likely to be part of the organic contaminants detected by TGA with EGA (Figure 5-14 and Figure 5-15) and FTIR (Figure 5-16 and Figure 5-18).

The O1s and C1s edges of the XPS spectrum for the aged sample of EN-Z-4 are presented in Figure 5-23 (a) and Figure 5-23 (b) and indicate that the surface of the sample has changed over time. The percentage concentrations of carbon, oxygen and zinc in the top few nanometres of the sample surface are reported in Table 5-9 and show a significant increase in the carbon content and an increase in the amount of oxygen on ageing. This is in agreement with FTIR investigations on the aged sample (Figure 5-16). The percentage concentrations of the different species of oxygen and carbon present in the as prepared and aged samples of EN-Z-4 are reported in Table 5-10. An increase in the oxygen peaks associated with chemically and physically adsorbed CO<sub>2</sub> and H<sub>2</sub>O (Peaks (1) and (2) in Figure 5-23) is observed. Additionally, an increase in carbon associated with chemically adsorbed CO<sub>2</sub> (Peak (2)) in Figure 5-23 (b) is observed.

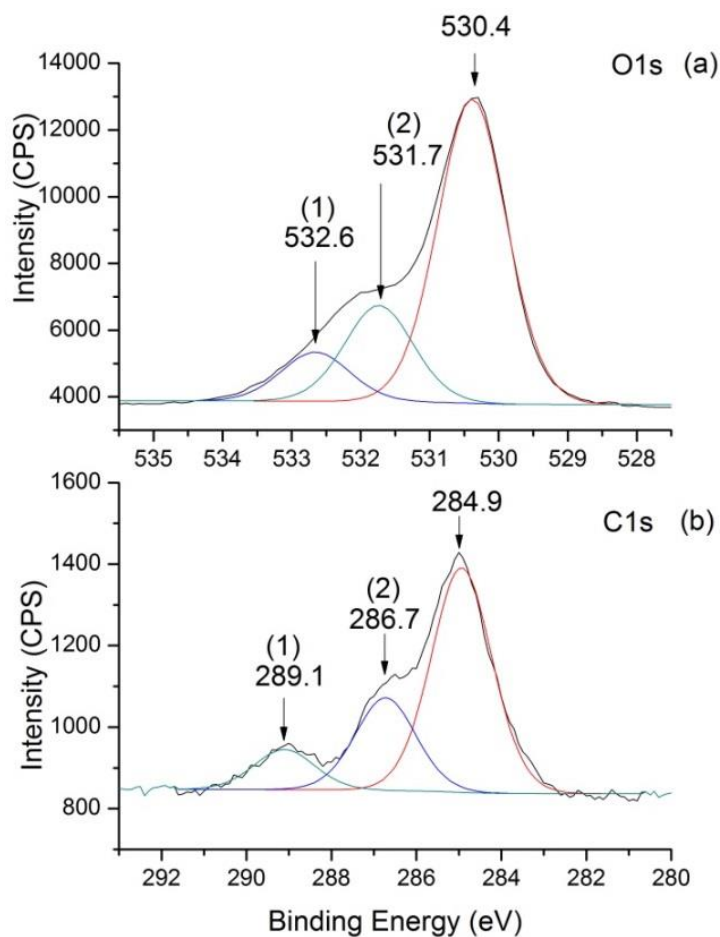


**Figure 5-23 XPS spectrum of (a) O1s and (b) C1s edges of EN-Z-4 after ageing.**

**Table 5-9 Table reporting the relative concentrations of Zn, O and C in the surface of the synthesized samples, obtained from XPS spectra**

Sample	Concentration (%)		
	Zn2p	O1s	C1s
EN-Z-4	44.3	50.9	4.8
EN-Z-6	34.5	54.7	10.8
EN-Z-4 aged	30.4	53.1	16.5

**Table 5-10 Table reporting the percentage concentrations of carbon and oxygen species present in the as prepared and aged sample of EN-Z-4, determined by XPS**

Sample	Concentration (%)					
	C1s			O1s		
	1	2	3	1	2	3
EN-Z-4	19.9	9.3	70.8	5.9	19.3	74.8
EN-Z-4 aged	11.2	25.9	62.9	14.1	23.8	62.1

### 5.3.2.3 Nuclear Magnetic Resonance Spectroscopy

The samples were analysed by solid state  $^{13}\text{C}$  NMR and the spectra obtained are displayed in Figure 5-24. The spectrum obtained for EN-Z-4 is presented in Figure 5-24 (a) and due to a very weak signal output from the sample, is a result of an overnight accumulation. A background roll is observed which in particular, accounts for the bump around 130 ppm. The small signal around 165 ppm is characteristic of carbonate that may be attributed to the surface carbonate previously detected by TGA with EGA (Figure 5-14), FTIR (Figure 5-16) and XPS (Figure 5-22). The signal around 30 ppm is most probably due to experimental background, caused by contaminants such as grease on the rotor.

The spectrum for EN-Z-6 presented in Figure 5-24 (b) has a more obvious range of signals, although the absolute intensity is still very low. The lines at 61.1 and 72.8 ppm are characteristic of the carbon associated with alcohol groups. The line at 21.6 ppm is indicative of methyl groups and the line at 180 ppm may correspond to carboxylic acid groups. All of these species may be attributed to either DEG or carboxylic acids resulting from DEG degradation, small amounts of which have previously been detected by TGA with EGA (Figure 5-15), FTIR (Figure 5-18) and XPS (Figure 5-22).

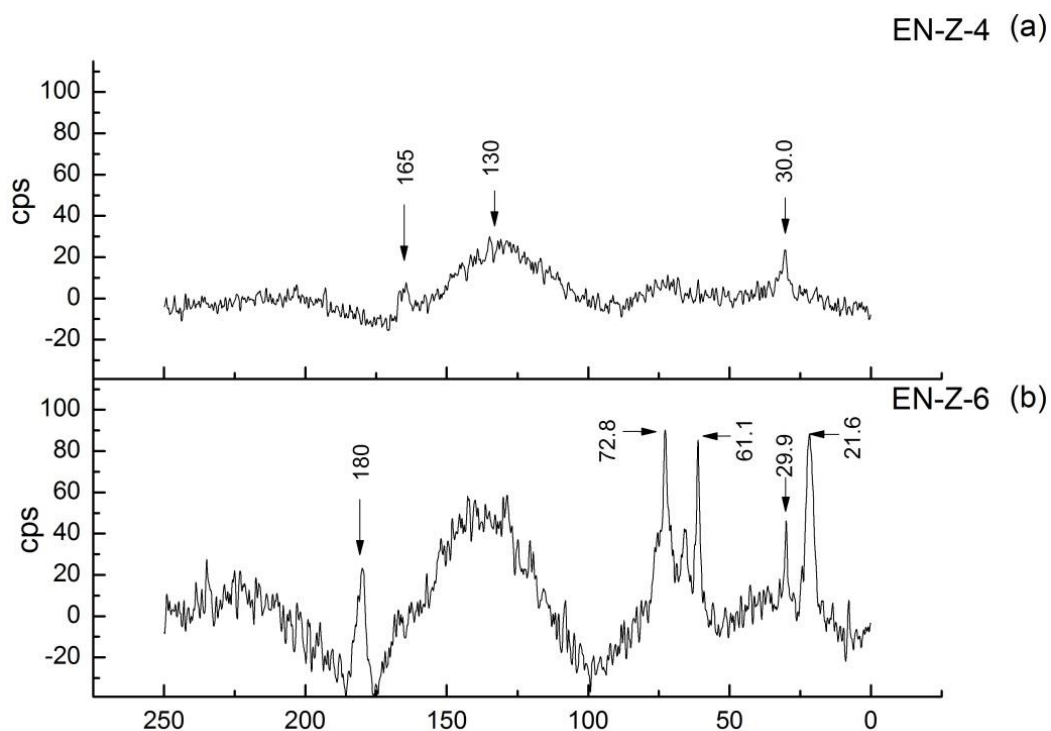


**Figure 5-24** The  $^{13}\text{C}$  NMR spectra for (a) EN-Z-4 and (b) EN-Z-6.

### 5.3.3 Nanoparticle Characterisation

The aforementioned techniques provide information with regard to the characteristics of the bulk and surface of the sample. In order to characterize the samples at the nanoparticle level, scanning electron microscopy (SEM), transmission electron microscopy (TEM) and dynamic light scattering techniques were employed.

#### 5.3.3.1 Scanning Electron Microscopy

Scanning electron microscope (SEM) images of EN-Z-4 and EN-Z-6 are presented in Figure 5-25 (a) and (b) respectively. Although the primary particles are discernible from the images, the sample is heavily agglomerated into sizes in the order of a few hundred nanometers, making it difficult to obtain an accurate distribution of primary particle size. Investigation of the samples by TEM is therefore required in order to obtain clearer definition of the primary particle sizes and morphologies.

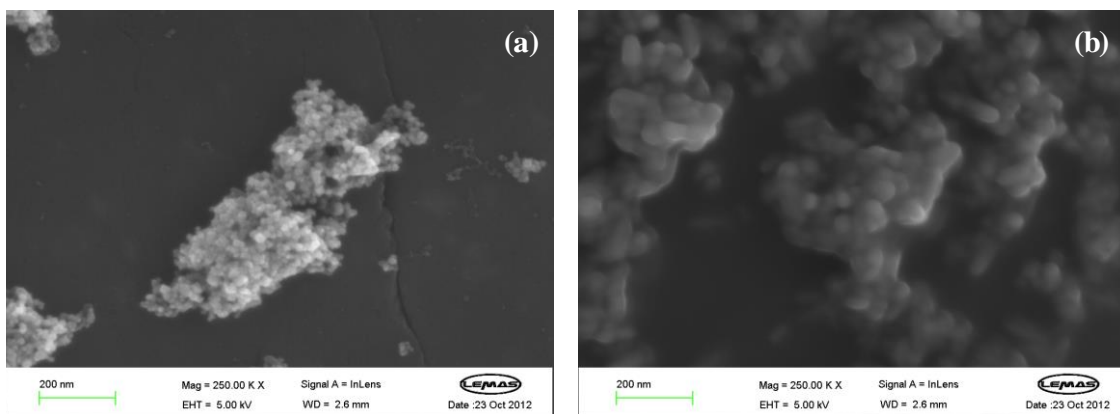


**Figure 5-25 SEM images of (a) EN-Z-4 and (b) EN-Z-6 synthesized ZnO NP samples.**

### 5.3.3.2 Transmission Electron Microscopy

Transmission electron microscope (TEM) images of clusters of the ZnO NPs in EN-Z-4 and EN-Z-6 are presented in Figure 5-26 (a) and Figure 5-27 (a) respectively. The widths and lengths of 250 particles from each sample were measured and the Feret ratio for each particle was calculated. The data are presented in histograms in Figure 5-26 (c) and Figure 5-27 (c) for EN-Z-4 and EN-Z-6 respectively. EN-Z-4 has an average particle length of  $23 \pm 8$  nm; width of  $14 \pm 4$  nm; and Feret ratio of  $1.6 \pm 0.4$ . These results indicate that the interparticle variation in size and morphology has a relatively narrow distribution and that the majority of the particles are elongated. EN-Z-6 has an average particle length of  $47 \pm 26$  nm; width of  $26 \pm 8$  nm; and Feret ratio of  $1.8 \pm 0.5$ . These results indicate that the distribution of particle size and morphology is wider than in the case of EN-Z-4 but still relatively narrow. Similarly with EN-Z-4, the particles present in the sample are predominantly elongated.

High resolution images of a single particle of EN-Z-4 and EN-Z-6 (outlined by a red box in Figure 5-26 (a) and Figure 5-27 (a)) are presented in Figure 5-26 (b) and Figure 5-27 (b) where the atomic planes are clearly discernible and are indexed to a single crystal of ZnO. The images confirm that the NPs in both samples are predominantly single crystal in nature. The indicated d-spacing of the planes

observed in the high resolution image of the EN-Z-4 particle (Figure 5-26 (c)) is 2.819 Å, which corresponds to the d-spacing of the  $\{10\bar{1}0\}$  planes of the ZnO crystal (JCP-DS ref: 01-079-0206). This indicates that the preferred direction of growth of the elongated ZnO particles is in a direction parallel to the  $\{10\bar{1}0\}$  planes, supporting the assumption that the ZnO NPs in this sample grow preferentially along the c-axis,  $\langle 0001 \rangle$ , as is typically observed with gas-phase synthesis techniques (Wang & Muhammed, 1999). The indicated d-spacing of the planes observed in the high resolution image of the EN-Z-6 particle (Figure 5-27 (c)) is 2.609 Å, which corresponds to the d-spacing of the  $\{0002\}$  planes of the ZnO crystal (JCP-DS ref: 01-079-0206). The particle imaged is equiaxial and therefore no preferred growth in any direction is observed for this particular particle.

The particle lengths and widths obtained by measurement from TEM images are in good agreement with those values reported for BET (Table 5-4) and XRD (Figure 5-5 (d) and Figure 5-9 (c)).

Selected area electron diffraction (SAED) patterns were obtained for the clusters of particles presented in Figure 5-26 (a) and Figure 5-27 (a) for EN-Z-4 and EN-Z-6 respectively. The SAED patterns are presented in Figure 5-26 (d) and Figure 5-27 (d) for EN-Z-4 and EN-Z-6 respectively. The d-spacings calculated from measurement of the ring diameters in the SAED patterns are reported in Table 5-11 are in good agreement with XRD data for Zincite (ref: 01-079-0206).

The energy dispersive X-ray (EDX) spectra obtained for EN-Z-4 and EN-Z-6 are presented in Figure 5-26 (e) and Figure 5-27 (e) respectively and confirm the presence of only zinc and oxygen in the samples. The copper peaks observed are from the copper grid bars on the TEM grid and also possibly from the sample holder. The carbon peaks present are mainly due to the holey carbon support film on the TEM grid.



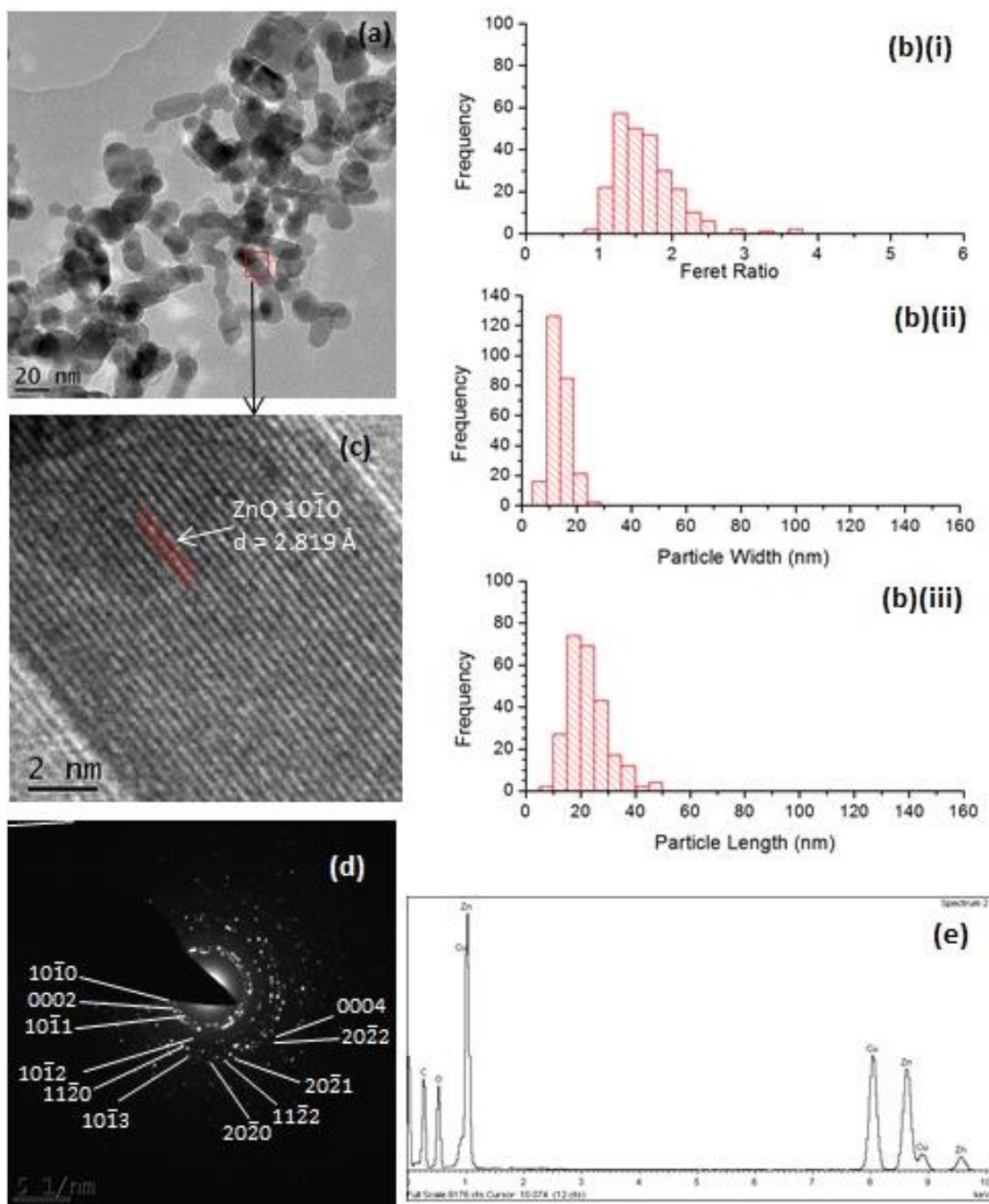


**Figure 5-26 (a) TEM image of a typical cluster of EN-Z-4 NPs (b) histograms to show the variation in particle length, width and Feret ratio. (c) Higher resolution image of a single particle showing crystal planes. (d) SAED pattern and (e) EDX spectrum obtained from the cluster of particles in (a).**

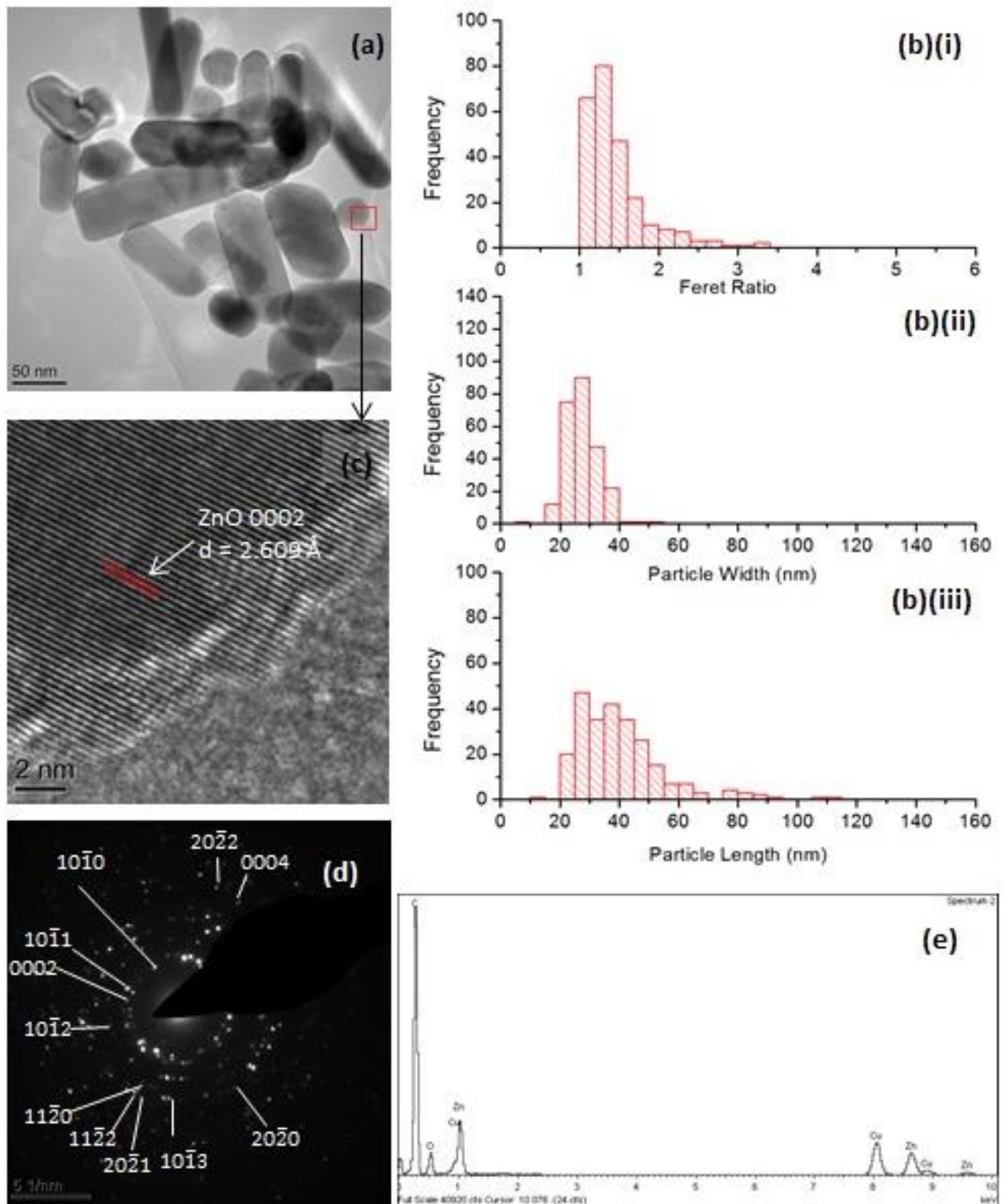


**Figure 5-27 (a) TEM image of a typical cluster of EN-Z-6 NPs (b) histograms to show the variation in particle length, width and Feret ratio. (c) Higher resolution image of a single particle showing crystal planes. (d) SAED pattern and (e) EDX spectrum obtained from the cluster of particles in (a).**

**Table 5-11 Table displaying the ring diameters and corresponding calculated d-spacings measured from SAED diffraction patterns of EN-Z-4 and EN-Z-6. Also displayed are the d-spacings for zincite extracted from the JCPDS reference file: 01-079-0206**

<i>hkl</i>	JCPDS Ref: 01-079-0206	FSP 18		Degsyn	
	d-spacing (Å)	Ring Diameter (1/nm)	d-spacing (Å)	Ring Diameter (1/nm)	d-spacing (Å)
10 $\bar{1}$ 0	2.815	7.10	2.818	7.12	2.809
0002	2.603	7.64	2.617	7.70	2.597
10 $\bar{1}$ 1	2.476	7.99	2.504	8.10	2.469
10 $\bar{1}$ 2	1.911	10.32	1.937	10.49	1.906
11 $\bar{2}$ 0	1.625	12.40	1.613	12.35	1.619
10 $\bar{1}$ 3	1.477	13.61	1.469	13.56	1.475
20 $\bar{2}$ 0	1.407	14.01	1.427	14.22	1.406
11 $\bar{2}$ 2	1.378	14.59	1.371	14.51	1.378
20 $\bar{2}$ 1	1.359	14.79	1.352	14.74	1.357
0004	1.302	15.32	1.305	15.40	1.299
20 $\bar{2}$ 2	1.238	16.06	1.245	16.18	1.236

### 5.3.3.3 Dynamic Light Scattering

Particle size distribution data obtained by DLS for EN-Z-4 and EN-Z-6 suspended in water at a concentration of 1000 µg/ml and a final solution pH of 7.8, are shown in Figure 5-28 (a) and (b) respectively.

Observation of the NP suspensions over time would suggest that EN-Z-6 has superior stability to EN-Z-4. EN-Z-6 does not appear to agglomerate and sediment for more than 48 hours, whereas EN-Z-4 begins to sediment and agglomerate after approximately 1 hour. This may be due to the residual DEG on the sample surface,

detected by TGA with EGA (Figure 5-15), FTIR (Figure 5-18), and XPS (Figure 5-22 (b)), acting as a stabilizing agent. Time dependent data for ZnO NP stability in water is presented in Chapter 6.

The light scattering profile of the suspension is converted into plots of intensity, volume and number using the instrumental software. The Rayleigh approximation states that the intensity of light scattered by a particle is proportional to the diameter of the particle ( $I \propto d^6$ ). The intensity profile for EN-Z-4 in Figure 5-28 (a) (red line) displays a modal peak at 1500 nm, a secondary peak at 185 nm and two smaller peaks at 550 and 5500 nm. The intensity plot shows the relative intensity of light scattered by each of the size groups. The volume profile for EN-Z-4 displayed on the same plot (Figure 5-28 (a)) (blue line) has a modal peak at 180 nm, a secondary peak at 1500 nm and two smaller peaks at 550 nm and 5500 nm. The volume plot is formed by conversion of the intensity profile using Mie theory which takes into account the greater relative scattering of the larger particles compared to the small (Malvern 2000) and hence explains the switch between the relative size of modal and secondary peaks. The number profile for EN-Z-4 (Figure 5-28 (a)) (black line) is derived from the volume plot and displays the relative percentage of particles in each size class. The number plot displays the narrowest particle size distribution, however as it is derived using a mathematical approximation, it is not necessarily the most accurate. The plot has a principal peak at 160 nm indicating that the majority of the NPs (with an average primary particle size of 18 nm) in the suspension are agglomerated into clusters of particles. The secondary peak at 500 nm accounts for a much smaller fraction of larger agglomerates present in the suspension. Although the number profile indicates that the majority of the agglomerates present in the sample are below 800 nm, it does not show the extremely low fraction of agglomerates present that are greater than 1000 nm in hydrodynamic diameter, as shown by the intensity and volume plots.

The light scattering profiles for EN-Z-6 are presented in Figure 5-28 (b). The intensity profile (red line) has a peak maximum at 170 nm which reduces to 160 nm in the volume profile (blue line). The number profile (black line) indicates that the size of the particles in the sample range between 65 and 200 nm in diameter with the majority of the particles around 110 nm in diameter. Comparing this to the average

particle size obtained by TEM measurements of  $47 \pm 26$  nm (Figure 5-27 (a)), it can be concluded that although the majority of the particles are agglomerated into small clusters of particles there are also likely to be isolated primary particles in the suspension.

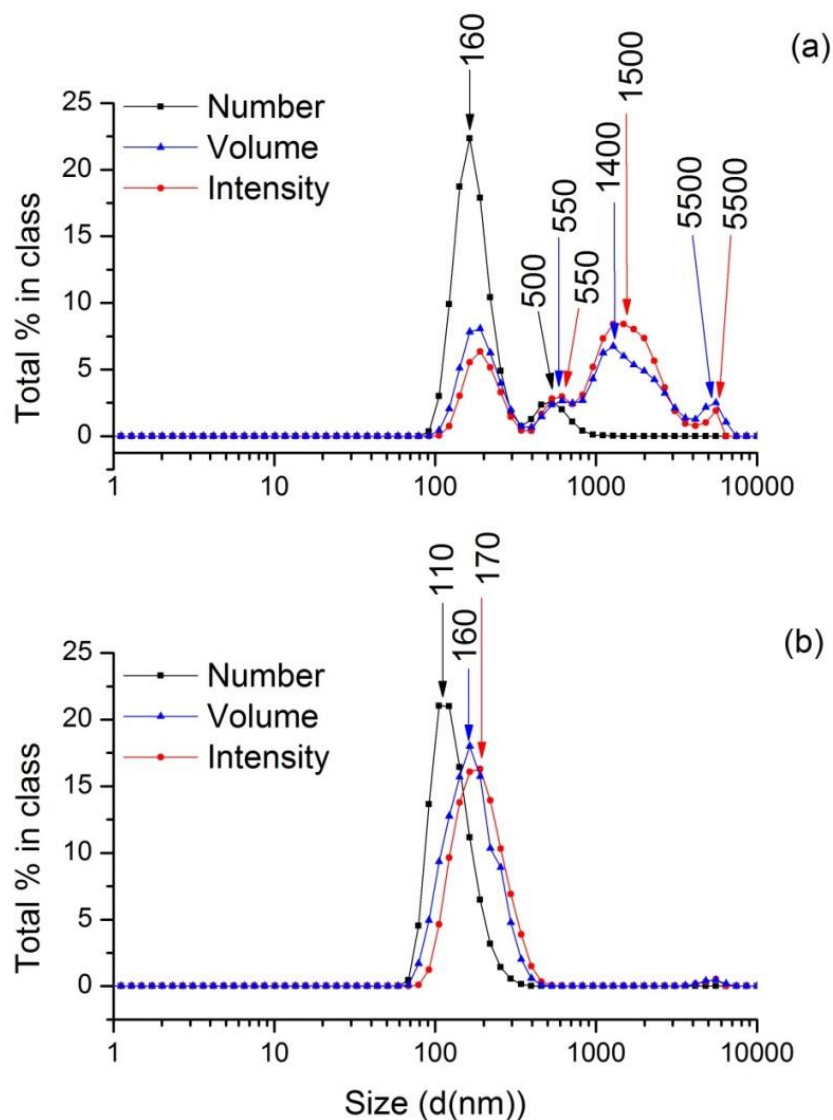


**Figure 5-28 DLS profile for (a) EN-Z-4 and (b) EN-Z-6 ZnO suspensions in water at a concentration of 1000  $\mu\text{g/ml}$  taken immediately after ultrasonication for 20 minutes. The intensity profile is shown in red, the profile converted to volume is shown in blue and the number profile is shown in black.**

The DLS measurements were taken immediately after the sample was removed from the ultrasonic bath and are therefore not an indication of how well the particles are dispersed as time progresses. The tendency of the particles to agglomerate may be explained by the solution pH of 7.8 which is relatively close to the isoelectric point of ZnO which is approximately pH 9 (Degen and Kosec, 2000; Bang et al., 2006).

Particle stability must be taken into account in toxicological assays which invariably take place in biological media such as Dulbecco's modified eagle medium (DMEM). The degree of particle agglomeration in suspensions will be affected by the dispersing medium i.e. the presence of salts and protein serum can affect NP stability. The results of investigations into the stability of the ZnO NP samples in DMEM are reported in Chapter 6. In addition to the NPs agglomeration behaviour, the solubility of the NPs at varying solution concentrations is also investigated.

#### **5.4 Summary**

ZnO NP samples have been synthesized by a flame spray pyrolysis technique and by a polyol route. ZnO NP samples with varying particle sizes were synthesized via the polyol route by altering the concentration of the ZnAc precursor. Increasing the concentration of ZnAc was found to increase the size of the ZnO crystallites obtained, while at the same time decreasing the tendency of the crystallites produced to agglomerate into spherical clusters. The reproducibility and scalability of the method was investigated. Repeats of experimental conditions did not always yield particles with the same size and morphological characteristics, demonstrating the sensitivity of the technique to unintentional small changes in reaction conditions, such as temperature fluctuations. It was determined that heterogeneous heating of the sample, as a result of employing a different hotplate for the repeat experiments resulted in polydisperse ZnO NPs, as compared to the original synthesis experiments for Degrain-0.15-100-1, Degrain-0.45-100-1 and Degrain-0.90-100-1. A sample with an average particle length of  $47 \pm 26$  nm was selected to put forward to toxicological investigations and was analyzed in detail using the characterisation protocol.

The size of the NPs produced was altered in the FSP route by varying the rate of flow of the precursor solution to the flame and changing the zinc precursor and

solvent. Increasing the rate of flow of the precursor solution to the flame from 1-5 ml/min increased the average size ( $d_{\text{BET}}$ ) of the NPs obtained from 11 to 18 nm, in good agreement with particles synthesized by Tani et al. (2002). The sample with a  $d_{\text{BET}}$  of 18 nm was selected to put forward to toxicological investigations and was therefore characterized using the protocol.

The FSP sample (EN-Z-4) has a narrow particle size distribution, measured from TEM (Figure 5-26) with an average particle length of  $23 \pm 8$  nm; width of  $14 \pm 4$  nm; and Feret ratio of  $1.6 \pm 0.4$ . The sample prepared by polyol route (EN-Z-6) has a somewhat wider distribution (Figure 5-27) with an average particle length of  $47 \pm 26$  nm; width of  $26 \pm 8$  nm; and Feret ratio of  $1.8 \pm 0.5$ . EN-Z-4 and EN-Z-6 synthesized samples both comprise monophasic wurtzite ZnO as determined by XRD (Figure 5-5 (d) and Figure 5-9 (c) respectively). Residual precursor was detected on the surface of the synthesized samples by TGA with EGA (Figure 5-14 and Figure 5-15), FTIR (Figure 5-16 and Figure 5-18), XPS (Figure 5-22), however the amounts detected were extremely small, especially when compared to the coating on EN-Z-1. As well as the residual precursor impurities detected, physically and chemically adsorbed  $\text{CO}_2$  and  $\text{H}_2\text{O}$  was identified at the surface of the synthesized samples, which was also present at the surface of commercial samples. EN-Z-6 has a greater stability in water compared to EN-Z-4, remaining in suspension for more than 48 hours compared with approximately 1 hour. EN-Z-6 remains stable for long enough that it will not agglomerate during an acute toxicity assay (i.e. a maximum time of 48 hours).

Comparing all 5 of the ZnO NP samples investigated in this thesis, EN-Z-4 has the narrowest distribution of particle sizes. EN-Z-6 has a narrower distribution than EN-Z-1 but is more polydisperse than EN-Z-3 and EN-Z-2. Synthesized ZnO NPs have higher purity than commercial samples. EN-Z-2 and EN-Z-3 commercial samples were found to contain a secondary phase of hydrozincite (Figure 4-2). EN-Z-1 dispersion is superior; however an unidentified aliphatic polyether coating is present on the particle surface.

In final summary, both of the samples synthesized in house have specific characteristics that are superior to the commercially available samples. The samples are monophasic ZnO and more information is known regarding the impurities on the surface of the particles, as well as smaller quantities being present. EN-Z-4 has the narrowest particle size distribution compared to the other samples and EN-Z-6 has greater stability than the other powders obtained.

The carbonate / hydroxide layer detected at the surface of the NPs in all five of the investigated samples may alter the weight of the samples resulting in an underestimated dose of ZnO being delivered to the toxicity assays. In addition, the impurities could significantly affect the chemical and physical properties such as their solubility which is known to affect ZnO toxicity (Xia et al., 2008; Reed et al, 2012).

In order to gain a comprehensive understanding of the state of the NPs when administered to the toxicity assays, it was essential to characterise their agglomeration behaviour and solubility in biological media. The results of these investigations are presented in Chapter 6.



## 6 Dispersion and Solubility of Zinc Oxide Nanoparticles in Solution

In order to administer ZnO NPs for toxicity assays, dispersion in a liquid medium is required. The *in vitro* assays carried out in this investigation use a cell culture solution called Dulbecco's Modified Eagle Medium (DMEM). This medium provides the cells with the nutrients required to remain viable. It is therefore essential to investigate NP characteristics, such as agglomeration and solubility, when suspended in DMEM. Cell culture media is often supplemented with serum proteins such as foetal calf serum (FCS) or bovine serum albumin (BSA) in cell in order to maintain the viability of the cells. Although the toxicity experiments reported in this investigation used serum free media, as a point of interest, the effect of the addition of BSA to DMEM on the agglomeration and solubility of the ZnO NP suspensions was also investigated.

With the exception of EN-Z-1, all samples were dispatched to the consortium members in the ENNSATOX project as 1000 µg/ml ZnO suspensions in MilliQ water. EN-Z-1 was sent out in the form it was received from the commercial supplier, which was as a  $4 \times 10^5$  µg/ml colloidal suspension in water. Therefore it was important to characterise the behaviour of the NPs in water as well as DMEM.

The dispersion of the commercial and synthesized ZnO NPs when suspended in MilliQ water is reported in Chapters 4 (Figure 4-19) and 5 (Figure 5-28) respectively, as determined by the dynamic light scattering (DLS) technique. The results indicate that all of the powder samples are not particularly stable over time, however there is no quantification of stability. A more extensive investigation of the dispersion and solubility characteristics of the ZnO samples in MilliQ water, DMEM and DMEM-BSA was carried out and the results are presented in this chapter. The magnitude of the charge on the NPs surface was determined by zeta potential measurements. Due to limitations associated with DLS, an alternative method of determining the size distribution of the agglomerates present in polydisperse, low NP concentration samples was investigated. The technique involves the plunge freezing of the sample on a TEM grid, warming under vacuum and then imaging in a conventional TEM (Hondow et al., 2012; Wallace et al., 2012). The solubility of

ZnO NP samples in water, DMEM and DMEM-BSA was determined by separating the NPs from the dispersion via ultracentrifugation at 14,500 rpm (14,100 x g) and then measuring the dissolved zinc concentration in a known volume of supernatant using inductively coupled plasma mass spectrometry (ICP-MS).

### **6.1 Solubility of ZnO Nanoparticles**

The equilibrium solubility of ZnO in water is highly pH dependent and is reported to range from >1000 µg/ml at pH 6 to 1 µg/ml at pH 8 (Stumm & Morgan 1995). Franklin et al. (2007) measured a stable equilibrium solubility level for ZnO in water at pH 7.6 and 24 °C, equivalent to the complete dissolution of 20 µg/ml ZnO (16 µg/ml Zn). The medium in which ZnO NPs are suspended will also affect the equilibrium solubility. For example, Song et al. (2010) and Xia et al. (2008) reported that suspensions of ZnO NPs in DMEM at 37 °C, tended to equilibrium when the concentration of dissolved ZnO reached 12.4 and 18.3 µg/ml respectively. Temperature can also affect equilibrium solubility for ZnO NP suspensions. For example Reed et al (2012) showed a lower ZnO solubility in DMEM at 37 °C as compared to at 20 °C, where the concentration of dissolved ZnO measured increased from 8.75 µg/ml (7 µg/ml Zn) to 16.25 µg/ml (13 µg/ml Zn) respectively. Chemical equilibrium modelling (Visual Minteq) predicts that less-soluble zinc hydrocarbonate (hydrozincite) and zinc phosphate hydrate (hopeite) will re-precipitate in moderately hard water and Roswell Park Memorial Institute (RPMI) cell culture medium respectively. This was verified experimentally by Reed et al. (2012) for solutions of ZnO NPs and by Turney et al. (2012) for soluble zinc salts in RPMI. For ZnO NP suspensions in DMEM (with and without BSA) Reed et al. also reported a rising Zn concentration in solution over time (1400 hrs), accompanied by a decreasing pH. The findings reported in the literature emphasize the variability of ZnO equilibrium solubility with solution characteristics such as composition, pH and temperature and highlight the importance of characterising ZnO NP suspensions used in toxicological investigations in a controlled environment.

In this section, dissolution kinetics of the ZnO NP samples are investigated. As well as this, the effect of the medium and the temperature of the medium on the equilibrium solubility of the sample are investigated. The pH of the solutions was

monitored as this too can affect solubility. Furthermore, the effect of increasing ZnO NP concentration on the amount of zinc in solution is investigated.

### **6.1.1 Dissolution of ZnO Nanoparticles in Varying Media**

In order to investigate ZnO dissolution in the medium in which the NPs are suspended, the solubility of the 5 ZnO samples was characterised in H<sub>2</sub>O and DMEM. The effect on the solubility when BSA was added to the suspensions at a concentration of 10 % w/w was also investigated. Toxicological investigations using cells are typically carried out at 37°C, therefore the solubility experiments for DMEM and H<sub>2</sub>O were carried out at both 37 °C and 21°C in order to investigate the effect of varying the temperature. The samples were prepared at a concentration of 100 µg/ml and stored for 24 hours in sealed vials before separating out the NPs by centrifugation (36 minutes at 14500 rpm) and analysing the supernatant using ICP-MS.

The zinc concentration obtained from the ICP-MS measurement was converted into a concentration of ZnO in µg/ml. The results are presented in Figure 6-1 and indicate that ZnO solubility is diminished at elevated temperature when suspended in both water and in DMEM. The concentration of dissolved ZnO measured, and increase in solubility observed with decreasing temperature is in agreement with findings reported by Reed et al. (2012).

The results indicate that for all samples, the dissolution of ZnO is greater in DMEM than in H<sub>2</sub>O. This is consistent with the results of similar studies reported in the literature (Reed et al., 2012). The EN-Z-1 sample, suspected to have a lower solubility than the other samples did not exhibit comparatively lower concentrations of dissolved ZnO. Therefore further investigation was required in order to obtain conclusive results. The addition of BSA to the suspension does not appear to significantly impact on the solubility of the ZnO NPs.

The error in the measured Zn concentration is approximately 2.5 % occurring as a result of inaccuracy of the ICP-MS instrument. However, this error may be overlooked when taking into account the error that might arise from variability in the actual concentration of ZnO in the suspensions compared to the nominal concentration. In the following section (6.1.2), it is determined that the error in the

total mass of ZnO in a suspension for EN-Z-1 is approximately 35 % and for the remaining 4 samples is approximately 20 % (Table 6-1). The differences in ZnO dissolution in water and DMEM, and at different temperatures, even when taking the percentage errors into consideration are still significant. However, the changes in ZnO solubility when DMEM is supplemented with BSA are very small and therefore do not present significant findings.

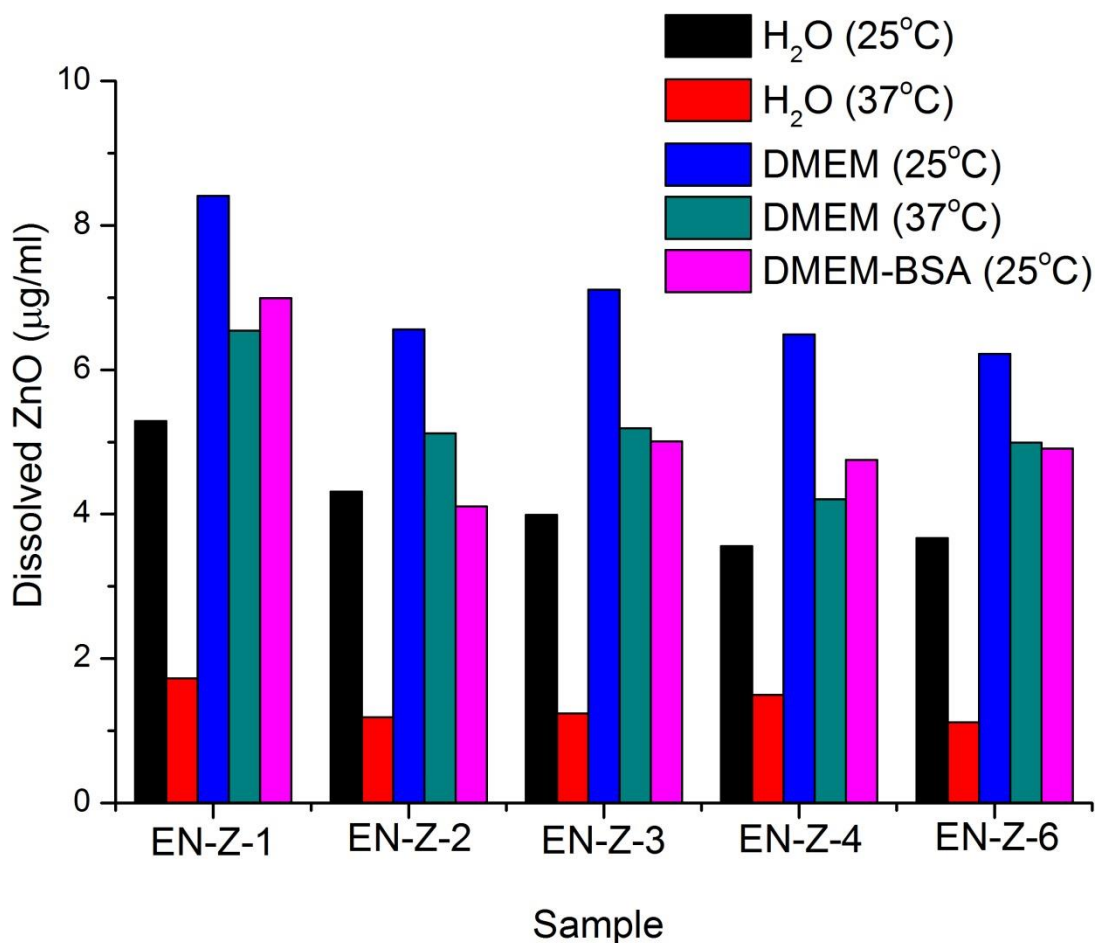


**Figure 6-1** Chart illustrating the effect of the type of media and the temperature on the dissolution of ZnO. Samples were suspended in both water and in DMEM at 25°C and at 37°C for 24 hrs. The solubility of ZnO in a solution of DMEM and BSA at 25°C is also reported. Concentration of Zn in solution was measured by ICP-MS.

### 6.1.2 ZnO Dissolution Kinetics and Equilibrium Solubility

In order to gain a more comprehensive understanding of ZnO NP dissolution characteristics, the solubility of the samples over time and at varying ZnO concentrations was investigated.

In order to replicate the suspensions administered to the cells, stock suspensions of the samples were prepared in MilliQ water at the relevant concentrations and allowed to equilibrate for 48 hour. The concentration of the EN-Z-1 stock is  $4 \times 10^5$   $\mu\text{g/ml}$  whereas the concentration of the other 4 samples' stock suspensions was 1000  $\mu\text{g/ml}$ . Immediately prior to the experiment, a 1000  $\mu\text{g/ml}$  stock suspension of EN-Z-1 was prepared. Serial dilutions of the stocks were carried out to make concentrations of 100, 30, 10, 3 and 1  $\mu\text{g/ml}$ . In order to ascertain the degree of variability between the aliquots taken from the stocks to prepare the serial dilutions, a 100  $\mu\text{l}$  volume of each stock solution was digested in acid and analysed by ICP-MS to measure the total concentration of ZnO. The results are reported in Table 6-1 and indicate that there is a relatively large amount of variation in the amount of ZnO measured in each aliquot. The measured concentration of ZnO in the EN-Z-1 sample is significantly higher than 1000  $\mu\text{g/ml}$  for all 3 of the aliquots analysed, with an average value of 1440  $\mu\text{g/ml}$ . The standard deviation of the measurements is more than half the nominal concentration at 520  $\mu\text{g/ml}$ . As this sample is purchased as a colloidal dispersion, this may suggest that the concentration quoted by the supplier is inaccurate. Alternatively, the discrepancies may occur as a result of the sample preparation. Prior to the aliquots being taken, the EN-Z-1 sample was only very recently diluted to a nominal concentration of 1000  $\mu\text{g/ml}$  from its original nominal concentration of  $4 \times 10^5$   $\mu\text{g/ml}$ . This will mean that there will be a higher concentration of undissolved ZnO, than will be present in the other 4 ZnO samples. Particles and small agglomerates of ZnO present in the 1000  $\mu\text{g/ml}$  stock suspension of EN-Z-1 will cause greater fluctuations in the concentration than dissolved species and hence the large variation in ZnO concentrations for the 3 measured aliquots of EN-Z-1 may be explained.

The average ZnO concentration and standard deviation for the 3 measured aliquots of EN-Z-2, EN-Z-3, EN-Z-4 and EN-Z-6 is  $850 \pm 120$   $\mu\text{g/ml}$ ,  $900 \pm 170$   $\mu\text{g/ml}$ ,  $850 \pm 180$   $\mu\text{g/ml}$  and  $830 \pm 120$   $\mu\text{g/ml}$  respectively. The average actual

concentration values measured for these 4 samples are consistently lower than the desired nominal concentrations. This may have arisen due to inaccurate weighing of the powder prior to making up the stock. Alternatively, due to the very fine nature of the powder, a loss of material may be occurring when transferring the weighed ZnO nanopowder to the stock container. Furthermore, the presence of carbonates on the surface of the samples, as well as the adsorbed moisture detected in all of the samples (by TGA with EGA, FTIR and XPS in sections 4.2 and 5.3 respectively) will marginally affect the weight of the sample.

To determine the rate of ZnO dissolution, a series of time intervals were selected to investigate: 0.6, 1.6, 4, 10, 24 and 48 hour. At these time points, 2 mls of each suspension was removed from vials in which the dispersed ZnO was sealed, particles were then separated from the solution by centrifugation at 14,500 rpm for 36 mins and the supernatant analysed by ICP-MS for soluble Zn.

The results reported in Table 6-1 indicate a large degree of variation in the actual ZnO concentration measured for suspensions with the same nominal ZnO concentration. Therefore for each of the ZnO samples, the actual concentration of ZnO was measured for suspensions at all of the nominal concentrations of ZnO investigated. As for the 1000 µg/ml nominal concentration, this was achieved by sampling a 100 µl volume from each suspension, dissolving all solid material by adding HNO<sub>3</sub> and then analysing by ICP-MS. The results of the analysis are presented in Table 6-2. The actual ZnO concentrations measured for the EN-Z-1 sample are higher than the nominal concentrations, whereas this is opposite for the other samples. These results can be explained by the concentrations of the corresponding stock solutions from which the serial dilutions were prepared.

The actual concentrations measured for each of the suspensions and the measured concentration of dissolved ZnO for the samples were both used to calculate the percentage of dissolved ZnO in each sample. Graphs displaying the percentage of dissolved ZnO compared with the actual concentration of ZnO in the sample, at each of the investigated time points, are presented in Figure 6-2. After 0.6 hour (Figure 6-2 (a)), the results indicate that EN-Z-1 is significantly less dissolved than the other 4 samples. For all concentrations of EN-Z-1 the amount of dissolved ZnO is less than 20 %. For the remaining 4 samples, the amount of dissolved ZnO is between 50 and

80 % for suspensions with nominal concentrations 1, 3 and 10  $\mu\text{g/ml}$ . With the exception of EN-Z-1, the percentage of dissolved ZnO drops significantly for all samples between 10 and 30  $\mu\text{g/ml}$ . For samples with a nominal concentration of 100  $\mu\text{g/ml}$ , the percentage of dissolved ZnO is between 10 and 20 % which is comparable with the values measured at 30  $\mu\text{g/ml}$ ; the exception is EN-Z-1 where only 7 % ZnO has dissolved in the 100  $\mu\text{g/ml}$  sample, however the actual concentration of ZnO in this sample is greater than the other 4 samples (Table 6-2) and therefore the absolute amount of dissolved ZnO is relatively similar. This may be due in part to the more recent dilution of 'as-received' EN-Z-1 to the stock concentration of 1000  $\mu\text{g/ml}$  as compared to the other samples. The solution would not have had the chance to equilibrate and would therefore have a larger than expected solid fraction of ZnO remaining.

The percentage of ZnO in solution for each sample after 1.6, 4 and 10 hour is presented in Figure 6-2 (b), Figure 6-2 (c) and Figure 6-2 (d) respectively. The solubility of EN-Z-1 after these times is more comparable with the other samples than for the 0.6 hr time point indicating that the initial difference was a result of EN-Z-1 having not yet reached equilibrium. This is consistent with investigations by David et al. (2012), who report that the kinetics of ZnO NP dissolution are on the order of a few hours. Furthermore the coating present in EN-Z-1 may slow the dissolution of the ZnO NPs in the sample further, as compared to the other uncoated samples, as has been previously been shown for EN-Z-1 by our group of scientists on the ENNSATOX project (Mu et al., 2013). Figure 6-2 (e) shows the percentage of ZnO in solution after 24 hour. This point was of major interest as the investigations determining the agglomerate size distributions, discussed in the following section (6.2), were carried out after 24 hour. The results presented in Figure 6-2 (e) indicate that for all ZnO NP samples, at all concentrations, a mixture of NPs and dissolved zinc is exposed to the cells. Although there is a smaller percentage of Zn in solution for EN-Z-1 (27 %) as compared to the other samples (from 35% to 40 %), the absolute level of dissolved Zn is approximately constant at around 5  $\mu\text{g ZnO/ml}$ , indicating the equilibrium solubility has been reached.

**Table 6-1 Table showing the actual concentration of ZnO suspended in DMEM at a nominal concentration of 1000 µg ZnO/ml. Quantities are determined by measurement of the zinc concentration by ICP-MS. The degree of variation occurring as a result of the inhomogeneity of the suspensions is reported by measuring 3 samples of the same concentration.**

Run	Nominal ZnO Concentration (µg/ml)	EN-Z-1		EN-Z-2		EN-Z-3		EN-Z-4		EN-Z-6	
		Actual ZnO Concentration (µg/ml)	Standard Deviation	Actual ZnO Concentration (µg/ml)	Standard Deviation	Actual ZnO Concentration (µg/ml)	Standard Deviation	Actual ZnO Concentration (µg/ml)	Standard Deviation	Actual ZnO Concentration (µg/ml)	Standard Deviation
1	1000	1197		975		815		653		710	
2	1000	1080	520	740	120	794	170	1010	180	816	120
3	1000	2040		835		1095		873		951	

**Table 6-2 Table showing the actual concentration of ZnO measured in suspensions of ZnO in DMEM with nominal concentrations of 1, 3, 10, 30 and 100 µg/ml. Quantities were obtained by measurement of the zinc concentration by ICP-MS.**

Nominal ZnO Concentration (µg/ml)	Actual ZnO Concentration (µg/ml)				
	EN-Z-1	EN-Z-2	EN-Z-3	EN-Z-4	EN-Z-6
1	4.71	0.89	1.15	1.48	0.94
3	11.30	4.21	2.63	2.51	2.40
10	18.67	12.76	12.51	6.87	8.09
30	58.25	32.55	41.82	23.77	31.80
100	138.16	68.46	85.89	93.98	79.16



However at shorter sampling intervals, far higher relative concentrations of dissolved ZnO are reported for EN-Z-2, EN-Z-3, EN-Z-4 and EN-Z-6 however for EN-Z-1 the highest percentage of ZnO measured to be in solution is 35 %. This means that a smaller quantity of zinc is precipitating out from solution as the suspensions age for EN-Z-1 than for the other samples. Other solid zinc compounds can precipitate out as the dissolution of ZnO proceeds, such as hydrozincite, zinc carbonate and hopeite have been observed (Reed et al. 2012; Turney et al., 2012). Figure 6-2 (f) shows the percentage of ZnO in solution after 48 hour. The amount of dissolved zinc after 48 hour can be seen to have decreased significantly from the 24 hr samples. Even for the suspensions with nominal concentrations of 1  $\mu\text{g/ml}$ , less than 30 % of the ZnO in all of the samples has dissolved.

An alternative representation of the data reported in Figure 6-2 is presented in Figure 6-3 and displays the percentage of ZnO in solution for all 5 ZnO samples with respect to time. The lower solubility and slower dissolution kinetics of EN-Z-1 compared to the other samples is more obvious. For example in Figure 6-3 (a) where the percentage of dissolved ZnO for 1  $\mu\text{g/ml}$  over time is presented, EN-Z-1 is lower than the other ZnO samples for the entire 48 hour sampling period. Similarly for 3 and 10  $\mu\text{g/ml}$  suspensions of ZnO displayed in Figure 6-3 (b) and (c) respectively, comparable concentrations of dissolved ZnO are not observed in EN-Z-1 as to the other four samples, until 48 and 10 hours respectively. Furthermore, Figure 6-3 displays more clearly the observed decrease in ZnO solubility for all samples over time, with the exception of EN-Z-1. The decrease in solubility of ZnO in DMEM with increasing age is contradictory to findings reported in the literature. Reed et al. (2012) found that the concentration of dissolved ZnO actually increased over time. The general trend in the decrease in solubility as the suspensions age in this investigation may be explained by the corresponding change in solution pH, which was recorded for all samples at each of the time points investigated. The pH at every time point, for all of the suspensions with nominal concentrations of 1, 3, 10, 30 and 100  $\mu\text{g/ml}$  are presented in Figure 6-4 (a), (b), (c), (d) and (e) respectively. In all 5 samples, over all concentrations, the pH was found to increase from approximately 7.5 to 8.5 over the 48 hour period. The reason for the pH increase is most probably due to the ambient level of exposure of  $\text{CO}_2$  to the DMEM suspensions. After each

sampling interval, the lids of the vials were removed and 2 mls of the suspensions were withdrawn in order to analyse and determine the concentration of zinc in solution by ICP-MS. Furthermore the lid remained off the vial in order to measure the pH which took approximately 2 minutes. In this time, the suspension was exposed to air and due to the reduction in the volume of the suspension in the vial, there was a greater volume of air trapped in the vial after the lid was replaced each time. The pH of DMEM will rise if the level of CO<sub>2</sub> falls below 5 % (Dontchos et al., 2008). The reason for this is reported by the manufacturer (Invitrogen). Sodium bicarbonate (NaHCO<sub>3</sub>) is present in DMEM in order to buffer the pH of the solution at approximately 7.4.

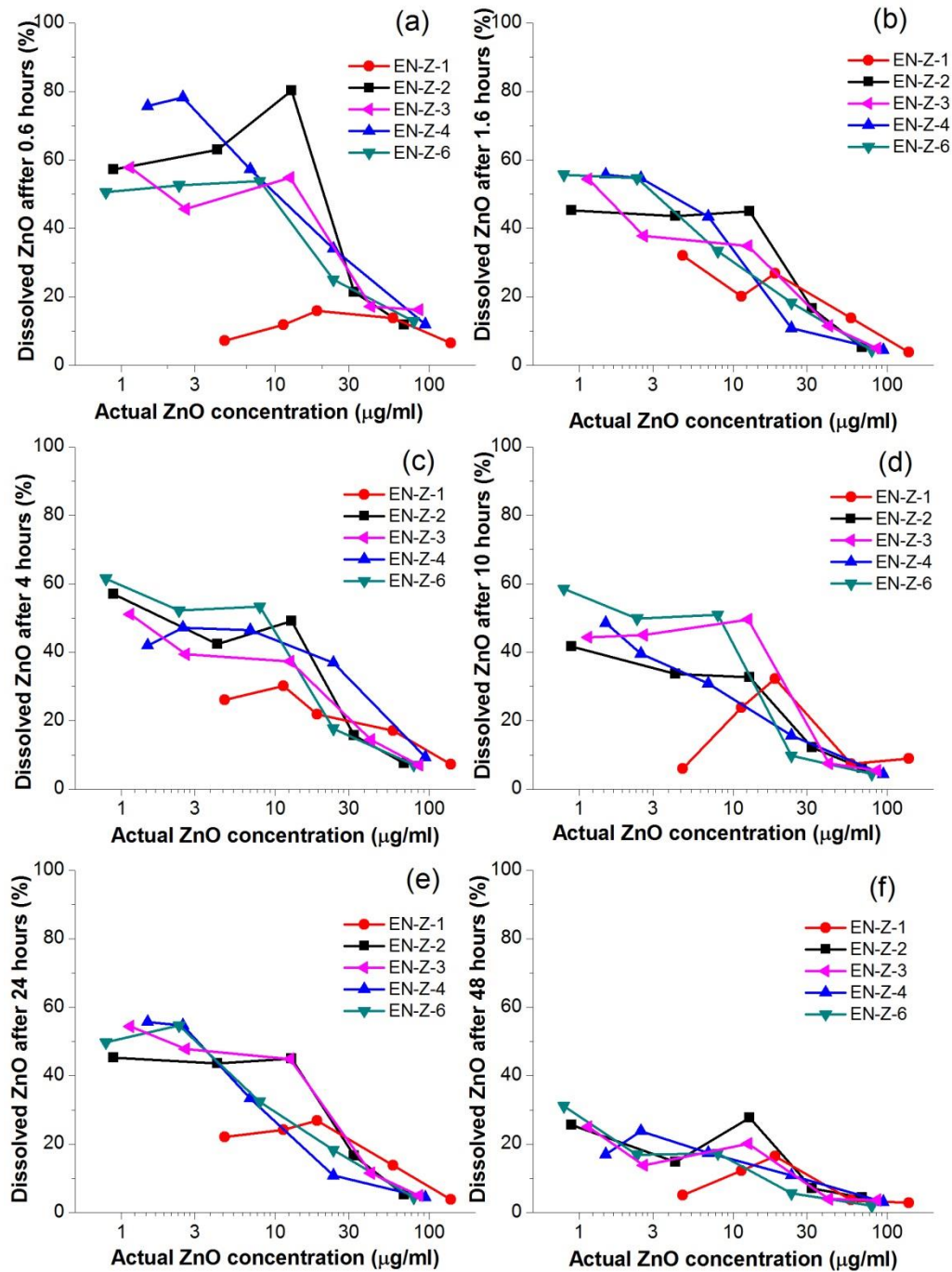


**Figure 6-2** Graphs showing the amount of ZnO that has dissolved into solution, expressed as a percentage of and plotted against the actual total concentration of ZnO in the suspension in DMEM at (a) 0.6, (b) 1.6, (c) 4, (d) 10, (e) 24, and (f) 48 hour.

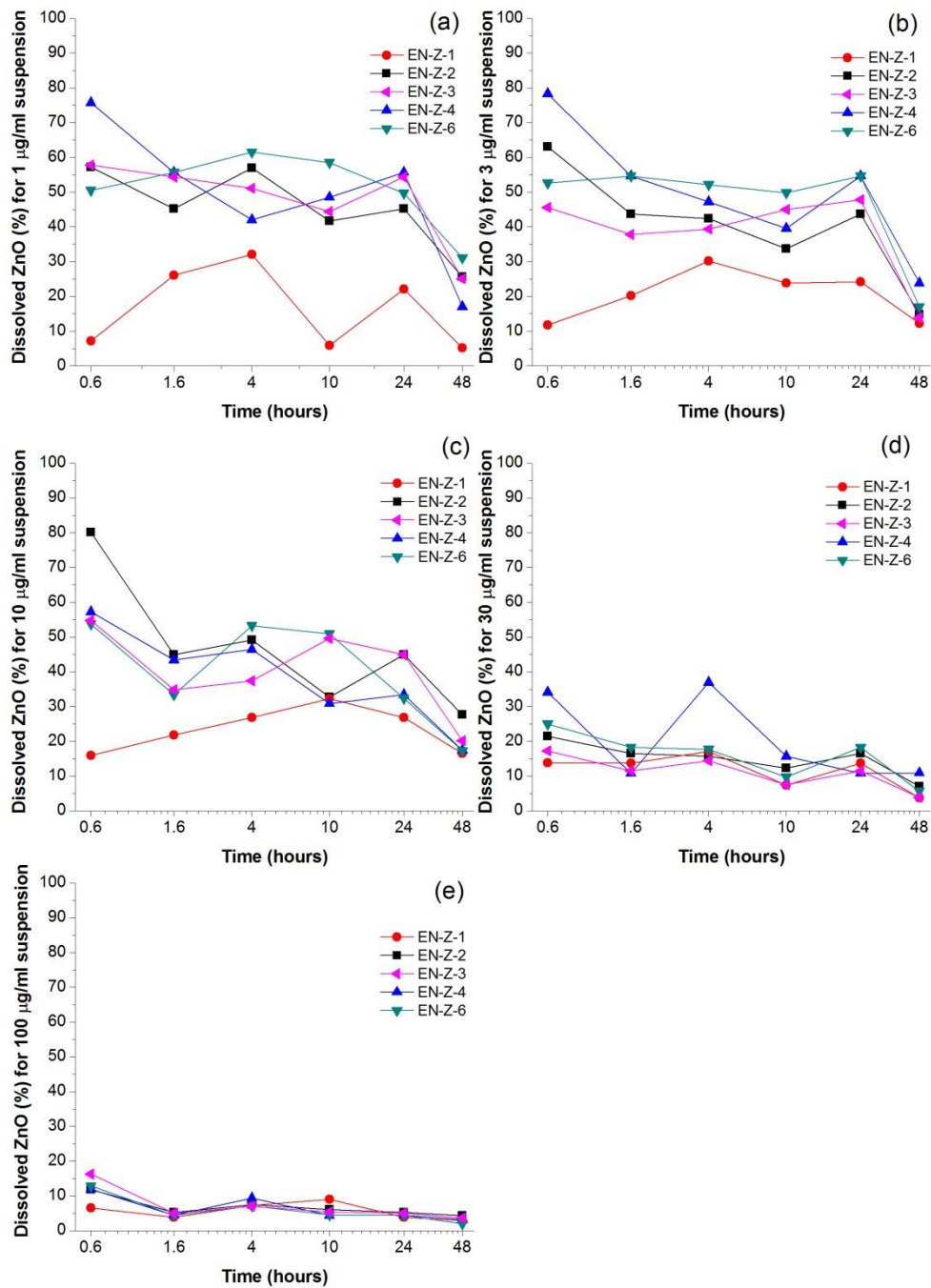


**Figure 6-3** Graphs showing the amount of ZnO that has dissolved into solution, expressed as a percentage of the actual ZnO concentration, plotted against time since sample preparation (hours) for solutions with nominal concentration (a) 1, (b) 3, (c) 10, (d) 30 and (e) 100 µg/ml. The absolute level of Zn in solution for the samples typically reaches a maximum of 9 µg ZnO/ml within 0.6 hour, with the exception of EN-Z-1 which reaches this value after 4 hours.

In order to maintain this pH, the concentration of  $\text{NaHCO}_3$  in the medium must be matched with the appropriate level of  $\text{CO}_2$  in the atmosphere above the medium. DMEM has been developed to buffer at physiological pH in 5-10 %  $\text{CO}_2$ . If  $\text{CO}_2$  levels are low, such as in this investigation, the level of  $\text{HCO}_3^-$  will be high and therefore the pH will become more alkaline.

In order to confirm that the ambient level of  $\text{CO}_2$  was responsible for the rise in pH, and not chemical reactions taking place due to the presence of ZnO NPs in the media, 3 blank samples of  $\text{NaHCO}_3$  buffered DMEM were treated to varying experimental conditions. 20 ml vials were filled to capacity with DMEM and stored for 48 hour at  $37^\circ\text{C}$ . For sample 1, the pH was recorded only at the beginning and the end of the experiment, with the vial remaining sealed for the duration. For sample 2, the lids were removed at each of the sampling intervals in order to monitor the pH. For sample 3, the lids were removed to measure the pH and a volume of 2 mls was removed from the vial at each of the sampling intervals. The results are presented in Figure 6-4 (f) and confirm that the observed rise in pH is due to the exposure of the suspension to ambient levels of  $\text{CO}_2$ .

For many of the samples at each of the time intervals investigated, there is a significant drop in the percentage of dissolved ZnO measured when the concentration is increased from 10 to 30  $\mu\text{g/ml}$ . This is indicative that the equilibrium solubility of ZnO is reached somewhere between these two concentrations. However, as a result of the rising pH measured throughout the experiment, the equilibrium solubility will not be constant (Stumm & Morgan 1995) At 24 hour, the concentration of ZnO in solution for all samples stabilizes at approximately 5  $\mu\text{g/ml}$ . This is lower than the dissolved equilibrium ZnO concentration reported in the literature for ZnO NPs suspended in DMEM at  $37^\circ\text{C}$  (values between 10 and 15  $\mu\text{g/ml}$ ), since here the pH at this point is 8 – 8.5, compared to in previous studies where  $\text{pH} < 7.6$  (Reed et al., 2012; Song et al., 2010). It has previously been shown that control of pH in near neutral solutions is extremely important, since a decrease of even 0.15 pH units from neutral pH leads to a doubling of the free Zn concentration of a suspension of ZnO NPs (David et al., 2012).

Unfortunately, the changing pH over the course of the experiment means that the 24 hour suspensions in the solubility experiments cannot be directly compared

with NP toxicity assays (because cell lines are buffered in 10% CO<sub>2</sub>) or the experiments investigating agglomerate size distributions by DLS and PF-TEM (because these solutions were stored in sealed vials). Therefore, we can only assume the pH of the suspensions will not have risen to the same extent as has been observed in the solubility experiments as the exposure to ambient levels of CO<sub>2</sub> is much lower (Figure 6-4 (e)). The solubility of ZnO is also unlikely to follow the trend reported by Reed et al. (2012), as in their experiment the pH decreases over time, indicating that the solutions they investigated were not correctly buffered. The ZnO solubility in the toxicity assays and agglomerate size distribution investigation experiments are more likely to follow a trend similar to that reported by our team of researchers on the ENNSATOX project (Mu et al., 2013). They found that up to 5.7 µg/ml of ZnO NPs fully dissolve in DMEM, while above this concentration, insoluble smithsonite (ZnCO<sub>3</sub>) is formed. This stable equilibrium was determined for ZnO NPs suspended in DMEM at 37 °C under 5% CO<sub>2</sub>/ 95% N<sub>2</sub> atmosphere at a pH of 7.68. They also investigated the solubility of EN-Z-1 and EN-Z-2 and found that EN-Z-1 did not reach equilibrium until > 48 hours, as compared to EN-Z-2 which reached equilibrium solubility within a few hours. This is presumed to be a result of the polymer coating present in EN-Z-1.

Therefore the ZnO NP suspensions in cellular exposures of 24 hours at concentrations below 5.7 µg/ml are likely to be administering only dissolved Zn. Above this concentration, suspensions will probably consist of a solid fraction of Zn (both re-precipitated zinc carbonate (and/or phosphate) particulates, and/or some ZnO NPs potentially with a ZnCO<sub>3</sub> coating).

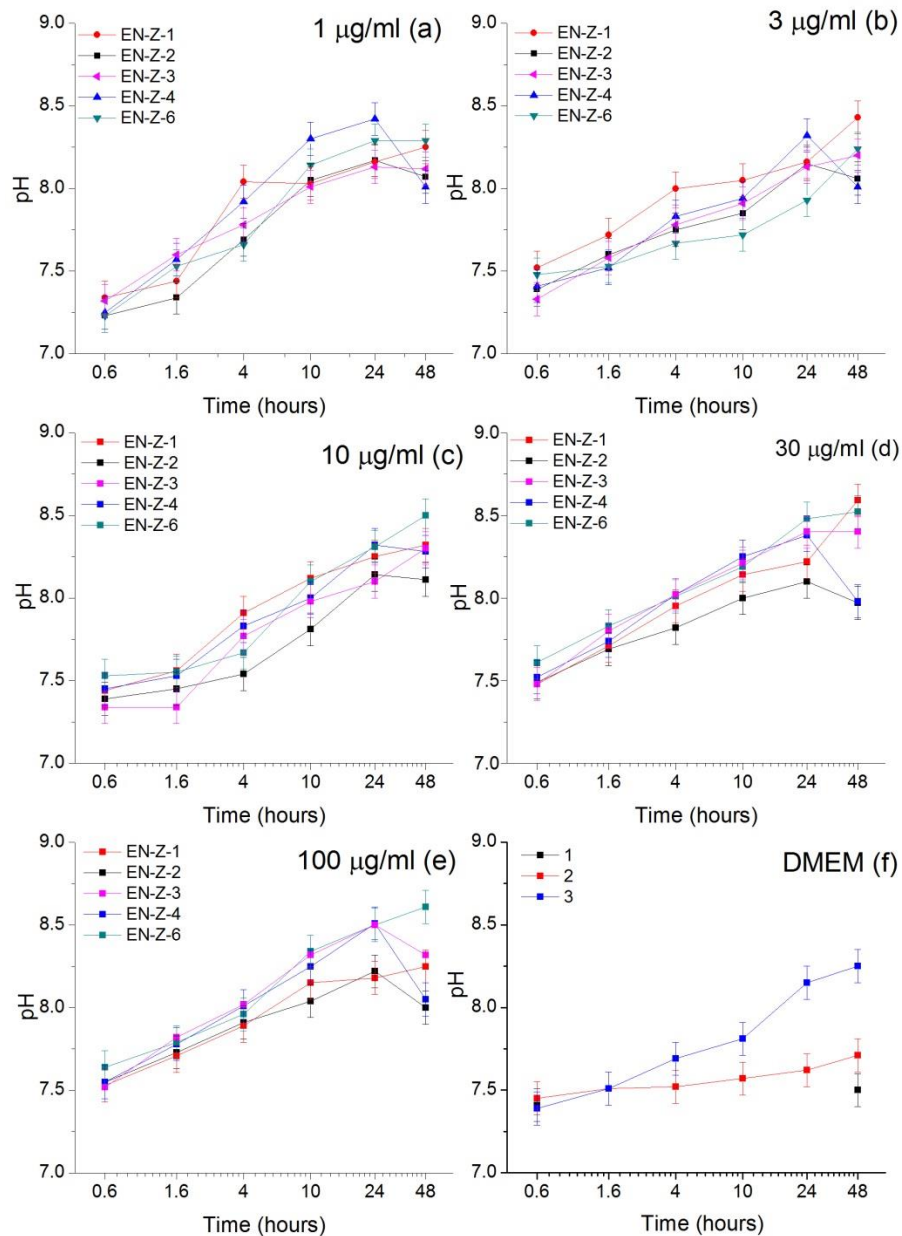


**Figure 6-4** Graphs showing the pH at increasing time points during the experiment (0.6, 1.6, 4, 10, 24 and 48 hour) for varying nominal concentrations of ZnO in DMEM, i.e. (a) 1 µg/ml, (b) 3 µg/ml, (c) 10 µg/ml, (d) 30 µg/ml, (e) 100 µg/ml. (f) Graph showing how the pH varies for blank DMEM samples where, (1) vials were sealed throughout the duration of the experiment (2) Lids were removed in order to measure the pH at each sampling interval and (3) Volume of 2 mls was removed and pH was measured at each of the sampling intervals. Error bars determined by reported accuracy of the pH meter which was  $\pm 0.1$  pH units.

## 6.2 Colloidal Stability of ZnO NPs in Suspension

Investigating NP stability in solutions is crucial as it provides information regarding the size of the particles and agglomerates being administered to the cells in the toxicity assays. Toxicity assays are carried out at a variety of ZnO NP concentrations and as such, the effect of concentration on ZnO NP colloidal stability was investigated. Furthermore, the effect of medium composition on ZnO NP colloidal stability was investigated. The dispersion of ZnO NP samples was investigated by zeta potential, dynamic light scattering (DLS) and plunge freezing transmission electron microscopy (PF-TEM) techniques.

Stock suspensions of EN-Z-2, EN-Z-3, EN-Z-4 and EN-Z-6 in MilliQ water were prepared at a concentration of 1000  $\mu\text{g/ml}$ , 72 hour prior to the stability investigations being carried out. A stock suspension of EN-Z-1 was prepared at a concentration of 1000  $\mu\text{g/ml}$ , immediately prior to the stability experiments being carried out.

### 6.2.1 Zeta Potential

The zeta potentials measured for each of the 5 ZnO NP samples are presented in Figure 6-5. The results indicate that EN-Z-1, EN-Z-4 and EN-Z-6 with zeta potentials of -14.3 and, +14.1 and -14.9 mV respectively, will have superior stability to EN-Z-2 and EN-Z-3 with zeta potentials of +5.2 and +8.5 mV respectively. A zeta potential of increased magnitude indicates greater dispersion stability because there is stronger coulombic repulsion between particles (hence reducing the tendency to agglomerate).

As well as the increased magnitude of the zeta potential measured for EN-Z-1 and EN-Z-6, the charge measured is the opposite of that measured for EN-Z-2, EN-Z-3 and EN-Z-4. This is likely to be characteristic of the coatings and impurities present on the surface of EN-Z-1 and EN-Z-6. An organic coating was detected on the surface of the ZnO NPs in the EN-Z-1 sample, by TGA with EGA (Figure 4-6), FTIR (Figure 4-9), XPS (Figure 4-13) and NMR (Figure 4-14). Residual DEG was identified on the surface of the ZnO NPs in the EN-Z-6 sample by TGA with EGA (Figure 5-15), FTIR (Figure 5-18), XPS (Figure 5-22) and NMR (Figure 5-24).



In order to investigate the effect of the medium composition on ZnO NP stability, ZnO NPs were suspended in DMEM and DMEM-BSA at a concentration of 100 µg/ml, with BSA at a concentration of 10 % w/w with respect to ZnO. However, owing to the high ionic strength of the DMEM, zeta potential measurements could not be obtained for these samples. Nevertheless, suspensions of ZnO NPs were prepared in MilliQ water at a concentration of 100 µg/ml supplemented with 10 % w/w BSA in order to investigate the effect of serum on the zeta potential of the particles. The results presented in Figure 6-6 show that the magnitude of the zeta potential is increased and is always negative, for all ZnO NP samples except for EN-Z-1. This indicates that with the exception of EN-Z-1, ZnO NP stability is significantly improved in the presence of BSA. The experiments were carried out at pH 7.4; at this pH the protein has an overall negative charge as a result of deprotonation of the carboxylic side chains (COO<sup>-</sup>) (Fologea et al., 2007). This may explain the increased stability of EN-Z-2, EN-Z-3 and EN-Z-4 due to the attraction of the negatively charged COO<sup>-</sup> groups to the positively charged particles and subsequent adsorption of BSA onto the surface of the ZnO NPs. This is confirmed by the negative zeta potential measured for the NPs in the presence of BSA and explains the increased stability as a result of electrostatic repulsion. Due to the negatively charged NPs in EN-Z-1, negatively charged groups on the BSA molecule will be repelled and will not result in adsorption to the NP surface; therefore no change in zeta potential is measured. For EN-Z-6 the negative magnitude of the zeta potential increases with the addition of BSA. As the zeta potential was already negative, it is unlikely that BSA has adsorbed to the surface of the NPs in this sample and therefore this requires further investigation in order to understand the processes involved here.

## **6.2.2 Dynamic Light Scattering**

This section reports the distributions of hydrodynamic diameters measured by dynamic light scattering (DLS) for a variety of ZnO NP suspensions.

### *6.2.2.1 ZnO Nanoparticle Colloidal Stability Over Time*

In order to investigate the colloidal stability of ZnO NP samples in water over a 24 hour period, stock suspensions were placed in an ultrasonic bath for 30 minutes,

after which the samples were removed and analysed immediately by DLS ( $T = 0$  hour). Subsequent DLS measurements of the samples were obtained at  $T = 1$ ,  $T = 4$ ,  $T = 10$  and  $T = 24$  hour. Prior to the samples being placed into the DLS instrument, the vial was turned upside down once and then returned to a standing position, in order to re-suspend the sedimented fraction of the sample. The results of the DLS experiments, investigating ZnO NP stability are presented in Figure 6-7 and are largely in agreement with the zeta potential measurements for the ZnO NP samples dispersed in MilliQ water (Figure 6-5). The DLS number profiles obtained for EN-Z-1, presented in Figure 6-7 (a), indicate that the stability of the sample does not change significantly over the course of 24 hour. The very small difference between the size distributions obtained at 10 and 24 hour, where the peak maximum increases from approximately 70 nm to 85 nm, may be an indication that the NPs are beginning to agglomerate.

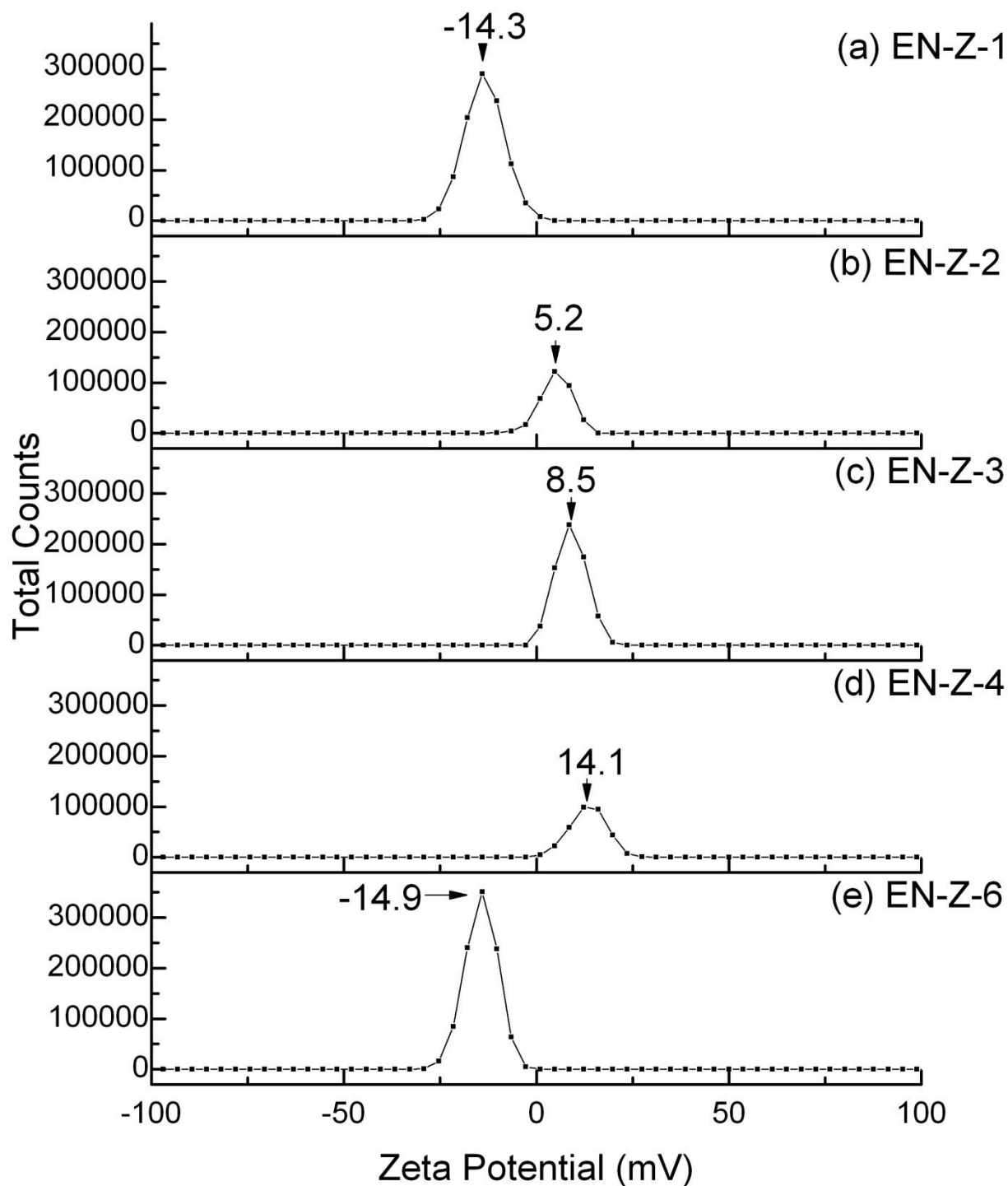


**Figure 6-5 Zeta potential measurements for (a) EN-Z-1, (b) EN-Z-2, (c) EN-Z-3, (d) EN-Z-4 and (e) EN-Z-6 ZnO NP suspensions in MilliQ water at a concentration of 1000  $\mu\text{g/ml}$  and pH of 7.4.**

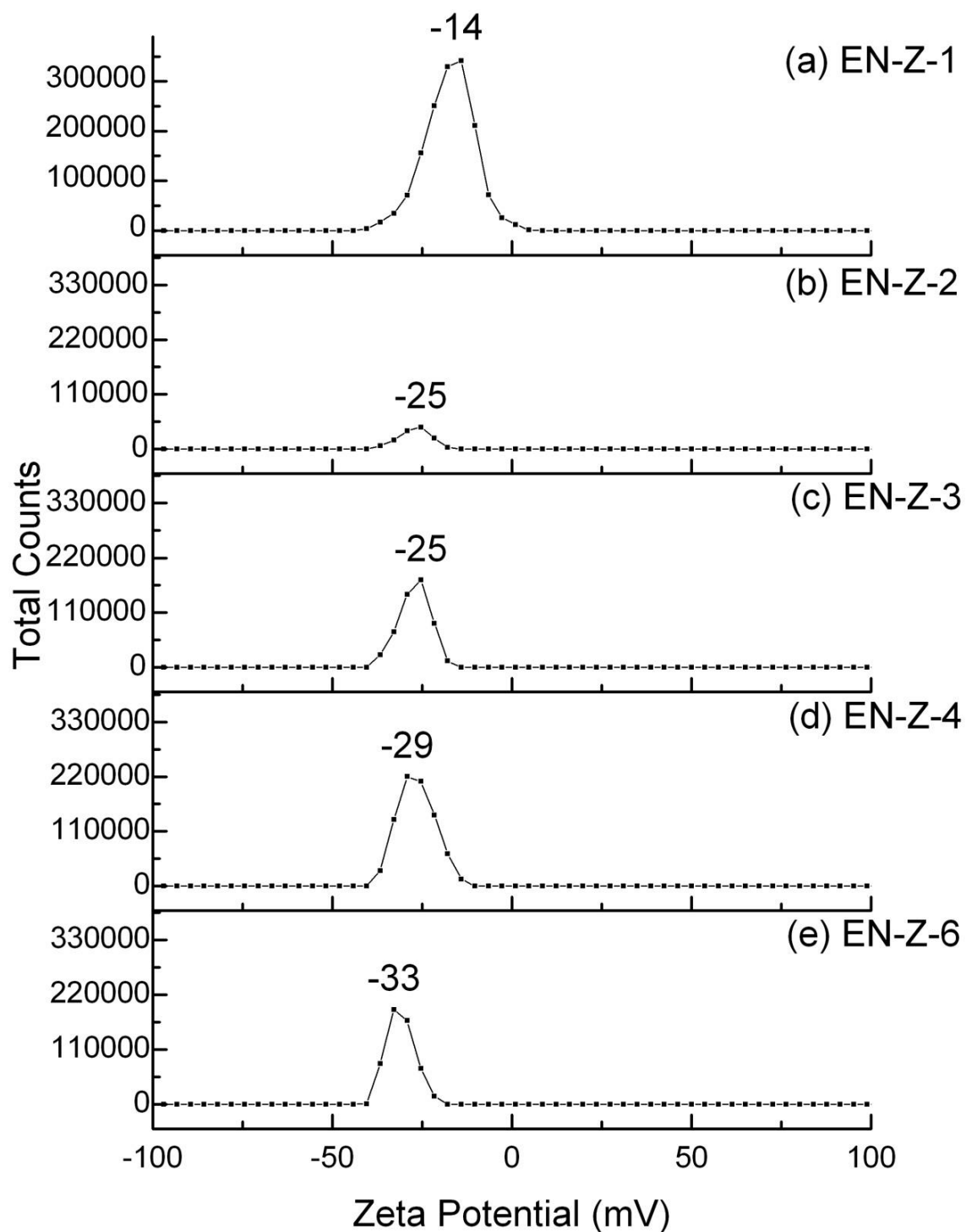


**Figure 6-6 Zeta potential measurements obtained at pH 7.4 for (a) EN-Z-1, (b) EN-Z-2, (c) EN-Z-3, (d) EN-Z-4 and (e) EN-Z-6 at a concentration of 100  $\mu\text{g/ml}$  in water with 10 % w/w BSA, indicating the magnitude of the charge on the particle surface.**

The DLS number profiles obtained for EN-Z-2 are presented in Figure 6-7 (b) and indicate that this sample is not stable over the 24 hour period investigated. After only 1 hour, the maximum of the primary peak has increased from 115 to 145 nm and the secondary peak at approximately 500 nm has increased in intensity. A small peak has also appeared at around 1700 nm indicating that as well as the primary particles and small clusters of particles agglomerating, large agglomerates are also forming and increasing in size. After 4 hour, the primary peak has increased to around 450 nm, and there is no longer any peak visible at a lower size range, indicating that all of the NPs have agglomerated into relatively large clusters. After 10 hour, the primary peak is at 2000 nm and after 24 hour the primary peak is at 2300 nm, with a small fraction of the agglomerates being in the size range of 6000 nm. The DLS number profile obtained for EN-Z-3 is presented in Figure 6-7 (c) and indicates that the sample is also unstable over 24 hour.

The DLS number profiles obtained for EN-Z-6 are presented in Figure 6-7 (e) and indicate that this sample has good stability in water over time as compared to the other powder samples of ZnO investigated. The superior stability observed by DLS for EN-Z-1 and EN-Z-6 as compared to EN-Z-2 and EN-Z-3, was previously indicated by the greater magnitude of the zeta potential measured for these samples (Figure 6-5).

The DLS number profiles obtained for EN-Z-4 are presented in Figure 6-7 (d) and indicate that the sample is not stable over 24 hours. From the magnitude of the zeta potential measured for EN-Z-4, one would expect this sample to have a similar stability to EN-Z-1 and EN-Z-6. The primary particle size however is significantly smaller than the NPs in the other samples, which will increase the surface energy of the sample and increase the tendency of the particles to agglomerate. The average length of the NPs in EN-Z-4, determined by TEM, is  $23 \pm 8$  nm (Figure 5-26), whereas the average particle length determined by TEM for EN-Z-1 (Figure 4-16) and EN-Z-6 (Figure 5-27) is  $30 \pm 20$  and  $47 \pm 26$  nm respectively.

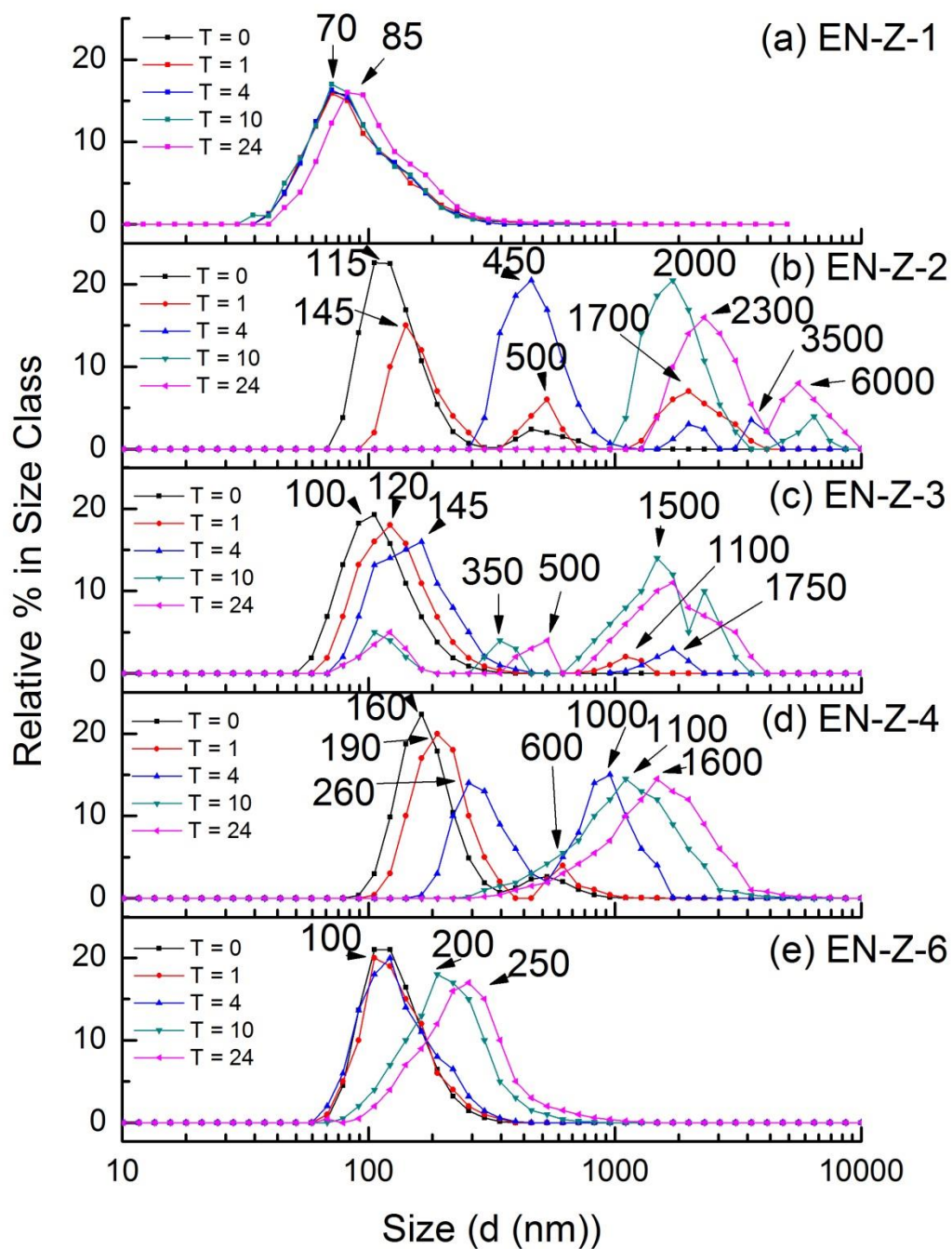


**Figure 6-7 DLS number profiles of (a) EN-Z-1, (b) EN-Z-2, (c) EN-Z-3, (d) EN-Z-4 and (e) EN-Z-6 suspensions in MilliQ water at a concentration of 1000  $\mu\text{g/ml}$ . Measurements were carried out at T = 0, T = 1, T = 4, T = 10, and T = 24 hour; where T = 0 is immediately after the sample is removed from the ultrasonic bath in which it is placed for 30 minutes after initial dispersion.**

These results demonstrate the variable nature of ZnO NPs when dispersed in water. As well as different samples of ZnO displaying varying degrees of agglomeration, most of the NP suspensions are unstable, changing in agglomeration behaviour as time progresses. These findings highlight the importance of characterising a ZnO NP suspension under exactly the same conditions as it would be administered to cells for a viability assay. Therefore, the stability of the 5 ZnO NP samples at toxicologically relevant concentrations and in cell culture media was subsequently investigated by DLS and PF-TEM.

#### 6.2.2.2 *Dispersion of ZnO Nanoparticles in Water at Varying Concentrations*

Toxicity assays are carried out over a variety of ZnO NP concentrations and therefore it is important to investigate how ZnO NP concentration affects colloidal stability. The 1000  $\mu\text{g/ml}$  stock suspensions prepared previously (section 6.2) were diluted appropriately to obtain concentrations of ZnO in MilliQ water at 100 and 10  $\mu\text{g/ml}$ . The toxicity assays carried out in this study were 24 hour exposures, therefore it was at this time point that the dispersion characteristics of the ZnO NP suspensions were of great interest. Hence, 24 hours after the dilutions were prepared, the suspensions were placed in an ultrasonic bath for 30 minutes and then analysed immediately by DLS. The time taken to transfer the sample from the ultrasonic bath to the cuvette for measurement, and also the time taken to insert the sample cuvette into the instrument and record the measurements must also be taken into account. In total the extra processing time contributed an additional 3 to 4 minutes.

The particle size distributions for 1000, 100 and 10  $\mu\text{g/ml}$  concentrations of EN-Z-1 in water, obtained by DLS are presented in Figure 6-8 (a). The results indicate that for the EN-Z-1 sample, there is no significant difference in the distribution of hydrodynamic diameters with varying concentration indicating that NP colloidal stability is not affected by ZnO NP concentration. For the 1000  $\mu\text{g/ml}$  suspension, the agglomerates present are in the range 30 -300 nm with a peak maximum at 73 nm. The agglomerate distribution measured by DLS for the 100  $\mu\text{g/ml}$  sample ranges between 50 and 250 nm with a peak maximum at 80 nm. The

agglomerate size distribution measured for the 10 µg/ml sample ranges between 20 and 200 nm with a peak maximum at 62 nm.

The particle size distributions for 1000, 100 and 10 µg/ml concentrations of EN-Z-2 in water, obtained by DLS are presented in Figure 6-8 (b). The results indicate that for the EN-Z-2 sample, there is a significant difference in the distribution of hydrodynamic diameters with varying concentration, but we know dissolution below approximately 15 µg ZnO/ml is complete (Franklin et al., 2007) and occurs within a few hours. Therefore, not surprisingly, the colloidal stability of the samples at each of the concentrations does not follow a particular trend.

The particle size distributions for 1000, 100 and 10 µg/ml concentrations of EN-Z-3 in water, obtained by DLS are presented in Figure 6-8 (c). Similar to EN-Z-2, the results indicate that for the EN-Z-3 sample, there is a significant difference in the distribution of hydrodynamic diameters with varying ZnO NP concentration. The DLS profiles for EN-Z-4 are presented in Figure 6-8 (d) and show a significant variation in the distribution of hydrodynamic diameters for different concentrations of ZnO. Again, there is no clear relationship between the ZnO NP concentration and the distribution of agglomerate sizes measured in the sample. Similarly, the DLS results for EN-Z-6 presented in Figure 6-8 (e) indicate that the distribution of hydrodynamic diameters in the sample varies with concentration, although the relationship is not clear.

At concentrations of 10 µg ZnO/ml, it is expected that the majority of NPs in the suspension have dissolved by 24 hours; this may explain why the hydrodynamic size distributions measured by DLS for ZnO NP suspensions with varying concentrations do not appear to follow any particular trend.

### 6.2.2.3 *Dispersion of ZnO Nanoparticles in Cell Culture Media (with and without serum proteins)*

In order to investigate the stability of ZnO NPs in biological media, the samples were dispersed in DMEM at a concentration of 100 µg/ml. Additionally samples were prepared with a BSA concentration of 10 µg/ml in order to investigate the effect on ZnO NP stability.



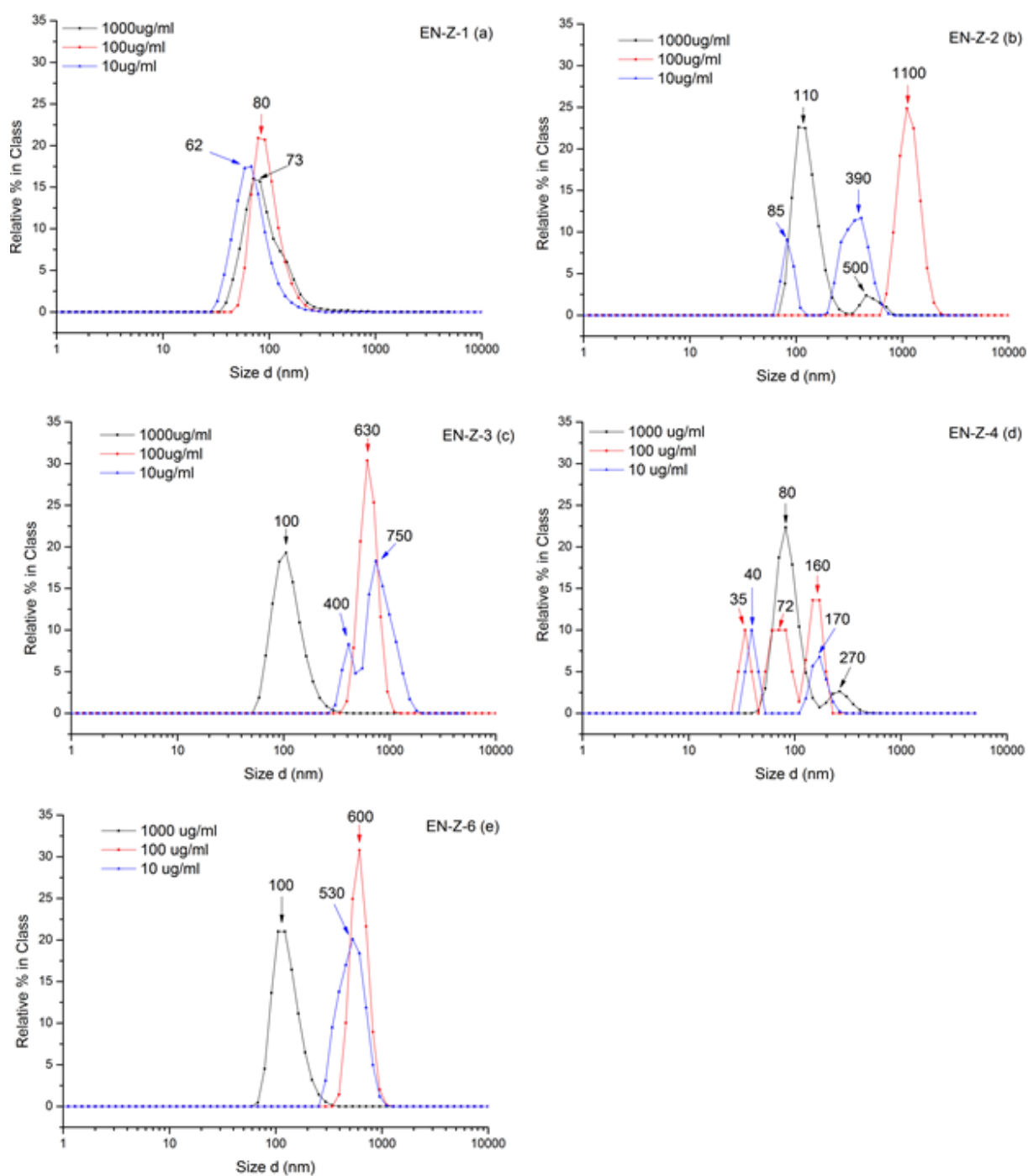


**Figure 6-8 Particle size number distributions for (a) EN-Z-1, (b) EN-Z-2, (c) EN-Z-3, (d) EN-Z-4 and (e) EN-Z-6 dispersed in water at varying concentrations (1000, 100 and 10 µg/ml) 24 hours after sample preparation, as determined by DLS.**

The agglomerate size distributions obtained for EN-Z-1, EN-Z-2, EN-Z-3, EN-Z-4 and EN-Z-6 in DMEM and DMEM-BSA are presented in Figure 6-9 (a), (b), (c), (d) and (e) respectively. For all samples, the addition of BSA has a stabilizing effect on the NPs in suspension, characterized by a reduction in the hydrodynamic diameters measured by DLS. With the exception of EN-Z-1 and EN-Z-6, these results can be explained by the adsorption of BSA onto the NP surface due to electrostatic attraction between the positively charged NP surface and the negatively charged BSA molecules. This is characterized by an oppositely charged and increased magnitude of the zeta potential measured for EN-Z-2, EN-Z-3 and EN-Z-4 upon addition of BSA to the suspension (Figure 6-5 and Figure 6-6). For EN-Z-1, evidence for BSA adsorbing on to the surface of the NPs is not apparent. The zeta potential with and without the addition of BSA is -14.3 mV (Figure 6-6 (a)) and -14 mV (Figure 6-5 (a)) respectively indicating that there is no effect on the surface charge of the NPs. Further investigation is required for EN-Z-6, as although a markedly improved dispersion is observed (Figure 6-8 (e)) and an increase in the magnitude of the zeta potential is measured when BSA is added (Figure 6-6 (e)), the NPs in this sample were already negatively charged (Figure 6-5 (e)) and therefore it is unlikely that BSA has adsorbed to the surface.

Comparing the size distributions in DMEM to those in water indicate that the colloidal stability of ZnO NPs is reduced in DMEM. We also know that the equilibrium dissolution level is reduced to 5.7  $\mu\text{g/ml}$  (Mu et al., 2013) but that above this secondary  $\text{ZnCO}_3$  precipitates form, which potentially may confound DLS measurements. For example, the particle size distribution measured by DLS for EN-Z-1 dispersed in water at a concentration of 100  $\mu\text{g/ml}$  has a principal peak at approximately 80 nm (Figure 6-8 (a)) compared with in DMEM where the peak is at 91 nm (Figure 6-9 (a)).

The DLS results presented for the samples at varying concentrations do not identify a specific relationship between ZnO NP colloidal stability and concentration. One would expect the agglomeration of NPs in a suspension to be reduced at lower concentration as the rate of direct particle to particle interaction is reduced (Allouni et al. 2009). However for some of the ZnO NP suspensions investigated in this study,

the opposite is true. An explanation for this may be due to the solubility of ZnO which has previously been investigated (Figure 6-2). DLS is capable of measuring the distribution of hydrodynamic diameters accurately for a stable monodisperse dispersion of NPs, however issues arise when an NP dispersion is unstable or polydisperse. This is because the intensity of light scattered by particles in a suspension is proportional to the diameter of the particle ( $I \propto d^6$ ). Therefore in a polydisperse or unstable suspension, there is a greater intensity of scattered light by larger particles or agglomerates leading to the smaller particles and finer agglomerate signal being swamped (Malvern, 2000). It has been shown that at low concentrations, depending on the pH of the suspension, a significant fraction if not all of the ZnO will be in solution (Figure 6-2). This reduces the concentration of ZnO NPs in the suspensions. A reduced NP concentration leads to a lower intensity of scattered light from the particles, which may reduce the accuracy of the measurement. Additionally, dissolution may occur more rapidly for fine agglomerates and individual NPs than for larger agglomerates, and hence the swamping effect of the larger agglomerates will be even more significant. Furthermore the sample processing time between sonication ending and the measurements having been recorded is approximately 4 minutes. This time will allow for sedimentation to initiate, especially in the case of suspensions with higher concentration. This may lead to inaccurate measurement of larger agglomerates as a result of their position in the sample cell, and hence lead to unrepresentative size distributions. Finally, the precipitation of ZnCO<sub>3</sub> in DMEM (Mu et al., 2013) or even hydrozincite in water (Reed et al., 2012) may further complicate these readings.

The distribution of hydrodynamic diameters measured for different concentrations of EN-Z-1 do not vary as significantly as for the other ZnO NP dispersions. This may be due the high stability of EN-Z-1 in suspension which gives rise to a narrower distribution of agglomerate sizes. This would reduce the signal being swamped by light reflected from larger agglomerates as there would be far fewer present in the dispersion. This may also reflect the slower dissolution rate of EN-Z-1 (Mu et al., 2013).

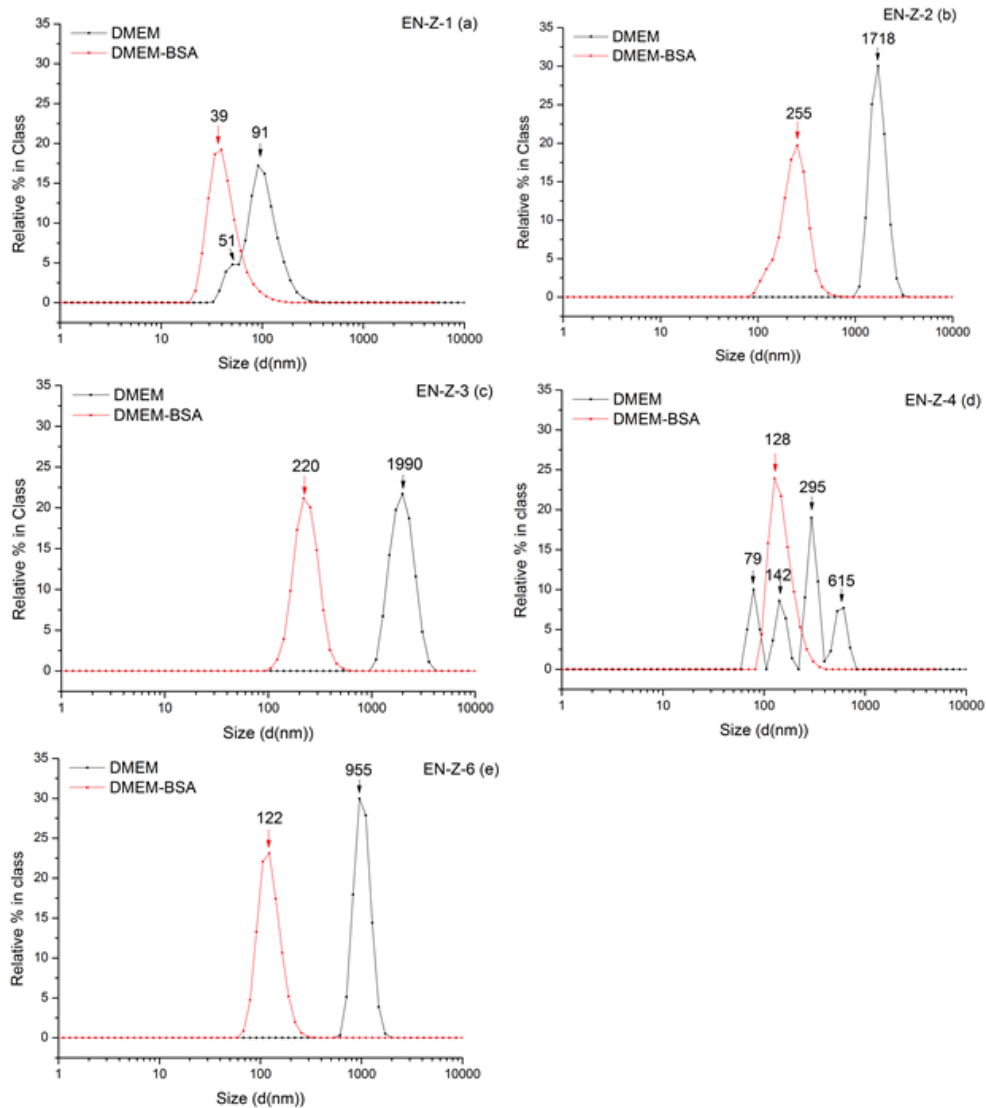


**Figure 6-9 Particle size number distributions for (a) EN-Z-1, (b) EN-Z-2, (c) EN-Z-3, (d) EN-Z-4 and (e) EN-Z-6 dispersed in DMEM and DMEM-BSA as determined by DLS.**

### 6.2.3 Plunge Freezing Transmission Electron Microscopy

Due to the limitations experienced using DLS to measure the distribution of ZnO NP agglomerates in suspension, such as inaccurate sizing of polydisperse suspensions with poor stability, especially at low NP concentrations, an alternative technique was investigated. For this technique, a 3.5  $\mu\text{l}$  volume of a NP suspension is placed onto a TEM grid, blotted and then plunged into liquid ethane in order to

suspend the NPs in a vitreous film of ice. The grid is then allowed to warm up under vacuum conditions and analysed by TEM. Hondow et al. (2012) previously reported that when a plunge frozen NP dispersion is warmed to room temperature under vacuum conditions, the NPs do not move.

NP samples analysed by TEM are typically prepared by drop casting a small volume of a suspension onto a TEM grid, however drying effects cause the NPs to agglomerate together such that any clusters of particles imaged in the TEM are not representative of those in a suspension. In order to compare the two sample preparation techniques, a 1000  $\mu\text{g/ml}$  suspension of EN-Z-6 in MilliQ was prepared by both the drop casting and plunge freezing method. For both techniques, a volume of 3.5  $\mu\text{l}$  of suspension was used. TEM images of the two samples are presented in Figure 6-10 (Wallace et al., 2012). It is clear from the images that the agglomerates present in the sample prepared by the drop casting route (Figure 6-10 (a)) are considerably larger than those present in the sample prepared by the plunge freezing method (Figure 6-10 (b)). This suggests that the drying processes that cause the NPs to agglomerate in the drop casting sample preparation route do not operate in the plunge freezing route, however the results do not give any indication as to whether the agglomerates in the image are an accurate representation of the agglomerates present when suspended in a liquid medium. In order to validate the technique, comparison with DLS of ZnO suspensions in water was achieved by measuring the Feret length of 250 agglomerates of ZnO NPs from TEM images of PF samples to obtain an agglomerate size distribution.

#### *6.2.3.1 Dispersion of ZnO Nanoparticles in Water at Varying Concentrations*

The PF-TEM method of obtaining an agglomerate size distribution for a ZnO NP suspension was investigated in order to explore the limitations experienced with DLS. Therefore, the PF-TEM technique was employed to investigate ZnO NP suspensions in MilliQ water at concentrations of 1000, 100 and 10  $\mu\text{g/ml}$ . Sample preparation was synonymous to that described for the DLS experiments in section 6.2.2.2.

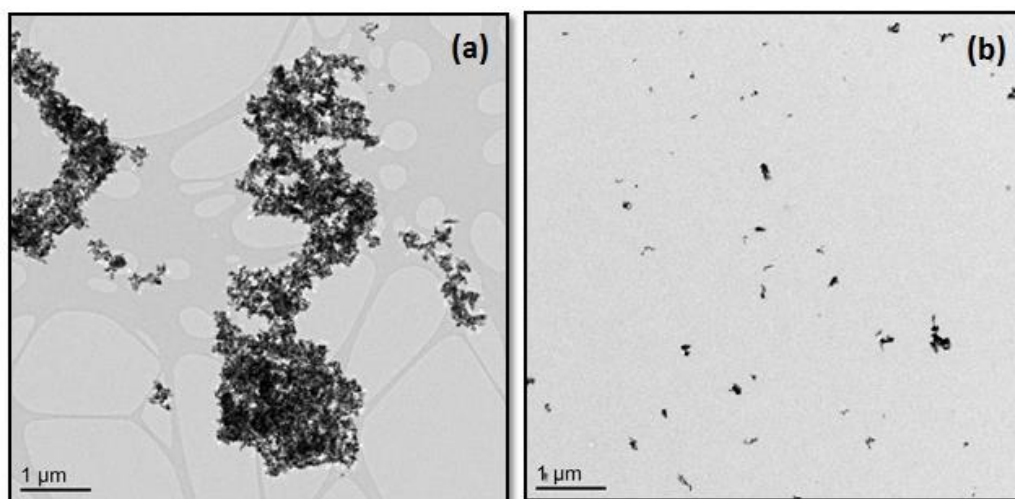


**Figure 6-10** Low magnification TEM images of EN-Z-6 at 1000 µg/ml in water, prepared by (a) the drop-casting method and (b) by the plunge-freezing method (Wallace et al., 2012).

Examples of TEM images from which agglomerate size distributions were measured for EN-Z-1, EN-Z-2, EN-Z-3, EN-Z-4 and EN-Z-6 are presented in Figure 6-11, Figure 6-12, Figure 6-13, Figure 6-14 and Figure 6-15 respectively, as well as EDX spectra identifying the agglomerates as ZnO.

A low magnification TEM image of EN-Z-1 dispersed in water at a concentration of 100 µg/ml is presented in Figure 6-11 (a). This magnification (1900 x) was found to be optimum in that the agglomerates were large enough to be visualized clearly and measure the size from, with sufficient field of view to rapidly select many. This accelerated the process of measuring 250 agglomerates from several images for each sample. A TEM image at higher magnification is presented in Figure 6-11 (b) where the individual ZnO NPs forming an agglomerate can be easily observed. In order to confirm that the agglomerate in Figure 6-11 (b) was ZnO, an EDX spectrum was also obtained for the agglomerate (Figure 6-11 (c)).

Images of EN-Z-2 dispersed in water at a concentration of 100 µg/ml, prepared by the plunge freezing route are presented in Figure 6-12. An example of the type of a low magnification TEM image used to measure the agglomerate sizes is presented in Figure 6-12 (a). In this sample, impurities were detected as well as the agglomerates of ZnO NPs, such as those presented in Figure 6-12 (b) (composition

confirmed by EDX (Figure 6-12 (d)). Particles of salts were present in a small number of ZnO NP agglomerates (Figure 6-12 (c)). The EDX spectrum obtained for the particles in Figure 6-12 (c), presented in Figure 6-12 (e), confirms the presence of zinc and oxygen, however the intensity of the oxygen peak compared to the zinc peaks is greater than expected. Additionally, there are small amounts of calcium and sulphur present; indicating that the salt present may be calcium sulphate. Salts were not detected in the 1000 and 10  $\mu\text{g/ml}$  suspensions and previous compositional analysis of EN-Z-2 by EDX (Figure 4-14) did not detect this type of impurity, therefore it is unlikely to have arisen from the ZnO nanopowder itself. A possible source of contamination is the water in which the sample is suspended which when analysed by ICP-MS was found to contain low levels of calcium and sulphur (Figure 4-1). However, salt particles were not identified in any of the other ZnO samples suspended in water and the source of the water was consistent for all of the suspensions prepared. The impurities therefore most probably arise from contamination of the vial in which the suspension was prepared.

A low magnification TEM image of EN-Z-3 dispersed in water at a concentration of 100  $\mu\text{g/ml}$  is presented in Figure 6-13 (a). A TEM image at higher magnification is presented in Figure 6-13 (b) where the primary ZnO NPs are easily discernible. An EDX spectrum obtained for the agglomerate shown in Figure 6-13 (b) is presented in Figure 6-13 (c) and confirms the presence of only zinc and oxygen. The presence of  $\text{ZnCO}_3$  cannot be identified by EDX as a result of the contribution to the carbon peak from the support film. This is the case for all of the PF samples analysed by EDX.

A low magnification TEM image of EN-Z-4 dispersed in water at a concentration of 100  $\mu\text{g/ml}$  is presented in Figure 6-14 (a). A TEM image at higher magnification, presented in Figure 6-14 (b), reveals an agglomerate of ZnO where the particles do not appear to have the same faceted edges observed in the TEM analysis reported in Chapter 5 (Figure 5-26). The TEM grids were prepared within minutes of the suspension being prepared for the images shown in Figure 5-26. Whereas for the plunge frozen sample, the nanopowder has been stored as a 1000  $\mu\text{g/ml}$  suspension for 48 hours before being diluted to 100  $\mu\text{g/ml}$  suspension and stored for a further 24 hours prior to the PF-TEM grids being prepared. The

morphology of the ZnO particles observed in Figure 6-14 (b) may be a result of partial dissolution of the sample arising from prolonged storage in water, as has previously been discussed (Figure 6-2). An EDX spectrum obtained for the agglomerate shown in Figure 6-14 (b), presented in Figure 6-14 (d) confirms the presence of only zinc and oxygen. There are also agglomerates present in the suspension that consist of NPs that more closely resemble the NPs observed in the original TEM images (Figure 5-26), i.e. without any sign of dissolution. An example of an agglomerate such as this is presented in Figure 6-14 (c), confirmed to be ZnO by EDX (Figure 6-14 (e)).

A low magnification TEM image of EN-Z-6 dispersed in water at a concentration of 100  $\mu\text{g/ml}$  is presented in Figure 6-15 (a). A TEM image showing a small agglomerate of particles at higher magnification is presented in Figure 6-15 (b). An EDX spectrum obtained for the agglomerate shown in Figure 6-15 (b), presented in Figure 6-15 (c) confirms the presence of only zinc and oxygen.

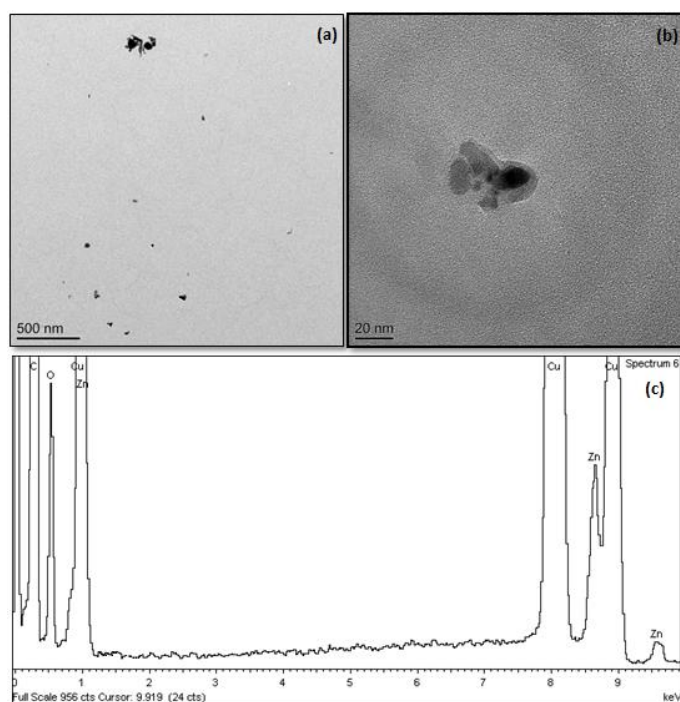


**Figure 6-11 TEM analysis of EN-Z-1 dispersed in water at a concentration of 100  $\mu\text{g/ml}$ , prepared by the plunge freezing route. (a) Low magnification TEM image, (b) TEM image at higher magnification and (c) EDX spectrum obtained for the cluster of particles shown in (b), confirming ZnO composition of NPs.**



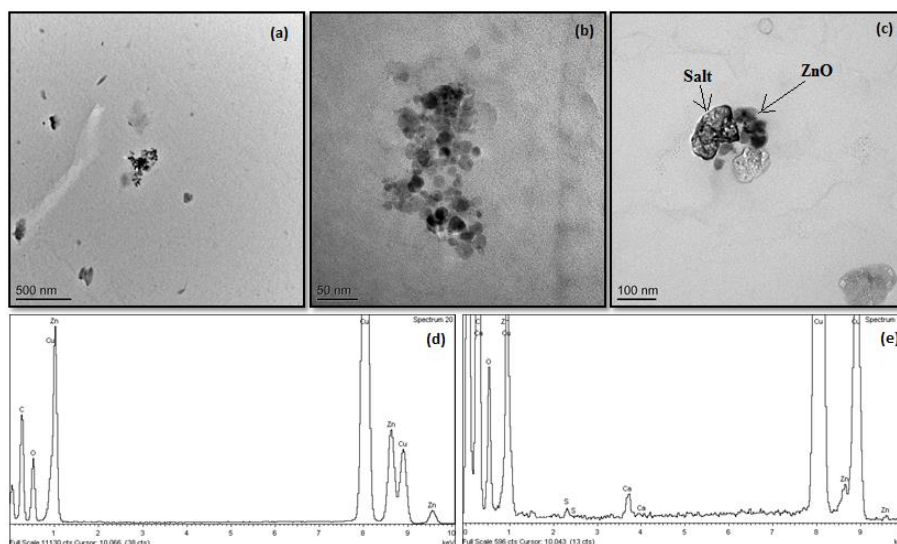


**Figure 6-12** TEM analysis of EN-Z-2 dispersed in water at a concentration of 100  $\mu\text{g/ml}$ , prepared by the plunge freezing route. (a) Low magnification TEM image of the sample. Higher magnification TEM images of (b) an agglomerate of ZnO NPs, (c) an agglomerate of ZnO NPs with salts present. (d) EDX spectrum obtained for the cluster of particles shown in (b) and (e) an EDX spectrum obtained for the area presented in (c).

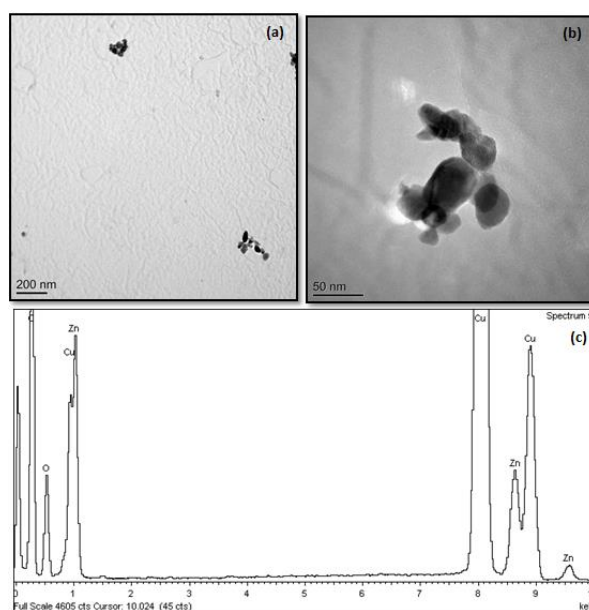


**Figure 6-13** TEM analysis of EN-Z-3 dispersed in water at a concentration of 100  $\mu\text{g/ml}$ , prepared by the plunge freezing route. (a) Low magnification TEM image, (b) TEM image at higher magnification and (c) EDX spectrum obtained for the cluster of particles shown in (b).

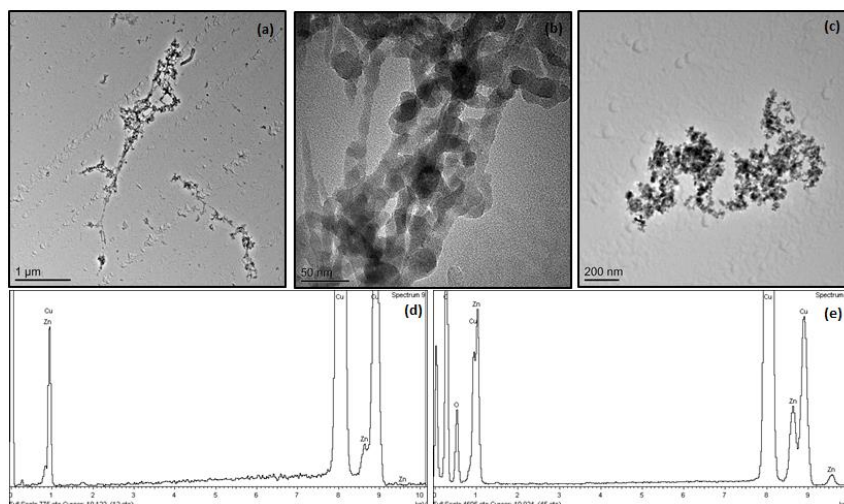


**Figure 6-14** TEM analysis of EN-Z-4 dispersed in water at a concentration of 100  $\mu\text{g/ml}$ , prepared by the plunge freezing route. (a) Low magnification TEM image, (b) TEM image at higher magnification showing NPs affected by dissolution, (c) TEM image showing NP agglomerate apparently unaffected by dissolution. (d) EDX spectrum obtained for the NPs presented in (b) and (e) EDX spectrum obtained for the NPs presented in (c).

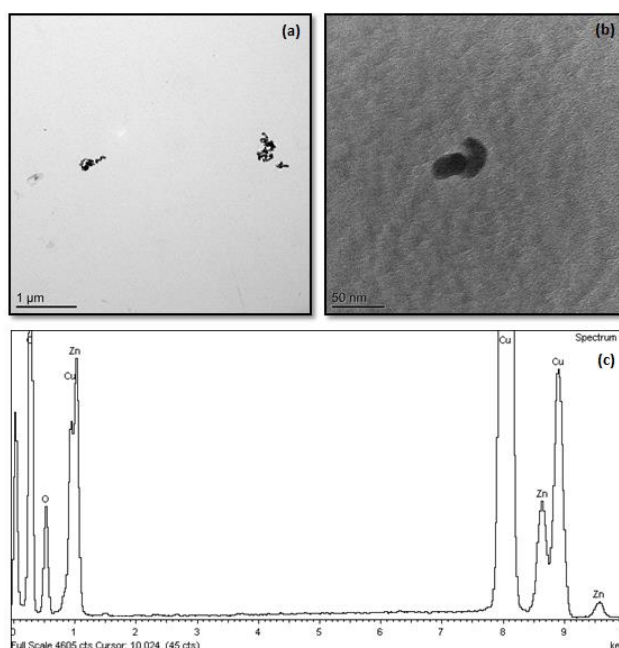


**Figure 6-15** TEM analysis of EN-Z-6 dispersed in water at a concentration of 100  $\mu\text{g/ml}$ , prepared by the plunge freezing route. (a) Low magnification TEM image, (b) TEM image at higher magnification and (c) EDX spectrum obtained for the cluster of particles shown in (b).

### 6.2.3.2 *Agglomerate Size Distributions by Plunge Freezing Transmission Electron Microscopy*

A particle size distribution was produced for each sample by measurement of the Feret lengths of 250 agglomerates imaged by PF-TEM. The size distributions obtained for each sample at concentrations of 1000, 100 and 10  $\mu\text{g/ml}$  are presented in Figure 6-16.

The agglomerate size distributions obtained for EN-Z-1 are presented in Figure 6-16 (a). The agglomerate size distribution decreases marginally when the concentration is lowered from 1000 to 100  $\mu\text{g/ml}$ . The size distribution of the agglomerates present in the 1000  $\mu\text{g/ml}$  suspension range in size between 8 and 1100 nm with a peak maximum at 50 nm, whereas for the 100  $\mu\text{g/ml}$  suspension, the size distribution obtained by PF-TEM indicates agglomerates between 10 and 400 nm are present in the sample with a peak maximum at 35 nm. However when the concentration of ZnO is decreased further to 10  $\mu\text{g/ml}$ , the size distribution measured for the agglomerates in the suspension increases to between 10 and 300 nm in size with a peak maximum at 65 nm. This may be due to the dissolution of individual NPs and finer agglomerates, resulting in an increased distribution of the ZnO agglomerates remaining. However, the differences in size distributions measured for EN-Z-1 at varying concentrations are very small and may be insignificant.

For the remaining samples, very few ( $< 10$ ) ZnO agglomerates were found in over 100 images recorded for the 10  $\mu\text{g/ml}$  suspensions prepared by PF-TEM, as might be expected given the known rate of dissolution and equilibrium solubility for ZnO. It would have taken a great deal of time to prepare more grids and record hundreds more images in order to obtain measurement of 250 agglomerates, therefore no PF-TEM size distributions are reported for this concentration.

The comparison of agglomerate size distributions measured by PF-TEM for 1000 and 100  $\mu\text{g/ml}$  concentrations of EN-Z-2 in water are presented in Figure 6-16 (b), and in contrast to the DLS results, an increase in the agglomerate size distribution is observed with increasing ZnO NP concentration. The PF-TEM results for EN-Z-3 at concentrations of 1000 and 100  $\mu\text{g/ml}$  in water are presented in Figure 6-16 (c), and also indicate that the agglomerate size distributions increase with increasing ZnO NP concentration.

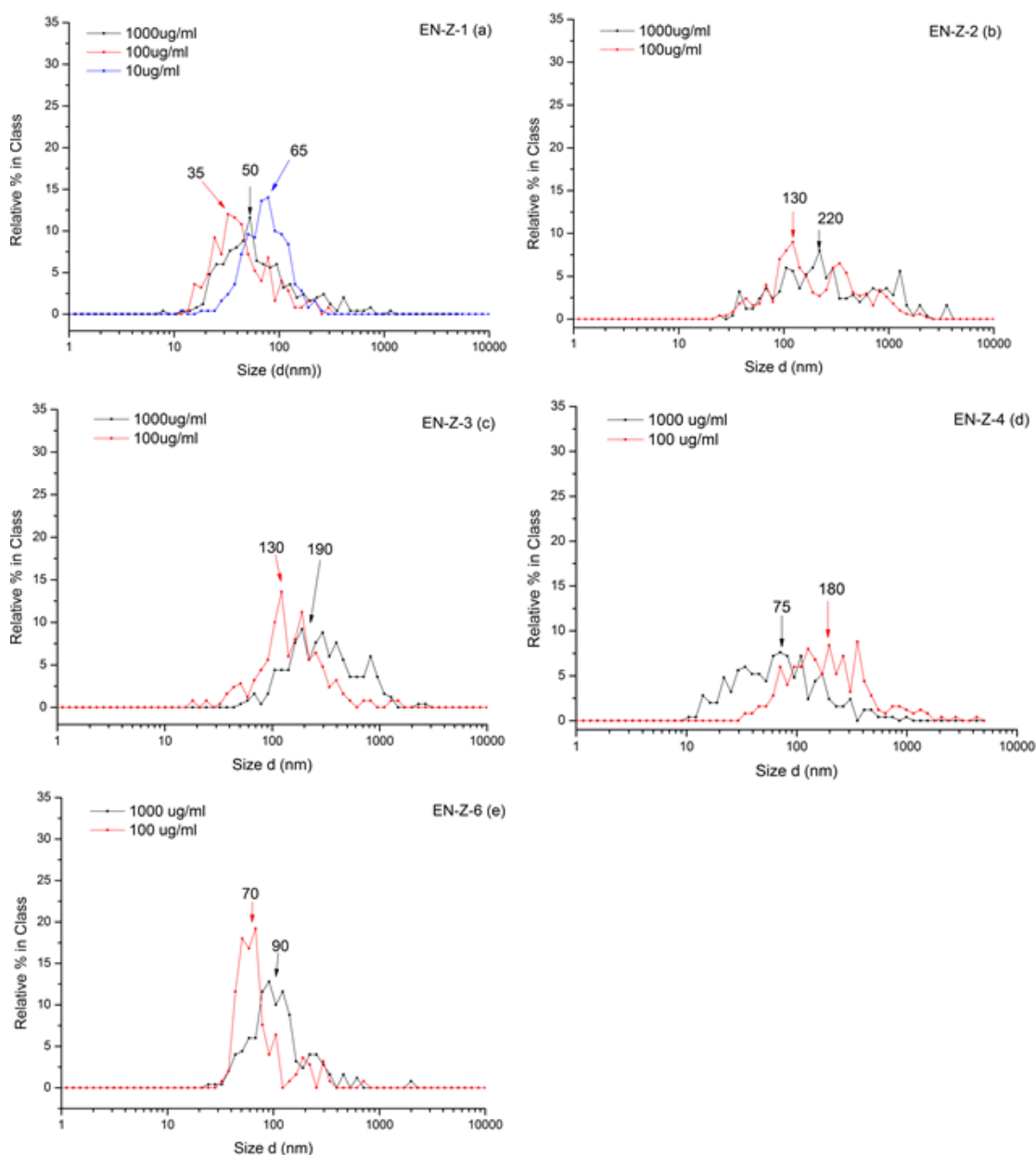


**Figure 6-16 Particle size distributions for (a) EN-Z-1, (b) EN-Z-2, (c) EN-Z-3, (d) EN-Z-4 and (e) EN-Z-6 dispersed in water at varying concentrations (1000, 100 and 10 µg/ml) as determined by PF-TEM.**

The particle size distributions for 1000 and 100 µg/ml concentrations of EN-Z-4 in water, obtained by PF-TEM, are presented in Figure 6-16 (d) and in contrast to the other 4 samples of ZnO, an increase in the agglomerate size distribution is

observed when the concentration is increased from 100 to 1000  $\mu\text{g/ml}$ . The particle size distributions for 1000 and 100  $\mu\text{g/ml}$  concentrations of EN-Z-6 in water, obtained by PF-TEM, are presented in Figure 6-16 (e) and indicate that the agglomerate size distribution increases with increasing ZnO NP concentration.

The increases in agglomerate size distributions measured for many of the ZnO samples with increasing ZnO concentration are small and therefore may be due to measurement error. In order to confirm that the increase in agglomerate sizes with increasing ZnO concentration observed are significant, a much larger number than 250 particles should be included in the measurements, or repeat experiments should be carried out.

### 6.2.3.3 *Dispersion of ZnO Nanoparticles in Biological Media*

In order to obtain an agglomerate size distribution for the ZnO NP suspensions in DMEM, 250 agglomerates were measured from TEM images for each sample. Furthermore, EDX was performed to confirm the presence of ZnO. Examples of TEM analysis of the plunge frozen samples of EN-Z-1, EN-Z-2, EN-Z-3, EN-Z-4 and EN-Z-6 are presented in Figure 6-17, Figure 6-18, Figure 6-19, Figure 6-20 and Figure 6-21 respectively. A significant difference with the TEM analysis for the samples in DMEM as compared to in water, is that there was a high concentration of salts precipitated onto the TEM grids in the DMEM samples as might be expected. Initially, EDX was employed to confirm that the salt particles were not ZnO NPs (Figure 6-20 (c)). However, once a number of salt particles had been identified and confirmed by EDX, it was possible to distinguish the salts from the NPs as the salt particles were beam sensitive and varied in morphology to the ZnO NPs.

Another difference for the samples in DMEM compared to in water was that there was clear evidence of dissolution in all 5 of the ZnO NP samples, supporting results of solubility investigations presented previously (Figure 6-1). In the majority of ZnO NP agglomerates, the edges of the particles looked to be affected by dissolution (Figure 6-17 (b), Figure 6-18 (b), Figure 6-19 (b), Figure 6-20 (b) and Figure 6-21 (c)). In some of the agglomerates of ZnO imaged, the individual NPs

could no longer be made out (Figure 6-17 (c) and Figure 6-18 (c)). EDX identified high concentrations of elements other than zinc and oxygen in these agglomerates (Figure 6-17 (e) and Figure 6-18 (e)). It is possible that these agglomerates are in fact lower solubility compounds of zinc that have precipitated from solution, such as zinc carbonate, hopeite or hydrozincite discussed previously in section 6.1.

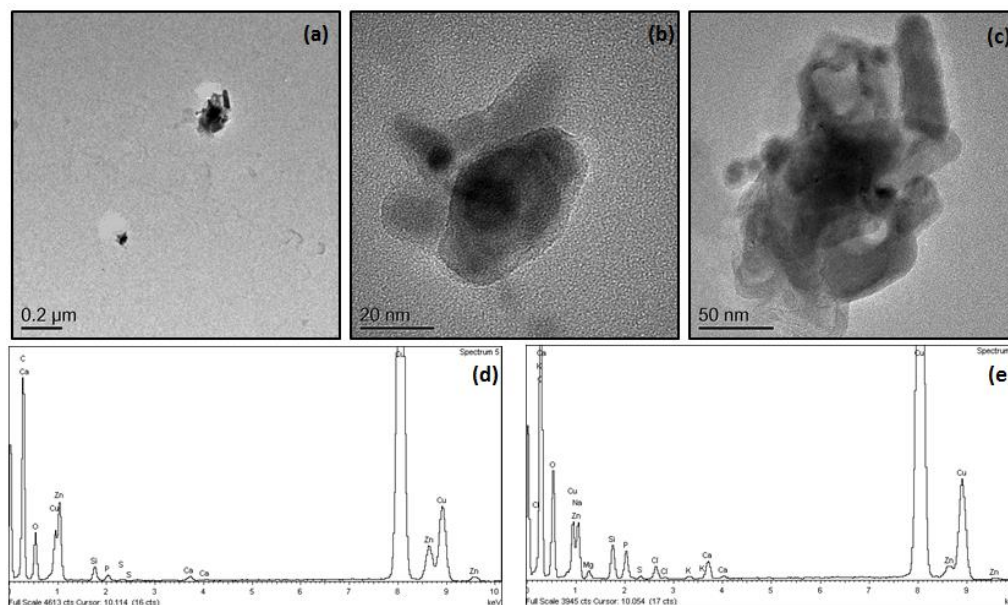


**Figure 6-17** TEM analysis of EN-Z-1 dispersed in DMEM at a concentration of 100  $\mu\text{g/ml}$ , prepared by the plunge freezing route. (a) Low magnification TEM image. (b) TEM images obtained at higher magnification for an agglomerate of particles and (c) a mixture of ZnO and components of DMEM. (d) EDX spectrum obtained for the cluster of particles shown in (b) and (e) EDX spectrum obtained for the particles shown in (c) with clear evidence for the additional presence of salts.

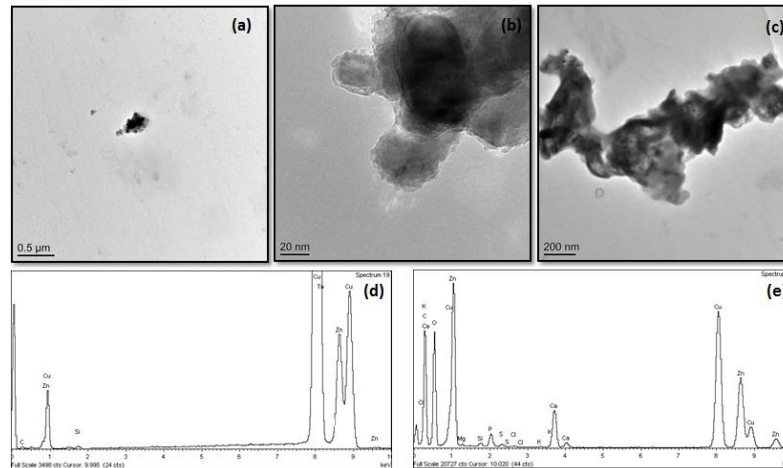


**Figure 6-18** TEM analysis of EN-Z-2 dispersed in DMEM at a concentration of 100  $\mu\text{g/ml}$ , prepared by the plunge freezing route. (a) Low magnification TEM image. TEM images obtained at higher magnification (b) showing the edges of the ZnO particles are dissolving and (c) showing an example of an agglomerate where the individual particles are no longer discernible due to dissolution of ZnO. (d) EDX spectrum obtained for the particles shown in (b) and (e) EDX spectrum obtained for the particles shown in (c).

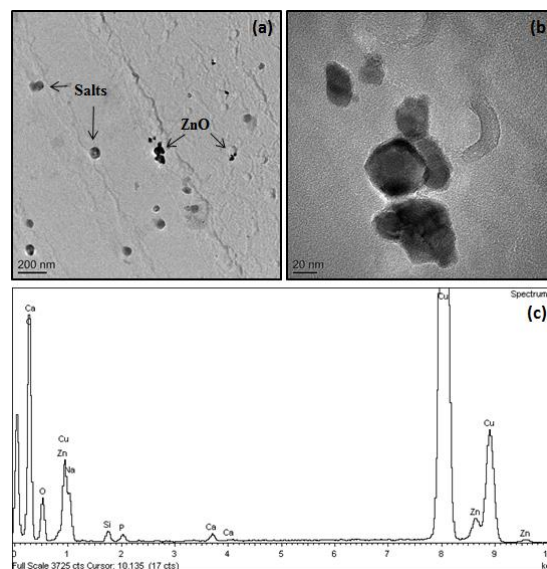


**Figure 6-19** TEM analysis of EN-Z-3 dispersed in DMEM at a concentration of 100  $\mu\text{g/ml}$ , prepared by the plunge freezing route. (a) Low magnification TEM image showing ZnO NPs and salts. (b) TEM image obtained at higher magnification showing an agglomerate of ZnO showing signs of dissolution at the NP surface. (c) EDX spectrum obtained for the particles shown in (b).



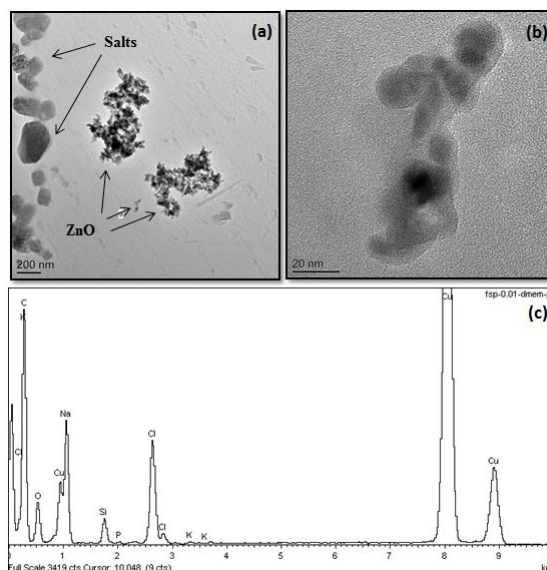


**Figure 6-20 TEM analysis of EN-Z-4 dispersed in DMEM at a concentration of 100  $\mu\text{g}/\text{ml}$ , prepared by the plunge freezing route. (a) Low magnification TEM image showing ZnO NP agglomerates and salts and (b) image of an agglomerate of ZnO at higher magnification showing evidence of dissolution and (c) EDX spectrum obtained for the NPs shown in (b).**

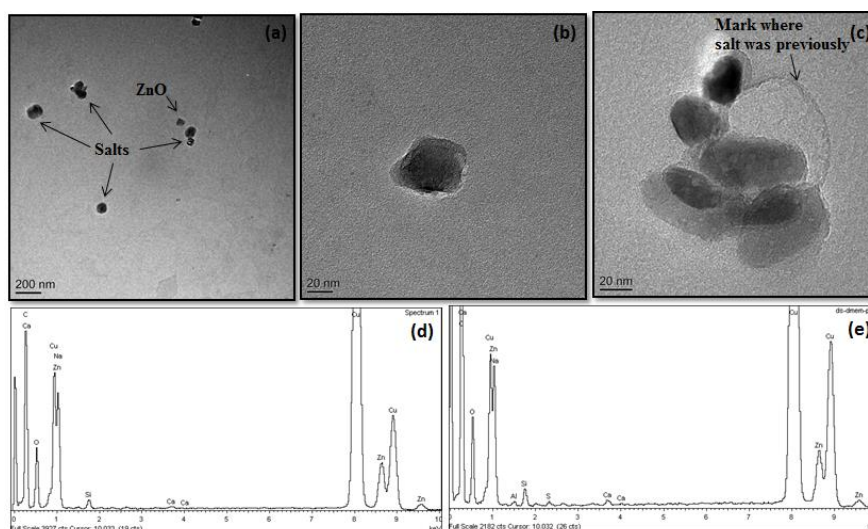


**Figure 6-21 TEM analysis of EN-Z-6 dispersed in DMEM at a concentration of 100  $\mu\text{g}/\text{ml}$ , prepared by the plunge freezing route. (a) Low magnification TEM image showing ZnO NPs and salts. TEM images obtained at higher magnification showing (b) the ZnO NP presented in (a) and, (c) an agglomerate of ZnO NPs with a salt present in the cluster, (d) EDX spectrum obtained for the NP shown in (b) and (e) EDX spectrum obtained for the NP shown in (c).**



The effect of serum on the dispersion of ZnO in DMEM was investigated by adding 10 % w/w BSA and analyzing the particle size distribution by PF-TEM. Images of ZnO NP agglomerates of EN-Z-1, EN-Z-2 and EN-Z-3 are presented in Figure 6-22 (a)(i), (b)(i) and (c)(i) respectively. In the EN-Z-2 and EN-Z-3 images, a coating of what is presumably BSA can be seen on the surface of the NPs. However, this coating is not clearly visible on the surface of the EN-Z-1 NPs. This may be due to the negatively charged EN-Z-1 NPs repelling negatively charged BSA and preventing adsorption onto the surface which is characterized by the unchanged zeta potential when BSA is added to the suspension (Figure 6-5 and Figure 6-6). EDX spectra obtained for the agglomerates in Figure 6-22 (a)(i), (b)(i) and (c)(i) are presented in Figure 6-22 (a)(ii), (b)(ii) and (c)(ii) respectively. As well as the expected peaks for zinc and oxygen, there are also peaks for phosphorus, calcium, chlorine, potassium and sulphur which may be attributed to the DMEM. BSA is comprised mainly of carbon, however the peak in the EDX spectrum for carbon is partly due to the carbon film on the TEM grid and therefore cannot be used as confirmation of the presence of BSA.

#### *6.2.3.4 Agglomerate Size Distributions by Plunge Freezing Transmission Electron Microscopy*

The agglomerate size distributions obtained by PF-TEM for EN-Z-1, EN-Z-2, EN-Z-3, EN-Z-4 and EN-Z-6 dispersed in DMEM and DMEM-BSA are presented in Figure 6-23 (a), (b), (c), (d) and (e) respectively. The results are in agreement with DLS, indicating that the addition of BSA to the suspensions has a stabilizing effect on the ZnO NPs. For all 5 samples of ZnO, the number of larger agglomerates present in the suspensions is reduced when BSA is added. With the exception of EN-Z-1, these findings can be explained by the increase in the magnitude of the zeta potential observed when BSA is added to the solution (Figure 6-6). Additionally, TEM images of the plunge frozen suspensions of EN-Z-2 and EN-Z-3 in DMEM-BSA are presented in Figure 6-22 (b) and (c) respectively showing the apparent adsorption of BSA to the surface of the NPs, and therefore stabilizing the NPs in dispersion. For EN-Z-1, the zeta potential with and without the addition of BSA is -

14.3 mV and -14 mV respectively indicating that there is no effect on the surface charge of the NPs in this sample. Furthermore, no BSA coating is identified on the surface of the NPs from TEM images of plunge frozen suspension of EN-Z-1 in DMEM-BSA.

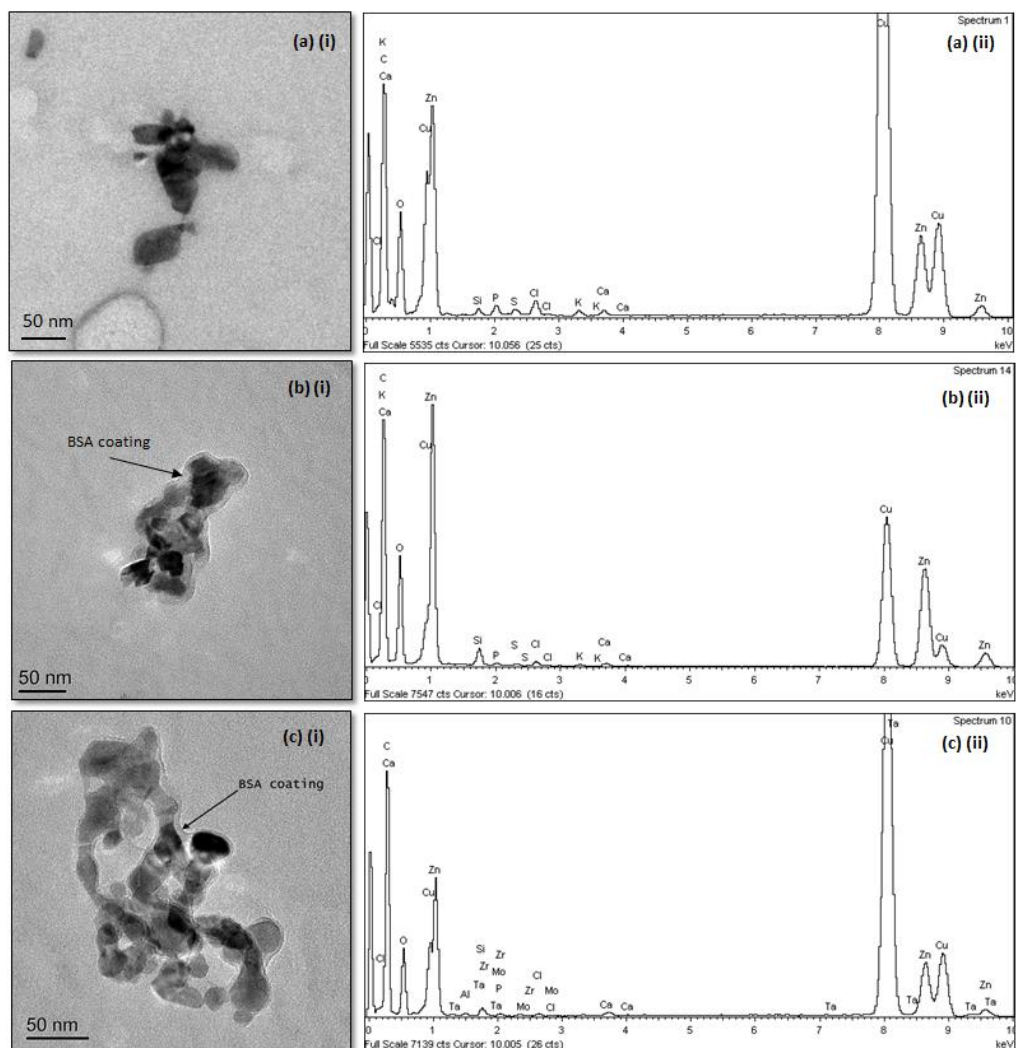


**Figure 6-22 TEM analysis of ZnO samples dispersed in DMEM and BSA at a concentration of 100  $\mu\text{g/ml}$ , prepared by plunge freezing route; (a)(i) TEM image of EN-Z-1 and (a)(ii) EDX spectrum for the cluster of particles in (a)(i); (b)(i) TEM image of EN-Z-2 and (b)(ii) EDX spectrum for the cluster of particles in (b)(i); (c)(i) TEM image of EN-Z-3 and (c)(ii) EDX spectrum for the cluster of particles in (c)(i).**

Comparing the size distributions obtained by PF-TEM for ZnO NPs suspended in DMEM (Figure 6-23) with those suspended in water (Figure 6-16) indicates that the colloidal stability of ZnO NPs is reduced in DMEM. For example, the maxima of the agglomerate size distributions for EN-Z-1 in water and DMEM are 35 nm (Figure 6-16 (a)) and 91 nm (Figure 6-23 (a)) respectively.

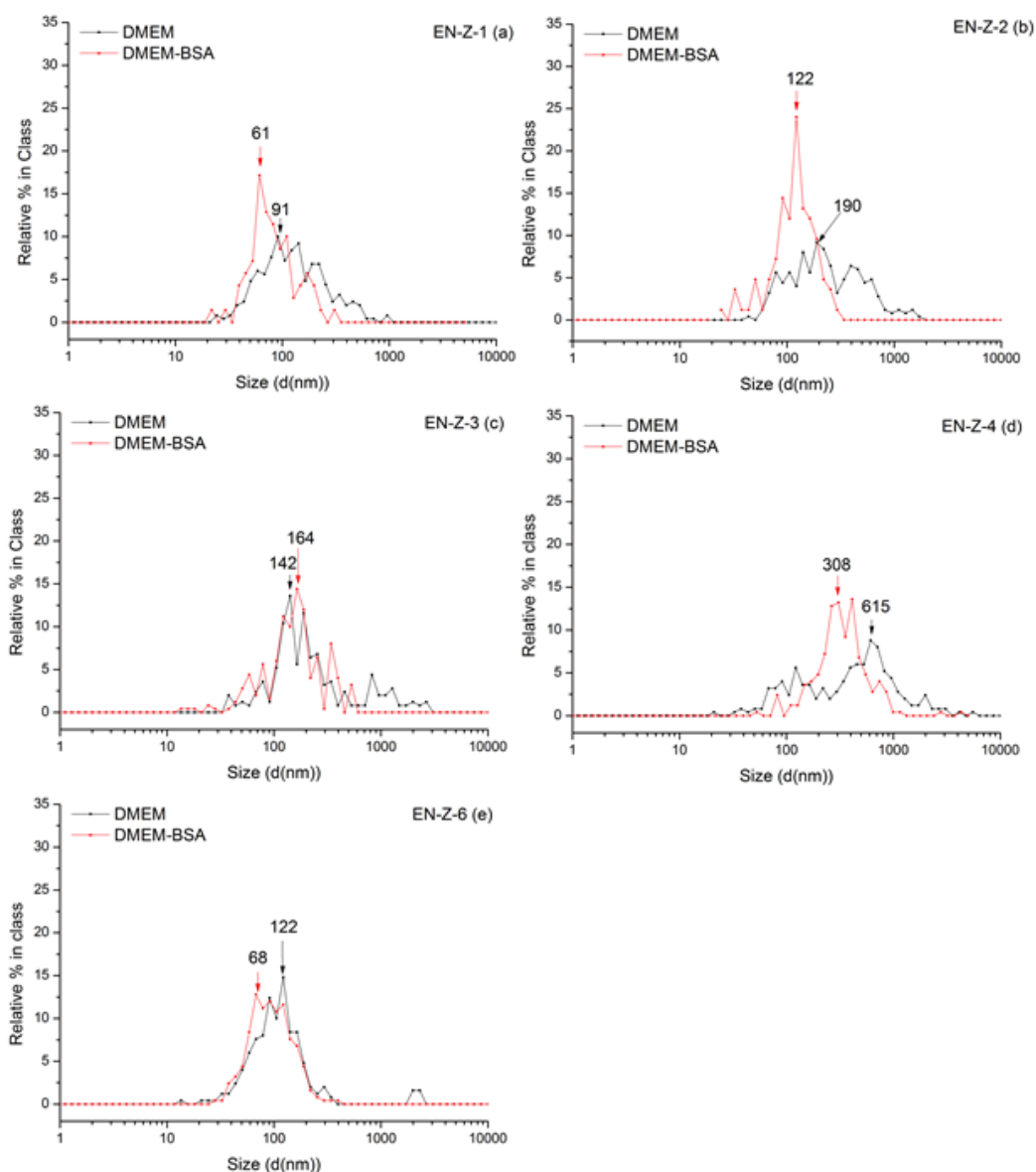


**Figure 6-23 Particle size distributions for (a) EN-Z-1, (b) EN-Z-2, (c) EN-Z-3, (d) EN-Z-4 and (e) EN-Z-6 dispersed in DMEM and DMEM-BSA, as determined by PF-TEM.**

### **6.3 Comparison of Agglomerate Size Distributions Measured by Plunge Freezing Transmission Electron Microscopy and Dynamic Light Scattering Techniques**

For 1000  $\mu\text{g/ml}$  suspensions of ZnO in water, the agglomerate size distributions measured by DLS and PF-TEM are in reasonable agreement with one another. For example, the distribution by DLS for EN-Z-1 (Figure 6-8 (a)) measured is between 30 and 300 nm with a peak at 73 nm, whereas the distribution obtained by PF-TEM (Figure 6-16 (a)) measures agglomerates between 10 and 1000 nm with a peak at 50 nm. However, it must be noted that the majority of the agglomerates in the sample measured by PF-TEM were smaller than 300 nm and that only a few agglomerates were measured that were larger than this.

The size distributions measured by DLS and PF-TEM for EN-Z-1 at different concentrations are in good agreement with one another. For the remaining samples, although the PF-TEM size distributions for varying concentrations are over relatively similar ranges, DLS measures significantly varied size distributions for the different concentrations of ZnO. In the case of EN-Z-2, EN-Z-3 and EN-Z-6, the primary peak in the DLS plot occurs at a significantly larger size when the concentration of ZnO is reduced from 1000 to 100  $\mu\text{g/ml}$  indicating a lower stability. The opposite result is in fact expected as a reduction in the concentration of particles in a sample will reduce the rate of NP collisions and hence reduce the formation of agglomerates (Allouni, 2009). This brings into question the accuracy of the size distributions measured by DLS at low concentrations of ZnO. A possible cause for the inaccuracy of the results may be due to a much larger fraction of the ZnO being dissolved at the lower concentration. The smaller agglomerates and primary particles will dissolve over a shorter time than the larger agglomerates. Therefore the suspension will comprise fewer small agglomerates and primary particles. A limitation of DLS is related to the greater scattering of light by larger particles. Therefore, the intensity of light scattered by the undissolved larger agglomerates would swamp the signal produced from the very low number of fine agglomerates. For EN-Z-1, the sample has a considerably lower distribution of sizes as compared to the other samples of ZnO as it has greater colloidal stability and it also has a slower dissolution rate (Mu et al., 2013). Therefore the effect of the high intensity of scattered light from the larger

agglomerates swamping the signal produced by light scattered from fine agglomerates is not as significant.

The PF-TEM results for ZnO NP suspensions in water over varying concentrations show that the average agglomerate size decreases with decreasing ZnO NP concentration (Figure 6-16).

The PF-TEM results for suspensions of EN-Z-2, EN-Z-3 and EN-Z-4 in water and in DMEM do not identify significant peak maxima, indicating that there is a continuous range of agglomerate sizes. The polydisperse nature of the suspensions identified by PF-TEM explains the potentially unrepresentative size distributions measured by DLS. For EN-Z-1 and EN-Z-6, PF-TEM indicates a defined distribution of sizes, confirming the superior stability of these samples, originally indicated by zeta potentials (Figure 6-5).

Even though the sampling size is much smaller for PF-TEM than for DLS, the PF-TEM size distributions for the 100  $\mu\text{g/ml}$  appear to give a more accurate representation of the whole range of sizes of agglomerates present in the suspensions. Although the DLS results indicate otherwise, the size distributions obtained from PF-TEM reveal that there are in fact still very small agglomerates present in the samples at lower concentrations. Therefore the DLS results for the 10  $\mu\text{g/ml}$  samples are likely to also be unrepresentative of the size distribution for the samples, however as there are no PF-TEM results to compare them with, this can't be confirmed. The DLS results for this concentration are probably not even relevant because of the equilibrium solubility in water and DMEM being just above or below 10  $\mu\text{g/ml}$ .

The distributions obtained from both PF-TEM and DLS indicate that BSA has a stabilizing effect on NP suspensions. The PF-TEM results show that the number of large agglomerates is reduced but that the distribution of sizes is not altered considerably. Whereas DLS results indicate that the addition of BSA drastically reduces the distribution of agglomerate sizes. This is evidence for the effect of large agglomerates swamping the signal from fine agglomerates, causing the size distribution measured by DLS to be concentrated on one fraction of sizes. The reduction in agglomerate size distribution of ZnO in suspension with the

addition of BSA has previously been reported in the literature (Tantra et al. 2010; Churchman et al. 2013).

The results indicate consistently that ZnO NP samples are more heavily agglomerated when they are suspended in DMEM than in MilliQ water. This effect has previously been reported by Hsiao and Huang (2011). The more pronounced agglomeration observed in DMEM is largely due to the high ionic strength of the medium which reduces the stability of ZnO NPs (Bian et al., 2011). Increasing the ionic strength of the suspension reduces the Debye length of the electrical double layer and therefore increases the tendency of the NPs to agglomerate (Verwey and Overbeek, 1948).

The results presented indicate that although DLS and PF-TEM are suitable techniques for determining particle size distributions in suspensions, dispersion characteristics such as low NP concentration due to dissolution, impact on the validity of the results and the time taken to acquire results. The results presented clearly highlight the limitations of DLS when analyzing polydisperse samples, especially with low NP concentrations. Alternative methods of determining the agglomerate size distribution of a NP suspension have therefore briefly been investigated and are discussed in section 6.3.1.

### **6.3.1 Alternative Techniques for Imaging Nanoparticle Dispersions**

The importance of characterising NP samples in solutions and the limitations encountered by DLS and PF-TEM prompted our investigation into alternative techniques such as atmospheric scanning electron microscope (ASEM) and liquid cell transmission electron microscopy (LC-TEM). The ASEM is capable of analysing samples held under atmospheric conditions and as such, can directly image a liquid sample. In LC-TEM, a liquid cell TEM holder is inserted into a TEM and imaged through an electron transparent membrane. The instruments are both located at the University of York. Due to the superior dispersion exhibited by EN-Z-1 as compared to the other ZnO samples, this sample was chosen to be analysed by the two techniques.

### 6.3.1.1 Atmospheric Scanning Electron Microscope

A 100  $\mu\text{g/ml}$  suspension was added to the sample chamber, details of which are provided in section 3.3.1.1. Images were recorded at reasonably low magnifications (approx. 10,000 x), an example of which is presented in Figure 6-24 (a). At higher magnifications ( $\geq 30,000$  x) the particles tended to dislodge from the silicon nitride membrane. This resulted in the images recorded displaying streaks where the particles moved. This effect is demonstrated in Figure 6-24 (b). A particle size distribution was produced by measurement of the agglomerates in the images recorded. The results are compared with size distributions obtained for the 100  $\mu\text{g/ml}$  EN-Z-1 suspension in water using DLS and PF-TEM in Figure 6-25, however it must be noted that due to a lack of images only 75 agglomerates were measured for the ASEM distribution. The size distributions obtained by PF-TEM, DLS and ASEM have peak maxima at 35, 80 and 200 nm respectively. The larger particle size distribution determined by ASEM may be explained by a number of reasons. The low magnification of the images may inhibit the visualization of the very small particles and agglomerates present in the sample. Some of the NPs in the EN-Z-1 sample are as small as 10 nm and the resolution of the instrument was quoted as being around 20 nm. Additionally, the particles observed in the ASEM images are those which are attached to the membrane. Smaller particles move around in a solution due to Brownian motion more rapidly than larger particles and will sediment more slowly so one might expect the particles observed to be the larger fraction of the sample resulting in a biased distribution. Furthermore, as a result of the low magnification at which the images had to be recorded, the edges of the NP agglomerates are not particularly well defined.

This method of characterisation of NP dispersions is advantageous in that it directly measures the NPs *in situ*. However, the problems our investigations encountered with regard to the biased particle size distribution determined by the technique would need to be addressed. Additionally, when the suspending media is something more complex than MilliQ distilled water, issues may arise distinguishing NPs from other components of the solution.

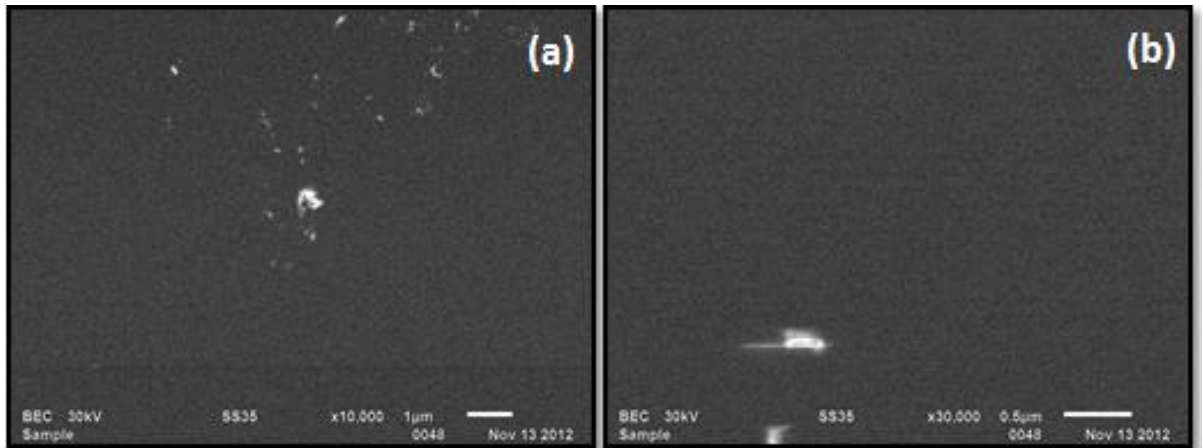


**Figure 6-24 ASEM analysis of a 100 µg/ml suspension of EN-Z-1. (a) Low magnification (10,000x) ASEM image of the dispersion showing both agglomerates and individual NPs; (b) Image at 30, 000 x magnification displaying a particle moving on the membrane as the image is recorded.**

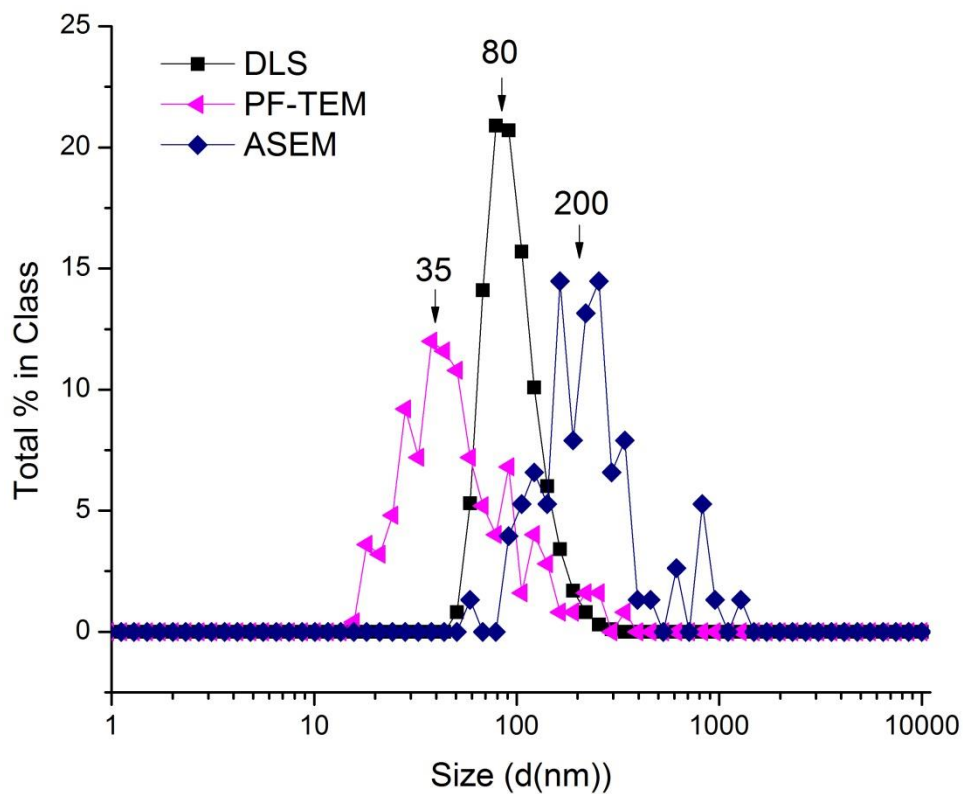


**Figure 6-25 Graph comparing the particle size distributions measured for a 100 µg/ml dispersion of EN-Z-1 in MilliQ water, obtained by DLS, PF-TEM and ASEM.**



### 6.3.1.2 *Liquid Cell Transmission Electron Microscopy*

A suspension of 100  $\mu\text{g/ml}$  EN-Z-1 in MilliQ water was characterized by liquid cell transmission electron microscopy (LC-TEM). Gold NPs (AuNP) (Average size  $\approx 100$  nm) were added to the suspension in order to help focus the beam. Unfortunately, the AuNPs were not easily distinguishable from the ZnO NPs. A low magnification image of the sample is presented in Figure 6-26 (a). The white spherical particles that can be seen on the image are likely to be the AuNP standard. An image of what is probably a small ZnO agglomerate is presented in Figure 6-26 (c). This image was recorded at the opposite side of the membrane to that in Figure 6-26 (b). On this particular side of the membrane, when the magnification was increased in order to investigate the particles presented in Figure 6-26 (c) in more detail, flocculates of what is suspected to be ZnO or zinc salts began to form. It is unclear whether these flocculates were solid particulates already present in the sample, that became visible as a result of attachment to the surface of the membrane, or whether the flocculates precipitated from solution as a result of the solution interaction with the electron beam. EDX was attempted on various regions of the sample, and although a gold signal was obtained for the particle present in Figure 6-26 (b), in the majority of cases no signal could be detected.

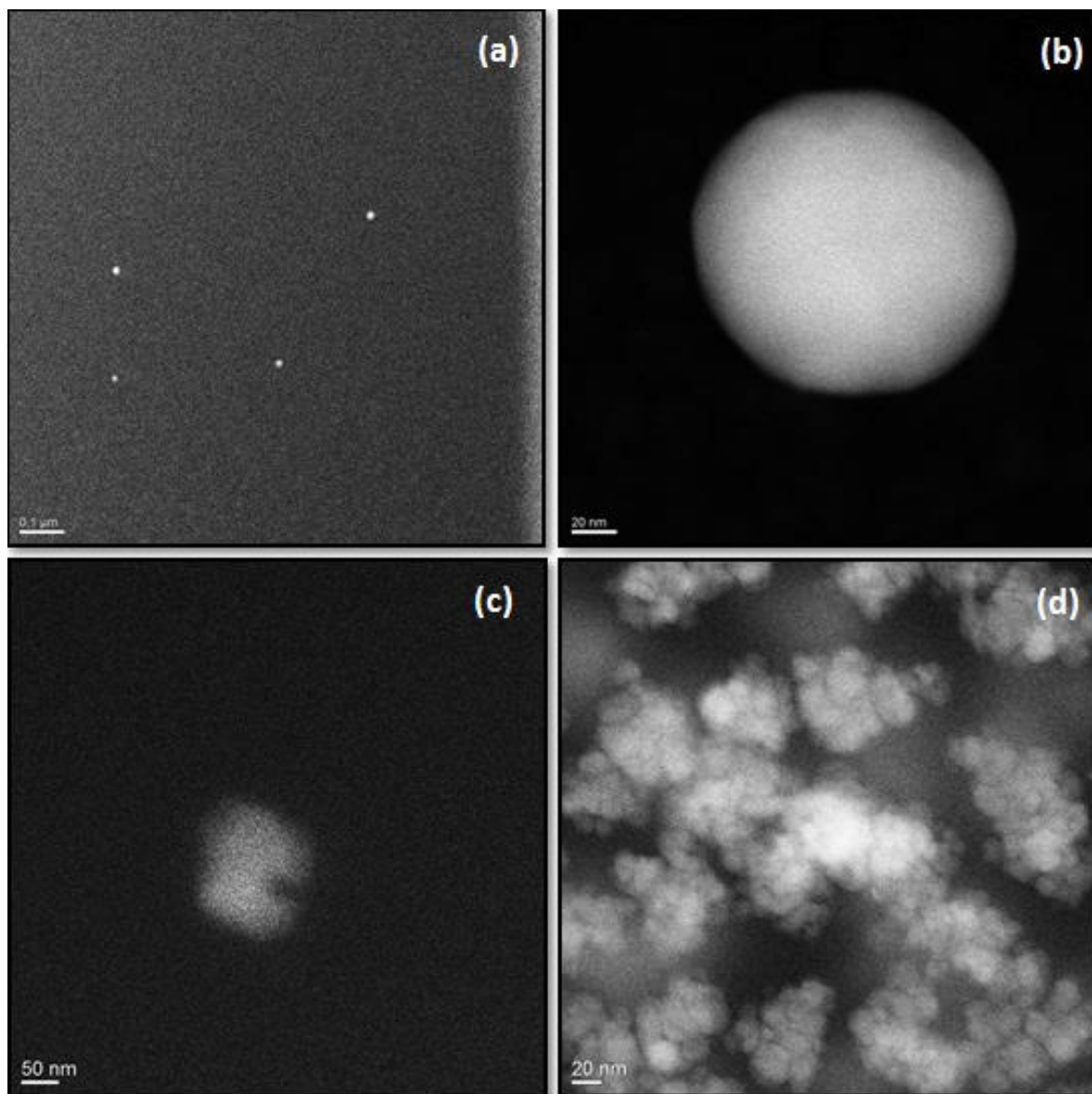


**Figure 6-26** Liquid cell TEM images of a 100 µg/ml suspension of EN-Z-1 (a) at low magnification showing AuNPs (b) showing an AuNP at high magnification, (c) displaying a ZnO NP agglomerate and (d) showing the flocculates of ZnO or zinc salts produced when the electron beam is focused on a region at high magnification for 10 seconds.

## 6.4 In Summary

Results from this chapter have emphasized the complexity of ZnO NP suspensions, the characteristics of which alter dependent on the liquid in which they are suspended. The ionic strength, temperature and pH of the solution all affect the physicochemical characteristics of the ZnO NPs.

The dispersion stability of ZnO NP powders EN-Z-2, EN-Z-3 and EN-Z-4 is poor, with agglomeration and sedimentation occurring within 1 hour of preparation. EN-Z-1 and EN-Z-6 samples have improved dispersion characteristics and remain in suspension for longer than 24 hour, most likely as a result of organic compounds present on the surface of the NPs.

General trends observed from the ZnO NP suspensions investigated in this chapter are:

1. The agglomeration of ZnO increases when suspended in DMEM as compared to in water (consistent with Hsiao & Huang, 2011)
2. The solubility of ZnO increases when suspended in DMEM as compared to in water (consistent with Reed et al. 2012)
3. Solubility of ZnO increases with decreasing solution temperature (consistent with Reed et al. 2012)
4. The addition of BSA has a dispersing effect on ZnO NP suspensions. This is due to an increase in the negativity of the zeta potential, consistent with findings reported by Tantra et al. (2010).

The dispersing effect of BSA is significant as there are many compounds present in the physiological and aquatic environment, such as human serum albumin and humic acid that may behave in a similar way. This reduction in the hydrodynamic size of the NPs can significantly affect their bioavailability and fate and alter their potential toxicity to organisms.

The results for the agglomerate size distributions obtained by PF-TEM and DLS were in good agreement when comparing varying concentrations of EN-Z-1 in water.

The DLS results for the other 4 ZnO samples showed considerable variations in the distribution of sizes with changing concentration. Whereas, PF-TEM size distributions measured for the other 4 ZnO samples were in reasonable agreement for different concentrations of ZnO, with a marginal reduction in the agglomerate size distribution with decreasing ZnO NP concentration indicated by most of the samples. This is expected as a result of fewer particle – particle collisions which lowers the potential for NP agglomeration and sedimentation (Allouni et al., 2009).

The variation in the size distributions measured by DLS for different ZnO concentrations may be explained by the solubility of ZnO. ICP-MS results indicate that as the concentration of the sample decreases, the percentage of the sample in solution increases. This is expected as a stable equilibrium solubility of ZnO in water at pH 7.6 and 24 °C has previously been reported as equivalent to the complete dissolution of 20 µg/ml ZnO (16 µg/ml Zn) (Franklin et al. (2007)). Hence, the concentration of solid ZnO NPs is much lower than the nominal concentration because a significant quantity is dissolving into solution. For low concentrations this means that a very small number of primary particles remain in suspension. This increases the swamping effect on the intensity of light measured from the larger agglomerates, hence skewing the size distribution measured for the sample.

The size distributions obtained for the samples by PF-TEM were an accurate representation of the range of agglomerates in the suspension, as this involved direct measurement of the sizes from TEM images. Additionally, the technique was validated by comparison with DLS for suspensions with high ZnO concentration (1000 µg/ml). However, with the exception of EN-Z-1, for the 10 µg/ml sample, a size distribution could not be obtained due to a lack of data collected. Taking into consideration the equilibrium solubility of ZnO measured by Franklin et al. (2007), this is likely to be due to dissolution of the majority of the sample. Although PF-TEM may give a more accurate representation of the agglomerates that are actually measured, the number of agglomerates used to obtain the sample size distribution (250) is very low when compared to how many agglomerates are actually present in the suspension and therefore this technique provides only semi-quantitative analysis.

With the exception of EN-Z-1, very few NPs were located in the PF-TEM images for the 10  $\mu\text{g/ml}$  concentration. It was thought that this may be due to the slower dissolution of EN-Z-1 (Mu et al., 2013). However, ICP-MS results show that after 24 hour in solution (the point at which the PF-TEM and DLS size distributions were obtained), a similar amount of ZnO is in solution for all ZnO NP samples. The different solubility for EN-Z-1 measured in this investigation, compared with that reported in our previous publication (Mu et al., 2013) most probably arises as a result of the controlled level of  $\text{CO}_2$  and buffered pH in the experiments reported in our prior investigation. Additionally, the results indicated that for all samples of ZnO, at a concentration of 10 $\mu\text{g/ml}$ , only between 20 and 50 % of the ZnO was in solution. However, the ICP-MS results were found to be unrepresentative of the samples used in the dispersion studies due to inconsistencies in experimental conditions, i.e. increasing volume of air in the vials over the course of the experiment, causing the pH to rise. This would reduce the solubility of ZnO. However, the ICP-MS results show a high quantity of dissolved ZnO at  $T = 0.6$  hour, with the exception of EN-Z-1. Reed et al. (2012) reported a continuous increase in the amount of zinc in solution as time proceeds with a similar experimental set up to the dispersion studies conducted here which could indicate that the ZnO in the 10  $\mu\text{g/ml}$  samples is mostly dissolved after 24 hour. The reason NPs were observed in EN-Z-1 and not in the other 4 samples at 10  $\mu\text{g/ml}$  may be due in part to the slower dissolution (Mu et al., 2013), but is also probably due to the higher actual concentration of ZnO measured for this sample. At a concentration of 10  $\mu\text{g/ml}$ , it is very close to the equilibrium solubility in DMEM at 37  $^\circ\text{C}$  measured by Song et al. (2010), Xia et al. (2008), and Reed et al. (2012) where the concentration of dissolved ZnO reached 12.4 , 18.3 and 8.75  $\mu\text{g/ml}$  respectively. Additionally, the equilibrium solubility for ZnO in DMEM was measured maintaining a pH of 7.6 as 5.7  $\mu\text{g/ml}$ . It is therefore not surprising that EN-Z-1 presented many more ZnO NPs in the PF-TEM images than the other samples of ZnO.

The ICP-MS results indicate that the concentration of ZnO in suspension at which the solubility is in equilibrium is between 10 and 30  $\mu\text{g/ml}$  which is in

agreement with Franklin et al. (2007), Song et al. (2010), Xia et al. (2008) and Reed et al. (2012). However, due to the increasing pH over the course of the experiment, the equilibrium solubility is not constant and therefore an exact value has not been reported. The dissolution of ZnO at low concentrations is significant to toxicity studies as it shows that at toxicologically relevant concentrations that are likely be encountered in the aquatic environment, there is a high quantity of dissolved zinc in solution.

The investigations carried out on the sample provide us with a good idea of the characteristics of the suspensions being administered to the toxicity assays. A table summarizing the information acquired for all 5 samples investigated is presented in Chapter 7 along with the toxicity results of cell viability assay and genotoxicity assays and additionally cell uptake studies.

Results emphasize the importance of investigating the behavior of NPs in toxicologically relevant media, in order to correctly interpret results of toxicity assays. Great care must be taken to identically replicate the experimental conditions of cell viability assays, in order to determine NP suspension characteristics accurately. As has been demonstrated, even factors such as the amount of air remaining in a vial can significantly influence the solution behavior.

## 7 Toxicity of ZnO Nanoparticles and Discussion

In this thesis, 5 ZnO NP samples were sourced and a characterisation protocol was implemented in order to obtain detailed physicochemical characteristics of the samples, the results of which are presented in Chapter 4 and 5, with dispersion and solubility reported in Chapter 6.

In order to assess the toxicity of the ZnO NP samples, *in vitro* toxicity assays have been carried out using A549 (human lung alveolar carcinoma) cells. Effects of the ZnO NPs on the viability and genetic fidelity of the cells were evaluated using the MTT (thiazolyl blue tetrazolium bromide) and Comet assays respectively. In addition, toxicity has been assessed by monitoring the uptake of NPs into the cells by TEM.

In this chapter, a summary of the physicochemical characteristics of the 5 ZnO NP samples is provided (Section 7.1) as well as the results of the MTT assay (Section 7.2.1), Comet assay (Section 7.2.2) and uptake experiments (Section 7.2.3). The key characteristics of ZnO NP samples contributing to their toxicity *in vitro* are identified.

### 7.1 Summary of ZnO Nanoparticle Physicochemical Characteristics

In order to interpret the results of NP toxicity assays, a detailed understanding with regard to the physicochemical characteristics of the samples used in the investigations is required. With this detailed information in hand, the effect of ZnO NP size, morphology, phase, composition, surface chemistry and solution chemistry on the toxicity to cells may be assessed. A summary of the physicochemical characteristics of the 5 ZnO NP samples investigated in this thesis is presented in Table 7-1. The toxicological investigations, for which the results are reported in this chapter, were carried out in DMEM at 37 °C, over 24 hours using a variety of ZnO concentrations. Therefore the results summarized in the table have been selected to provide information on the state of the NPs under these particular exposure conditions.

XRD revealed EN-Z-1, EN-Z-4 and EN-Z-6 to be monophasic ZnO; whereas EN-Z-2 and EN-Z-3 contained a small amount of a secondary phase, which was identified as hydrozincite ( $\text{Zn}_5(\text{CO}_3)_2\text{OH}_6$ ). It was not determined whether this phase was residual to the synthesis process or had formed afterwards via the adsorption of atmospheric  $\text{CO}_2$  and  $\text{H}_2\text{O}$ .

Zinc carbonate ( $\text{ZnCO}_3$ ) was found to be present at the surface of all of the dry powder samples, identified by TGA with EGA, FTIR and XPS (Sections 4.2 and 5.3). In addition to this, all of the dry powder samples contained moisture. An organic compound which was identified as an aliphatic polyether was detected on the surface of the EN-Z-1 NPs by TGA-EGA, FTIR, XPS and NMR (Figure 4-6, Figure 4-9, Figure 4-13 and Figure 4-14 respectively). Additionally, residual DEG precursor was detected on the surface of the EN-Z-6 NPs by FTIR, XPS and NMR (Figure 5-18, Figure 5-22 and Figure 5-24 respectively).

The primary particle sizes were determined by BET, XRD and TEM. All of the samples were polydisperse, with EN-Z-4 having the narrowest size distribution of the synthesized samples and EN-Z-3 having the narrowest size distribution of the commercial samples. The average particle Feret ratio calculated for the samples was  $> 1$  for all 5 samples, indicating that the majority of particles in the samples were elongated. In EN-Z-1, EN-Z-4 and EN-Z-6, the elongation was significantly more prominent than in EN-Z-2 and EN-Z-3 samples.

EN-Z-1 was found to have the greatest colloidal stability over time; this was to be expected as the sample was purchased as a colloidal suspension in water. EN-Z-6 dispersed in water was found to be stable after 24 hours, which may be attributed to the residual DEG on the surface of the NPs. The remaining 3 samples were unstable over 24 hours. Analysis of the agglomerate size distributions for ZnO samples in water and DMEM, revealed that ZnO NPs are more prone to agglomeration when dispersed in DMEM than in water. This was thought to be due to the high ionic strength of the cell culture medium. The zeta potential of the EN-Z-1 sample in water



was negative, whereas for the other samples the zeta potentials measured were positive. This may be attributed to the aliphatic polyether coating present on the EN-Z-1 NP surface.

The agglomerate size distributions measured by PF-TEM, for the samples after 24 hours in DMEM (and then sonicated for 20 minutes) reveal that for all samples, there are a wide distribution of sizes present, ranging from individual primary particles up to large agglomerates, thousands of nanometres in diameter. The EN-Z-1 and EN-Z-6 samples have the narrowest and smallest size distribution of agglomerates. Unfortunately, the PF-TEM size measurements do not give an accurate representation of the agglomerates present in the cell assay solutions after 24 hours as there is no sonication in the toxicity assay. However, the measurements give an indication into the agglomeration of the ZnO NP samples and the way in which the agglomerate size distributions compare at this stage in the investigation.

The amount of dissolved ZnO was determined by ICP-MS over a range of concentrations. This was measured in DMEM at 37 °C after 24 hours in suspension. It must be noted that the experimental set up for the solubility measurements differed from the *in vitro* assays, which resulted in an increase in the pH of the solution which led to a lower ZnO solubility. Therefore the absolute amount of ZnO in solution measured by the solubility experiment will differ from the actual amount of ZnO in solution administered to the cells *in vitro*. Our investigations on the ENNSATOX project have shown by electroanalytical methods that the actual amount is likely to be 5.7 µg ZnO/ml (Mu et al., (2013)). The dissolution experiments revealed that for all samples of ZnO at all concentrations, a fraction of ZnO was dissolved in solution after 24 hours. The amount of dissolved ZnO was reasonably consistent for all 5 samples of ZnO after 24 hours indicating that solubility did not vary considerably between samples, however the dissolution rate for coated EN-Z-1 was found to be slower than that of the uncoated samples (consistent with Mu et al., (2013)). Over the course of the solubility experiments, it was determined that the total actual amount of ZnO in the suspensions varied significantly between samples, and was inconsistent with the nominal concentrations dispersed in solution. In particular, the actual

concentration of EN-Z-1 was consistently higher than the concentrations of the other ZnO NP samples (Table 6-1 and Table 6-2). This was assumed to be due to an error in the commercial supplier's quoted concentration and issues and also due to issues arising in sampling when preparing dilutions of the ZnO NP suspension. This is a crucial finding as many studies have reported significantly increased toxicity for only small variations in ZnO NP concentration (Lin et al., 2008; Hsiao &Huang, 2011).

The overview of physicochemical characteristics of the 5 ZnO NPs, reveals the variable nature of ZnO NP samples, regarding particle size, morphology and purity. Additionally, the complexity of characterizing ZnO NPs in solutions has also been highlighted, however consistent themes have been identified:

1. ZnO NPs reach an equilibrium solubility in DMEM within a few hours. At concentrations above this equilibrium, the NPs are agglomerated as either ZnO or ZnO and re-precipitated ZnCO<sub>3</sub>.
2. The polymer coating on EN-Z-1 increases the time to reach equilibrium to between 24 and 48 hours and stabilises the colloidal suspension.

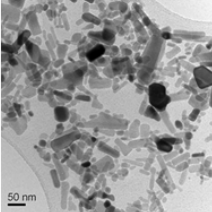
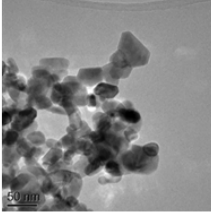
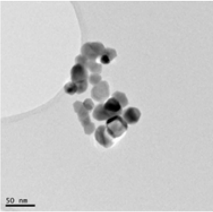
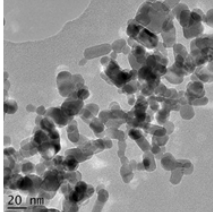
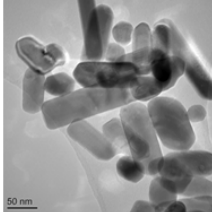
## **7.2 Toxicity**

In order to assess the potential cyto- and genotoxicity of ZnO NPs to cells, the MTT and Comet assay were performed, using 5 ZnO NP samples at concentrations in the range 0.01 to 1000 µg/ml. All of the toxicity experiments conducted in this study were carried out using A549 (human lung alveolar carcinoma) cells in DMEM (no serum); exposures were incubated for 24 hours at 37 °C with 5 % CO<sub>2</sub>. A549 cells were selected as there is evidence that when ZnO NPs uptake into the lungs, they rapidly dissolve and induce toxicity (Cho et al., 2011).

### **7.2.1 Cytotoxicity**

The MTT assay was employed in order to assess the cytotoxicity of the ZnO NP samples. The MTT assay is a colorimetric assay which measures cellular metabolic activity and can therefore give an indication as to the number of viable cells.

**Table 7-1 Summary of the physicochemical properties of ZnO nanoparticles samples selected for toxicological investigations**

Name		EN-Z-1	EN-Z-2	EN-Z-3	EN-Z-4	EN-Z-6
Source (Catalogue Number)		Alfa Aesar (45409)	Alfa Aesar (44533)	Micronisers Pty Ltd (Nanosun™)	Synthesized in House	Synthesized in House
Phase and Purity (XRD)		Zincite (01-079-0206) = hexagonal ZnO	Zincite (01-079-0206) = hexagonal ZnO Secondary phase present consistent with hydrozincite (00-014-0256)	Zincite (01-079-0206) = hexagonal ZnO Secondary phase present consistent with hydrozincite (00-014-0256)	Zincite (01-079-0206) = hexagonal ZnO	Zincite (01-079-0206) = hexagonal ZnO
Surface Composition/Purity (TGA, FTIR, XPS,NMR)		Organic compound, possibly an aliphatic polyether is present on the surface of the NP	ZnCO <sub>3</sub> present at NP surface	ZnCO <sub>3</sub> present at NP surface	ZnCO <sub>3</sub> present at NP surface	ZnCO <sub>3</sub> + residual DEG on NP surface
TEM						
Particle Size (nm) (TEM) (a)		Length = 30 ± 20; Width = 16 ± 10	Length = 40 ± 20; Width = 30 ± 12	Length = 38 ± 10; Width = 30 ± 7	Length = 23 ± 8; Width = 14 ± 4	Length = 47 ± 26; Width = 26 ± 8
Ferret Ratio (TEM) (a)		Feret Ratio = 1.9 ± 0.8	Feret Ratio = 1.45 ± 0.3	Feret Ratio = 1.34 ± 0.25	Feret Ratio = 1.6 ± 0.4	Feret Ratio = 1.8 ± 0.5
Stability in water over time (DLS) (b)		Stable over 24 hours	Unstable over 24 hours	Unstable over 24 hours	Unstable over 24 hours	Stable over 24 hours
Zeta Potential in Water (mV) (c)		-14	5.2	8.5	14	15
Agglomerate Size Distribution in Water (nm) (PF-TEM) (d)		Range = 10 - 400 (max at 35)	Range = 20 - 3000 (max at 130)	Range = 50 - 1100 (max at 130)	Range = 30 - 5000 (max at 180)	Range = 30 - 900 (max at 70)
Agglomerate Size Distribution in DMEM (nm) (PF-TEM) (e)		Range = 30 - 300 (max at 91)	Range = 40 - 2000 (max at 190)	Range = 10 - 4000 (max at 142)	Range = 20 - 700 (max at 615)	Range = 10 - 400 (max at 122)
Nominal ZnO concentration (µg/ml)	1	22	45	54	56	50
	3	24	44	48	55	55
	10	27	45	45	33	32
	30	13	17	11	11	18
	100	4	5	5	4	4

(a) Primary particle size measured from 250 nanoparticles in TEM images; (b) Stability measured in water at 25 °C 1000 µg/ml, (c) Zeta potential measured in water at 25 °C at 1000 µg/ml; Agglomerate size distribution measured in (d) Water at 37 °C at 100 µg/ml and (e) DMEM at 37 °C at 100 µg/ml; (f) Dissolved ZnO concentration measured DMEM at 37 °C after 24 hours

All of the MTT experiments were performed by Qingshan Mu and Ritta Partanen at the University of Leeds. The results of the MTT assay, presented in Figure 7-1 display the amount of viable cells remaining after a 24 hour exposure to a range of ZnO NP concentrations, as a percentage of viable cells measured in the control sample. Exposures were carried out in triplicate; the data plotted is an average of the 3 measurements and the error bar is determined by the standard deviation of the measurements.

In addition to the 5 ZnO samples, the MTT assay was also performed using a solution of zinc sulphate heptahydrate ( $\text{ZnSO}_4 \cdot 7(\text{H}_2\text{O})$ ). The concentration was adjusted such that the quantity of zinc was the same as for the ZnO experiments. As  $\text{ZnSO}_4 \cdot 7(\text{H}_2\text{O})$  was used, this meant that the dry weight of the powder was 3.5 times higher for the  $\text{ZnSO}_4 \cdot 7(\text{H}_2\text{O})$  than for the ZnO NPs.

Our team of researchers on the ENNSATOX project found  $\text{ZnSO}_4$  to be more toxic than ZnO NP samples (Mu et al., 2013). A continuously increasing  $\text{Zn}^{2+}$  concentration was measured with increasing  $\text{ZnSO}_4$  concentration such that the  $\text{Zn}^{2+}$  solubility limit was exceeded by supersaturation. It was concluded that ZnO NPs reach a solubility limit ( $\sim 5.7 \mu\text{g ZnO/ml}$ ), above which they either remain intact or dissolve and re-precipitate in DMEM as  $\text{ZnCO}_3$ . Either way, the particles were found to induce lower toxicity than  $\text{Zn}^{2+}$ . The toxicity of EN-Z-1 and EN-Z-2 was investigated (Mu et al., 2013). EN-Z-1 induced higher toxicity than EN-Z-2 which was attributed to the presence of the coating on EN-Z-1 NPs. The coating was found to enhance interaction with a model membrane, and also compromised the membrane to a greater extent than EN-Z-2. They found that for EN-Z-1, there was direct interaction between non-dissolved NPs and cells by measuring an increased cytoplasmic concentration of  $\text{Zn}^{2+}$  as compared to EN-Z-2, providing evidence for intracellular dissolution of EN-Z-1 NPs. Therefore, it was postulated that the increased toxicity of EN-Z-1 was due to enhanced uptake, either passively by compromising the plasma membrane or endocytically by promoting interaction with the plasma membrane, and hence enabling intracellular release of  $\text{Zn}^{2+}$ . Furthermore, ZnO NPs with needle-like morphology were found to enhance toxicity by frustrated

endocytosis, i.e. disrupting the cell membrane, leading to the release of toxic enzymes resulting in inflammation.

The MTT assay results acquired in this investigation (Figure 7-1) indicate that even at very low ZnO concentrations, i.e. 0.01  $\mu\text{g/ml}$ , there is a statistically significant ( $p < 0.05$ ) reduction in cell viability for many of the samples.

EN-Z-3 exhibits an unusual response in that there is an increase in viability measured when ZnO NPs are added up to a concentration of 10  $\mu\text{g/ml}$ . It could be that cell growth is stimulated by the particles, however this is unlikely as the effect is not observed for the other samples. A statistically significant reduction in cell viability is measured at 1000  $\mu\text{g/ml}$ , however the toxicity measured is still much lower than for the other ZnO NP samples. It may be argued that the EN-Z-3 sample elicited a lower toxic response as compared to the other ZnO NPs due to the more equiaxial nature of the NPs in the sample. For example, Hsiao & Huang (2011) reported on the higher toxicity of ZnO nanorods as compared to ZnO nanospheres to A549 cells after an exposure of 24 hours. Our previous investigations also reported on the lower toxicity of equiaxed ZnO NPs as compared to NPs with high aspect ratio (Mu et al., 2013). However, the EN-Z-2 sample has a similar average particle Feret ratio and therefore this is unlikely to be the reason for the lower measured toxicity for the EN-Z-3 sample. For now, the results will be treated as abnormal and the MTT assay should be repeated with a newly prepared suspension of EN-Z-3.

EN-Z-1, EN-Z-6 and soluble  $\text{ZnSO}_4$  all induce significant cytotoxicity at 0.01  $\mu\text{g/ml}$ . However  $\text{ZnSO}_4$  reduces cell viability by a higher percentage across all of the concentrations investigated. This indicates that even at concentrations as low as 1  $\mu\text{g/ml}$ , where one would expect all of the ZnO NPs to dissolve, there is a fraction of undissolved zinc remaining (in agreement with solubility data (Table 7-1)). This indicates that there is a higher concentration of zinc in solution for  $\text{ZnSO}_4$ , since for the ZnO NP samples, the NPs may act as nucleation sites for the re-precipitation of zinc to form lower solubility nanoparticulate  $\text{ZnCO}_3$  (Reed et al., 2012; Mu et al., 2013) thus implying that  $\text{ZnCO}_3$  nanoparticles are less cytotoxic than  $\text{Zn}^{2+}$ .

At 10 and 100  $\mu\text{g/ml}$  all of the samples elicit a statistically significant toxic response however the results for EN-Z-1 compared with the other NP samples are in

stronger agreement with cell viability measurements reported in the literature, determined by the MTT assay for 24 hour ZnO NP exposures to A549 cells. For example, Ahamed et al. (2011) administered suspensions of ZnO nanorods ( $d_{TEM} = 52$  nm;  $d_{DLS} = 97$  nm; aspect ratio = 2.88) to A549 cells and found that increasing the ZnO NP concentration from 10 to 100  $\mu\text{g/ml}$ , induced a reduction in cell viability from 72 to 40 % respectively.

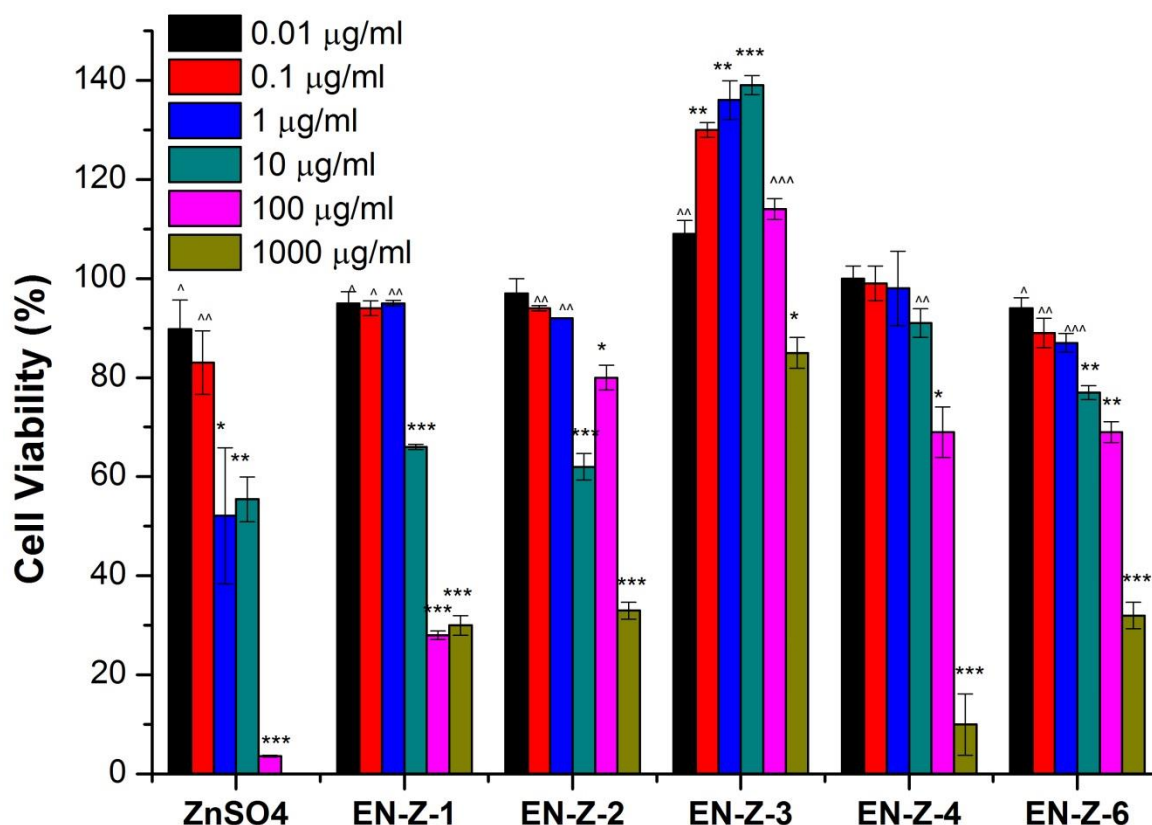


**Figure 7-1** Effect of different samples of ZnO NPs on the viability of A549 lung epithelial cells determined by MTT assay. Cells were exposed to varying concentrations of ZnO NP suspensions in DMEM for 24 hours and at 37°C. Cell viability is plotted as a percentage of the control cell viability. Values plotted are the mean of 3 replicate experiments ( $n = 3$ ); error bars are  $\pm$  one standard deviation. ( $\wedge = p < 0.05$ ,  $\wedge\wedge = p < 0.02$ ,  $\wedge\wedge\wedge = p < 0.01$ ,  $* = p < 0.005$ ,  $** = p < 0.002$ ,  $*** = p < 0.001$ )

EN-Z-2 and EN-Z-4 elicit significant toxicity at concentrations of 0.1 and 10 µg/ml respectively. The physicochemical characteristics that have been obtained for the samples (Table 7-1) give some indications as to why EN-Z-1 and EN-Z-6 are toxic at lower concentrations than the other NP samples. For example, EN-Z-1 and EN-Z-6 are most stable in suspension and therefore the cells will be exposed to agglomerates with smaller dimensions, which may uptake into cells more readily and hence elicit higher toxicity by intracellular dissolution. The increased toxicity for EN-Z-1 is most probably due to the presence of the aliphatic polyether present on the NP surface, as was demonstrated previously by our group of scientists on the ENNSATOX project (Mu et al., 2013). The coating was found to damage the integrity of the lipid membrane, and also increase NP interaction with the membrane. Therefore increased toxicity is a result of enhanced uptake of EN-Z-1 NPs, leading to increased intracellular release of Zn<sup>2+</sup>. The residual DEG detected on the surface of EN-Z-6 may have a similar effect as the coating on EN-Z-1. It may be that the negative surface charge of the NPs measured for EN-Z-1 and EN-Z-6 (Figure 6-5) increases interaction with the plasma membrane. Conversely it is reported in the literature that NPs with positive surface charge display enhanced cellular uptake (and therefore increased toxicity) in non-phagocytic cells, than their negatively charged counterparts (Bhattacharjee et al., 2010; El Badawy et al., 2011). An overview of the role of NP surface charge in cellular uptake and cytotoxicity is provided by Fröhlich et al. (2012). At higher concentrations i.e. 10 and 100 µg/ml EN-Z-1 is more toxic than all other NP samples. This may be because EN-Z-1 dissolves more slowly than the other ZnO NP samples (Figure 6-2), which may indicate that ZnO NPs induce increased toxicity compared to ZnCO<sub>3</sub> NPs.

When assessing the ZnO NP samples solubility, it was found that EN-Z-1 suspensions prepared had higher actual ZnO concentrations than the other samples, and it is therefore likely that this was the case in the toxicity assay exposures as well. The results from the MTT assay show that toxicity increases with increasing ZnO NP concentration (Figure 7-1) and therefore it is a possibility that EN-Z-1 is more toxic simply because the concentration of ZnO is higher. Investigations in the literature have reported that cell viability is reduced significantly by small changes in ZnO NP concentration. For example Hsiao & Huang (2011) observed a reduction in cell

viability from 70 to 20 % when the concentration of ZnO was increased from 6.25 to 12.5  $\mu\text{g/ml}$ . The ZnO NPs used in the study were uncoated and had primary particle sizes between 50 and 122 nm. Lin et al. (2008) measured a drop in cell viability from 85 to 30 % after exposure to ZnO NPs when the concentration was increased from 10 to 18  $\mu\text{g/ml}$ . These results indicate that the toxicity of ZnO NPs is very sensitive to concentrations in the region of 10  $\mu\text{g/ml}$ . This may be a result of this concentration being close to the equilibrium solubility concentration of ZnO (Section 6.1.2). Therefore, it is possible that the higher toxicity of the EN-Z-1 sample at 10  $\mu\text{g/ml}$  is due to the actual concentration of ZnO NPs being greater than the other 4 samples of ZnO. However, the largest amount by which the actual concentration of the EN-Z-1 sample varied as compared to the actual concentration of other ZnO NP samples with the same nominal concentrations was by a factor of 2. For the 100  $\mu\text{g/ml}$  samples, the difference in cell viability between the EN-Z-1 and other samples of ZnO NPs is approximately 40 %. From the MTT results presented in Figure 7-1, it does not seem likely that if the concentration of the 4 powder samples was doubled, the cell viability would reduce by as much as 40 %.

In the majority of studies reported in the literature, a much larger reduction in cell viability has been reported for ZnO NP concentrations of 100  $\mu\text{g/ml}$  than have been measured for EN-Z-2, EN-Z-3, EN-Z-4 and EN-Z-6 (Lin et al., 2008; Hsiao & Huang, 2011; Ahamed et al. 2012). This may be explained as contrary to the studies reported in the literature, in this investigation the cells have been incubated with ZnO NPs for 24 h in the absence of foetal bovine serum. The addition of serum has been shown to increase ZnO NP stability by altering the surface charge (Figure 6-6) and therefore this may be an indication that it is the colloidal nature of ZnO NP suspensions that increases toxicity. Alternatively, this may provide evidence for the damaging potential of the protein corona upon interaction with the plasma membrane. It must also be noted that in this study, for the MTT assay, the light adsorption was corrected for the dispersion of light by the ZnO NPs using intensities from control wells containing no cells. This has not been carried out in many of the literature studies and therefore may account for the reduced toxicity exhibited by the ZnO NPs in this investigation. However the cytotoxicity of EN-Z-1 is in good



agreement with values reported in the literature therefore this is unlikely to be the reason for the discrepancy.

An alternative reason for the lower toxicity between 10 and 100  $\mu\text{g/ml}$  measured in this study for powder samples of ZnO NP may be due to the presence of chemically and physically adsorbed carbonate that has been detected on the surface of these 4 samples. Due to the increased amount of carbonate in the solution, a larger quantity of zinc carbonate may precipitate thus reducing the amount of zinc in solution. It is clear that  $\text{ZnCO}_3$  is not as soluble as ZnO in DMEM and so a surface coating may inhibit dissolution of a ZnO core. It has previously been reported that  $\text{ZnCO}_3$  forms at the surface of ZnO NPs exposed to ambient conditions (Pan et al., 2011). The particles used in this study had been stored for a number of months before the suspensions were prepared for the toxicity assays. In section 5.3.2, it is identified by FTIR (Figure 5-16) and XPS (Figure 5-23) that the amount of  $\text{ZnCO}_3$  at the surface of EN-Z-4 increases with ageing and therefore, it may be that the samples used in this investigation have an increased amount of surface carbonate as compared to alternative studies and hence induce lower toxicity.

The hydrozincite phase detected in EN-Z-2 and EN-Z-3 samples does not apparently alter the toxicity as compared to monophasic samples of ZnO such as EN-Z-4 and EN-Z-6.

### **7.2.2 Genotoxicity**

The results obtained from the comet assay, investigating the DNA damaging potential of the commercial and synthesized ZnO NP samples are presented in Figure 7-2 and Figure 7-3 respectively. The formation of a comet tail after electrophoresis indicates DNA damage and as such in this study, genotoxicity was assessed by measurement of the percentage of DNA in the comet tails. Exposures were performed in triplicate; the value plotted on the chart is an average of the 3 measurements and the error bars are determined by calculation of the standard deviation. Genotoxicity measurements are only interpretable on viable cells and

therefore the results from the MTT assay are used in order to determine the concentrations to investigate. The comet assay for the commercially sourced samples was performed by Mrs Kay White and Rachel Mu in the Leeds Institute of Genetics, Health and Therapeutics at the University of Leeds.

For the commercial samples, A549 lung epithelial cells were exposed to various concentrations of ZnO NP ranging from 0.01 to 1 µg/ml, as the significant cell death observed at higher concentrations (Figure 7-1) will hamper the interpretation of comet assay results. For the synthesized samples, A549 lung epithelial cells were exposed to only 2 concentrations of ZnO NP at 1 and 10 µg/ml. In addition to the 2 concentrations of ZnO NPs, the cells were also exposed to the supernatant of a 10 µg/ml suspension of each of the synthesized samples which had been centrifuged for 35 minutes at 14,500 rpm. The results for the commercial samples of ZnO NPs presented in Figure 7-2 indicate that minor DNA damage is observed for all dosages, including the control cells. For EN-Z-1 and EN-Z-2, no significant genotoxicity is measured at any of the concentrations investigated as the DNA damage observed is similar to that of the control cells. For EN-Z-3, a small but statistically significant increase in DNA damage is measured at ZnO NP concentrations of 0.1 and 1 µg/ml as compared to the control cells. It is difficult to attribute a particular physicochemical characteristic of EN-Z-3 to the apparent increase in genotoxicity for the sample as it is very similar in size, shape and composition to EN-Z-2. Of the samples without organic surface contamination, EN-Z-3 shows the highest stability (Figure 6-7). The smaller agglomerates administered to the cells for EN-Z-3 may be taken up more readily and alter the genotoxicity.

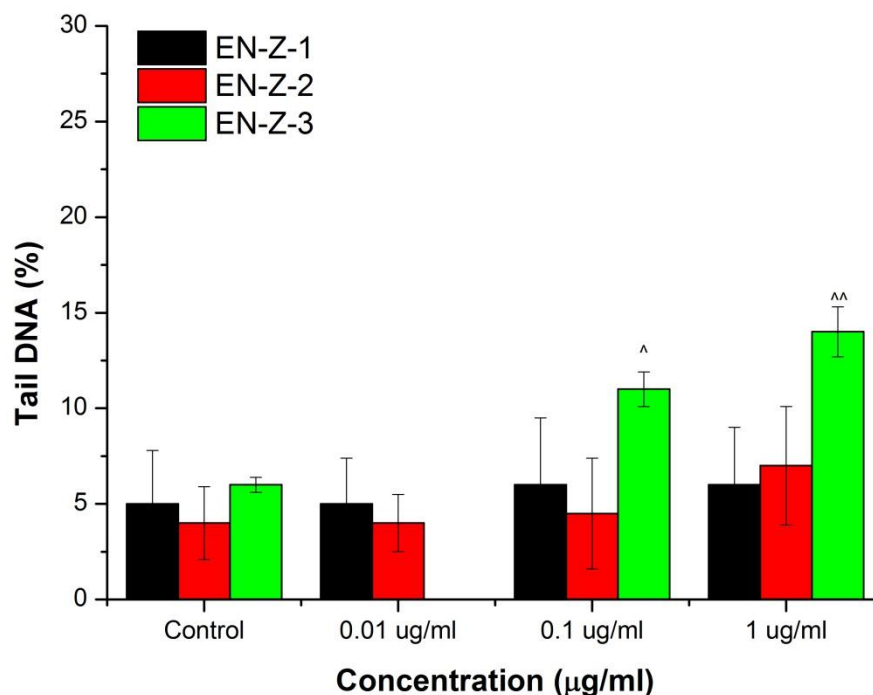


**Figure 7-2 Effect of commercial samples of ZnO NPs on the DNA of A549 lung epithelial cells determined using the Comet Assay, by measurement of the percentage of DNA in the Comet tail. Cells were exposed to varying concentrations of ZnO NP suspensions in DMEM for 24 hours and at 37°C. Values plotted are mean (n = 3); error bars are ± one standard deviation. (^ = p < 0.05, ^^= p < 0.02)**

The comet assay results for the synthesized samples of ZnO are presented in Figure 7-3. Neither of the ZnO NP concentrations investigated induce a significantly higher degree of DNA damage as compared to the respective control experiments. The experiments investigating the effect of the supernatant of the 10 µg/ml on the cells indicate that there is no significant different in DNA damage as compared to the respective ZnO NP 10 µg/ml samples. The percentage of tail DNA measured at 10 µg/ml is between 5 and 15 %, which is inconsistent with results reported in the literature carried out at the same concentration for 24 hour exposures and using A549 cells. For example Lin et al. (2008), using uncoated ZnO NPs with primary particle size of 70 nm, reported a much higher level of DNA damage; they measured 40 % DNA damage at a concentration of 10 µg/ml which increased to 90 % damage when the ZnO NP concentration was raised to 14 µg/ml. This may be attributed to the use

of serum by Lin et al. (2008) which will enhance NP stability and has also been shown to enhance the lipid membrane activity of ZnO NPs (Churchman et al., 2013), thus affecting uptake and toxicity.

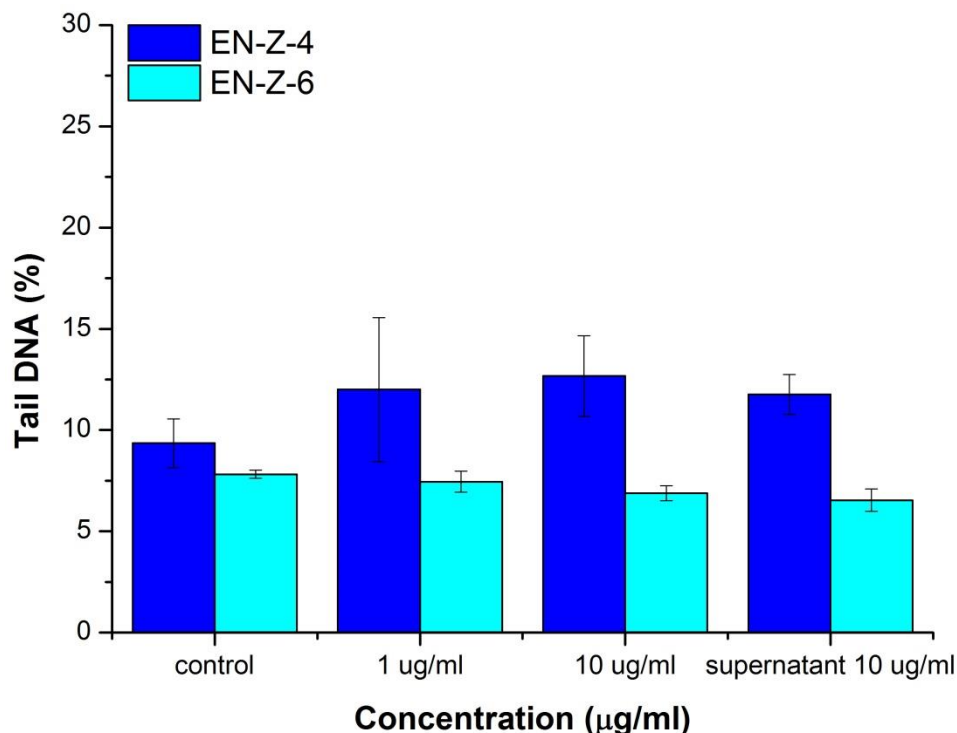


**Figure 7-3 Effect of synthesized samples of ZnO NPs on the DNA of A549 lung epithelial cells determined using the Comet Assay, by measurement of the percentage of DNA in the Comet tail. Cells were exposed in DMEM for 24 hours and at 37°C to 1 and 10 µg/ml suspensions of ZnO NPs suspensions and additionally to the supernatant of a centrifuged 10 µg/ml suspension of ZnO NPs. Values plotted are mean (n = 3); error bars are ± one standard deviation.**

### 7.2.3 Cellular Uptake

The cellular uptake for EN-Z-1 by A549 lung epithelial cells was investigated previously (Mu et al., 2013) using a ZnO concentration of 1000 µg/ml and exposure time of 1 hour under conditions identical to the MTT and comet assays performed in this investigation. The cellular uptake of EN-Z-4 and EN-Z-6 was investigated for ZnO concentrations of 10 and 100 µg/ml over an exposure of 24 hours. Additionally, for EN-Z-4 and EN-Z-6, the 100 µg/ml suspension was centrifuged at 14,500 rpm for

35 minutes, and exposures were carried out under the same conditions using the supernatant. As a large reduction in cell viability was measured using the MTT assay for some samples at 100  $\mu\text{g/ml}$ , it was hoped that by investigating the supernatant of a 100  $\mu\text{g/ml}$  ZnO NP suspension, toxicity would be attributable to either the dissolved Zn or to the presence of ZnO NPs. As 10  $\mu\text{g ZnO/ml}$  is close to the equilibrium solubility concentration for ZnO it was thought to be an important concentration to investigate in the cellular uptake experiments and it was hoped that this may provide further evidence for significant ZnO NP dissolution at this concentration, and the presence of ZnCO<sub>3</sub> particles. Controls were also prepared by exposing A549 cells to 500  $\mu\text{l}$  of MilliQ water in DMEM at 37°C for 24 hours. Cell sections were prepared and cut to a nominal thickness of 100 nm and then placed on a copper grid which could then be examined in the TEM. The high angle annular dark field scanning transmission electron microscopy (HAADF STEM) imaging mode was employed in order to more easily identify ZnO NPs, as zinc has a much higher atomic weight than the elements present in the cell and therefore would show increased contrast. All HAADF STEM images presented in this Chapter have inverted contrast in order to make them comparable with bright field TEM images.

A low magnification TEM image of an entire grid square, presented in Figure 7-4 (a) shows control A549 cells presented in the typical morphology exhibited by this cell type. The majority of cells are joined to their neighbouring cells at desmosome junctions. Figure 7-4 (b) presents an increased magnification TEM image of a single cell where some of the features such as microvilli and the nucleus can be identified. An EDX of the area outlined by the box in Figure 7-4 (b) is presented in Figure 7-4 (c). The fixative used in the cell section preparation procedure is glutaraldehyde and 2 % osmium tetroxide which accounts for the osmium signal in the EDX spectrum and probably also some of the oxygen signal. The copper signal may be attributed to the copper bars on the TEM grid on which the cell section lies. The remaining elements identified in the EDX spectrum are components of the cell.

The TEM results from cellular uptake investigations for EN-Z-1 are presented in Figure 7-5 (Mu et al., 2013). A contrast inverted HAADF STEM image of a typical cell is shown in Figure 7-5 (a); the majority of the cells in the sample

appear intact. A contrast inverted HAADF STEM image of the region outlined by the box in Figure 7-5 (a) is presented in Figure 7-5 (b), showing what appear to be ZnO NPs. A TEM image of the area indicated by the boxed region in Figure 7-5 (b) is shown in Figure 7-5 (d) where the particles, which are located in the cytoplasm of the cell, can be seen more clearly and show signs of dissolution. The size of the particles is comparable with that of the primary particle size for EN-Z-1 and EDX confirms the presence of zinc indicating that the particles are likely to be EN-Z-1 NPs that have been taken up by the cell following exposure. The exposure took place over 1 hour and the rapid uptake of the NPs by the cells may be attributed to the aliphatic polyether coating the sample; as has previously been discussed, the coating has been found to enhance uptake either by compromising the plasma membrane and enabling passive uptake of NPs, or by promoting interaction with the membrane leading to increased endocytic uptake of NPs (Mu et al., 2013).

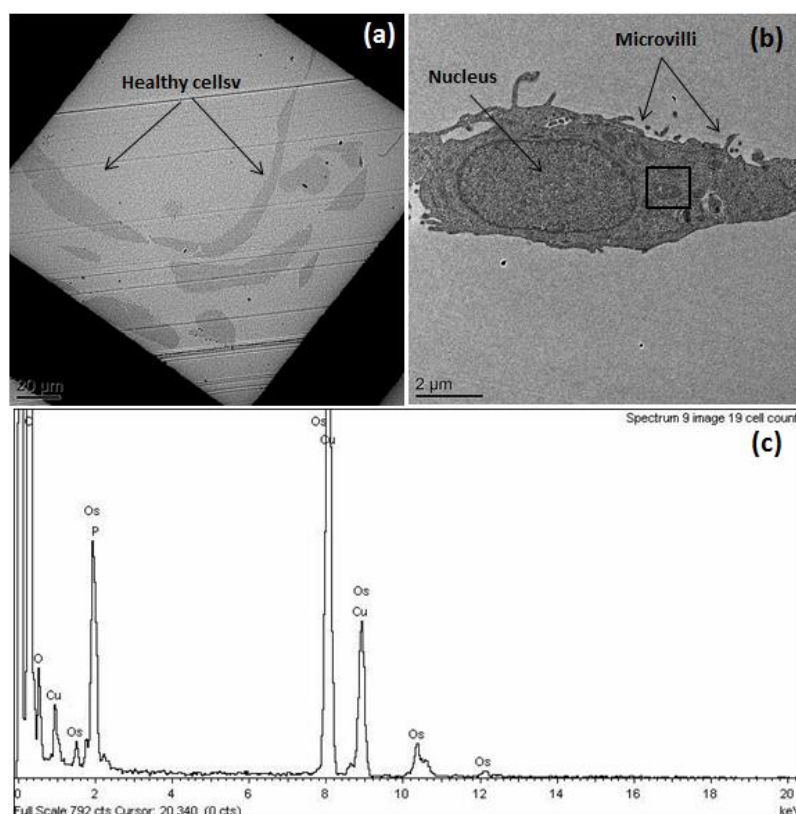


**Figure 7-4** A549 cells exposed to MilliQ water for 24 hours at 37°C. (a) TEM image of whole grid square showing numerous cells; (b) TEM image of a whole cell; (c) EDX spectrum of the area outlined by the box in (b).

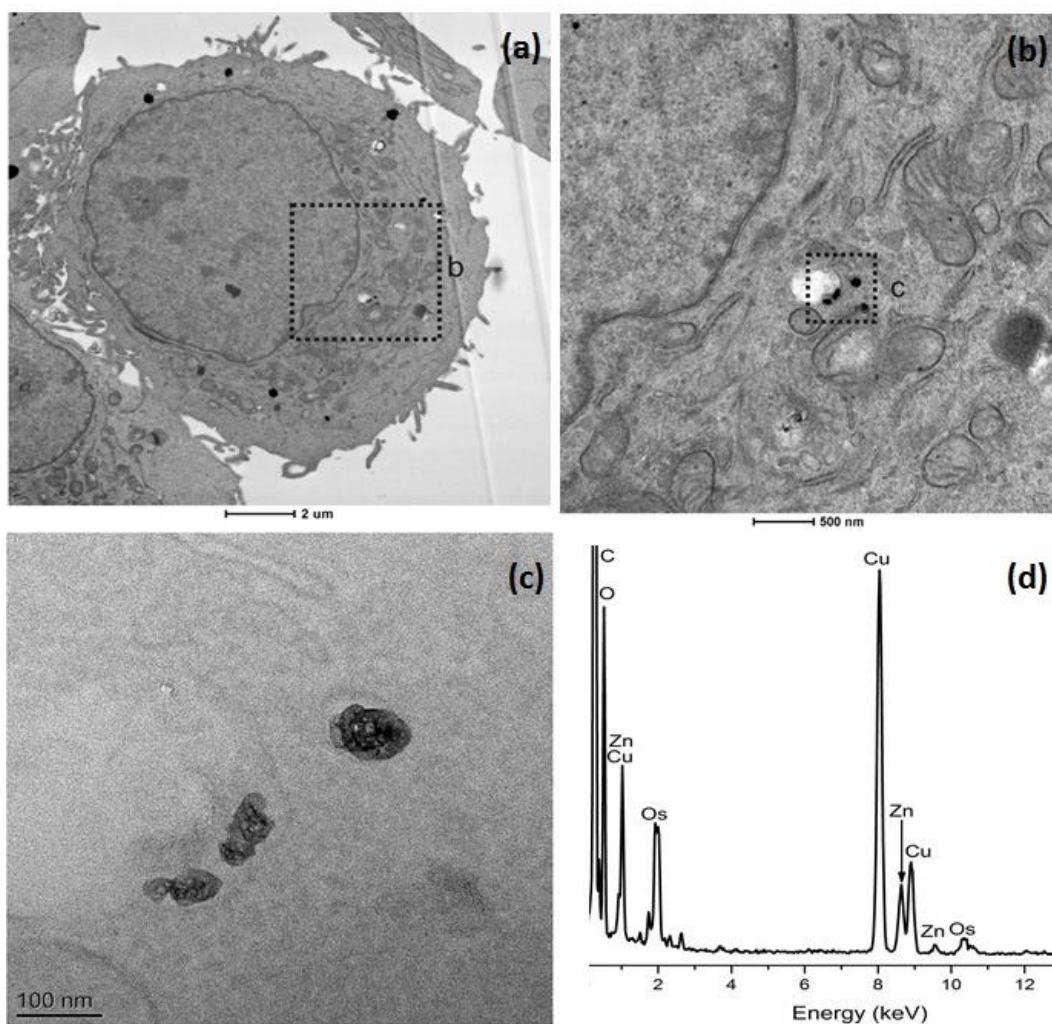


**Figure 7-5** A549 cells exposed to 1000  $\mu\text{g/ml}$  EN-Z-1 for 1 hour. (a) Contrast inverted HAADF STEM image of a whole cell; (b) Contrast inverted HAADF STEM image of the area indicated by the boxed region in (a); (c) TEM image of the area indicated by the boxed region in (b); (d) EDX spectrum from the top nanoparticle in (c) (from Mu et al. 2013).

The TEM analysis presented in Figure 7-6, Figure 7-7 and Figure 7-8 is of A549 cells exposed to EN-Z-6 at 100  $\mu\text{g/ml}$ , the supernatant of a 100  $\mu\text{g/ml}$  sample and 10  $\mu\text{g/ml}$  respectively, for 24 hours in DMEM at 37  $^{\circ}\text{C}$ . Figure 7-6 (a) is a low magnification TEM image showing numerous cells which have been exposed to EN-Z-6 at 100  $\mu\text{g/ml}$ . The image reveals that the morphology of the A549 cells has

altered as a consequence of the ZnO NP exposure. 29 of the 30 cells imaged are isolated and rounded, which is in contrast to the long, thin adjoined cells observed in the control sample (Figure 7-4). The rounded morphology observed for the A549 cells is indicative of cell stress (Patra et al., 2007). Hsiao & Huang (2011) reported the abnormally rounded nature of A549 cells that had been exposed to 50  $\mu\text{g/ml}$  ZnO NPs for 24 hours, indicating that the cells were either damaged or dead. A contrast inverted HAADF STEM image of the cell outlined by the box in Figure 7-6 (a) is presented in Figure 7-6 (b) and reveals additional signs of cell distress, possibly the onset of necrosis, characterized by vacuolization. Vacuolization occurred to varying degrees across 29 of the cells imaged and has previously been reported in damaged and apoptotic A549 cells (Wang & Chen, 2012). A contrast inverted HAADF STEM image of the region outlined by the box in Figure 7-6 (b) is presented in Figure 7-6 (c) and identifies what are potentially ZnO NPs bound within the nuclear membrane of the cell. A high magnification TEM image of the region outlined by the dotted box in Figure 7-6 (c) is presented in Figure 7-6 (d) and an EDX spectrum of the top particle in the image is presented in Figure 7-6 (e). The NPs located here are similar in length to that of the primary particles in EN-Z-6 (approximately 40 nm) and the presence of ZnO confirmed by EDX analysis forms a strong argument that these are indeed EN-Z-6 ZnO NPs that have been taken up by the cell following exposure. ZnO NPs have previously been located in A549 cells following a 24 hour exposure. For example, Lin et al. (2008) identified agglomerated ZnO NPs within a vesicle. The ZnO concentration was 12 $\mu\text{g/ml}$ , and the NPs identified within the vesicle in the cell were similar in size to that of the primary particles (approx. 70 nm).

A high magnification TEM image of the region outlined by the dashed box in Figure 7-6 (c) is presented in Figure 7-6 (f) and an EDX spectrum of the cluster of particles is presented in Figure 7-6 (g). EDX confirms the presence of zinc and therefore it may be assumed that these are ZnO NPs. However, the average size of the particles determined by 50 measurements is 14 nm, which is substantially smaller than the primary particle size of EN-Z-6. The particles identified in Figure 7-6 (f) may be remnant of an agglomerate of EN-Z-6 ZnO NPs that have dissolved to form smaller NPs. Alternatively, dissolved zinc may have precipitated into NPs of zinc compounds such as  $\text{Zn}_3(\text{PO}_4)_2$  or  $\text{ZnCO}_3$ , as a result of a change in the chemical



environment, which may have arisen through entering the nuclear environment. The zinc ions forming these particles may be present as a result of intercellular ZnO NP dissolution, e.g. in a lysosome, or extracellular ZnO NP dissolution in the exposure media. The particles may be  $\text{ZnCO}_3$  that has precipitated from solutions of ZnO and DMEM in the extracellular environment (Mu et al., 2013) and have been taken up by the cells. A further 3 clusters of these smaller NPs were identified at various other locations in the cells imaged in Figure 7-6 (b) and additionally in numerous other cells in the samples. 10 cells were examined in detail and 16 clusters of small NPs were located in 8 of the cells. One more area was found that contained ZnO NPs of similar sizes to that of the primary particles in EN-Z-6.

A low magnification TEM image of the cells treated with the supernatant of the 100  $\mu\text{g}/\text{ml}$  sample is presented in Figure 7-7 (a). The cell morphology is similar to that observed in the control sample indicating that the cells are healthy. A TEM image of a typical cell (outlined by the box Figure 7-7 (a)) shows the plasma membrane with numerous microvilli and the nucleus is also clearly discernible. Higher magnification images of the cytoplasm and nucleus of the cell in Figure 7-7 (b) are presented in Figure 7-7 (c) and Figure 7-7 (d) respectively. In Figure 7-7 (c) the normal cytoplasmic inclusions such as the vacuoles and mitochondria can be seen and in Figure 7-7 (d), the nucleolus is visible. All 20 of the cells imaged appear healthy. The results indicate that the toxicity to the A549 cells in this experiment was induced as a result of the ZnO NPs present in the suspension. When the solid component of the 100  $\mu\text{g}/\text{ml}$  sample was removed and only the remaining zinc ions, were administered to the cells, no toxicity, assessed as a function of cell morphology, was observed; this is consistent with Moos et al. (2010) who found that NP contact with the cell is required in order to induce toxicity. The supernatant will presumably have a  $\text{Zn}^{2+}$  concentration close to the equilibrium solubility ( $\sim 5.7 \mu\text{g ZnO}/\text{ml}$ ), which is not particularly toxic to cells (Figure 7-1), hence the apparent viability of the cells imaged here. There were no small NPs found in the cells administered to the supernatant which indicates that there was no precipitation of zinc from solution.

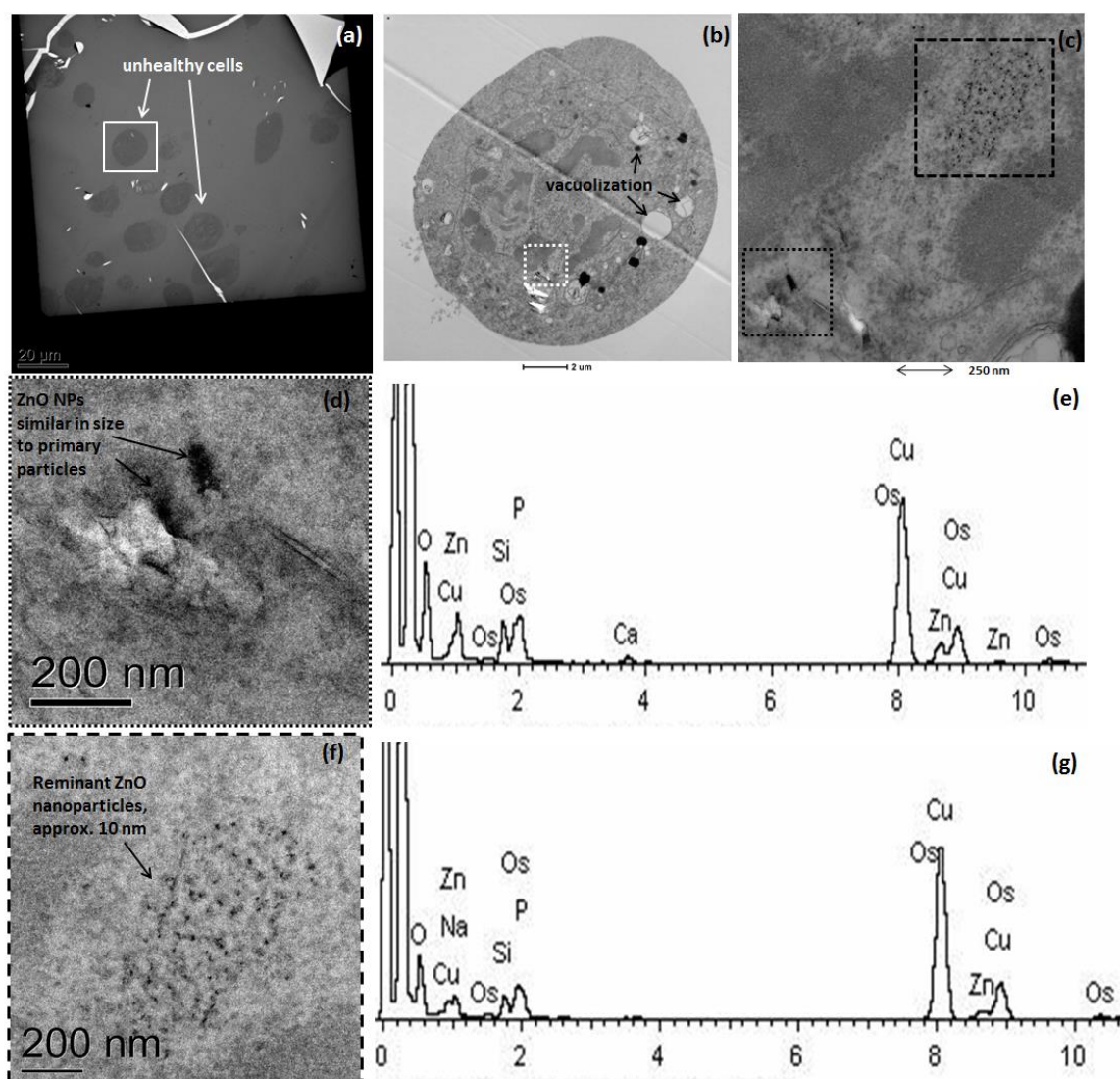


**Figure 7-6** A549 cells exposed to 100  $\mu\text{g/ml}$  EN-Z-6 for 24 hours at 37°C. (a) Low magnification image of grid square showing numerous cells; (b) contrast inverted HAADF STEM image of a whole cell indicated by the boxed region in (a); (c) contrast inverted HAADF STEM image of the area indicated by the boxed region in (b); (d) TEM image of the area indicated by the box with the dotted outline in (c); (e) EDX spectrum from the top NP in (d); (f) TEM image of the area indicated by the box with the dashed outline in (c); (g) EDX spectrum from the cluster of NPs in (f).

A low magnification TEM image showing cells exposed to 10  $\mu\text{g/ml}$  EN-Z-6 for 24 hours at 37°C is presented in Figure 7-8 (a). The cell morphology is consistent

with that of the control cells indicating that the cells are healthy. A contrast inverted HAADF STEM image of an entire cell is presented in Figure 7-8 (b) where the nucleus and nuclear membrane are clearly discernible as well as microvilli around the plasma membrane. Higher magnification images of the nucleus and cytoplasm presented in Figure 7-8 (c) and Figure 7-8 (d) respectively reveal that there are small white particles present in a number of vacuoles. An EDX of the region outlined by a box in Figure 7-8 (d) reveals that they are not ZnO NPs but rather clumps of osmium fixative.

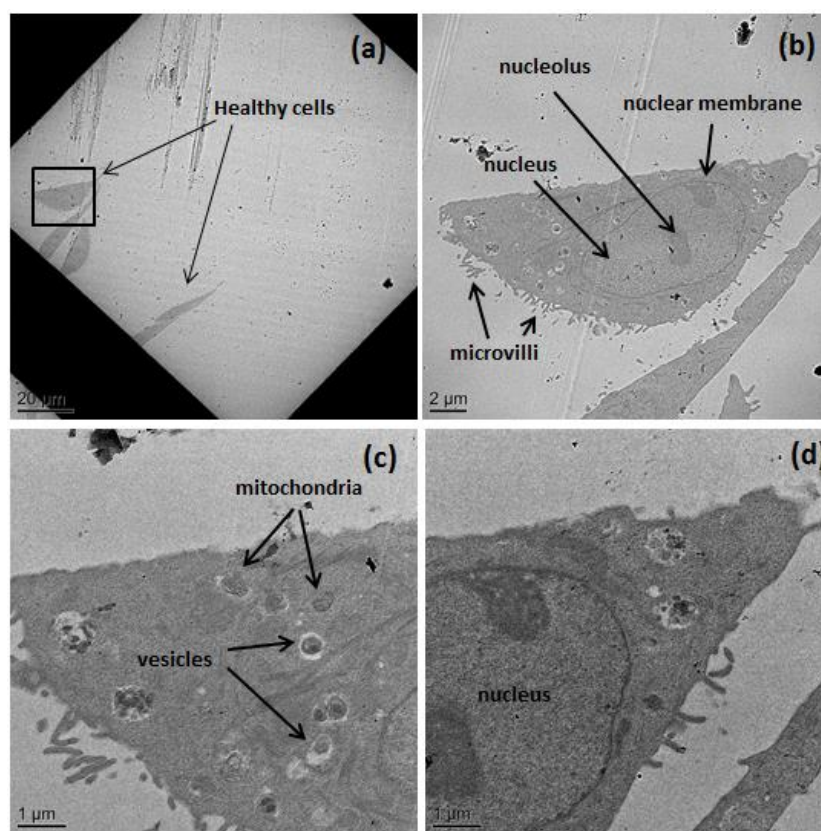


**Figure 7-7** A549 cells exposed to the supernatant of a 100  $\mu\text{g/ml}$ , centrifuged suspension of EN-Z-6, for 24 hours at 37°C. (a) Low magnification image of grid square showing numerous cells; (b) TEM image of a whole cell indicated by the boxed region in (a); (c) TEM image of the cell showing area indicated by the box with the dotted outline (b); (d) TEM image of the area indicated by the box with the dashed outline in (b).

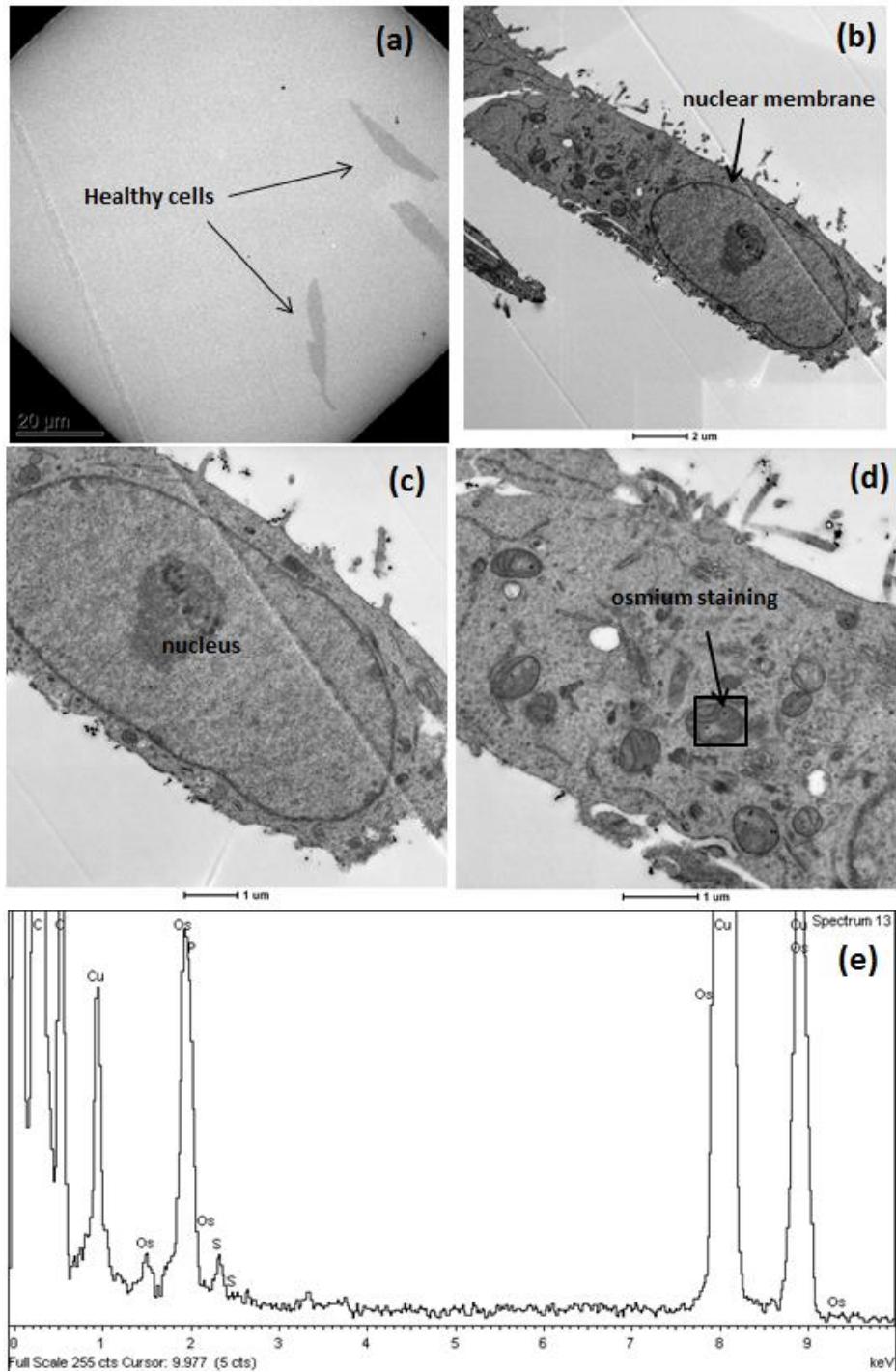


**Figure 7-8** A549 cells exposed to 10 µg/ml EN-Z-6 for 24 hours at 37°C. (a) Low magnification image of grid square showing numerous cells; (b) contrast inverted HAADF STEM image of a whole cell; (c) contrast inverted HAADF STEM image of the nucleus of the cell shown in (b); (d) contrast inverted HAADF STEM image of the left hand side of the cell shown in (b); (e) EDX spectrum of the area indicated by the boxed region in (d).

The TEM analysis presented in Figure 7-9, Figure 7-10 and Figure 7-11 are of A549 cells exposed to EN-Z-4 at 100  $\mu\text{g/ml}$ , the supernatant of a 100  $\mu\text{g/ml}$  sample and 10  $\mu\text{g/ml}$  respectively. In the case of the 100  $\mu\text{g/ml}$  sample, a similar effect on cell morphology is observed as with the EN-Z-6 100  $\mu\text{g/ml}$  exposure. Evidence for this is provided in Figure 7-9 (a) where the A549 cells are isolated and rounded. Of the 30 cells imaged, 28 appear rounded. As well as morphological changes, vacuolization is also apparent in 26 cells imaged in the sample; an example of this can be seen in Figure 7-9 (b) which shows a TEM image of the whole cell outlined by the box in Figure 7-9 (a). A contrast inverted HAADF STEM image of the region outlined by the box in Figure 7-9 (b) is presented in Figure 7-9 (c). Imaging in this mode facilitated in the identification of clusters of small ZnO NPs within the nucleus, similar to those observed in the EN-Z-6 100  $\mu\text{g/ml}$  sample. A contrast inverted HAADF STEM image of the region outlined by the box in Figure 7-9 (c) is displayed in Figure 7-9 (d) and clearly shows 3 clusters of the small NPs observed. EDX of the bottom cluster in Figure 7-9 (d), presented in Figure 7-9 (e) revealed the presence of zinc. The NPs were smaller than the primary particles in the EN-Z-4 sample which may indicate that they are formed from EN-Z-4 NP agglomerates that have undergone significant dissolution. Alternatively the small NPs may be formed from zinc ions which have precipitated to form lower solubility compounds such as  $\text{ZnCO}_3$ , either in the intracellular or extracellular environment. A detailed examination of 10 cells was performed and the small NPs discussed were located in 8.

A TEM image of cells exposed to the supernatant of the 100  $\mu\text{g/ml}$  EN-Z-4 suspension is presented in Figure 7-10 (a). The cells have the typical morphology observed in the control cells and are grouped together indicating that they are healthy. TEM images of the cells outlined by the dashed and dotted boxes in Figure 7-10 (a), are presented in Figure 7-10 (b) and Figure 7-10 (c) respectively. In both images the nucleus and microvilli are discernible and the cells appear healthy. EDX over several areas including the region outlined by the box in Figure 7-10 (c), which is presented in Figure 7-10 (d) does not identify the presence of zinc in the cells.



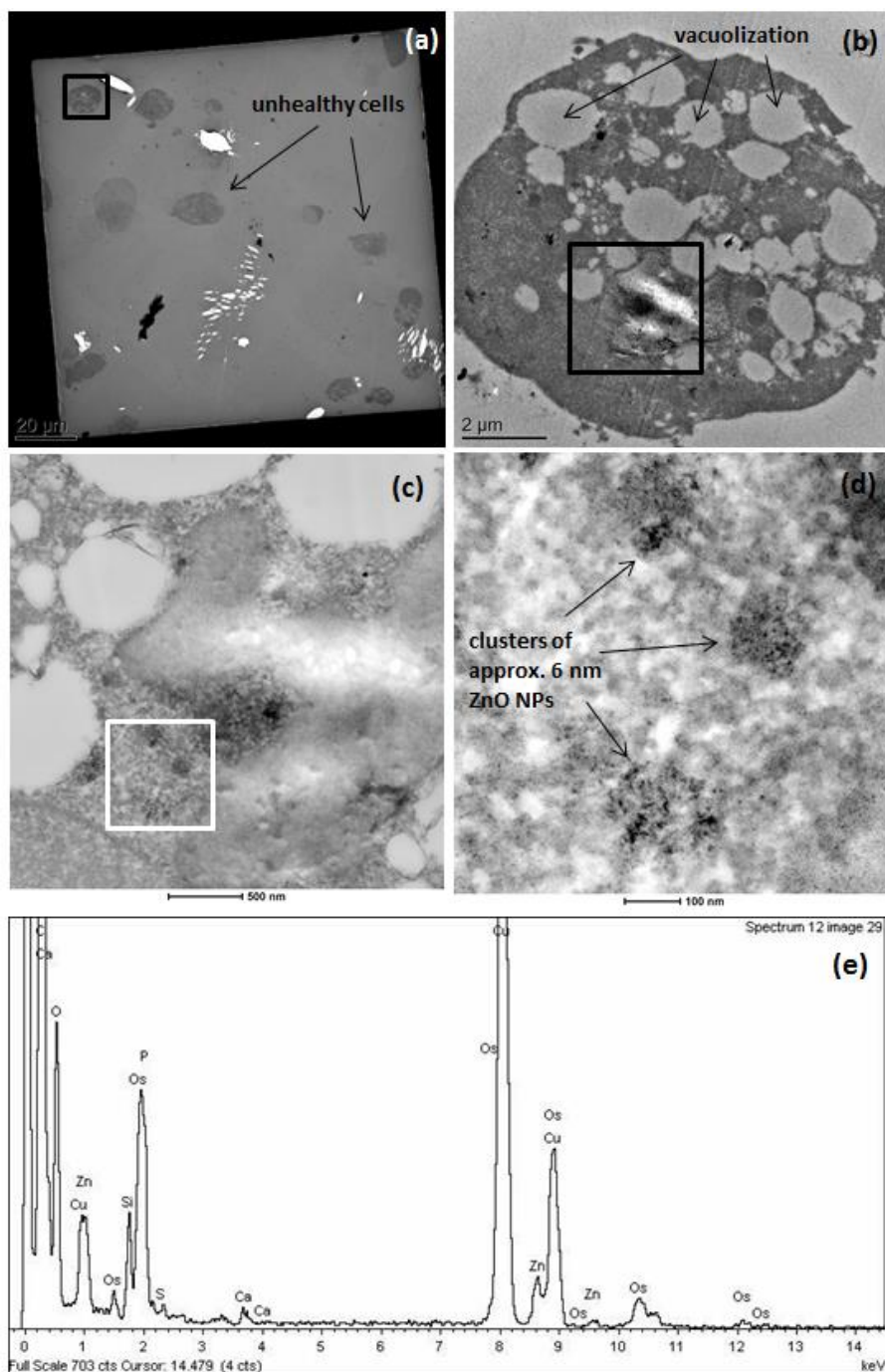


**Figure 7-9** A549 cells exposed to 100  $\mu\text{g/ml}$  EN-Z-4 for 24 hours at 37°C. (a) Low magnification image of grid square showing numerous cells; (b) TEM image of a whole cell; (c) contrast inverted HAADF STEM image of region indicated by the boxed area in (b); (d) contrast inverted HAADF STEM image of the region indicated by the boxed area shown in (c); (e) EDX spectrum of the bottom cluster of NPs in (d).

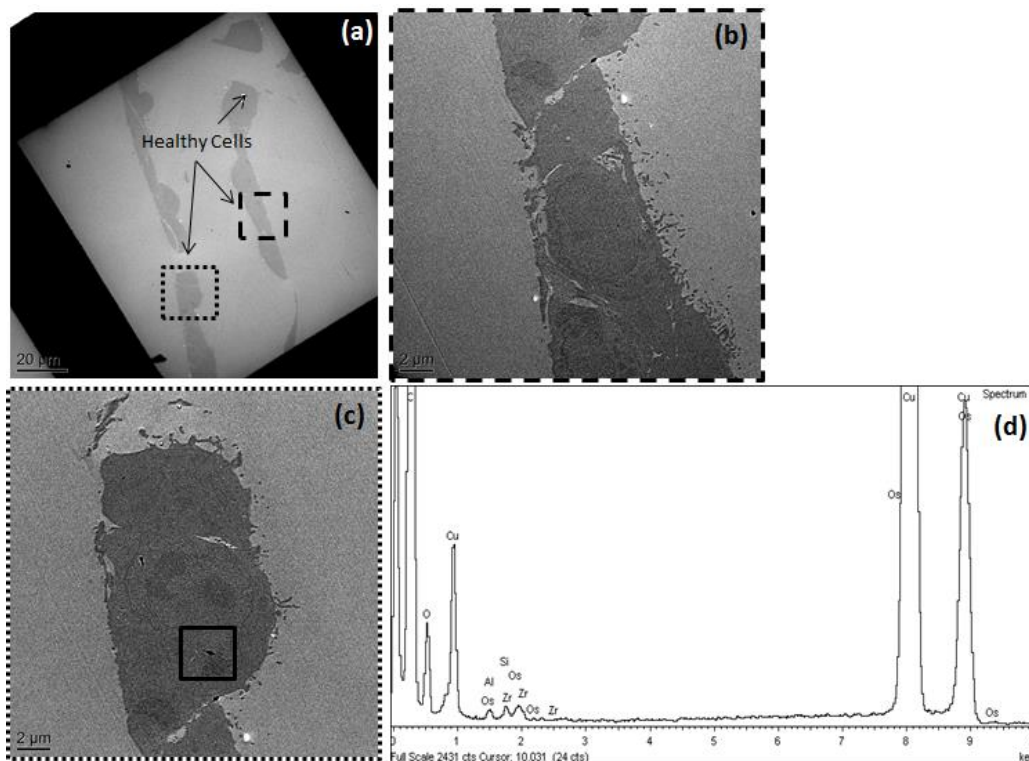


**Figure 7-10 A549 cells exposed to the supernatant of a 100  $\mu\text{g/ml}$ , centrifuged suspension of EN-Z-4, for 24 hours at 37°C. (a) Low magnification image of grid square showing numerous cells; (b) TEM image of cells indicated by the box with dashed outline in (a); (c) TEM image of the cell indicated by the box with the dotted outline in (a); (d) EDX spectrum of the area indicated by the boxed region in (c).**

A TEM image of the cells exposed to 10  $\mu\text{g/ml}$  EN-Z-4 is presented in Figure 7-11 (a) and indicates that the cells are healthy. A contrast inverted HAADF STEM image of the cell outlined by the box in Figure 7-11 (a) is presented in Figure 7-11 (b). A contrast inverted HAADF STEM image of the region outlined by the box in Figure 7-11 (b) is presented in Figure 7-11 (c). There are white flecks present in the vacuoles and mitochondria and additionally a large clump is present which has been outlined by a box. EDX of the clump in the box (Figure 7-11 (d)) and the other white flecks indicates that they consist of osmium which arises from the fixative used.

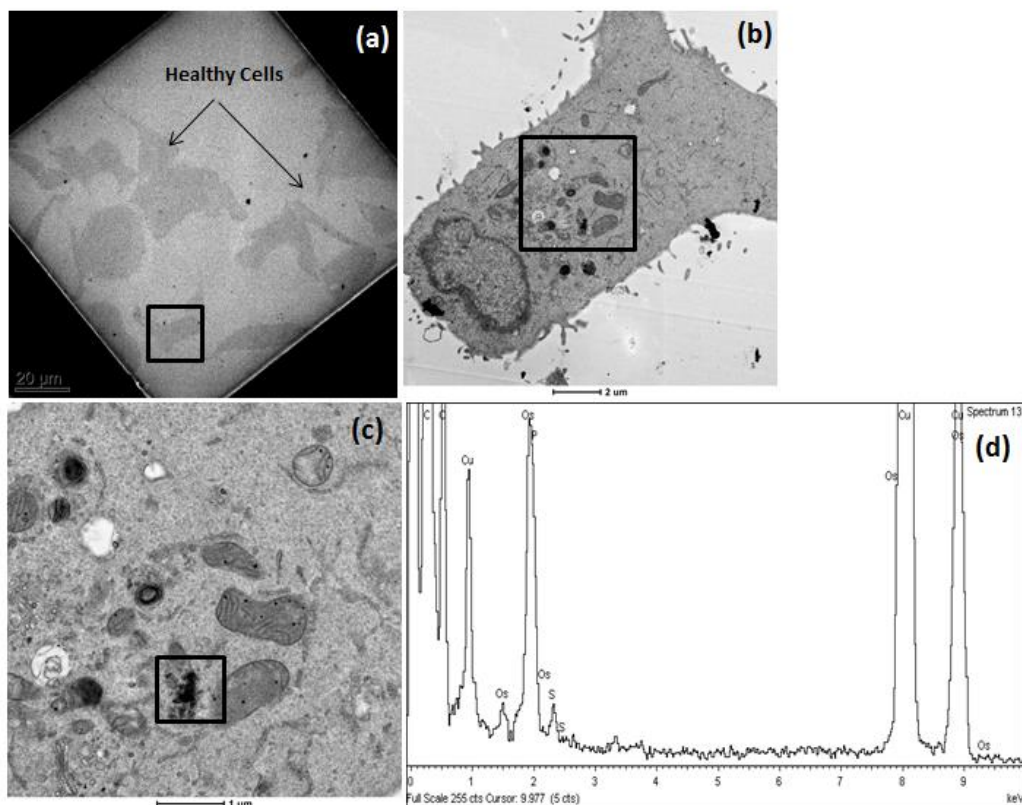


**Figure 7-11** A549 cells exposed to 10  $\mu\text{g/ml}$  EN-Z-4, for 24 hours at 37°C. (a) Low magnification image of grid square showing numerous cells; (b) contrast inverted HAADF STEM image of the cell indicated by the box in (a); (c) contrast inverted HAADF STEM image of the area indicated by the boxed region in (b); (d) EDX spectrum of the area indicated by the boxed region in (c).

For EN-Z-1 at a concentration of 1000  $\mu\text{g/ml}$  EN-Z-1, it can be noted that no clusters of NPs significantly smaller than EN-Z-1 primary particles were located in the cells, as opposed to the 100  $\mu\text{g/ml}$  samples of EN-Z-4 and EN-Z-6 where lots of these clusters were observed. This may be an indication as to the differences in toxicity exhibited by the EN-Z-1 samples as compared to EN-Z-4 and EN-Z-6, as a result of varying mechanisms of cellular uptake. For example EN-Z-1 dissolves more slowly than E-Z-Z-4 and EN-Z-6 (Figure 6-2), which may explain why there were no small NPs located in the cells for EN-Z-1. The coating on EN-Z-1 has been shown to promote phospholipid membrane interaction and also compromise the plasma



membrane leading to enhanced uptake into cells either passively or endocytically, thus inducing greater toxicity by intracellular dissolution of NPs (Mu et al., 2013). The enhanced uptake measured for EN-Z-1 may provide evidence that the small NPs located in EN-Z-4 and EN-Z-6 are formed in the intracellular environment, as one would not expect so many particles to have been taken up by the cells for EN-Z-4 and EN-Z-6. However in order to directly compare cellular uptake investigations and to further clarify these findings, cellular uptake for EN-Z-1 must be investigated at a concentration of 100 µg/ml over a 24 hour exposure.

The 100 µg/ml EN-Z-6 and EN-Z-4 exposures appear to have induced significant levels of damage to the cells, i.e. of the 30 cells imaged in each of the samples, more than 90 % show signs of damage (characterized by a rounded morphology). This does not correlate with the cytotoxicity results measured by the MTT assay, which have been reported in this investigation where for EN-Z-6 and EN-Z-4, cell viability for both was measured as 69 % (Figure 7-1). These results may indicate that EM is a more sensitive technique for determining cell viability than the MTT assay. EM has previously been found to be a sensitive technique for measuring cell viability. For example, changes in element concentrations occur before many other markers that are usually used to demonstrate cell death (Fernandez-Segura & Warley, 2008). EM has previously been employed in order to measure element concentrations such as K/Na ratios by EDX in order to establish cell viability (Di Francesco et al., 1998).

### 7.3 In Summary

Physicochemical characterisation of ZnO NPs is essential for interpreting the results of toxicity assays. The actual concentrations of ZnO NP suspensions can vary considerably from the nominal concentrations desired. This is crucial as small changes in ZnO NP concentration may significantly affect toxicity.

ZnO NP solutions induced lower cytotoxicity than solutions of  $Zn^{2+}$  with equivalent concentrations of Zn. This may be due to the solution of  $ZnSO_4$  leading to supersaturation of  $Zn^{2+}$  in the absence of NPs acting as a nucleation sites for the re-precipitation of zinc to form  $ZnCO_3$ . This implies that  $ZnCO_3$  particles are less cytotoxic than  $Zn^{2+}$ .

EN-Z-1 induced greater cytotoxicity in A549 cells in DMEM over 24 hour exposures at 37°C. The higher toxicity of the EN-Z-1 sample may be due to a number of reasons. The aliphatic polyether present on the NP surface may affect the mechanism of toxicity induced by EN-Z-1 as compared to the 4 powder ZnO NP samples. Polymer coatings can promote strong interaction with lipid membranes and promote uptake of ZnO NPs into cells. Therefore, the enhanced uptake of the ZnO NPs in this sample may lead to intracellular NP dissolution, increasing zinc levels internally in the cell and inducing higher toxicity. Alternatively, the coating may be disrupting the plasma membrane, and the ZnO NPs may be taken up passively. Again, this results in intracellular dissolution and increased levels of zinc internally (Mu et al., 2013).

Alternatively or additionally, the increased toxicity observed for EN-Z-1 may be due to the actual concentration of ZnO in the suspensions being higher than the actual concentration measured for the other 4 samples.

The toxicity induced by EN-Z-2, EN-Z-3, EN-Z-4 and EN-Z-6 to A549 cells over 24 hours is lower compared with results reported in the literature. This may be due to the absence of FBS in the exposure media used in this investigation. Serum has been shown to adsorb to the surface of ZnO NPs and therefore this may increase toxicity by enhancing endocytic NP uptake into cells, or by disrupting the plasma membrane and allowing passive uptake of NPs. Alternatively, the large amount of physically and chemically adsorbed carbonate present on the surface of the dry powder samples may be reducing toxicity by lowering the level of zinc in solution by inhibiting ZnO dissolution of the NP core.

Coated and uncoated ZnO NPs are taken up by A549 cells and have been located in both the cytoplasm and the nucleus. In the cells exposed to 100 µg/ml EN-Z-4 and EN-Z-6, very small NPs (smaller than primary particle sizes of the samples) containing zinc were found in the cells. These are probably ZnCO<sub>3</sub> particles formed from dissolved zinc precipitating from solution in the extracellular or intracellular environment. For both samples at this ZnO NP concentration, the majority of cells appeared damaged, despite the MTT assay suggesting ~70 % viability, indicating that there are differences in sensitivity when using different *in vitro* toxicity assays. Although the exposure conditions were not identical, the EN-Z-1 sample appeared to

undergo an alternative uptake mechanism as no NPs smaller than primary particle size were located in the cells exposed to EN-Z-1. This may be attributed to the enhanced uptake due to the coating present on the NPs and also the slower dissolution measured for EN-Z-1.

## 8 Summary of Findings and Conclusions

A characterisation protocol is required in order to assess the physicochemical characteristics of ZnO NPs intended for use in toxicological studies. This thesis presents a protocol that extracts information from a sample with regard to the NP size, morphology, composition, phase content, purity, surface chemistry, surface area, solubility and dispersion. The protocol consists of the following techniques: Inductively coupled plasma mass spectrometry (ICP-MS), X-ray diffraction (XRD), BET gas adsorption, thermogravimetric analysis with evolved gas analysis by Fourier transform infra-red spectroscopy (TGA-EGA with FTIR), FTIR, X-ray photoelectron spectroscopy (XPS), nuclear magnetic resonance spectroscopy (NMR), scanning electron microscopy (SEM), transmission electron microscopy (TEM), dynamic light scattering (DLS), plunge freezing transmission electron microscopy (PF-TEM) and Zeta potential measurement. This protocol should be applied in future toxicity studies on different NPs.

Commercially sourced ZnO NP samples are relatively variable in size, size distribution and morphology; some samples have coatings present on the surface of the NPs or contain secondary phases. EN-Z-1 has a wide distribution of sizes and morphologies. Due to the presence of a coating (possibly an aliphatic polyether), the particles have excellent stability in aqueous dispersion remaining in suspension for weeks after preparation. EN-Z-2 has a narrower size distribution however there is an additional phase of  $\text{Zn}_5(\text{CO}_3)_2(\text{H}_2\text{O})_6$  present in the sample. The powder does not disperse into primary particles when suspended in water, and even immediately after sonication relatively large agglomerates still exist. EN-Z-3 has a relatively narrow size distribution and only a few varieties of particle morphology. Characterisation indicates that there is a very low concentration of hydrozincite present in the sample. The particles disperse well in water initially however the primary particle size is not achieved and sedimentation of the particles occurs within hours of preparing the dispersion.

ZnO NP samples were synthesized by flame spray pyrolysis technique and by polyol route. The FSP route produces the most monodispersed NPs of all the samples investigated in this study.

For the polyol route, increasing the concentration of ZnAc increases the size of the ZnO crystallites obtained, while at the same time decreasing the tendency of the crystallites produced to agglomerate into spherical clusters. Inhomogeneous heating of the precursor solution leads to polydisperse ZnO NPs.

For the FSP route, varying the rate of flow of the precursor solution to the flame and changing the zinc precursor and solvent alters the size of the NPs produced. Increasing the rate of flow of the precursor solution to the flame from 1-5 ml/min increased the average size ( $d_{\text{BET}}$ ) of the NPs obtained from 11 to 18 nm.

EN-Z-4 (prepared by FSP) and EN-Z-6 (prepared by the polyol route) were selected to put forward to toxicological investigations. Synthesized samples both comprise monophasic wurtzite ZnO. Residual precursor was detected on the surface of the synthesized samples, however the amounts detected were extremely small compared to the coating on EN-Z-1.

The actual ZnO NP concentration can vary significantly from the nominal concentration which will lead to unrepresentative results from toxicological investigations. Error in determining the mass of ZnO may result from adsorbed CO<sub>2</sub> and H<sub>2</sub>O at the surface of samples. These impurities could also affect solubility.

The agglomeration and solubility of ZnO is sensitive to solution characteristics. Due to high ionic strength, agglomeration of ZnO NPs increases when suspended in DMEM as compared to in water. The addition of BSA has a dispersing effect on ZnO NP suspensions, due to the formation of a protein corona. The solubility of ZnO increases when suspended in DMEM as compared to in water. Solubility also increases with decreasing solution temperature. Perhaps most critically, the pH of the solution significantly influences ZnO solubility.

PF-TEM is an excellent complementary technique to DLS for determining agglomerate size distributions of NP suspensions. The results for the agglomerate

size distributions obtained by PF-TEM and DLS were in good agreement when comparing varying concentrations of EN-Z-1 in water. DLS struggles with accurately measuring hydrodynamic diameters of ZnO suspensions with low concentration due to polydispersity of the sample and dissolution.

The toxicity of ZnO NPs to cells is dependent on dispersion and dissolution in cell culture media. ZnO will dissolve in DMEM completely up to a concentration of 5.7 µg/ml, above which zinc carbonate precipitates; uncoated ZnO NPs induce lower toxicity than ionic zinc as a result of this precipitation. Coated ZnO NPs induce higher toxicity than uncoated ZnO NPs due to slower dissolution kinetics, enhanced cellular uptake and intracellular dissolution leading to increased zinc levels internally in the cell. The presence of serum in cell culture media during toxicity assays may impact on ZnO NP toxicity as EN-Z-2, EN-Z-3, EN-Z-4 and EN-Z-6 induced lower toxicity to A549 cells over 24 hours compared to results reported in the literature.

Characterising cellular uptake by TEM is a more sensitive technique for assessing cell viability than the MTT assay.

There is currently a lack of adequate characterisation of NPs, used in toxicity studies, reported in the literature. This study highlights the importance of carrying out detailed physicochemical characterisation of NPs used in toxicological investigations in order to accurately interpret results. Many characterisation techniques have been investigated in this work and although it would be beneficial for nanotoxicologists to carry out all of the techniques included in the protocol, it is perhaps not a realistic expectation. Therefore, where necessary priority may be given to certain techniques to acquire key information from the sample, knowledge of which this investigation has identified as essential for interpreting NP toxicity studies. Primary particle size, composition and crystalline phase may be determined by TEM. This study found that the agglomerate size distribution, solubility and presence of coatings may impact on the potential toxicity of NPs. Hence, it is recommended that as a minimum, techniques to determine these characteristics should be implemented. Therefore DLS, ICP-MS and FTIR may be used for

preliminary investigations. For polydisperse samples and suspensions with low NP concentration, it is recommended that an alternative method of investigating agglomerate size distribution, such as PF-TEM, is employed to complement DLS. A significant issue with the investigation presented in this thesis has been a lack of repeat experiments for DLS and ICP-MS measurements. It is strongly recommended that measurements are carried out in triplicate in order to validate and increase confidence in the results acquired.

### **8.1 Future Work**

- Monitor the temperature of the precursor solution for polyol synthesis of ZnO NPs in order to determine if inconsistencies between batches is attributable to inhomogenous heating.
- Repeat the experiments investigating dissolution over time but maintain a constant pH for the duration. Store the suspensions under identical conditions experienced in toxicity assays.
- Investigate the dispersion of ZnO NPs in DMEM and water by DLS and PF-TEM without sonication immediately prior to analysis. Sedimented NPs must be removed from the bottom of the vial in order to analyse by sizing techniques. Agitation of the sedimented NPs by gently shaking the vial may be more akin to the motion experienced by the NPs when in suspension with the cells.
- In order to determine the effect of carbonate on the NP surface, freshly prepared samples will be stored under dry conditions with silica gel. The solubility and toxicity of pure ZnO may then be investigated.
- The effect of NP solubility on the toxicity will be investigated further. Investigate the synthesis of ZnO NPs with varying solubility by varying level of dopant material such as iron. Analyse the effect of the altered solubility on the toxicity of the particles.
- The MTT assay for EN-Z-3 will be repeated.
- The MTT and Comet assay will be performed using a positive control in order to increase the reliability of the results presented in this thesis.

- The weight of the sample will be measured using more accurate scales, and the concentration will be checked by ICP-MS.
- When analysing samples by ICP-MS and DLS, experiments will be repeated in triplicate in order to improve the accuracy and interpretation of results.



## References

- Ahamed, M., Akhtar, M. J., Raja, M., Ahmad, I., Siddiqui, M. K. J., AlSalhi, M. S., & Alrokayan, S. a. (2011). ZnO nanorod-induced apoptosis in human alveolar adenocarcinoma cells via p53, survivin and bax/bcl-2 pathways: role of oxidative stress. *Nanomedicine : nanotechnology, biology, and medicine*, 7(6), 904–13. doi:10.1016/j.nano.2011.04.011
- Allouni, Z. E., Cimpan, M. R., Høl, P. J., Skodvin, T., & Gjerdet, N. R. (2009). Agglomeration and sedimentation of TiO<sub>2</sub> NPs in cell culture medium. *Colloids and surfaces. B, Biointerfaces*, 68(1), 83–7. doi:10.1016/j.colsurfb.2008.09.014
- Andersen, FA, and L Brecevic (1991) Infrared spectra of amorphous and crystalline calcium carbonate. *Acta Chemica Scandinavica* 45:1018–1024.
- Athanassiou, E. K., Grass, R. N., & Stark, W. J. (2010). Chemical Aerosol Engineering as a Novel Tool for Material Science: From Oxides to Salt and Metal NPs. *Aerosol Science and Technology*, 44(2), 161–172. doi:10.1080/02786820903449665
- Au, C., Hirsch, W., & Hirschwald, W. (1988). Adsorption of carbon monoxide and carbon dioxide on annealed and defect zinc oxide (0001) surfaces studied by photoelectron spectroscopy (XPS and UPS). *Surface science*, 197, 391–401.
- Auer, G., Woditsch, P., Westerhaus, K., Kischkewitz, J., Griebler, W.-D., & De Liedekerke, M. (2009). Ullmann's encyclopedia of industrial chemistry (6th ed., pp. 286–289). Weinheim: Wiley.
- Auffan, M., Rose, J., Bottero, J.-Y., Lowry, G. V, Jolivet, J.-P., & Wiesner, M. R. (2009). Towards a definition of inorganic NPs from an environmental, health and safety perspective. *Nature nanotechnology*, 4(10), 634–41. doi:10.1038/nnano.2009.242

- Bang, J., Yang, H., & Holloway, P. H. (2006). Enhanced and stable green emission of ZnO NPs by surface segregation of Mg. *Nanotechnology*, *17*(4), 973–8. doi:10.1088/0957-4484/17/4/022
- Barcelo, D., & Farre, M. (2012). *Analysis and Risk of Nanomaterials in Environmental and Food Samples* (1st ed., pp. 17–32). Oxford, Amsterdam: Elsevier B.V.
- Baruah, S., & Dutta, J. (2009). Hydrothermal growth of ZnO nanostructures. *Science and Technology of Advanced Materials*, *10*(1), 013001. doi:10.1088/1468-6996/10/1/013001
- Batley, G. E., & J, M. M. (2012). *Fate of Manufactured Nanomaterials in the Australian Environment*. CSIRO Niche Manufacturing Flagship Report, Retrieved from: <http://www.environment.gov.au/settlements/biotechnology/publications/pubs/manufactured-nanomaterials.pdf>
- Benn, T. M., & Westerhoff, P. (2008). Nanoparticle Silver Released into Water from Commercially Available Sock Fabrics. *Environmental Science & Technology*, *42*(11), 4133–4139. doi:10.1021/es7032718
- Berne, B. J., & Pecora, R. (2000). *Dynamic light scattering: With applications to chemistry, biology and physics*. *Biochemical Education* (Vol. 5). Dover Publications.
- Berntsen, P., Park, C. Y., Rothen-Rutishauser, B., Tsuda, A., Sager, T. M., Molina, R. M., Donaghey, T. C., Alencar, A. M., Kasahara, D. I., Ericsson, T., Millet, E. J., Swenson, J., Tschumperlin, D. J., Butler, J. P., Brain, J. D., Fredberg, J. J., Gehr, P., Zhou, E. H. (2010). Biomechanical effects of environmental and engineered particles on human airway smooth muscle cells. *Journal of the Royal Society, Interface / the Royal Society*, *7 Suppl 3*, S331–40. doi:10.1098/rsif.2010.0068.focus

- Bhattacharjee, S., De Haan, L. H. J., Evers, N. M., Jiang, X., Marcelis, A. T. M., Zuilhof, H., Rietjens, I. M. C. M., Alink, G. M. (2010). Role of surface charge and oxidative stress in cytotoxicity of organic monolayer-coated silicon NPs towards macrophage NR8383 cells. *Particle and fibre toxicology*, 7, 25. doi:10.1186/1743-8977-7-25
- Bian, S.-W., Mudunkotuwa, I. a, Rupasinghe, T., & Grassian, V. H. (2011). Aggregation and dissolution of 4 nm ZnO NPs in aqueous environments: influence of pH, ionic strength, size, and adsorption of humic acid. *Langmuir : the ACS journal of surfaces and colloids*, 27(10), 6059–68. doi:10.1021/la200570n
- Bitenc, M., Podbršček, P., Dubček, P., Bernstorff, S., Dražić, G., Orel, B., & Orel, Z. C. (2012). The growth mechanism of zinc oxide and hydrozincite: a study using electron microscopies and in situ SAXS. *CrystEngComm*, 14(9), 3080. doi:10.1039/c2ce06134a
- Borm, P. J. A, Robbins, D., Haubold, S., Kuhlbusch, T., Fissan, H., Donaldson, K., Schins, R., Stone, V., Kreyling, W., Lademann, J., Krutmann, J., Warheit, D., Oberdorster, E. (2006). The potential risks of nanomaterials: a review carried out for ECETOC. *Particle and fibre toxicology*, 3, 11. doi:10.1186/1743-8977-3-11
- Bouwmeester, H., Dekkers, S., Noordam, M. Y., Hagens, W. I., Bulder, A. S., De Heer, C., Ten Voorde, S. E. C. G., Wijnhoven, S W P., Marvin, H J P., Sips, A J A M. (2009). Review of health safety aspects of nanotechnologies in food production. *Regulatory toxicology and pharmacology : RTP*, 53(1), 52–62. doi:10.1016/j.yrtph.2008.10.008
- Bouwmeester, H., Lynch, I., Marvin, H. J. P., Dawson, K. A., Berges, M., Braguer, D., Byrne, H. J., Casey, A, Chambers, G, Clift, M J D, Elia, G, Fernandes, T F, Fjellsbø, L B, Hatto, P, Juillerat, L, Klein, C, Kreyling, W G, Nickel, C, Riediker, M, Stone, V. (2011). Minimal analytical characterisation of

engineered nanomaterials needed for hazard assessment in biological matrices. *Nanotoxicology*, 5(1), 1–11. doi:10.3109/17435391003775266

Brayner, R., Dahoumane, S. A., Yéprémian, C., Djediat, C., Meyer, M., Couté, A., & Fiévet, F. (2010). ZnO NPs: synthesis, characterisation, and ecotoxicological studies. *Langmuir : the ACS journal of surfaces and colloids*, 26(9), 6522–8. doi:10.1021/la100293s

Brown, D. M., Kinloch, I. a., Bangert, U., Windle, a. H., Walter, D. M., Walker, G. S., Scotchford, C. A., Donaldson, K., Stone, V. (2007). An in vitro study of the potential of carbon nanotubes and nanofibres to induce inflammatory mediators and frustrated phagocytosis. *Carbon*, 45(9), 1743–1756. doi:10.1016/j.carbon.2007.05.011

Cao, G. (2004). *Nanostructures and Nanomaterials: Synthesis, Properties and Applications* (pp. 51–105). London: Imperial College Press.

Carlson, C., Hussain, S. M., Schrand, A. M., Braydich-Stolle, L. K., Hess, K. L., Jones, R. L., & Schlager, J. J. (2008). Unique cellular interaction of silver NPs: size-dependent generation of reactive oxygen species. *The journal of physical chemistry. B*, 112(43), 13608–19. doi:10.1021/jp712087m

Carroz, J. W., Odencrantz, F. K., Finnegan, W. G., & Drehmel, D. C. (1980). Aerosol generation to simulate specific industrial fine particle effluents. *American Industrial Hygiene Association journal*, 41(2), 77–84. doi:10.1080/15298668091424401

Cassee, F. R., Van Balen, E. C., Singh, C., Green, D., Muijser, H., Weinstein, J., & Dreher, K. (2011). Exposure, health and ecological effects review of engineered nanoscale cerium and cerium oxide associated with its use as a fuel additive. *Critical reviews in toxicology*, 41(3), 213–29. doi:10.3109/10408444.2010.529105

- CERAM. (2012) Brunauer-Emmett-Teller (BET) Surface Area Analysis and Barrett-Joyner-Halenda (BJH) Pore Size and Volume Analysis. *Testing and Analysis Techniques*. Retrieved February 5, 2012, from <http://www.ceram.com/testing-analysis/techniques/brunauer-emmett-teller-surface-area-analysis-barrett-joyner-halenda-pore-size-and-volume-analysis/>
- Chen, J.-F., Wang, Y.-H., Guo, F., Wang, X.-M., & Zheng, C. (2000). Synthesis of Nanoparticles with Novel Technology: High-Gravity Reactive Precipitation. *Industrial & Engineering Chemistry Research*, 39(4), 948–954. doi:10.1021/ie990549a
- Chen, L., Xu, N., Yang, H., Zhou, C., & Chi, Y. (2011). Zinc oxide quantum dots synthesized by electrochemical etching of metallic zinc in organic electrolyte and their electrochemiluminescent properties. *Electrochimica Acta*, 56(3), 1387–1391. doi:10.1016/j.electacta.2010.10.050
- Chen, X., Liu, L., Yu, P. Y., & Mao, S. S. (2011). Increasing solar absorption for photocatalysis with black hydrogenated titanium dioxide nanocrystals. *Science (New York, N.Y.)*, 331(6018), 746–50. doi:10.1126/science.1200448
- Chithrani, B. D., Ghazani, A. a, & Chan, W. C. W. (2006). Determining the size and shape dependence of gold NP uptake into mammalian cells. *Nano letters*, 6(4), 662–8. doi:10.1021/nl052396o
- Cho, W.-S., Duffin, R., Howie, S. E. M., Scotton, C. J., Wallace, W. a H., Macnee, W., Bradley, M., Megson, I. L., Donaldson, K. (2011). Progressive severe lung injury by zinc oxide nanoparticles; the role of Zn<sup>2+</sup> dissolution inside lysosomes. *Particle and fibre toxicology*, 8(1), 27. doi:10.1186/1743-8977-8-27
- Christensen, F. M., Johnston, H. J., Stone, V., Aitken, R. J., Hankin, S., Peters, S., & Aschberger, K. (2010). Nano-silver - feasibility and challenges for human health risk assessment based on open literature. *Nanotoxicology*, 4(3), 284–95. doi:10.3109/17435391003690549

- Churchman, A. H., Wallace, R., Milne, S. J., Brown, A. P., Brydson, R., & Beales, P. a. (2013). Serum albumin enhances the membrane activity of ZnO NPs. *Chemical communications (Cambridge, England)*, 4–6. doi:10.1039/c3cc37871c
- Clifton, J., Rossiter, W., & Brown, P. (1985). Degraded aqueous glycol solutions: pH values and the effects of common ions on suppressing pH decreases. *Solar energy materials*, 12, 77–86. Retrieved from <http://www.sciencedirect.com/science/article/pii/0165163385900267>
- Collins, I. R., & Taylor, S. E. (1992). Non-aqueous thermal decomposition route to colloidal inorganic oxides. *Journal of Materials Chemistry*, 2(12), 1277. doi:10.1039/jm9920201277
- Coutanceau, C., Baranton, S., & Napporn, T. (2012). Platinum Fuel cell NP syntheses: effect on morphology, structure and electrocatalytic behavior. In A. A. Hashim (Ed.), *The Delivery of Nanoparticles*. InTech.
- Cullity, B. D., & Stock, S. R. (2001). *Elements of X-ray Diffraction* (3rd ed.). London: Prentice Hall.
- Daughton, C., & Ternes, T. (1999). Pharmaceuticals and personal care products in the environment: agents of subtle change? *Environmental Health Perspectives*, 107(6). Retrieved from <http://www.ncbi.nlm.nih.gov/pmc/articles/PMC1566206/>
- David, C. A., Galceran, J., Rey-Castro, C., Puy, J., Companys, E., Salvador, J., Monné, J., Wallace, R., Vakourov, A. (2012). Dissolution Kinetics and Solubility of ZnO NPs Followed by AGNES. *The Journal of Physical Chemistry C*, 116(21), 11758–11767. doi:10.1021/jp301671b
- De Jong, W. H., & Borm, P. J. a. (2008). Drug delivery and NPs: applications and hazards. *International journal of nanomedicine*, 3(2), 133–49.

- De Jonge, N., & Ross, F. M. (2011). Electron microscopy of specimens in liquid. *Nature nanotechnology*, 6(11), 695–704. doi:10.1038/nnano.2011.161
- De Volder, M. F. L., Tawfick, S. H., Baughman, R. H., & Hart, a J. (2013). Carbon nanotubes: present and future commercial applications. *Science (New York, N.Y.)*, 339(6119), 535–9. doi:10.1126/science.1222453
- Degen, A., & Kosec, M. (2000). Effect of pH and impurities on the surface charge of zinc oxide in aqueous solution. *Journal of the European Ceramic Society*, 20(6), 667–673. Retrieved from <http://linkinghub.elsevier.com/retrieve/pii/S0955221999002034>
- Deng, X., Luan, Q., Chen, W., Wang, Y., Wu, M., Zhang, H., & Jiao, Z. (2009). Nanosized ZnO particles induce neural stem cell apoptosis. *Nanotechnology*, 20(11), 115101. doi:10.1088/0957-4484/20/11/115101
- Derjaguin, B., & Landau, L. (1993). Theory of the stability of strongly charged lyophobic sols and of the adhesion of strongly charged particles in solutions of electrolytes. *Progress in Surface Science*, 43(1-4), 30–59. doi:10.1016/0079-6816(93)90013-L
- Di Francesco, A., Desnoyer, R. W., Covacci, V., Wolf, F. I., Romani, A., Cittadini, A., Bond, M., (1998). Changes in Magnesium Content and Subcellular Distribution during Retinoic Acid-Induced Differentiation of HL60 Cells, *360(2)*, 149–157. doi:hb
- Dobro, M. J., Melanson, L. A., Jensen, G. J., & McDowall, A. W. (2010). Plunge freezing for electron cryomicroscopy. *Methods in Enzymology*, 481(10), 63–82. Retrieved from <http://www.ncbi.nlm.nih.gov/pubmed/20887853>
- Dodd, a. C., McKinley, a. J., Saunders, M., & Tsuzuki, T. (2006). Effect of Particle Size on the Photocatalytic Activity of Nanoparticulate ZnO. *Journal of Nanoparticle Research*, 8(1), 43–51. doi:10.1007/s11051-005-5131-z

- Donaldson, K., Murphy, F. A., Duffin, R., & Poland, C. A. (2010). Asbestos, carbon nanotubes and the pleural mesothelium: a review of the hypothesis regarding the role of long fibre retention in the parietal pleura, inflammation and mesothelioma. *Particle and fibre toxicology*, 7(1), 5. doi:10.1186/1743-8977-7-5
- Dollimore, D., France, J. A., Krupay, B. W., & Whitehead, R. (1980). Kinetic Ferets of the thermal decomposition of zinc carbonate. *Thermochimica Acta*, 36(3), 343–349. doi:10.1016/0040-6031(80)87029-8
- Dussert, A. S., Gooris, E., & Hemmerle, J. (1997). Characterisation of the mineral content of a physical sunscreen emulsion and its distribution onto human stratum corneum. *International Journal of Cosmetic Science* 19 (3), 119–29. doi:10.1046/j.1467-2494.1997.171707.x
- Dutta, D., Sundaram, S. K., Teeguarden, J. G., Riley, B. J., Fifield, L. S., Jacobs, J. M., Addleman, S. R., (2007). Adsorbed proteins influence the biological activity and molecular targeting of nanomaterials. *Toxicological sciences : an official journal of the Society of Toxicology*, 100(1), 303–15. doi:10.1093/toxsci/kfm217
- El Badawy, A. M., Silva, R. G., Morris, B., Scheckel, K. G., Suidan, M. T., & Tolaymat, T. M. (2011). Surface charge-dependent toxicity of silver nanoparticles. *Environmental science & technology*, 45(1), 283–7. doi:10.1021/es1034188
- Elsaesser, A., & Howard, C. V. (2012). Toxicology of nanoparticles. *Advanced drug delivery reviews*, 64(2), 129–37. doi:10.1016/j.addr.2011.09.001
- Feldmann, C., & Merikhi, J. (2000). Adhesion of Colloidal ZnO Particles on ZnS-Type Phosphor Surfaces. *Journal of colloid and interface science*, 223(2), 229–234. doi:10.1006/jcis.1999.6648



- Ferin, J., Oberdörster, G., & Penney, D. P. (1992). Pulmonary retention of ultrafine and fine particles in rats. *American journal of respiratory cell and molecular biology*, 6(5), 535–42. doi:10.1165/ajrcmb/6.5.535
- Fernandez-Segura, E., & Warley, A. (2008). Electron probe X-ray microanalysis for the study of cell physiology. *Methods in cell biology*, 88, 19–43. doi:10.1016/S0091-679X(08)00402-0
- Ferraro, J. R., & Krishnan, K. (1990). *Practical Fourier transform infrared spectroscopy: industrial and laboratory chemical analysis*. San Diego, London: Academic Press.
- Fologea, D., Ledden, B., McNabb, D. S., & Li, J. (2007). Electrical characterization of protein molecules by a solid-state nanopore. *Applied physics letters*, 91(5), 539011–539013. doi:10.1063/1.2767206
- Franklin, N. M., Rogers, N. J., Apte, S. C., Batley, G. E., Gadd, G. E., & Casey, P. S. (2007). Comparative Toxicity of Nanoparticulate ZnO, Bulk ZnO, and ZnCl<sub>2</sub> to a Freshwater Microalga (*Pseudokirchneriella subcapitata*): The Importance of Particle Solubility. *Environmental Science & Technology*, 41(24), 8484–8490. doi:10.1021/es071445r
- Fröhlich, E., Samberger, C., Kueznik, T., Absenger, M., Roblegg, E., Zimmer, A., & Pieber, T. R. (2009). Cytotoxicity of nanoparticles independent from oxidative stress. *The Journal of toxicological sciences*, 34(4), 363–75.
- Fultz, B., & Howe, J. M. (2002). *Transmission Electron Microscopy and Diffractometry of Materials*. (2nd ed.). Verlag Berlin Heidelberg New York:: Springer.
- Future Markets Incorporated. (2012). *The Global Market for Zinc Oxide Nanopowders 2012* (p. 56). Retrieved from [http://www.researchandmarkets.com/reports/2116313/the\\_global\\_market\\_for\\_zinc\\_oxide\\_nanopowders\\_2012](http://www.researchandmarkets.com/reports/2116313/the_global_market_for_zinc_oxide_nanopowders_2012).

- Gasparro, F. P., Mitchnick, M., & Nash, J. F. (1998). A review of sunscreen safety and efficacy. *Photochemistry and Photobiology*, *68*(3), 243–256.
- George, S., Pokhrel, S., Xia, T., Gilbert, B., Ji, Z., Schowalter, M., Rosenauer, A., Damoiseaux, R., Bradley, K. A., Mädler, L., Nel, A. E. (2010). Use of a rapid cytotoxicity screening approach to engineer a safer zinc oxide NP through iron doping. *ACS nano*, *4*(1), 15–29. doi:10.1021/nn901503q
- Gilbert, B., Fakra, S. C., Xia, T., Pokhrel, S., Mädler, L., & Nel, A. E. (2012). The fate of ZnO NPs administered to human bronchial epithelial cells. *ACS nano*, *6*(6), 4921–30. doi:10.1021/nn300425a
- Gontier, E., Habchi, C., Pouthier, T., Aguer, P., Barberet, P., Barbotteau, Y., Incerti, S., Ynsa, M. D., Surleve-Bazeille, J. E. Moretto, P., (2004). Nuclear microscopy and electron microscopy studies of percutaneous penetration of NPs in mammalian skin. *34th EDSR Meeting*. Abstract 64.
- Goodman, C. M., McCusker, C. D., Yilmaz, T., & Rotello, V. M. (2004). Toxicity of gold NPs functionalized with cationic and anionic side chains. *Bioconjugate chemistry*, *15*(4), 897–900. doi:10.1021/bc049951i
- Gottschalk, F., Sonderer, T., Scholz, R. W., & Nowack, B. (2009). Modeled environmental concentrations of engineered nanomaterials (TiO<sub>2</sub>, ZnO, Ag, CNT, Fullerenes) for different regions. *Environmental science & technology*, *43*(24), 9216–22. doi:10.1021/es9015553
- Gottschalk, F., Sonderer, T., Scholz, R. W., & Nowack, B. (2010). Possibilities and limitations of modeling environmental exposure to engineered nanomaterials by probabilistic material flow analysis. *Environmental toxicology and chemistry / SETAC*, *29*(5), 1036–48. doi:10.1002/etc.135
- Gratton, S. E. a, Ropp, P. a, Pohlhaus, P. D., Luft, J. C., Madden, V. J., Napier, M. E., & DeSimone, J. M. (2008). The effect of particle design on cellular

- internalization pathways. *Proceedings of the National Academy of Sciences of the United States of America*, 105(33), 11613–8. doi:10.1073/pnas.0801763105
- Gröhn, A. J., Pratsinis, S. E., & Wegner, K. (2012). Fluid-particle dynamics during combustion spray aerosol synthesis of ZrO<sub>2</sub>. *Chemical Engineering Journal*, 191, 491–502. doi:10.1016/j.cej.2012.02.093
- Height, M. J., Mädler, L., Pratsinis, S. E., & Krumeich, F. (2006). Nanorods of ZnO Made by Flame Spray Pyrolysis. *Chemistry of Materials*, 18(2), 572–578. doi:10.1021/cm052163y
- Herd, H. L., Malugin, A., & Ghandehari, H. (2011). Silica nanoconstruct cellular toleration threshold *in vitro*. *Journal of controlled release : official journal of the Controlled Release Society*, 153(1), 40–8. doi:10.1016/j.jconrel.2011.02.017
- Hondow, N., Brydson, R., Wang, P., Holton, M. D., Brown, M. R., Rees, P., Summers, H. D., Brown, A. (2012). Quantitative characterisation of NP agglomeration within biological media. *Journal of NP Research*, 14(7). doi:10.1007/s11051-012-0977-3
- Hore, P. J. (1995). *Nuclear Magnetic Resonance* (pp. 1–4). New York: Oxford University Press.
- Hsiao, I.-L., & Huang, Y.-J. (2011). Effects of various physicochemical characteristics on the toxicities of ZnO and TiO NPs toward human lung epithelial cells. *The Science of the total environment*, 409(7), 1219–28. doi:10.1016/j.scitotenv.2010.12.033
- Hsiao, I.-L., & Huang, Y.-J. (2011). Titanium oxide shell coatings decrease the cytotoxicity of ZnO nanoparticles. *Chemical research in toxicology*, 24(3), 303–13. doi:10.1021/tx1001892
- Hsieh, C.-H. (2007). Spherical ZnO nano particles from zinc acetate in the precipitation method. *Journal of the Chinese Chemical Society*, (54), 31–34.

- Hutter, E., Boridy, S., Labrecque, S., Lalancette-Hébert, M., Kriz, J., Winnik, F. M., & Maysinger, D. (2010). Microglial response to gold NPs. *ACS nano*, 4(5), 2595–606. doi:10.1021/nn901869f
- Invitrogen. (2012). Do high or low levels of sodium bicarbonate affect the pH of my tissue culture media? Retrieved April 24, 2013, from <http://www.invitrogen.com/search/support/supportSearchAction.action?query=dmem&supportSearchArea=Product+FAQs&initialSearch=true&refineSearch=true&mode=and>
- Islam, M. N., Ghosh, T. B., Chopra, K. L., & Acharya, H. N. (1996). XPS and X-ray diffraction studies of aluminum-doped zinc oxide transparent conducting films. *Thin Solid Films*, 280(1-2), 20–25. doi:10.1016/0040-6090(95)08239-5
- Jensen, J. R., Johannessen, T., & Livbjerg, H. (2000). Synthesis of nano-particles of ZnO/ Al<sub>2</sub>O<sub>3</sub> in a premixed flame. *Journal of Aerosol Science*, 31(1), 216.
- Jézéquel, D., Guenot, J., Jouini, N., & Fiévet, F. (1995). Submicrometer ZnO particles: Elaboration in polyol medium and morphological characteristics. *Journal of Materials Research*, 10(1), 77–83. doi:10.1557/JMR.1995.0077
- Ji, Z., Jin, X., George, S., Xia, T., Meng, H., Wang, X., Suarez, E., Zhang, H., Hoek, E M V., Godwin, H., Nel, A E., Zink, J. I. (2010). Dispersion and stability optimization of TiO<sub>2</sub> NPs in cell culture media. *Environmental science & technology*, 44(19), 7309–14. doi:10.1021/es100417s
- Jiang, Z., Zhao, X., & Manthiram, A. (2013). Sulfonated poly(ether ether ketone) membranes with sulfonated graphene oxide fillers for direct methanol fuel cells. *International Journal of Hydrogen Energy*, 38(14), 5875–5884. doi:10.1016/j.ijhydene.2013.02.129
- Kahru, A., & Dubourguier, H.-C. (2010). From ecotoxicology to nanoecotoxicology. *Toxicology*, 269(2-3), 105–19. doi:10.1016/j.tox.2009.08.016

- Klimm, D., Schulz, D., & Ganschow, S. (2011). Growth of Bulk ZnO. In *Comprehensive Semiconductor Science and Technology* (pp. 302–338). Bhattacharya, R. Fornari, & H. Kamimura (Eds.), Elsevier.
- Kreyling, W. G., Semmler-Behnke, M., & Chaudhry, Q. (2010). A complementary definition of nanomaterial. *Nano Today*, 5(3), 165–168. doi:10.1016/j.nantod.2010.03.004
- La Mer, V. K., & Dinegar, R. H. (1950). Theory, Production and Mechanism of Formation of Monodispersed Hydrosols.pdf. *Journal of the American Ceramic Society*, 72(11), 4847.
- Lam, C.-W., James, J. T., McCluskey, R., & Hunter, R. L. (2004). Pulmonary toxicity of single-wall carbon nanotubes in mice 7 and 90 days after intratracheal instillation. *Toxicological sciences: an official journal of the Society of Toxicology*, 77(1), 126–34. doi:10.1093/toxsci/kfg243
- Lankoff, A., Sandberg, W. J., Wegierek-Ciuk, A., Lisowska, H., Refsnes, M., Sartowska, B., Schwarze, P. E., Meczynska-Wielgosz, S., Wojewodzka, M., Kruszewski, M. (2012). The effect of agglomeration state of silver and titanium dioxide NPs on cellular response of HepG2, A549 and THP-1 cells. *Toxicology letters*, 208(3), 197–213. doi:10.1016/j.toxlet.2011.11.006
- Lansdown, A. B., & Taylor, A. (1997). Zinc and titanium oxides: promising UV-absorbers but what influence do they have on the intact skin? *International journal of cosmetic science*, 19(4), 167–72. doi:10.1046/j.1467-2494.1997.171712.x
- Li, J., Fan, H., & Jia, X. (2010). Multilayered ZnO Nanosheets with 3D Porous Architectures: Synthesis and Gas Sensing Application. *The Journal of Physical Chemistry C*, 114(35), 14684–14691. doi:10.1021/jp100792c
- Li, M., Pokhrel, S., Jin, X., Mädler, L., Damoiseaux, R., & Hoek, E. M. V. (2011). Stability, bioavailability, and bacterial toxicity of ZnO and iron-doped ZnO NPs

in aquatic media. *Environmental science & technology*, 45(2), 755–61.  
doi:10.1021/es102266g

Li, X. Y., Gilmour, P. S., Donaldson, K., & MacNee, W. (1996). Free radical activity and pro-inflammatory effects of particulate air pollution (PM10) *in vivo* and *in vitro*. *Thorax*, 51(12), 1216–22.

Li, Y., Wu, K., & Zhitomirsky, I. (2010). Electrodeposition of composite zinc oxide–chitosan films. *Colloids and Surfaces A: Physicochemical and Engineering Aspects*, 356(1-3), 63–70. doi:10.1016/j.colsurfa.2009.12.037

Li, Zhongjun, Xiaoqing Shen, Xun Feng, Peiyuan Wang, and Zhishen Wu. 2005. “Non-isothermal kinetics studies on the thermal decomposition of zinc hydroxide carbonate.” *Thermochimica Acta* 438(1-2):102–106.

Liewhiran, C., & Phanichphant, S. (2007). Influence of Thickness on Ethanol Sensing Characteristics of Doctor-bladed Thick Film from Flame-made ZnO Nanoparticles. *Sensors*, 7(2), 185–201. doi:10.3390/s7020185

Lin, W., Xu, Y., Huang, C.-C., Ma, Y., Shannon, K. B., Chen, D.-R., & Huang, Y.-W. (2008). Toxicity of nano- and micro-sized ZnO particles in human lung epithelial cells. *Journal of Nanoparticle Research*, 11(1), 25–39. doi:10.1007/s11051-008-9419-7

Liqiang, J., Baiqi, W., Baifu, X., Shudan, L., Keying, S., Weimin, C., & Honggang, F. (2004). Investigations on the surface modification of ZnO nanoparticle photocatalyst by depositing Pd. *Journal of Solid State Chemistry*, 177(11), 4221–4227. doi:10.1016/j.jssc.2004.08.016

Liu, Y., Li, W., Lao, F., Liu, Y., Wang, L., Bai, R., Zhao, Y., Chen, C.. (2011). Intracellular dynamics of cationic and anionic polystyrene NPs without direct interaction with mitotic spindle and chromosomes. *Biomaterials*, 32(32), 8291–303. doi:10.1016/j.biomaterials.2011.07.037

- López, G., Castner, D., & Ratner, B. (1991). XPS O 1s binding energies for polymers containing hydroxyl, ether, ketone and ester groups. *Surface and Interface Analysis*, *17*, 267–272.
- Love, S. a, Maurer-Jones, M. a, Thompson, J. W., Lin, Y.-S., & Haynes, C. L. (2012). Assessing nanoparticle toxicity. *Annual review of analytical chemistry (Palo Alto, Calif.)*, *5*, 181–205. doi:10.1146/annurev-anchem-062011-143134
- Luyts, K., Napierska, D., Nemery, B., & Hoet, P. H. M. (2013). How physico-chemical characteristics of NPs cause their toxicity: complex and unresolved interrelations. *Environmental Science: Processes & Impacts*, *15*(1), 23. doi:10.1039/c2em30237c
- Ma, H., Williams, P. L., & Diamond, S. a. (2013). Ecotoxicity of manufactured ZnO nanoparticles--a review. *Environmental pollution (Barking, Essex : 1987)*, *172*, 76–85. doi:10.1016/j.envpol.2012.08.011
- Mädler, L., Kammler, H., Mueller, R., & SE, P. (2002). Controlled synthesis of nanostructured particles by flame spray pyrolysis. *Journal of Aerosol Science*, *33*, 369–389.
- Mahmoud, W. E., & El-Mallah, H. M. (2009). Synthesis and characterisation of PVP-capped CdSe NPs embedded in PVA matrix for photovoltaic application. *Journal of Physics D: Applied Physics*, *42*(3), 035502. doi:10.1088/0022-3727/42/3/035502
- Malugin, A., & Ghandehari, H. (2010). Cellular uptake and toxicity of gold NPs in prostate cancer cells: a comparative study of rods and spheres. *Journal of applied toxicology : JAT*, *30*(3), 212–7. doi:10.1002/jat.1486
- Malvern Instruments Ltd. n.d. “Dynamic Light Scattering: An Introduction in 30 Minutes.” *DLS Technical Note* 1–8. Retrieved February 6, 2013 (<http://www.malvern.com/common/downloads/campaign/MRK656-01.pdf>).

- Malvern Instruments Ltd. n.d. "Zeta Potential An Introduction in 30 Minutes." *Zetasizer Nano series technical note* 2:1–6. Retrieved February 6, 2012 ([http://www.nbtc.cornell.edu/facilities/downloads/Zeta potential - An introduction in 30 minutes.pdf](http://www.nbtc.cornell.edu/facilities/downloads/Zeta_potential_-_An_introduction_in_30_minutes.pdf)).
- Manson, J., Kumar, D., Meenan, B. J., & Dixon, D. (2011). Polyethylene glycol functionalized gold nanoparticles: the influence of capping density on stability in various media. *Gold Bulletin*, *44*(2), 99–105. doi:10.1007/s13404-011-0015-8
- Mar, L. G., Timbrell, P. Y., & Lamb, R. N. (1993). An XPS study of zinc oxide thin film growth on copper using zinc acetate as a precursor. *Thin Solid Films*, *223*(2), 341–347. doi:10.1016/0040-6090(93)90542-W
- Marshall, B. S., Telford, I., & Wood, R. (1971). A field method for the determination of ZnO fume in air. *The Analyst*, *96*(145), 569–78.
- Matsoukas, T., & Friedlander, S. K. (1991). Dynamics of aerosol agglomerate formation. *Journal of Colloid and Interface Science*, *146*(2), 495–506. doi:10.1016/0021-9797(91)90213-R
- Maurer-Jones, M. a, Gunsolus, I. L., Murphy, C. J., & Haynes, C. L. (2013). Toxicity of engineered NPs in the environment. *Analytical chemistry*, *85*(6), 3036–49. doi:10.1021/ac303636s
- Meng, H., Yang, S., Li, Z., Xia, T., Chen, J., Ji, Z., Zhang, H., Wang, X., Lin, S., Huang, C., Zhou, Z H., Zink, J I., Nel, A E. (2011). Aspect ratio determines the quantity of mesoporous silica NP uptake by a small GTPase-dependent macropinocytosis mechanism. *ACS nano*, *5*(6), 4434–47. doi:10.1021/nn103344k
- Meulenkamp, E. a. (1998). Synthesis and Growth of ZnO Nanoparticles. *The Journal of Physical Chemistry B*, *102*(29), 5566–5572. doi:10.1021/jp980730h



- Midander, K., Cronholm, P., Karlsson, H. L., Elihn, K., Möller, L., Leygraf, C., & Wallinder, I. O. (2009). Surface characteristics, copper release, and toxicity of nano- and micrometer-sized copper and copper(II) oxide particles: a cross-disciplinary study. *Small (Weinheim an der Bergstrasse, Germany)*, 5(3), 389–99. doi:10.1002/sml.200801220
- Miller, R. J., Lenihan, H. S., Muller, E. B., Tseng, N., Hanna, S. K., & Keller, A. a. (2010). Impacts of metal oxide nanoparticles on marine phytoplankton. *Environmental science & technology*, 44(19), 7329–34. doi:10.1021/es100247x
- Mitchnick, M., Fairhurst, D., & Pinell, S. (1999). Microfine ZnO (Z-Cote) as a photostable UVA/UVB sunblock agent. *Journal of the American Academy of Dermatology*, 40(1), 85–90. doi:10.1016/S0190-9622(99)70532-3
- Mondelaers, D., Vanhoyland, G., Van Den Rul, H., D'haen, J., Van Bael, M., Mullens, J., & Van Poucke, L. (2002). Synthesis of ZnO nanopowder via an aqueous acetate-citrate gelation method. *Materials Research Bulletin*, 37(5), 901–914.
- Monopoli, M. P., Aberg, C., Salvati, A., & Dawson, K. A. (2012). Biomolecular coronas provide the biological identity of nanosized materials. *Nature nanotechnology*, 7(12), 779–86. doi:10.1038/nnano.2012.207
- Moos, P. J., Chung, K., Woessner, D., Honegger, M., Cutler, N. S., & Veranth, J. M. (2010). ZnO particulate matter requires cell contact for toxicity in human colon cancer cells. *Chemical research in toxicology*, 23(4), 733–9. doi:10.1021/tx900203v
- Mortimer, M., Kasemets, K., & Kahru, A. (2010). Toxicity of ZnO and CuO NPs to ciliated protozoa *Tetrahymena thermophila*. *Toxicology*, 269(2-3), 182–9. doi:10.1016/j.tox.2009.07.007
- Mu, Q., David, C. A., Galceran, J., Rey-Castro, C., Krzemiński, Ł., Wallace, R., Bamiduro, F., Milne, S. J., Hondow, N. S., Brydson, R., Vizcay-Barrena, G.,

- Routledge, M. N., Jeuken, L. J. C., and Brown, A. P. A systematic investigation of the physico-chemical factors that contribute to the toxicity of ZnO nanoparticles. Submitted to *Particle and Fibre Toxicology*, July 2013.
- Mueller, N. C., & Nowack, B. (2008). Exposure modeling of engineered nanoparticles in the environment. *Environmental science & technology*, 42(12), 4447–53.
- Müller, K. H., Kulkarni, J., Motskin, M., Goode, A., Winship, P., Skepper, J. N., Ryan, M. P., et al. (2010). pH-dependent toxicity of high aspect ratio ZnO nanowires in macrophages due to intracellular dissolution. *ACS nano*, 4(11), 6767–79. doi:10.1021/nn101192z
- Murray, C. B., Kagan, C. R., & Bawendi, M. G. (2000). Synthesis and Characterisation of Monodispersed Nanocrystals and Close-Packed Nanocrystal Assemblies. *Annual Review of Materials Science*, 30, 545–610.
- Musić, S, S Popović, M Maljković, and Đ Dragčević. 2002. “Influence of synthesis procedure on the formation and properties of zinc oxide.” *Journal of Alloys and Compounds* 347(1-2):324–332.
- Nakamoto, K. (1986). *Infrared and Raman Spectra of Inorganic and Coordination Compounds* (4 th., p. 3). New York: John Wiley & Sons.
- Nguyen, T., & Do, T. (2011). Size- and Shape-Controlled Synthesis of Monodisperse Metal Oxide and Mixed Oxide Nanocrystals. In Y. Masuda (Ed.), *Nanocrystal*. InTech.
- Nguyen, T., Raupach, M., & Janik, L. (1987). Fourier-transform infrared study of ethylene-glycol monoethyl ether adsorbed on montmorillonite—implications for surface-area measurements of clays. *Clays and Clay Minerals*, 35(1), 60–67. Retrieved from [http://www.clays.org/journal/archive/volume 35/35-1-60.pdf](http://www.clays.org/journal/archive/volume%2035/35-1-60.pdf)

- Nishiyama, H., Suga, M., Ogura, T., Maruyama, Y., Koizumi, M., Mio, K., Kitamura, S., et al. (2010). Atmospheric scanning electron microscope observes cells and tissues in open medium through silicon nitride film. *Journal of Structural Biology*, 169(3), 438–449. doi:10.1016/j.jsb.2010.01.005
- Nohynek, G. J., Lademann, J., Ribaud, C., & Roberts, M. S. (2007). Grey goo on the skin? Nanotechnology, cosmetic and sunscreen safety. *Critical reviews in toxicology*, 37(3), 251–77. doi:10.1080/10408440601177780
- Oberdörster, G., Ferin, J., & Lehnert, B. E. (1994). Correlation between particle size, *in vivo* particle persistence, and lung injury. *Environmental health perspectives*, 102 Suppl, 173–9.
- Oberdörster, G., Maynard, A., Donaldson, K., Castranova, V., Fitzpatrick, J., Ausman, K., Carter, J., et al. (2005). Principles for characterizing the potential human health effects from exposure to nanomaterials: elements of a screening strategy. *Particle and fibre toxicology*, 2, 8. doi:10.1186/1743-8977-2-8
- Oberdörster, G., Oberdörster, E., & Oberdörster, J. (2005). Nanotoxicology: An Emerging Discipline Evolving from Studies of Ultrafine Particles. *Environmental Health Perspectives*, 113(7), 823–839. doi:10.1289/ehp.7339
- Pan, Y., Neuss, S., Leifert, A., Fischler, M., Wen, F., Simon, U., Schmid, G., et al. (2007). Size-dependent cytotoxicity of gold NPs. *Small (Weinheim an der Bergstrasse, Germany)*, 3(11), 1941–9. doi:10.1002/sml.200700378
- Pan, Z., Tao, J., Zhu, Y., Huang, J.-F., & Paranthaman, M. P. (2010). Spontaneous Growth of ZnCO<sub>3</sub> Nanowires on ZnO Nanostructures in Normal Ambient Environment: Unstable ZnO Nanostructures. *Chemistry of Materials*, 22(1), 149–154. doi:10.1021/cm902734e
- Park, J., Lim, D.-H., Lim, H.-J., Kwon, T., Choi, J., Jeong, S., Choi, I.-H., et al. (2011). Size dependent macrophage responses and toxicological effects of Ag

NPs. *Chemical communications (Cambridge, England)*, 47(15), 4382–4. doi:10.1039/c1cc10357a

Pastorin, G., Wu, W., Wieckowski, S., Briand, J.-P., Kostarelos, K., Prato, M., & Bianco, A. (2006). Double functionalization of carbon nanotubes for multimodal drug delivery. *Chemical communications (Cambridge, England)*, (11), 1182–4. doi:10.1039/b516309a

Patra, H. K., Banerjee, S., Chaudhuri, U., Lahiri, P., & Dasgupta, A. K. (2007). Cell selective response to gold nanoparticles. *Nanomedicine: nanotechnology, biology, and medicine*, 3(2), 111–9. doi:10.1016/j.nano.2007.03.005

Project on Emerging Nanotechnologies. (2011). *Project on Emerging Nanotechnologies Consumer Product Inventory*. Woodrow Wilson International Centre for Scholars Washington, DC. Retrieved from: <http://www.nanotechproject.org/inventories>.

Pujalté, I., Passagne, I., Brouillaud, B., Tréguer, M., Durand, E., Ohayon-Courtès, C., & L'Azou, B. (2011). Cytotoxicity and oxidative stress induced by different metallic NPs on human kidney cells. *Particle and fibre toxicology*, 8(1), 10. doi:10.1186/1743-8977-8-10

Qi, L., & Gao, X. (2008). Emerging application of quantum dots for drug delivery and therapy. *Expert opinion on drug delivery*, 5(3), 263–7. doi:10.1517/17425247.5.3.263

Rabolli, V., Thomassen, L. C. J., Princen, C., Napierska, D., Gonzalez, L., Kirsch-Volders, M., Hoet, P. H., et al. (2010). Influence of size, surface area and microporosity on the *in vitro* cytotoxic activity of amorphous silica NPs in different cell types. *Nanotoxicology*, 4(3), 307–18. doi:10.3109/17435390.2010.482749

Ray, L., Hales, M. C., & Frost, R. L. (2008). Thermal analysis of smithsonite and hydrozincite. *Journal of Thermal Analysis and Calorimetry*, 91(3), 855–860.

- Reddy, K. M., Feris, K., Bell, J., Wingett, D. G., Hanley, C., & Punnoose, A. (2007). Selective toxicity of ZnO NPs to prokaryotic and eukaryotic systems. *Applied physics letters*, *90*(213902), 2139021–2139023. doi:10.1063/1.2742324
- Reed, R. B., Ladner, D. a, Higgins, C. P., Westerhoff, P., & Ranville, J. F. (2012). Solubility of nano-zinc oxide in environmentally and biologically important matrices. *Environmental toxicology and chemistry / SETAC*, *31*(1), 93–9. doi:10.1002/etc.708
- Rosi, N. L., & Mirkin, C. a. (2005). Nanostructures in biodiagnostics. *Chemical reviews*, *105*(4), 1547–62. doi:10.1021/cr030067f
- Rossiter, W., Brown, P., & Godette, M. (1983). The determination of acidic degradation products in aqueous ethylene glycol and propylene glycol solutions using ion chromatography. *Solar Energy Materials*, *9*, 267–279. Retrieved from <http://www.sciencedirect.com/science/article/pii/0165163383900497>
- Rossiter, W., Godette, M., Brown, P., & Galuk, K. (1985). An investigation of the degradation of aqueous ethylene glycol and propylene glycol solutions using ion chromatography. *Solar energy materials*, *11*, 455–467. Retrieved from <http://www.sciencedirect.com/science/article/pii/0165163385900164>
- Sapkota, A., Anceno, A. J., Baruah, S., Shipin, O. V, & Dutta, J. (2011). ZnO nanorod mediated visible light photoinactivation of model microbes in water. *Nanotechnology*, *22*(21), 215703. doi:10.1088/0957-4484/22/21/215703
- Sharma, V., Singh, P., Pandey, A. K., & Dhawan, A. (2012). Induction of oxidative stress, DNA damage and apoptosis in mouse liver after sub-acute oral exposure to zinc oxide NPs. *Mutation research*, *745*(1-2), 84–91. doi:10.1016/j.mrgentox.2011.12.009
- Shen, L., Bao, N., Yanagisawa, K., Domen, K., Gupta, A., & Grimes, C. a. (2006). Direct synthesis of ZnO NPs by a solution-free mechanochemical reaction. *Nanotechnology*, *17*(20), 5117–5123. doi:10.1088/0957-4484/17/20/013

- Smijs, T., & Pavel, S. (2011). Titanium dioxide and ZnO NPs in sunscreens: focus on their safety and effectiveness. *Nanotechnology, Science and Applications*, 95–112.
- Socrates, G. (2001). *Infrared and Raman Characteristic Group Frequencies* (3rd ed.). Chichester: John Wiley and Sons Ltd.
- Solid State NMR service (2012) Durham, Private Communication with David Apperly
- Song, K., Xu, P., Meng, Y., Geng, F., Li, J., Li, Z., Xing, J., et al. (2013). Smart gold NPs enhance killing effect on cancer cells. *International journal of oncology*, 42(2), 597–608. doi:10.3892/ijo.2012.1721
- Song, W., Zhang, J., Guo, J., Zhang, J., Ding, F., Li, L., & Sun, Z. (2010). Role of the dissolved zinc ion and reactive oxygen species in cytotoxicity of ZnO nanoparticles. *Toxicology letters*, 199(3), 389–97. doi:10.1016/j.toxlet.2010.10.003
- Stoch, J., & Gablankowska-Kukucz, J. (1991). The effect of carbonate contaminations on the XPS O 1s band structure in metal oxides. *Surface and Interface Analysis*, 17(3), 165–167. doi:10.1002/sia.740170308
- Strobel, R., & Pratsinis, S. E. (2011). Effect of solvent composition on oxide morphology during flame spray pyrolysis of metal nitrates. *Physical chemistry chemical physics : PCCP*, 13(20), 9246–52. doi:10.1039/c0cp01416h
- Strobel, R., Baiker, A., & Pratsinis, S. E. (2006). Aerosol flame synthesis of catalysts. *Advanced Powder Technology*, 17(5), 457–480. doi:10.1163/156855206778440525
- Stumm, W., & Morgan, J. J. (1995). *Aquatic Chemistry: Chemical Equilibria and Rates in Natural Waters* (3rd ed.). New York: Wiley-Interscience.

- Suchanek, W. L. (2009). Systematic study of hydrothermal crystallization of ZnO (ZnO) nano-sized powders with superior UV attenuation. *Journal of Crystal Growth*, 312(1), 100–108. doi:10.1016/j.jcrysgro.2009.09.051
- Suga, M., Nishiyama, H., Konyuba, Y., Iwamatsu, S., Watanabe, Y., Yoshiura, C., Ueda, T., et al. (2011). The Atmospheric Scanning Electron Microscope with open sample space observes dynamic phenomena in liquid or gas. *Ultramicroscopy*, 111(12), 1650–1658. doi:10.1016/j.ultramic.2011.08.001
- Światowska-Mrowiecka, J., Zanna, S., Ogle, K., & Marcus, P. (2008). Adsorption of 1,2-diaminoethane on ZnO thin films from p-xylene. *Applied Surface Science*, 254(17), 5530–5539. doi:10.1016/j.apsusc.2008.02.170
- T Distribution Critical Values Table, (2013). Available: <http://easycalculation.com/statistics/t-distribution-critical-value-table.php>; Last accessed 10/12/2013
- Takenaka, S., Karg, E., Kreyling, W. G., Lentner, B., Schulz, H., Ziesenis, A., Schramel, P., et al. (2004). Fate and toxic effects of inhaled ultrafine cadmium oxide particles in the rat lung. *Inhalation toxicology*, 16 Suppl 1, 83–92. doi:10.1080/08958370490443141
- Tan, W. B., & Zhang, Y. (2005). Surface modification of gold and quantum dot NPs with chitosan for bioapplications. *Journal of biomedical materials research. Part A*, 75(1), 56–62. doi:10.1002/jbm.a.30410
- Tang, E., Cheng, G., & Ma, X. (2006). Preparation of nano-ZnO/PMMA composite particles via grafting of the copolymer onto the surface of zinc oxide NPs. *Powder Technology*, 161(3), 209–214. doi:10.1016/j.powtec.2005.10.007
- Tani, T., Mädler, L., & Pratsinis, S. (2002). Homogeneous ZnO NPs by flame spray pyrolysis. *Journal of Nanoparticle Research*, 4(4), 337–343. doi:10.1023/1021153419671

- Tantra, R., Tompkins, J., & Quincey, P. (2010). Characterisation of the de-agglomeration effects of bovine serum albumin on NPs in aqueous suspension. *Colloids and surfaces. B, Biointerfaces*, 75(1), 275–81. doi:10.1016/j.colsurfb.2009.08.049
- Taroco, H. A., Santos, J. A. F., Domingues, R. Z. and Matencio, T.. 2011. “Ceramic Materials for Solid Oxide Fuel Cells.” in *Advances in Ceramics - Synthesis and Characterisation, Processing and Specific Applications*, edited by Cosats Sikalidis. InTech.
- Taylor, H. E. (2001). *Inductively Coupled Plasma Mass Spectrometry: Practices and Techniques*. Academic Press.
- Techservices, e-mail correspondence 29/08/2012 Alfa Aesar, [avocado.techservices@alfa.com](mailto:avocado.techservices@alfa.com)
- Tenzer, S., Docter, D., Rosfa, S., Wlodarski, A., Kuharev, J., Rezik, A., Knauer, S. K., et al. (2011). Nanoparticle size is a critical physicochemical determinant of the human blood plasma corona: a comprehensive quantitative proteomic analysis. *ACS nano*, 5(9), 7155–67. doi:10.1021/nn201950e
- Teoh, W. Y., Amal, R., & Mädler, L. (2010). Flame spray pyrolysis: An enabling technology for NPs design and fabrication. *Nanoscale*, 2(8), 1324. doi:10.1039/c0nr00017e
- Tiwari, D., Behari, J., & Sen, P. (2008). Application of NPs in waste water treatment. *World Appl Sci J*, 3(3), 417–433.
- Turney, T. W., Duriska, M. B., Jayaratne, V., Elbaz, A., O’Keefe, S. J., Hastings, A. S., Piva, T. J., et al. (2012). Formation of zinc-containing nanoparticles from Zn<sup>2+</sup> ions in cell culture media: implications for the nanotoxicology of ZnO. *Chemical research in toxicology*, 25(10), 2057–66. doi:10.1021/tx300241q



- Umar, A., Rahman, M. M., Vaseem, M., & Hahn, Y.-B. (2009). Ultra-sensitive cholesterol biosensor based on low-temperature grown ZnO NPs. *Electrochemistry Communications*, *11*(1), 118–121. doi:10.1016/j.elecom.2008.10.046
- Vakurov, A., Lopez, G. M., Drummond-Brydson, R., Wallace, R., Svendsen, C., & Nelson, A. (2013). ZnO nanoparticle interactions with phospholipid monolayers. *Journal of Colloid and Interface Science*, *404*, 161–168. doi:10.1016/j.jcis.2013.05.010
- Vandebriel, R., & De Jong, W. (2012). A review of mammalian toxicity of ZnO NPs. *Nanotechnology, Science and Applications*, *61*. doi:10.2147/NSA.S23932
- Vaseem, M., Umar, A., & Hahn, Y. (2010). ZnO NPs: Growth, Properties, and Applications. In A. Umar & Y.-B. Hahn (Eds.), *Metal Oxide Nanostructures and their Applications* (Vol. 5, pp. 1–36).
- Vayssieres, L., Keis, K., Hagfeldt, A., & Lindquist, S.-E. (2001). Three-Dimensional Array of Highly Oriented Crystalline ZnO Microtubes. *Chemistry of Materials*, *13*(12), 4395–4398. doi:10.1021/cm011160s
- Verwey, E. J. W., & Overbeek, J. T. G. (1948). *Theory of the stability of lyophobic colloids : the interaction of sol particles having an electric double layer*. New York ; London: Elsevier.
- Viswanatha, R., & D.D. Sarma. (2007). Growth of Nanocrystals in Solution. In C. N. R. Rao, A. Müller, & A. K. Cheetham (Eds.), *Nanomaterials Chemistry* (pp. 139–170). Weinheim: WILEY-VCH Verlag GmbH & Co. KGaA.
- Wahab, R., Ansari, S. G., Kim, Y. S., Song, M., & Shin, H.-S. (2009). The role of pH variation on the growth of zinc oxide nanostructures. *Applied Surface Science*, *255*(9), 4891–4896. doi:10.1016/j.apsusc.2008.12.037

- Wallace, R., Brown, A. P., Brydson, R., Milne, S. J., Hondow, N., & Wang, P. (2012). Characterisation of ZnO nanoparticle suspensions for toxicological applications. *Journal of Physics: Conference Series*, 371, 012080. doi:10.1088/1742-6596/371/1/012080
- Wallace, R., Brown, A. P., Brydson, R., Wegner, K., & Milne, S. J. (2013). Synthesis of ZnO nanoparticles by flame spray pyrolysis and characterisation protocol. *Journal of Materials Science*, 48(18), 6393–6403. doi:10.1007/s10853-013-7439-x
- Wang, C., & Chen, T. (2012). Intratumoral injection of taxol in vivo suppresses A549 tumor showing cytoplasmic vacuolization. *Journal of cellular biochemistry*, 113(4), 1397–406. doi:10.1002/jcb.24012
- Wang, L., & Muhammed, M. (1999). Synthesis of ZnO NPs with controlled morphology. *Journal of Materials Chemistry*, 9(11), 2871–2878. doi:10.1039/a907098b
- Wang, L., Wang, L., Ding, W., & Zhang, F. (2010). Acute toxicity of ferric oxide and zinc oxide NPs in rats. *Journal of nanoscience and nanotechnology*, 10(12), 8617–24.
- Wang, Z. L. (2004). ZnO nanostructures: growth, properties and applications. *Journal of Physics: Condensed Matter*, 16(25), R829–R858. doi:10.1088/0953-8984/16/25/R01
- Warheit, D. B., Webb, T. R., Colvin, V. L., Reed, K. L., & Sayes, C. M. (2007). Pulmonary bioassay studies with nanoscale and fine-quartz particles in rats: toxicity is not dependent upon particle size but on surface characteristics. *Toxicological sciences : an official journal of the Society of Toxicology*, 95(1), 270–80. doi:10.1093/toxsci/kfl128
- Watts, J. F., & Wolstenholme, J. (2003). *Introduction-Surface-Analysis-XPS-AES*. Chichester: John Wiley and Sons Ltd.

- White, H. D., Walker, M. L., & Trinick, J. (1998). A computer-controlled spraying-freezing apparatus for millisecond time-resolution electron cryomicroscopy. *Journal of structural biology*, *121*(3), 306–13. doi:10.1006/jsbi.1998.3968
- Williams, D. B., & Carter, C. B. (1996). *Transmission Electron Microscopy: A Textbook for Materials Science*. Springer.
- Winek, C. L., Shingleton, D. P., & Shanor, S. P. (1978). Ethylene and diethylene glycol toxicity. *Clinical toxicology*, *13*(2), 297–324. doi:10.3109/15563657808988239
- Wu, R., Xie, C., Xia, H., Hu, J., & Wang, A. (2000). The thermal physical formation of ZnO NPs and their morphology. *Journal of Crystal Growth*, *217*(3), 274–280. doi:10.1016/S0022-0248(00)00506-6
- Xia, T., Kovochich, M., Liong, M., Mädler, L., Gilbert, B., Shi, H., Yeh, J. I., et al. (2008). Comparison of the mechanism of toxicity of ZnO and cerium oxide NPs based on dissolution and oxidative stress properties. *ACS nano*, *2*(10), 2121–34. doi:10.1021/nm800511k
- Xia, T., Zhao, Y., Sager, T., George, S., Pokhrel, S., Li, N., Schoenfeld, D., et al. (2011). Decreased dissolution of ZnO by iron doping yields NPs with reduced toxicity in the rodent lung and zebrafish embryos. *ACS nano*, *5*(2), 1223–35. doi:10.1021/nm1028482
- Xiong, G., Pal, U., & Serrano, J. G. (2007). Correlations among size, defects, and photoluminescence in ZnO nanoparticles. *Journal of Applied Physics*, *101*(2), 024317. doi:10.1063/1.2424538
- Xu, R., & Di Guida, O. A. (2003). Comparison of sizing small particles using different technologies. *Powder Technology*, *132*(2-3), 145–153. doi:10.1016/S0032-5910(03)00048-2

- Yah, C. S., Simate, G. S., & Iyuke, S. E. (2012). NPs toxicity and their routes of exposures. *Pakistan journal of pharmaceutical sciences*, 25(2), 477–91. Retrieved from <http://www.ncbi.nlm.nih.gov/pubmed/23332175>
- Yong, K.-T., Law, W.-C., Hu, R., Ye, L., Liu, L., Swihart, M. T., & Prasad, P. N. (2013). Nanotoxicity assessment of quantum dots: from cellular to primate studies. *Chemical Society reviews*, 42(3), 1236–50. doi:10.1039/c2cs35392j
- Yu, T., Malugin, A., & Ghandehari, H. (2011). Impact of silica NP design on cellular toxicity and hemolytic activity. *ACS nano*, 5(7), 5717–28. doi:10.1021/nn2013904
- Zhang, K., Fang, H., Chen, Z., Taylor, J.-S. a, & Wooley, K. L. (2008). Shape effects of NPs conjugated with cell-penetrating peptides (HIV Tat PTD) on CHO cell uptake. *Bioconjugate chemistry*, 19(9), 1880–7. doi:10.1021/bc800160b
- Zhang, L., Chen, Z., Tang, Y., & Jia, Z. (2005). Low temperature cathodic electrodeposition of nanocrystalline zinc oxide thin films. *Thin Solid Films*, 492(1-2), 24–29. doi:10.1016/j.tsf.2005.06.028
- Zhang, Q., Chou, T. P., Russo, B., Jenekhe, S. a, & Cao, G. (2008). Aggregation of ZnO nanocrystallites for high conversion efficiency in dye-sensitized solar cells. *Angewandte Chemie (International ed. in English)*, 47(13), 2402–6. doi:10.1002/anie.200704919
- Zhao, Q., Wang, L., Cheng, R., Mao, L., Arnold, R. D., Howerth, E. W., Chen, Z. G., et al. (2012). Magnetic NP-based hyperthermia for head & neck cancer in mouse models. *Theranostics*, 2(1), 113–21. doi:10.7150/thno.3854
- Zheng, Jie, Melinda S. Stevenson, Robert S. Hikida, and P. Gregory Van Patten. 2002. “Influence of pH on Dendrimer-Protected NPs.” *The Journal of Physical Chemistry B* 106(6):1252–1255. Retrieved (<http://pubs.acs.org/doi/abs/10.1021/jp013108p>).